E -T D G V C : N N ?

Inauguraldissertation
zur
Erlangung der Würde eines Doktors der Philosophie
vorgelegt der
Philosophisch-Naturwissenschaftlichen Fakultät
der Universität Basel

von

T L

aus Erlangen (Deutschland)

Basel, 2007

Genehmigt von der Philosophisch-Naturwissenschaftlichen Fakultät

auf Antrag von
Prof. Dr. Eva K. Grebel und Prof. Dr. Bruno Binggeli

Basel, den 23. Januar 2007

Prof Dr. Hans-Peter Hauri
Dekan

E -T D G V C : N N ?

T L

Submitted for the Degree of Doctor of Philosophy

Department of Physics and Astronomy

University of Basel, Switzerland

January 2007

D R

Contents

Preface

"What is a human lifetime in the vastness of the Universe?"
Ignacio Ferreras

To deserve a doctorate in philosophy, I think I should at least write a few semi-philosophical lines here. What the heck is it that I have been working on so intensively in the last 27 months? Some product that will make our lives easier? Some starship that will allow us to conquer Mars? Or maybe a giant leap towards controllable nuclear fusion? Not really. It was only a tiny bit of new knowledge. Knowledge that you can only understand with a huge amount of previous knowledge. Knowledge about something that we will never reach, never touch, never get to see from the inside. Some people would call it a waste of time. And money. They would say it doesn't bring society forward. They would say it cannot be sold to anybody. They would say that the vast majority of honest, tax-paying citizens neither benefit from it nor even know about it.
So what should we do? Should we justify our profession with a few well-known examples on how it relates to other, more "useful" fields of research, like the astonishing progress in the development of high-quality optical systems or more and more powerful charge-coupled devices? I don't think so. Imagine a clear, starry night. Don't tell me you wouldn't take at least one look at the sky. Don't tell me you never found yourself asking what all these shimmering lights are. It might sound a bit pathetic, but isn't it the striving for knowledge that defines us? Isn't it this desperate attempt to go beyond our simple, three-dimensional imagination that has been said to make us more than just another species on this planet?
I could go on now about how doing academic research can train you in a number of skills that are considered to be highly useful in today's economy, like assessing the different aspects of a problem, combining previous knowledge such that it leads you to new results, and presenting the significance of your work to a larger audience. But beyond all this, I think it simply wouldn't be human if nobody wanted to know what's going on up there. That's my personal bottom line. No pseudo-justifications needed. No becauses. Except for one. High up on El Capitan, Kirk explains to Spock the most important reason for climbing a mountain:

"Because it's there!"

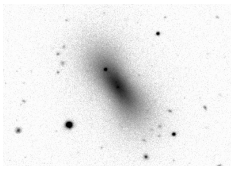

CHAPTER 1

I : - ?

"Classification is intuitive physics."
Bruno Binggeli

Since most astronomical research can only be done through observation, the luminosity and physical size of the objects under study typically scales with their distance. Stars can be analyzed mainly within our own galaxy and the Local Group of galaxies. Further out, galaxies cannot be resolved into individual stars, and so we can only measure their combined light. While at the distance of the Virgo cluster ($d \approx 15.8$ Mpc, $z \approx 0.004$), faint galaxies can still be studied fairly easily as far as exposure time is concerned, analyses at higher redshifts need to focus on the brighter galaxies. This, too, is a problem of resolution: although the surface brightness of a galaxy does not depend on its distance, the number of detector pixels covered by it does, and thus the *total* signal-to-noise ratio is inversely proportional to distance.

Figure 1.1 gives an impression of what is possible with a one-minute exposure and a 2.5 m-telescope at a site where the seeing conditions are far from ideal for astronomical observations. These images – actually a combination of three bands – were taken by the Sloan Digital Sky Survey (SDSS), and show three "bright" or "giant" elliptical galaxies (left) as well as two dwarfs (right) of the Virgo cluster, chosen such that they form a sequence in brightness. The definition of "dwarf galaxy" is mainy a division in magnitude: galaxies fainter than an absolute B magnitude of -18^{m} are commonly termed dwarfs. However, while Figure 1.1 might suggest a continuum in luminosity and surface brightness from dwarf to giant ellipticals, there has been a controversy since decades about whether or not systematic structural differences exist between them. But let us back up, and explain what an "elliptical" galaxy is, and why the term "early-type" is used in the thesis title instead.

The term "elliptical galaxy" (class "E" in the Hubble scheme, developed by Hubble in 1925; see Figure 1.2) is obviously a two-dimensional description — yet what is usually meant by it is a (three-dimensional) ellipsoidal object. Most lenticular galaxies (class "S0") would, from their two-dimensional appearance, also qualify for the term "elliptical", but they are classified differently, since they have a disk component. Now, there is one practical and one physical reason why Es and S0s

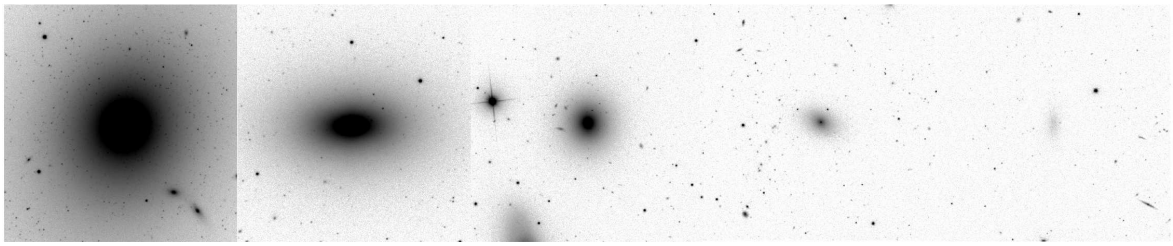

F 1.1. **Elliptical galaxies.** SDSS images, constructed by co-adding the *g*, *r*, and *i* bands, for VCC 1316 (M 87), VCC 1231, VCC 1146, VCC 0750, and VCC 0011 (from left to right), shown with the same scale, contrast, and intensity mapping.

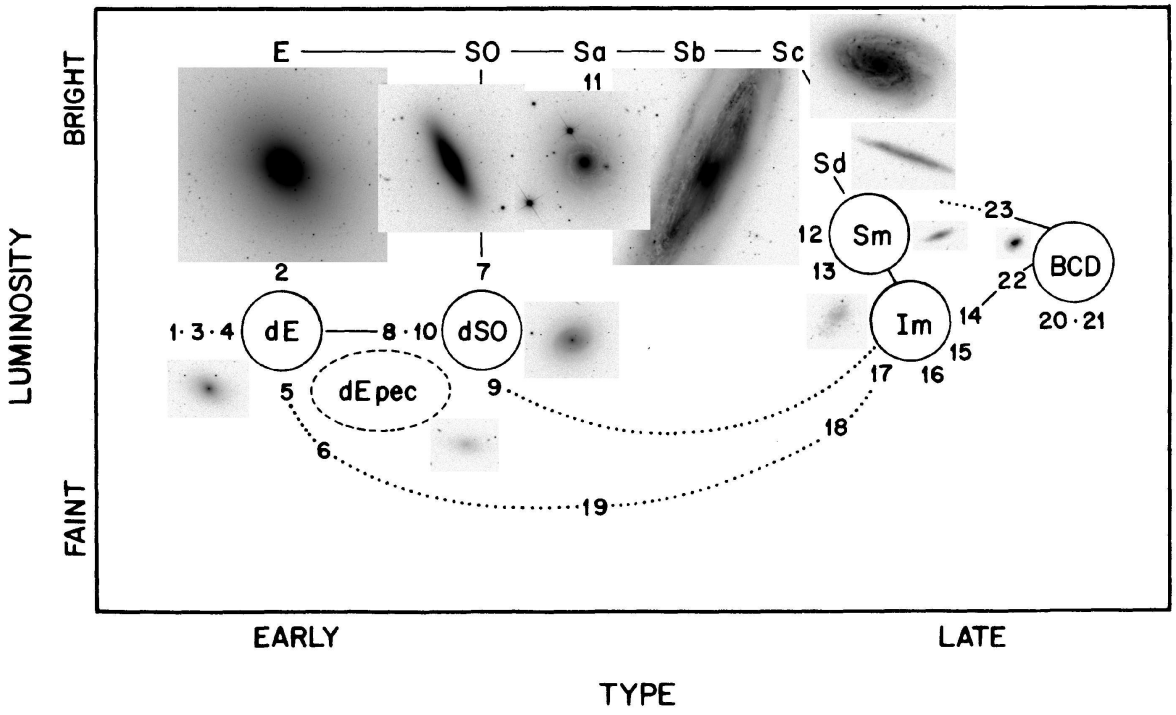

F 1.2. **Galaxy classification.** Adopted from Sandage & Binggeli (1984, their Figure 1), and illustrated with SDSS images (constructed by co-adding the *g*, *r*, and *i* bands). The galaxies shown are: E – VCC 0731, S0 – VCC 0685, Sa – VCC 1330, Sb – VCC 0092, Sc – VCC 0157, Sd – VCC 0162, Sm – VCC 0453, Im – VCC 0017, BCD – VCC 0144, dE – VCC 0750, dS0 – VCC 1010, dE(pec.) – VCC 0611. All images are shown with the same scale, contrast, and intensity mapping.

are often combined into a single dataset. The practical reason is that it is difficult to distinguish them, especially when S0s are seen nearly face on. The physical reason is that both of them are, in contrast to all other galaxy classes of the Hubble scheme, characterized by a smooth, regular, and axisymmetric[1] intensity distribution. Since Hubble originally believed that elliptical galaxies were an early form that might later evolve into spiral galaxies, Es and S0s are commonly termed "early-type" galaxies, while everything rightward of type Sb in Figure 1.2 is termed "late-type".[2]

Figure 1.2 illustrates the extension of the Hubble scheme to dwarf galaxies that has been presented by Sandage & Binggeli (1984, the main figure has been adopted from their publication, and SDSS images have been added to it). Here, the situation for the early-type dwarf galaxies is the same as for the giants: besides the "dwarf ellipticals" (class "dE"), there are "dwarf S0s" (class "dS0"), for which indications of a disk component were found. Both of them are characterized by a low surface brightness as compared to their giant counterparts, and, again, by a smooth and regular appearance. For our analyses presented in this thesis, we decided to not separate dEs and dS0s initially, in order to avoid any possible preselection bias. The reason for this is that the criteria for classifying a galaxy as "dS0" were rather diverse, like, e.g., high flattening, a bulge+disk-like profile, or the presence of asymmetric central features; moreover, they were indications only. For practical purposes, we shall therefore use the abbreviation "dE" for the *combined* sample of dwarf ellipticals and dwarf S0s throughout our studies, referring to them as early-type dwarfs.

[1] A spiral galaxy can, in principle, be perfectly symmetric about a 180-degree rotation, but it can never be perfectly *axisymmetric*, due to the spiral arms.

[2] The latter term is less accurately defined and depends somewhat on the area of research. One can, for example, also speak of early-type spirals and late-type spirals.

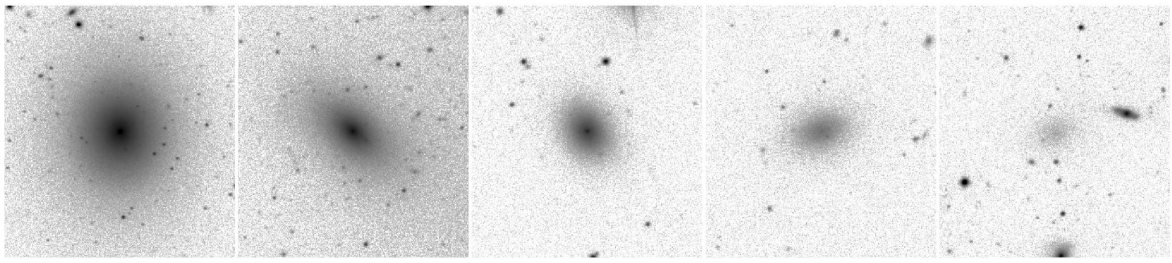

F 1.3. **Early-type dwarfs.** SDSS images, constructed by co-adding the *g*, *r*, and *i* bands, for VCC 0929, VCC 0745, VCC 0230, VCC 0273, and VCC 0244 (from left to right). All images are shown with the same scale, contrast, and intensity mapping.

Now that we have defined the class of early-type dwarf galaxies, let us turn to explaining our motivation in studying them, or more precisely, in studying those dEs that are members of the Virgo cluster. Early-type dwarfs are the most numerous type of galaxy in clusters, making them valuable probes for cluster assembly and evolution. This is of particular interest for the Virgo cluster, since it is known to be a dynamically young and largely unrelaxed structure — if the majority of dEs had formed in groups before they were accreted to the cluster, the assembly history of the cluster might be reflected in their stellar populations. Beyond this possibility of so-called preprocessing of dEs in groups, numerous other formation mechanisms have been suggested, mostly invoking the structural transformation of late-type galaxies falling into the cluster. The latter idea is mainly based on the pronounced morphology-density relation that exists both between clusters and the field, and within clusters themselves: early-type galaxies, including dEs, are preferentially located in regions of higher galaxy number density (i.e., towards the cluster center), while late-type galaxies are predominantly found in the outskirts of the cluster, i.e., in regions of lower density. Infalling late-type galaxies could thus lose their gas due to ram-pressure stripping, or tidal encounters with more massive cluster galaxies, or both — leading to cessation of star formation and eventually to the smooth and regular appearance of early-type galaxies.

One reason why there is still a lot of discussion about possible dE formation mechanisms and about their respective significance is that, despite the proximity of the Virgo cluster, dwarf galaxies are expensive to observe. This applies particularly to spectroscopy, which could provide more detailed insight into the stellar content than photometry can, but is difficult due to the low surface brightnesses of the dEs. The photographic survey of the Virgo cluster by Binggeli et al. (1985) has proven to be a milestone for studying dEs, and today, the resulting Virgo cluster catalog (VCC) is still the standard source of reference for follow-up analyses of Virgo dEs. Note that the study of galaxies belonging to a cluster has the advantage that one can roughly assume all galaxies to be at the same distance, thus allowing to use apparent magnitude as if it were absolute magnitude. The difficulty in obtaining data for a statistically significant sample of Virgo dEs is the large area covered by the cluster, namely about 100 square degrees. Even wide-field imagers are not able to target more than a handful of dwarfs at a time. Thus, more than twenty years after the Virgo cluster survey of Binggeli et al. (1985), the SDSS provides a unique opportunity to study cluster galaxies, and dEs in particular. While it is not deeper than the VCC dataset was, it provides homogeneous photometry in five optical bands, covering almost all VCC galaxies, and thus allowing a multicolour analysis of the Virgo dEs. Moreover, it has the obvious advantage of digital CCD imaging over photographic plates when it comes to data analysis — and we shall make extensive use of this advantage, e.g. by co-adding images of different bands, or by searching for substructure in our galaxies through the construction of unsharp mask images.

Before we start with describing our research, let us present a few “more favorable” images of the dEs than the ones shown in the previous figures. Our working sample of Virgo dEs spans a range of more than 4 magnitudes in apparent brightness, which is illustrated in Figure 1.3. The leftmost panel shows one of the brightest dEs of our sample (VCC 0929, $m_B = 13\overset{m}{.}7$), while the rightmost panel shows one of the faintest dEs (VCC 0244, $m_B = 18\overset{m}{.}0$). With a Virgo cluster distance modulus

of $m - M = 31\overset{m}{.}0$, corresponding to a distance of 15.8 Mpc, these galaxies would cover a range in absolute B magnitude from $-13\overset{m}{.}0$ to $-17\overset{m}{.}3$. Note that Binggeli et al. (1985) assumed $m - M = 31\overset{m}{.}7$, in which case VCC 0929 would have a B magnitude of $-18\overset{m}{.}0$, and would thus be at the magnitude limit commonly used for dwarf galaxies.

We will now begin with an analysis of the structural properties of dEs: in Chapter 2, we describe a systematic search for disk features in them. We then continue with another sort of dEs that show a "special feature", namely those with a blue center (Chapter 3). Having defined these two subclasses, we proceed with comparing their shapes and distributions to those of the "ordinary" dEs, thereby subdividing the latter into those with and without a nucleus (Chapter 4). After having established the morphological subdivision of the dE class, the next step is to analyze and compare their colour properties, and attempt to translate these into ages and metallicities of their stellar populations (Chapter 5). We then explore in Chapter 6 the distribution of colours, ages, and metallicities across the Virgo cluster. Finally, we present in Chapter 7 the analysis of a small subsample of our dEs with near-infrared photometry. A discussion about the possible mechanisms for dE formation is given in Chapter 8, attempting to answer the question of "nature or nurture." We conclude with a brief summary of the most important results in Chapter 9.

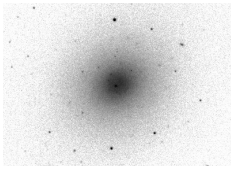

CHAPTER 2

S

"Is this all that I am? Is there nothing more?"
Spock, quoting V'ger

We present a systematic search for disk features in 476 Virgo cluster early-type dwarf (dE) galaxies. This is the first such study of an almost-complete, statistically significant dE sample which includes all certain or possible cluster members with $m_B \leq 18$ *that are covered by the optical imaging data of the Sloan Digital Sky Survey Data Release 4. Disk features (spiral arms, edge-on disks, or bars) were identified by applying unsharp masks to a combined image from three bands (g, r, i), as well as by subtracting the axisymmetric light distribution of each galaxy from that image. 14 objects are unambiguous identifications of disks, 10 objects show 'probable disk' features, and 17 objects show 'possible disk' features. The number fraction of these galaxies, for which we introduce the term dE(di), reaches more than 50% at the bright end of the dE population, and decreases to less than 5% for magnitudes* $m_B > 16^m$. *Although part of this observed decline might be due to the lower signal-to-noise ratio at fainter magnitudes, we show that it cannot be caused solely by the limitations of our detection method. The luminosity function of our full dE sample can be explained by a superposition of dE(di)s and ordinary dEs, strongly suggesting that dE(di)s are a distinct type of galaxy. This is supported by the projected spatial distribution: dE(di)s show basically no clustering and roughly follow the spatial distribution of spirals and irregulars, whereas ordinary dEs are distributed similarly to the strongly clustered E/S0 galaxies. While the flattening distribution of ordinary dEs is typical for spheroidal objects, the distribution of dE(di)s is significantly different and agrees with their being flat oblate objects. We therefore conclude that the dE(di)s are not spheroidal galaxies that just have an embedded disk component, but are instead a population of genuine disk galaxies. Several dE(di)s display well-defined spiral arms with grand design features that clearly differ from the flocculent, open arms typical for late-type spirals that have frequently been proposed as progenitors of early-type dwarfs. This raises the question of what process is able to create such spiral arms – with pitch angles like those of Sab/Sb galaxies – in bulgeless dwarf galaxies.*

This study was done together with Eva K. Grebel and Bruno Binggeli.
It has been published in The Astronomical Journal (2006, vol. 132, p. 497).

1. I

At first glance, early-type dwarf galaxies (dEs) are characterized by their smooth appearance, having no recent or ongoing star formation and apparently no gas or dust content. Since they are the most numerous type of galaxy in clusters, it is self-evident that most of the proposed formation scenarios for dEs reflect the vigorous gravitational forces acting within the very environment in which these galaxies typically reside. Ram-pressure stripping (Gunn & Gott 1972), galaxy harassment (Moore et al. 1996), and tidal stirring (Mayer et al. 2001a) are all based on the removal of gas and the morphological transformation of a late-type spiral or irregular galaxy, thereby attempting to reproduce the seemingly plain appearance of dEs. On the other hand, differences in the chemical abundances of early-type and late-type galaxies may argue against a simple morphological transformation (Grebel et al. 2003). In any case, such structural transformations would be well-suited to explain the famous morphology-density relation (Dressler 1980): the higher the density is, the more efficiently are infalling spirals and irregulars transformed into dEs, thereby skewing the relative abundance of different types of galaxy towards massive early-type objects as compared to abundances in the field. Moreover, Conselice et al. (2001) point out that the number of Virgo cluster dEs is more than a factor of 3 larger than what would be expected from just adding groups to the cluster. This strongly favours the idea that the majority of dEs were formed through a morphological transformation of galaxies that fell into the cluster.

Especially in recent years, small or intermediate-sized samples of early-type dwarfs have been studied in a large variety of ways. Boselli et al. (2005) found the relation of far-UV–near-UV colour and luminosity to behave opposite for early-type dwarfs and giants. Van Zee et al. (2004a) derive intermediate ages and subsolar to solar metallicities for dEs via optical multiband photometry. Similar values were reported by Geha et al. (2003) from a Lick index analysis of high-resolution spectra. These spectra and similar studies by van Zee et al. (2004b) and Simien & Prugniel (2002a) also revealed a significant amount of rotation in some dEs. Finally, Buyle et al. (2005) presented HI 21 cm line observations as a first study of the interstellar medium of a dE outside the Local Group.

However, no formation scenario could yet be clearly confirmed or rejected. This might be due to a very basic piece of the puzzle still lacking: the unambiguous characterization of early-type dwarf morphology. Following common definition, early-type dwarfs comprise both dwarf ellipticals and dwarf S0 (dS0) galaxies – we are not considering the fainter dwarf spheroidal galaxies (e.g. Grebel et al. 2003) or the ultra-compact dwarfs (e.g. Hilker et al. 1999) here. The morphological appearance and overall profile of a dwarf elliptical are clearly defined. In contrast, dS0 galaxies are loosely defined as objects whose overall appearance is similar to that of a dwarf elliptical, but where a more detailed examination shows non-elliptical properties such as lens shape or (central) asymmetries. Binggeli & Cameron (1991) argued that most of these characteristics were indicative of a disk nature, and the authors conjectured that “many, if not most, dS0 systems must be disk galaxies”. However, their existence as a separate class of objects has been put in question by several authors (e.g. Ryden et al. 1999), and dS0s have frequently been treated as a subclass of dwarf ellipticals (e.g. Barazza et al. 2003).

The unambiguous discovery of disk substructure (spiral arms and/or bars) in some dwarf ellipticals and dS0s (Jerjen et al. 2000; Barazza et al. 2002; Geha et al. 2003; Graham et al. 2003; De Rijcke et al. 2003) eventually proved the presence of a disk in at least some early-type dwarfs. At the same time, however, this raised the question of whether these objects are genuine disk galaxies, i.e. of flat oblate shape and without significant stellar spheroid, or whether they are spheroids hosting just a small disk component like the two low-luminosity ellipticals presented by Morelli et al. (2004). On the theoretical side, Mastropietro et al. (2005) showed that a fraction of the progenitor galaxy’s disk is able to survive the morphological transformation from galaxy harassment, providing a possible explanation for disks in early-type dwarfs.

Since up to now, a systematic analysis of a large sample of early-type dwarfs for the presence of disk features has been lacking, common practice has been to continue using the original classification of the Virgo cluster catalog (VCC, Binggeli et al. 1985), therefore calling some objects ’dwarf

elliptical', some 'dS0', and some 'dwarf elliptical with embedded disk'. In order to avoid confusion we assign the common abbreviation 'dE' to early-type dwarfs in general, thereby meaning both dwarf ellipticals and dS0s. We shall then examine each object for potential disk substructure, and introduce the term 'dE(di)' for a dE with disk features.

Clearly, the small sample of dE(di)s discovered so far can neither serve as basis for a revised classification nor is it sufficient to feed formation theories with quantitative input concerning the fraction and properties of such objects. A systematic search for disk features in dEs is thus required, and is made possible by the Sloan Digital Sky Survey (SDSS) Data Release 4 (DR4, Adelman-McCarthy et al. 2006) which covers almost the whole Virgo cluster with multiband optical imaging. With these data at hand, our study can properly address the following questions: a) whether all objects listed as dS0 in the VCC indeed show disk features, b) how large the fraction of galaxies with disk features is among dEs, c) how this fraction is distributed with respect to luminosity, d) where in the cluster these objects are located, and e) whether they appear to be genuine disk galaxies, or just spheroids with a disk component. The catalog of dE(di)s and dE(di) candidates resulting from this study will serve as important input for all future work on dEs, since the observables under study (e.g. dE colours) can then be correlated with the presence or absence of a disk.

Recently, Aguerri et al. (2005) have introduced a two-component definition of a dS0 based on one-dimensional profile fits, with those (Coma cluster) objects being called dS0s where a single Sérsic fit did not lead to a satisfying result and instead a combined Sérsic plus exponential fit was necessary. Our goal in this study, in contrast, is to uncover disk features on the two-dimensional image without any presumption on one-dimensional profile shapes. To investigate whether or not the two definitions go hand in hand is beyond the scope of this study, since it requires that accurate profile fits be done for all our SDSS galaxies. This will be the subject of a future paper.

Our data and sample selection is described in Section 2, followed by an outline of the techniques for image analysis in Section 3. Identifications of disk features are presented in Section 4. Section 5 focuses on the quantitative measurement of spiral features. The flattening distributions of the disk features and galaxies are analyzed in Section 6. The luminosity function and number fraction of dEs with and without disk features is the subject of Section 7, and the limitations in detecting disk features are considered in Section 8. In Section 9 we show how our objects are spatially distributed within the Virgo cluster, and a discussion and summary is given in Section 10.

2. D

2.1. SDSS images

The SDSS DR4 covers all galaxies listed in the Virgo Cluster Catalog (VCC, Binggeli et al. 1985) with a declination of $\delta \lesssim 16\overset{\circ}{.}25$, except for an approximately $2^\circ \times 2\overset{\circ}{.}5$ area at $\alpha \approx 186\overset{\circ}{.}2$, $\delta \approx +5\overset{\circ}{.}0$ (see Figure 2.1). It provides reduced and calibrated images taken in the u, g, r, i, and z band with a pixel scale of $0\overset{\prime\prime}{.}396$, which corresponds to a physical size of 30 pc when adopting $m - M = 31\overset{\mathrm{m}}{.}0$, i.e. $d = 15.85$ Mpc. The SDSS imaging camera takes data in drift-scanning mode nearly simultaneously in five photometric bands, u, g, r, i, and z, and thus combines very homogeneous multicolour photometry with large area coverage, good resolution, and sufficient depth to enable a systematic analysis of early-type dwarfs. The images have an absolute astrometric accuracy of RMS$\leq 0\overset{\prime\prime}{.}1$ per coordinate, and a relative accuracy between the r band and each of the other bands of less than 0.1 pixels (Pier et al. 2003). They can thus easily be aligned using their astrometric calibration and need not be registered manually. The effective exposure time of 54 s leads for a bright dE ($m_\mathrm{B} \approx 14^\mathrm{m}$) to a typical total signal-to-noise ratio (S/N) of about 1000 in the r-band within an aperture radius of approximately two half-light radii. For a faint dE ($m_\mathrm{B} \approx 18^\mathrm{m}$) this value is typically about 50. The RMS of the noise per pixel corresponds to a surface brightness of approximately 24.2 mag/arcsec^2 in the u-band, 24.7 in g, 24.4 in r, 23.9 in i, and 22.4 in z.

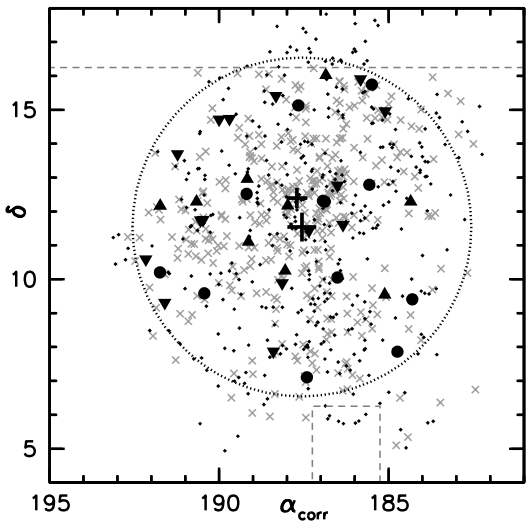

F 2.1. **Distribution of dE(di)s within the cluster.** Coordinates are given for J2000, and right ascension is corrected for the factor cos(δ), see text. Black circles are certain dE(di)s, black upward-pointing triangles are probable dE(di)s, and black downward-pointing triangles are possible dE(di)s. Grey crosses represent dEs where no disk was found. All other Virgo cluster galaxies with $m_B \leq 18\overset{m}{.}0$ are shown as small black dots. Only certain cluster members are considered. The upper black cross gives the position of M87, the lower black cross marks our cluster center, chosen such that the radius of a circle enclosing all dE(di)s (dotted black line) is minimized ($r = 5\overset{\circ}{.}0$). Boundaries of the SDSS coverage are shown as grey dashed lines.

2.2. Image stacking

In order to reach a higher S/N than that of the individual images, we produced a combined image by co-adding the g, r, and i-band images. The u and z-band images were not used, since their S/N is significantly lower and would thus lead to a decrease of the S/N of the combined image. When determining the sky level, proper object masks are required, so that pixels containing light from a star or a galaxy are excluded from the sky level calculation and only 'sky pixels' (i.e. pixels that contain nothing but sky background) remain unmasked. For this purpose, we applied the Source Extractor Software (Bertin & Arnouts 1996) to each object's image and each band to yield a 'segmentation image' which marks the pixels of all detected sources by assigning them non-zero values. To ensure proper masking of all objects, we expanded the source areas on the segmentation image by smoothing it with a Gaussian filter, using *IRAF*[1] (Tody 1993). The resulting image serves as object mask. The sky level was then determined with *IRAF*/*imstat* on the so-masked images along with the noise level, and was subtracted from the images. The g and i band images were shifted with *IRAF*/*imshift* to match the r band image; shifts were determined from the SDSS astrometry provided for each image (see above). We then applied weights $w_{g,r,i}$ to each image, following Kniazev et al. (2004):

$$w_{g,i} = \frac{S_{g,i}\,\sigma_r^2}{S_r\,\sigma_{g,i}^2}, \quad w_r = 1, \tag{1}$$

with $S_{g,r,i}$ being the sky level and $\sigma_{g,r,i}$ the noise level. The weighted g, r, and i-band images were then summed to form the final combined image for each object. The resulting total S/N is about a factor of $\sqrt{3}$ larger than in the r-band image.

[1] IRAF is distributed by the National Optical Astronomy Observatories, which are operated by the Association of Universities for Research in Astronomy, Inc., under cooperative agreement with the National Science Foundation.

2.3. Sample selection

From visual inspection of the combined images we chose a magnitude limit of $m_B = 18\overset{m}{.}0$ for our study, with m_B provided by the VCC. This is the same magnitude limit up to which the VCC was found to be complete (Binggeli et al. 1985). Adopting $m - M = 31\overset{m}{.}0$, it corresponds roughly to a limit in absolute magnitude of $M_B \leq -13\overset{m}{.}0$. A more thorough examination of our limitations in detecting disk features is presented later in Section 8. Initially, we selected all 552 cluster member and possible member galaxies with $m_B \leq 18\overset{m}{.}0$ that were classified as dwarf elliptical or dS0 in the VCC, including those with uncertainties. We took into account the revised membership and classification from Binggeli et al. (1993), as well as updated classifications for several objects given by Barazza et al. (2002, 2003), Geha et al. (2003), and Lotz et al. (2004b). 25 galaxies are not covered by the SDSS DR4. 25 objects with a classification 'dE/dIrr' were excluded, and also all the remaining objects were visually examined and excluded if they appeared to be possible dwarf irregulars due to asymmetric features in their image, which applied to 18 galaxies. Thereby we avoid biasing our sample by the inclusion of potential non-early-type objects (which might be disk galaxies anyway). Three more objects (VCC 0184, VCC 0211, VCC 1941) were classified as possible cluster members but appear to be probable background spirals because of their small size and their spiral arm structure, and were therefore excluded as well. Five more objects (VCC 0615, VCC 0811, VCC 1052, VCC 1776, VCC 1884) are of such low surface brightness that no examination for potential disk features is possible; these were also excluded. Our final sample comprises 476 early-type dwarfs, 414 of which are definite members of the Virgo cluster according to Binggeli et al. (1985, 1993).

3. I

For bringing to light weak features that are hidden by the dominating and mostly smooth and symmetric overall light distribution, two methods have proven suitable. Unsharp masks are a common technique in detecing and enhancing weak substructure like e.g. nuclear bars or spirals (e.g. Lisker et al. 2006a; Erwin 2004). They are produced by first smoothing an image and then dividing the original by the smoothed one, which can easily be performed automatically on a large dataset. Another technique is to model the smooth axisymmetric light distribution of a galaxy and subtract it from the original image (e.g. Barazza et al. 2002), with non-axisymmetric features like spiral arms remaining. Both methods have been used to identify spiral arms, bars, or edge-on disks in eight Virgo cluster early-type dwarfs so far (VCC 0490, VCC 0856, VCC 0940, VCC 1010, VCC 1036, VCC 1422, VCC 1488, VCC 1695; Jerjen et al. 2000, 2001; Barazza et al. 2002; Geha et al. 2003; Ferrarese et al. 2006). These techniques are described below, along with the derivation of an elliptical aperture for each galaxy, which is required as input for both methods.

From our analysis of dEs with blue central regions (Chapter 3) we know that a significant fraction of dEs where no disk features were detected show obvious colour substructure. Since we analyze the combined images from three bands in our search for disks, it could happen that colour substructure within the galaxy mimics the presence of a disk feature. To test this, we produced (uncalibrated) colour maps by dividing the aligned g and i-band images. Any detection of a disk feature with the methods outlined below can then be compared to the corresponding colour map and can thus be judged for reliability. To investigate whether or not there are any dEs in which colours do trace disk substructure requires a quantitative colour analysis that will be the subject of a future paper.

3.1. Elliptical apertures

An elliptical aperture for each galaxy was determined by performing ellipse fits with *IRAF/ellipse* on the combined image, allowing center, position angle, and ellipticity to vary. One of the outer elliptical isophotes – usually between 1 and 2 half-light radii – was then chosen by eye to trace best the *outer* shape of each galaxy, as exemplified for VCC 1010 in the upper left panel of Figure 2.2. This ellipse was adopted to define the ellipticity and position angle of the galaxy.

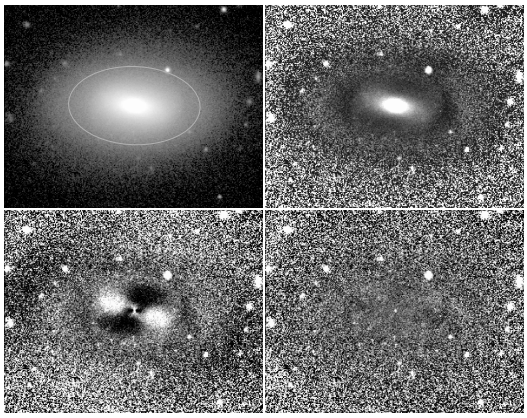

F 2.2. **Image analysis techniques.** *Upper left panel:* Combined image of VCC 1010, along with the elliptical isophote defining its shape. *Upper right panel:* Elliptical unsharp mask with kernel size $\sigma = 20$ pix. *Lower left panel:* 'Fixed model' residual image, i.e. produced via ellipse fits with fixed ellipticity and position angle. *Lower right panel:* 'Variable model' residual image, i.e. produced via ellipse fits with variable ellipticity and position angle. Each panel has a horizontal scale of 300 pixels (119″ or 9.13 kpc with $d = 15.85$ Mpc, i.e. $m - M = 31\overset{\mathrm{m}}{.}0$).

3.2. Unsharp masks

We produced a set of unsharp masks for each object by smoothing the combined image with a two-dimensional circular and elliptical Gaussian, one at a time, of various kernel sizes σ. A small value of σ will enhance small structures and weaken large features at the same time, while a large kernel size will enhance large structures over small ones. For each set of unsharp masks we chose values of $\sigma = 2, 4, 6, 9, 13, 20$, and 30 pixels. With $d = 15.85$ Mpc ($m - M = 31\overset{\mathrm{m}}{.}0$) and a subsequent pixel scale of 77 pc/arcsec (30 pc/pixel), these values correspond to 0.06, 0.12, 0.18, 0.27, 0.40, 0.61, and 0.91 kpc, respectively.

It is desirable to produce both masks created with a circular Gaussian (hereafter referred to as 'circular masks') and masks with an elliptical Gaussian ('elliptical masks') corresponding to the galaxy's ellipticity and position angle. Circular masks of non-circular artificial galaxies show a characteristic narrow shape along the major axis that could easily be confused with an edge-on disk and does not occur when applying elliptical masks. We demonstrate this in Figure 2.3, where a dE is represented by a two-dimensional exponential surface brightness profile with an elliptical shape created with *IRAF*/*mkobjects* (left panel). A circular unsharp mask with a Gaussian kernel of $\sigma = 4$ pix, feigning an edge-on disk, is shown in the middle panel. In the right panel, an elliptical mask with position angle and ellipticity matching that of the galaxy has been applied: no substructure is seen. This is due to the fact that the scale radius of the light profile is smaller along the minor axis; therefore an isotropic Gaussian will blur the object much stronger along the minor than along the major axis. For detection of egde-on disk features or bars that are roughly parallel to the major axis, elliptical masks are thus clearly preferred. However, frequently the inner isophotes of an object are significantly rounder than the outer ones that define the Gaussian's ellipticity. In these cases, again an artificial narrow (bar-like) structure will appear along the *minor* axis, due to the very same effect as described above. Here, circular masks serve as a complementary check whether an apparent elongated feature along the minor axis is real or is only caused by varying ellipticity.

3.3. Residual images from ellipse fits

A galaxy's surface brightness distribution can be modeled by performing ellipse fits (with *IRAF*/*ellipse*) and then feeding the output directly into the task *bmodel*. The resulting model image is then subtracted from the original object, yielding a residual image. Any information contained in the

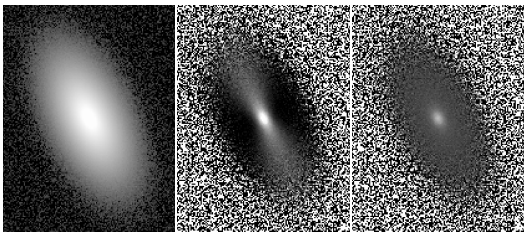

F 2.3. **Circular and elliptical unsharp masks.** *Left panel:* Simulated galaxy image created with *IRAF/mkobjects*, with exponential intensity profile, scale length along major axis 20 pixels, and axial ratio 0.5. *Middle Panel:* 'Circular' unsharp mask of the simulated galaxy, created with a circular Gaussian of kernel size $\sigma = 4$ pix. An elongated feature appears due to the application of a circular Gaussian to an elliptical object. *Right Panel:* 'Elliptical' unsharp mask with the same kernel size along the major axis, created with an elliptical Gaussian matching the position angle and axial ratio of the galaxy. Each panel has a horizontal scale of 138 pixels.

results of ellipse fitting directly enters the model. This can nicely be demonstrated on VCC 1010, which hosts a bar. If we construct a model through ellipse fits with *variable* position angle and ellipticity, the bar is not seen at all in the residual image (lower right panel of Figure 2.2) since it has been fully reproduced by the model. If position angle and ellipticity are instead fixed at a value taken well outside the bar (namely the chosen elliptical aperture as described above), a strong residual double-cone is seen (lower left panel of Figure 2.2), which has already been explained by Barazza et al. (2002) as characteristic shape of a changing position angle, and therefore of a bar. Similarly, spiral arms can be reproduced to a large extent by varying ellipses, and thus do not appear in the residual image unless position angle and ellipticity are kept fixed.

From the above considerations it is obvious that any disk feature can best be detected with a model built through fixed ellipticity and position angle (later referred to as 'fixed model'). However, in principle any *additional* weak, asymmetric features would require *variable* ellipse parameters ('variable model'), so that the bar or spiral is properly reproduced in the model and fully subtracted from the image, and the additional substructure remains. Therefore, both types of residual images were visually examined along with the unsharp masks for each object.

3.4. Artificial galaxies

In addition to the SDSS data we produced artificial dE galaxies with *IRAF/mkobjects*, adopting a two-dimensional exponential surface brightness profile with an elliptical shape (left panel of Figure 2.3). This 'primary' object was then superposed by another 'secondary' exponential light distribution with the same or higher ellipticity, representing an (inclined) disk within a spheroid (Figure 2.4). Various primary-to-secondary flux ratios, scale ratios, position angles and inclinations were reproduced, in order to provide a model counterpart for real galaxies that potentially are spheroids hosting a disk. The noise characteristics of the artificial images were chosen to be similar to a typical SDSS image, and galaxies covering a range of S/N values were created.

4. R : -

Close visual inspection of the combined image, the set of unsharp masks, and the two residual images was performed for each galaxy, using the *SAOImage DS9* tool (Joye & Mandel 2003). It turned out that unsharp masks are the primary means to search for substructure: especially for small elongated features, they often provide a more reliable and clearer detection than the residual images do. In turn, only in very few cases did the residual images show hints of substructure where the unsharp masks did not. However, in these cases the features were weak and their shape hard to define.

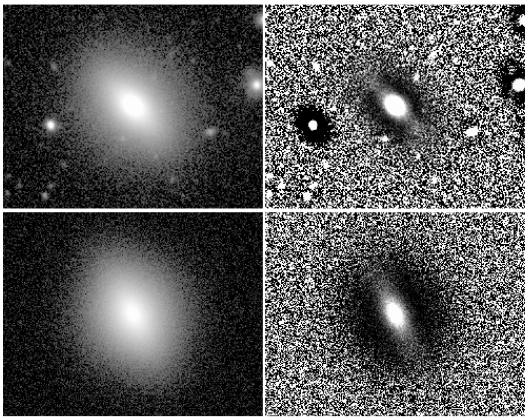

F 2.4. **Simulated vs. observed dE(di).** *Upper panels:* Combined image of VCC 0990 along with its elliptical unsharp mask (σ = 9 pix). *Lower panels:* Simulated two-component galaxy image along with its elliptical unsharp mask (σ = 9 pix). The 'primary' component has an exponential intensity profile with scale length 30 pixels, axial ratio 1. The 'secondary' component has an exponential intensity profile with equal scale length, axial ratio 0.5, and a total magnitude $0\overset{m}{.}5$ fainter than that of the primary component. The parameters are chosen to roughly match the appearance of VCC 0990. Note that the simulation contains no nucleus, which is why the central region of the unsharp mask is brighter in the observed image than in the simulated one. Each panel has a horizontal scale of 248 pixels (98″ or 7.55 kpc with d = 15.85 Mpc).

Therefore we adopted a conservative approach and did not consider them as possible substructure. As Barazza et al. (2003) pointed out, care must be taken with features seen solely on the residual images, since the models can be deceived by e.g. changing ellipticity and position angle, so that the resulting residual image would feign some substructure where none is present. Furthermore, the variable model turned out to be of little use, since it either reproduces substructure completely and yields a blank residual image (see Figure 2.2), or leaves only weak features that are readily seen in the unsharp masks and the fixed model residual image. The situation described above that the variable model would bring to light secondary features by reproducing and subtracting the primary ones did not occur, i.e. no secondary substructure remained in the residual image other than weak and highly doubtful features.

4.1. Disk detections

We identified 14 out of 476 early-type dwarfs that unambiguously show disk features, as exemplified in the upper three panels of Figure 2.5. Moreover, we find 'probable disks' in 10 objects (third panel from bottom of Figure 2.5), and 'possible disks' in 17 objects (lower two panels of Figure 2.5). This distinction between 'unambiguous', 'probable', and 'possible' disks is based on the visual judgement of all three authors, and is intended to be an honest representation of the (un)ambiguity and the S/N of disk features. In the case of a possible edge-on or inclined disk, we used comparisons with artificial two-component galaxies to check whether our interpretation is consistent with such a structure. This is exemplified in Figure 2.4, where the galaxy VCC 0990 – classified as 'probable' dE(di) – is compared to an artificial galaxy consisting of a 'primary' and a 'secondary' component, the latter being fainter and having a larger ellipticity (i.e. representing a larger inclination angle). The simulated image is chosen to be similar in S/N and size, and indeed the shape of the galaxy images as well as their unsharp masks look similar.

In two cases (VCC 1684 and VCC 1779), the colour maps (see Section 3) show a blue central region that is similar in appearance to the possible disk features. As a further test we produced unsharp masks for the two galaxies from the i-band images only. However, in both cases we can

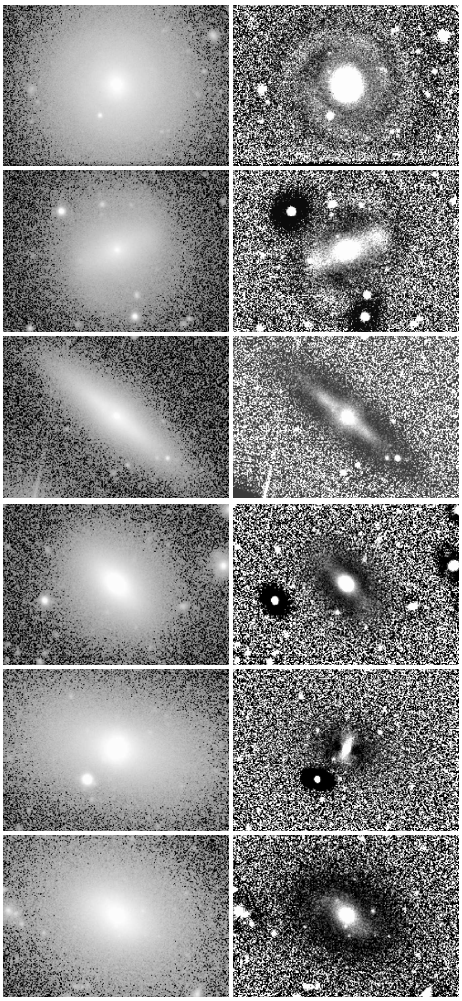

F 2.5. **Early-type dwarfs with disk features: dE(di)s.** Combined images and unsharp masks for three dEs with unambiguous disk features (top three rows), one probable dE(di) (fourth row), and two possible dE(di)s (last two rows). The galaxies are, from top to bottom: VCC 0308 (spiral arms; unsharp mask kernel size $\sigma = 20$ pix), VCC 1896 (bar and weak spiral arms; $\sigma = 13$ pix), VCC 1304 (edge-on disk; $\sigma = 20$ pix), VCC 0990 (inclined disk, also see Figure 2.3; $\sigma = 9$ pix), VCC 1183 (bar; $\sigma = 6$ pix), VCC 2019 (possibly inclined disk, maybe warped or distorted; $\sigma = 13$ pix). Each panel has a horizontal scale of 98″ (7.55 kpc with $d = 15.85$ Mpc).

neither reject nor unambiguously confirm the presence of an inclined disk. We thus list both objects as showing 'possible disk' features.

In several cases we could not decide whether we see an edge-on disk or a bar; nevertheless, both were taken as disk feature, since the presence of a bar commonly requires a disk. Moreover, apart from the simple category 'no substructure detected' (applying to 406 objects listed in Appendix E), we labelled 29 galaxies as objects where substructure of some kind is present, but not necessarily indicative of a disk ('other substructure'; objects listed in Appendix E). 17 of these show irregular central features (also see Section 4.2), five have a boxy shape, in four objects a feature like a dust lane is seen, and for three objects the unsharp masks appear to show a luminosity excess in the inner part.

Of the eight Virgo dEs for which disk features have been reported, five (VCC 0490, VCC 0856, VCC 1010, VCC 1036, VCC 1695) are contained in our 14 unambiguous detections, and one is a probable detection (VCC 1422). Both VCC 0940 (reported by Barazza et al. 2002) and VCC 1488 (reported by Geha et al. 2003) were not even identified as a dE(di) candidate by us. The reason might

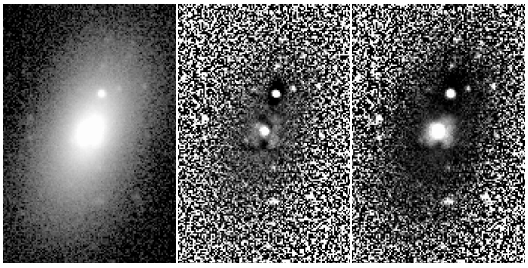

F 2.6. **A dE with irregular central substructure.** Combined image of VCC 0781 (left panel), unsharp mask image with kernel size $\sigma = 4$ pix (middle panel), and unsharp mask with $\sigma = 9$ pix (right panel). Of those dEs where substructure other than disk features was found, this galaxy represents the subgroup of objects with central irregularities likely to be caused by gas and/or dust. Each panel has a horizontal scale of 46″ (3.53 kpc with $d = 15.85$ Mpc).

be twofold: first, those studies (as well as De Rijcke et al. 2003) use a boxcar or median filter to create their unsharp masks. As we demonstrated above (see Figure 2.3 and Section 3.2), applying such a filter to a perfectly smooth elliptical light distribution will yield an artificial elongated structure in the unsharp mask. This effect might well apply to VCC 1488 with its axial ratio of 0.55, but less likely to VCC 0940 which has an axial ratio of 0.76. However, the disk features of both galaxies were also reported to be seen in the residual images resulting from ellipse fits and subsequent modeling of the light distribution. Given that both the data from Geha et al. (2003) and from Barazza et al. (2002) are of higher depth and resolution than our SDSS images, the non-detection of ours might simply reflect our limitations in detecting disks, and shows that more dE(di)s might exist than those identified by us (see also Sections 7 and 8).

We list the dE(di)s and dE(di) candidates in Table 2.1. We do, however, not attempt to reclassify objects, since classification schemes in the VCC were fairly complex and based on the surface brightness distribution, whereas we aim solely at stating whether or not a dE's image shows features of a disk. In principle, it would be desirable to establish a 'pure' definition of the dS0 class as those (and only those) dEs hosting (or being) a disk. Unfortunately, this is not possible: apart from the fact that many objects can only be termed candidates due to the limited S/N, those where no disk was *found* do not necessarily have to *have* no disk. It appears therefore most useful to not touch the original VCC classification, but instead to provide a list of (candidate) dE(di)s that can be correlated with all sorts of observables in future studies of dEs. A thorough reclassification of all galaxies is deferred to a future study. We point out that our objects are *not* related to the so-called dwarf spiral galaxies defined by Schombert et al. (1995): while those have a classical bulge, our objects do not.

4.2. Correlation with the original dS0 class

Binggeli & Cameron (1991) described five cases in which a galaxy was classified dS0, with characteristics mostly indicative of a disk nature of the galaxy. Briefly, criteria for dS0s were a bulge-disk-like profile, high flattening, a lens-like appearance, a global asymmetry (like a bar or boxiness), and an irregularity in the central part.

Our initial sample – prior to exclusion of possibly irregular objects – contained 47 out of 50 galaxies classified as dS0 or candidate dS0 (e.g. 'dE or dS0') in the VCC. Two objects were then exluded due to a possible irregular nature; thus 45 (candidate) dS0s are left in our working sample. 22 of these are indeed classified by us as dE(di)s or dE(di) candidates, constituting 54% of our dE(di) sample. 14 objects have 'other substructure' which reflects the criteria of Binggeli & Cameron (1991): 3 of them have a boxy shape, and 9 show irregular or clumpy central features likely caused by gas and dust. As an example for the latter, we show in Figure 2.6 the image and unsharp masks of VCC 0781, which looks somewhat similar to the well-known dwarf elliptical NGC205 in the Local Group. Interestingly, all of these 9 objects with central gas/dust features have a blue central region with ongoing

T 2.1. **Early-type dwarfs with disk features.** Objects are sorted by B magnitude m_B as given by Binggeli et al. (1985). Cluster membership is provided by Binggeli et al. (1985, 1993): M = certain cluster member, P = possible member. The last column contains information about the nature of the identified features: 1 = bar or edge-on disk, 2 = inclined disk, 3 = bar, 4 = disk, 5 = spiral arms, 6 = too flat for a spheroid, 7 = central gas or dust. The latter is an additional feature, but is not counted as disk. Numbers in brackets give uncertain features of which only a hint is present.

VCC	m_B	α_{J2000}	δ_{J2000}	M	N
Certain disks					
1010	$13\overset{m}{.}72$	$12^h27^m27\overset{s}{.}4$	$+12°17'25''$	M	3,4,(5)
0523	13.75	12 22 04.1	+12 47 15	M	3,4,(5)
2048	13.85	12 47 15.3	+10 12 13	M	1
1036	14.03	12 27 41.2	+12 18 57	M	2
0308	14.30	12 18 50.9	+07 51 43	M	5
0490	14.33	12 21 38.8	+15 44 42	M	5
0856	14.42	12 25 57.9	+10 03 14	M	5
1695	14.60	12 36 54.9	+12 31 12	M	1,5
1896	14.78	12 41 54.6	+09 35 05	M	3,5
1671	14.80	12 36 32.2	+06 10 11	P	5
0216	14.90	12 17 01.1	+09 24 27	M	5,(3)
0278	15.10	12 18 14.4	+06 36 14	P	5
1304	15.50	12 30 39.9	+15 07 47	M	2
1204	16.60	12 29 38.0	+07 06 24	M	2
Probable disks					
1422	13.81	12 32 14.2	+10 15 06	M	1
1949	14.19	12 42 57.8	+12 17 14	M	2,3,(4)
1947	14.56	12 42 56.4	+03 40 36	P	3,4
1392	14.62	12 31 55.9	+12 10 28	M	2
0407	14.64	12 20 18.8	+09 32 44	M	2
0990	14.81	12 27 16.9	+16 01 28	M	2
0218	14.88	12 17 05.4	+12 17 22	M	2,(6)
2050	15.20	12 47 20.6	+12 09 59	M	2
0336	16.20	12 19 17.6	+05 52 33	P	1
1691	17.30	12 36 51.1	+12 57 31	M	6,(5)
Possible disks					
1910	14.17	12 42 08.7	+11 45 15	M	1
1183	14.32	12 29 22.5	+11 26 02	M	3
0389	14.40	12 20 03.3	+14 57 42	M	4
2019	14.55	12 45 20.4	+13 41 34	M	4,(5)
0608	14.70	12 23 01.7	+15 54 20	M	2
2042	14.79	12 46 38.2	+09 18 27	M	4,(5)
1779	14.83	12 39 04.7	+14 43 52	M	2
1684	14.87	12 36 39.4	+11 06 07	M	2,(7)
1836	14.92	12 40 19.6	+14 42 55	M	5
0397	15.00	12 20 12.2	+06 37 24	P	2,4,(3)
1514	15.10	12 33 37.7	+07 52 17	M	2
1444	15.60	12 32 35.9	+09 53 11	M	6
0788	15.80	12 25 16.8	+11 36 19	M	2
1921	15.90	12 42 26.5	+11 44 25	M	2
2080	16.20	12 48 58.4	+10 35 12	M	2
0854	17.30	12 25 55.7	+12 46 11	M	6
1505	18.00	12 33 24.7	+15 24 28	M	6

star formation or at least very young stars, similar to NGC205 and also to the galaxy presented by Gu et al. (2006). This nicely confirms Binggeli's & Cameron's conclusion, "the irregularity must stem from recent or ongoing star formation" (drawn without colour information or unsharp masks!). None of these galaxies shows (additional) disk features; thus caution must be taken when treating them as dE(di)s only because of their dS0 class: not all classified dS0s are dE(di)s. These objects might prove highly important for investigating possible formation channels for dEs; therefore they are the subject of Chapter 3.

Finally, for 9 of the 45 (candidate) dS0s, neither a disk nor other substructure was found. However, three of these are classified 'dE or dS0', three are 'dS0?' (i.e. high uncertainty), and two are 'dS0:' (i.e. some uncertainty); hence we most probably did not miss any significant disk or irregular substructure. The one unambiguously classified dS0 (VCC 1912) had been classified as such mainly due to high flattening. While our measured axial ratio of 0.33 is small, it is not small enough that we would classify it as dE(di) based on flattening only.

5. P

5.1. Relative strength

For those three dE(di)s with the best-defined spiral arms, we now attempt to obtain an estimate of the relative amount of light that constitutes the spiral arms, as compared to the smooth and axisymmetrically distributed light. We thus need to measure the flux of the residual image (showing only the spiral arms) within a given aperture, and compare it to the total flux of the galaxy within the same aperture. We shall term this flux ratio the 'strength' of the spiral features. However, in the residual image the flux level in between the spiral arms is significantly negative: when fitting ellipses, the average flux value of each elliptical isophote is affected by the spiral arms and thus comes out slightly too high. Consequently, somewhat too much flux is assigned to the smoothly distributed light component, resulting in negative flux values when subtracted from the original image. To avoid or at least minimize this effect, we obtain optimized residual images through an iterative procedure outlined in detail in Appendix A, yielding a lower and an upper limit for the strength of the residual features.

The resulting residual images for our three dE(di)s are presented in Figure 2.7. Note that it is *not* the case that our disk detections would have been more efficient if we had used such optimized residual images from the beginning: the *contrast* of residual features like spiral arms does not differ with respect to the initial residual images – only the average flux level is offset systematically.

Apertures enclosing the spiral arms were now chosen manually, and the strength of the spirals was measured from the residual and the model flux within the same aperture. The nucleus as well as foreground stars or background objects were masked to avoid any bias. The results are listed in Table 2.2: VCC 0490 has the strongest spiral features, which amount to 12-13% of the total light. The spiral of VCC 0308 constitutes 8-11% of the light, and VCC 0856 only reaches 6-8%.

With these results at hand, we can now for the first time in the course of this study address the question of whether dE(di)s are disk galaxies, i.e. are of flat oblate shape like VCC 1304 (third row in Figure 2.5), or whether they are spheroids hosting a disk component. The ratio of the light within the spiral features to the smoothly distributed light has been measured to be within 6-12% for our three galaxies. Therefore, when assuming that these objects are spheroidal galaxies hosting an embedded disk, the total light within the disk cannot be much larger than the light within the spiral features, since otherwise the disk would be the dominating component and the object would not be a spheroidal galaxy in the common sense. Therefore, assuming the light within the spiral features to be of the same order as the total light of the disk component, the above ratio of 'spiral light' to the smoothly distributed light should be comparable to the ratio of the secondary to the primary component in our two-component model images. If, however, our galaxies would be genuine disk galaxies, the spiral features might well contain just a fraction of the total light of the disk. Consequently, if the disk is seen edge-on and compared to a suitable two-component model image, the ratio of its secondary

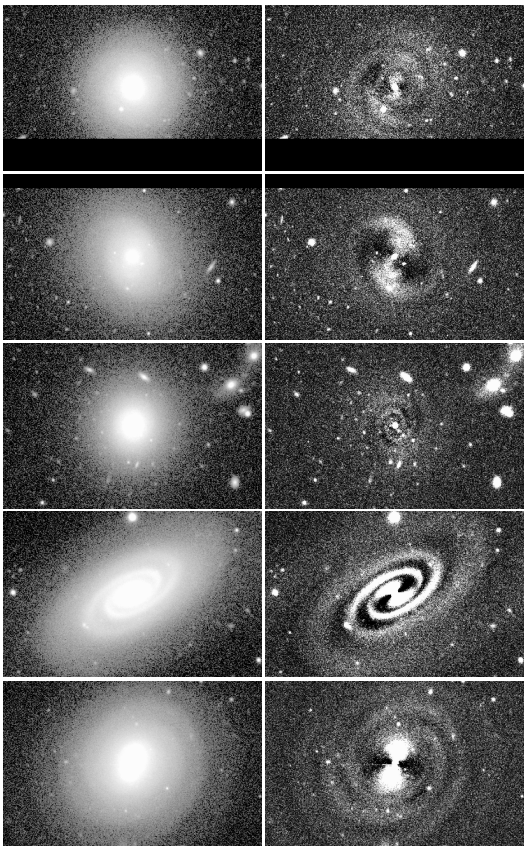

F 2.7. **Residual images of spiral arms.** Combined images as well as optimized residual images as described in Section 5.1 are shown for the three dE(di)s with the best-defined spiral structure (VCC 0308, VCC 0490, and VCC 0856 from top), as well as for the two dwarf-like S0/Sa galaxies (Section 5.2) VCC 0522 and VCC 1902 (bottom). Each panel has a horizontal scale of 162″ (12.48 kpc with d = 15.85 Mpc).

T 2.2. **Relative strength of spirals.** Columns 2-4 give measured values for the optimized residual image *without* median smoothing, columns 5-7 give the same quantities for the version *with* smooting (see text for details). Columns 2 and 5 give the ratio of the flux of the residual image to the flux of the model image within the chosen aperture. Columns 3 and 6 give the same as a magnitude difference, and columns 4 and 7 give the fraction of residual to total light.

VCC	$\frac{f_{\rm res}}{f_{\rm mod}}$	Δm	$\frac{f_{\rm res}}{f_{\rm total}}$	$\left(\frac{f_{\rm res}}{f_{\rm mod}}\right)_{\rm smoo}$	$\Delta m_{\rm smoo}$	$\left(\frac{f_{\rm res}}{f_{\rm total}}\right)_{\rm smoo}$
0308	0.107	2.43	0.097	0.082	2.71	0.076
0490	0.132	2.20	0.117	0.122	2.29	0.108
0856	0.075	2.81	0.070	0.059	3.07	0.056
0522	0.159	2.00	0.137	0.127	2.24	0.113
1902	0.150	2.06	0.131	0.102	2.47	0.093

to primary component should be significantly larger than the value measured for the (face-on) spiral features. Indeed, for those dE(di)s with apparent inclined disks that could not be confused with a bar, the secondary component of the similar-looking model images is only 0.5-1 magnitudes fainter than the primary component, whereas the spirals measured above are 2.2-3.1 magnitudes fainter than the smooth axisymmetric component. Although this is no final proof due to the small number of objects

considered, it points towards dE(di)s *being* disk galaxies, instead of just *having* a disk component. Further arguments supporting this view will be presented in Section 6.

5.2. A possible connection to faint S0/Sa galaxies

Since the strengths of the three spirals measured above already differ within a factor of two, it might be interesting to see how the galaxies' images would appear if their spirals were stronger by a certain amount. For this purpose, we simply multiplied the residual images by a certain factor and added them to the model of the smooth component, thereby mimicking a stronger spiral. Strikingly, with only a $0\overset{m}{.}5$-1^m enhancement, the galaxy does not look like a dwarf elliptical or dwarf S0 anymore, but instead like a spiral galaxy, although without a bulge.

It might thus be no coincidence that more than a decade ago, one of us (B.B.) identified a handful of "faint, dwarfish looking S0/Sa" galaxies in the Virgo cluster (VCC 0522, VCC 1326, VCC 1368, VCC 1757, VCC 1902) whose appearance is very similar to what has been just described (Figure 2.7). These objects differ from normal (i.e. giant) S0/Sa galaxies: their surface brightness profiles are similar to early-type dwarfs and remain flatter than the flattest possible King profile when going inwards, i.e. they apparently have no bulge (Binggeli, unpublished). Thus, they are hardly normal S0/Sa galaxies, which typically have a high bulge-to-disk ratio. Instead they have a central luminosity excess just like the early-type dwarfs.

One might thus term these objects 'dwarf-like S0/Sa' galaxies, to distinguish them from their giant counterparts. A further investigation of their characteristics and a detailed comparison with early-type dwarfs will be the subject of a future paper. For our present study, we selected those two with the best-defined spiral structure (VCC 0522, classified Sa, and VCC 1902, classified S0/Sa), in order to measure the spiral strength like we did above and compare it to the dE(di)s. Their strengths turn out to be slightly larger than the average value of the three dE(di)s and similar to the strongest dE(di) spiral (VCC 0490): 9%-13% for VCC 1902 and 11-14% for VCC 0522. Both objects are about half a magnitude brighter than the brightest dE(di)s. It thus appears plausible that the dE(di)s and these objects belong to the same population of galaxies that extends to magnitudes brighter than those of dEs and differs from the 'classical' dwarf ellipticals.

5.3. Pitch angle

In order to confirm our above hypothesis, we measured the pitch angle of the spiral arms of both dE(di)s and the dwarf-like S0/Sa galaxies on the residual images. We used the method described by Ma (2001): a spiral arm is traced by manually selecting a series of image positions that follow the arm. These are then fitted by a logarithmic spiral, taking into account the galaxy's inclination and position angle which we adopt from our elliptical apertures (in the case of VCC 1896 these values were taken from the axial ratio measurement of the disk). We measured two arms of VCC 0308, VCC 0490, VCC 0856, and VCC 1896, one arm of each of the two possible cluster members VCC 0278 and VCC 1671, and two arms of the two faint S0/Sa galaxies VCC 0522 and VCC 1902. The resulting values are shown in Figure 2.8 as black symbols and compared to the values for various Hubble types from Ma et al. (1999) (grey). The dwarf-like Sa VCC 0522 falls within the range of values of the dE(di)s while the dwarf-like S0/Sa VCC 1902 lies slightly below. The dE(di)s best agree with Hubble type Sab/Sb while the dwarf-like S0/Sa galaxies – if taken together – fall in the range of type Sab. An independent check of our measurements is provided by Jerjen et al. (2000) who found a pitch angle of $12\overset{\circ}{.}1$ for VCC 0856. For the two arms, we derive the values $10\overset{\circ}{.}5$ and $12\overset{\circ}{.}1$, respectively, thus being in good agreement with those VLT-data measurements. Our derived pitch angles are incompatible with spirals of very late type (>Sc), which are often considered as potential progenitors for dEs; see Section 10 for a discussion.

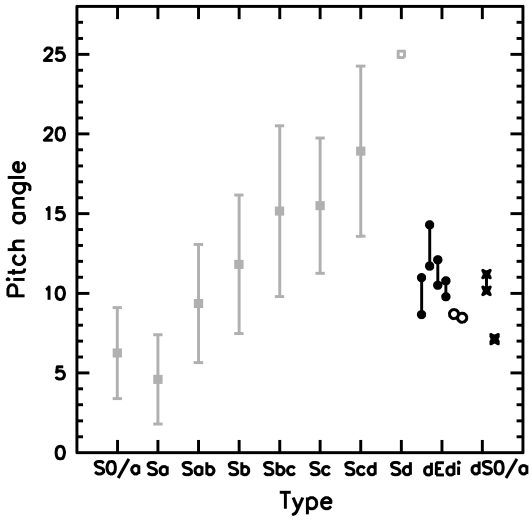

F 2.8. **Pitch angle vs. morphology.** *Grey symbols:* Mean pitch angle and 1-σ error bars of the spiral arms for various Hubble types as given by Ma et al. (1999). The value for type Sd was only derived from two objects. *Black filled circles:* Pitch angle for the certain cluster members VCC 0308, VCC 0490, VCC 0856, VCC 1896 (left to right) for two spiral arms each (connected symbol pairs). *Black open circles:* Pitch angle for the possible cluster members VCC 0278 (left) and VCC 1671 for one spiral arm each; in both cases the other arm could not be traced well enough. *Black asterisks:* Pitch angle for the dwarf-like S0/Sa galaxies (see text for details) VCC 0522 and VCC 1902 for two spiral arms each (connected symbol pairs; the values for the arms of VCC 1902 are almost equal).

6. F

A flattening distribution for our galaxies can be obtained in two ways: for the disk features themselves by directly measuring or estimating their axial ratio, and for the galaxies as a whole, based on their ellipticities. The first distribution – which we shall term the flattening distribution of the disks – serves as a basic test that the features we see are indeed disk features. This is of particular importance for the inclusion of 'probable' and 'possible' disk features into our working sample of dE(di)s. In order to have a statistically significant sample, e.g. to derive the luminosity function (Section 7), we would like to include not only those dEs with unambiguous disk features, but also those with probable and possible disk features into our dE(di) working sample. This requires the flattening distribution of disk features to be consistent with the assumption of an intrinsic flat oblate (and circular) shape, which shall be examined in the following subsection.

The flattening distribution of the *galaxies* – presented below in Section 6.2 – serves a different purpose: it will allow us to consider the question of the possible disk nature of the dE(di)s again. If they were spheroidal galaxies with a (weak) disk component, the distribution of axial ratios should be significantly different from that of disk galaxies. In turn, if their flattening distribution would be consistent with them having an intrinsic disk shape, they would very likely be genuine disk galaxies.

6.1. Flattening distribution of the disks

Although not possible with perfect accuracy, still an estimate of the inclinations of the disks (not the galaxies) can be obtained from either the unsharp mask or the residual images. An ellipse was manually (by eye) fitted to the disk using that unsharp mask or residual image where the respective features stand out most prominently (exemplified in Figure 2.9). The results are shown in the left panel of Figure 2.10 as a running histogram (black lines), i.e. at each data point we consider the number of objects within the chosen bin-width of 0.1 ($\pm$0.05). We take into account all 36 dE(di)s and candidates

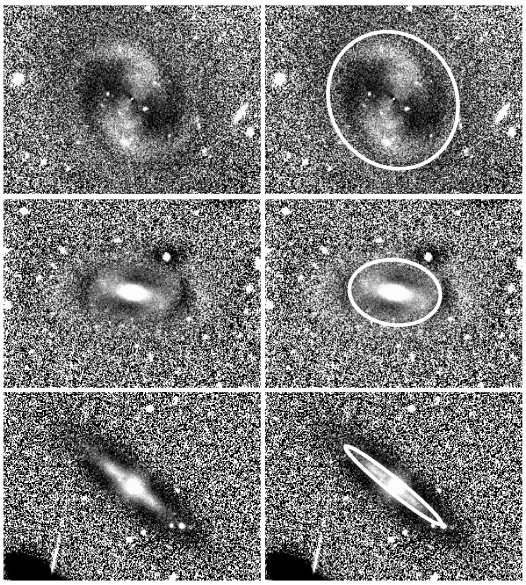

F 2.9. **Disk axial ratio measurement.** Illustration of manual choice of a best-fitting elliptical aperture (right panels) for each disk feature. From top to bottom: VCC 0490 (residual image), VCC 1010 (unsharp mask with kernel size $\sigma = 13$ pix), and VCC 1304 (unsharp mask with $\sigma = 20$ pix). Each panel has a horizontal scale of 116″ (8.95 kpc with $d = 15.85$ Mpc).

that are certain cluster members. Galaxies where we cannot decide whether we see a bar or an edge-on disk were assigned two values: a lower limit assuming an inclined disk (solid line), and an upper limit from the axial ratio of the galaxy as a whole, assuming the feature was a bar (dashed line). A theoretical distribution assuming a disk with an intrinsic axial ratio following a narrow Gaussian around a mean value $\mu = 0.25$ with $\sigma = 0.01$ and a randomly distributed inclination is shown as grey solid line for comparison (Mihalas & Binney 1981). Within the expected uncertainties for our relatively crude measurements, the observed and theoretical curve are nicely consistent with each other. This strongly corroborates the hypothesis that the features we see *are* disks, and moreover, it supports the approach of including not only the unambiguous but also the candidate objects into our dE(di) working sample for the purposes of our analysis. As a further test, we examined the flattening distribution for 'possible disks' only – it turns out to be very similar to the distribution for all dE(di)s. It therefore seems plausible that most of our 'possible' disk detections actually are disks. Nevertheless we prefer to keep the term 'possible' in order to reflect that uncertainties *are* present in our visual identification of disk features.

6.2. Flattening distribution of the galaxies

Based on the elliptical apertures described in Section 3.1 we put together the distribution of axial ratios of the (candidate) dE(di)s, shown in the right panel of Figure 2.10 as running histogram (black line). For comparison, we show the theoretical curve assuming an intrinsic axial ratio distribution given by a narrow Gaussian with $\mu = 0.35$ and $\sigma = 0.02$. Obviously, there is almost perfect agreement of observed and theoretical distribution, a compelling indication for an intrinsic disk nature of the dE(di)s! This view gains further support from the comparison with the distribution of dEs where no disk features were found (Figure 2.11): these objects are clearly consistent with a population of spheroids, and differ significantly from the dE(di) distribution. It thus appears very likely that dE(di)s are genuine disk galaxies. A prototypical representation of how these disk galaxies appear when viewed egde-on might be given by VCC 1304 (third row in Figure 2.5) with its axial ratio of 0.32.

While Binggeli & Popescu (1995) already found dS0s to be significantly flatter than dwarf ellipticals, the difference is even more pronounced for our comparison of dE(di)s and dEs with no disk

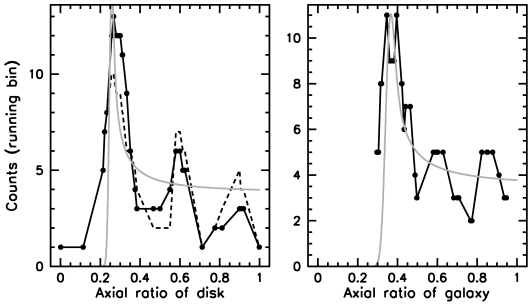

F 2.10. **Axial ratio distribution for disks and galaxies.** Running histogram with bin-width 0.1 for all 36 dE(di)s with certain cluster membership. *Left panel:* Distribution of axial ratio measurements of disk features as illustrated in Figure 2.9. For the solid black line we assume that all elongated features where we could not decide between an inclined disk or a bar actually are an inclined disk. For the dashed black line, we assume that these features are bars, and thus adopt the axial ratio of the *galaxy* as an upper limit. The grey line shows the theoretical distribution for an intrinsic axial ratio represented by a narrow Gaussian of $\mu = 0.25$, $\sigma = 0.01$, following Mihalas & Binney (1981). It is normalized to the same area under the curve as the black solid line. *Right panel:* Distribution of axial ratios of the galaxies. The grey line represents an intrinsic axial ratio that follows a a narrow Gaussian of $\mu = 0.35$, $\sigma = 0.02$, and is normalized like above.

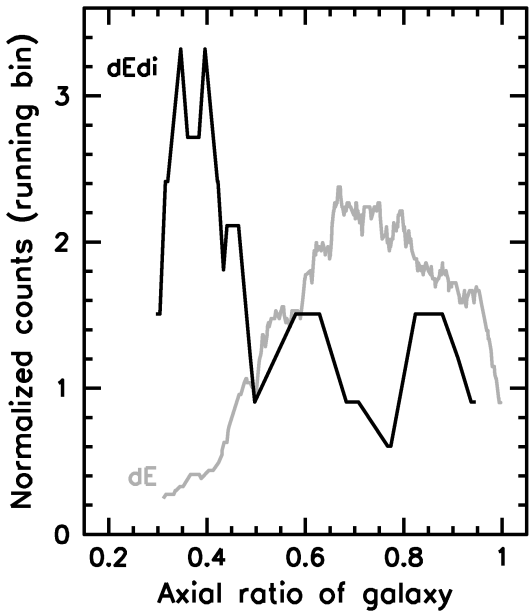

F 2.11. **Galaxy axial ratio distribution.** Running histogram of the galaxy axial ratio distribution of dE(di)s (black) and dEs where no disk features were found (grey). Both histograms are normalized to an area of 1.

detection. This is explained by the fact that not all dS0s are dE(di)s and vice versa: at least some galaxies that were classified as dS0 might be spheroids (see Section 4.2).

The flattening distribution also allows us to test whether or not *all* bright dEs might actually be dE(di)s, but are not identified as such due to limitations of our detection method. When we modify Figure 2.11 such that only galaxies of the brightest one-(two-)magnitude-interval are considered (not shown), the distribution of dEs with no disk detection is inconsistent with all of them being dE(di)s as well. Therefore, while we might miss *some* dE(di)s in our search for disk features as outlined in Section 8, we can exclude the possibility that *all* of the brightest dEs are disk galaxies – a significant number of objects need to be spheroids.

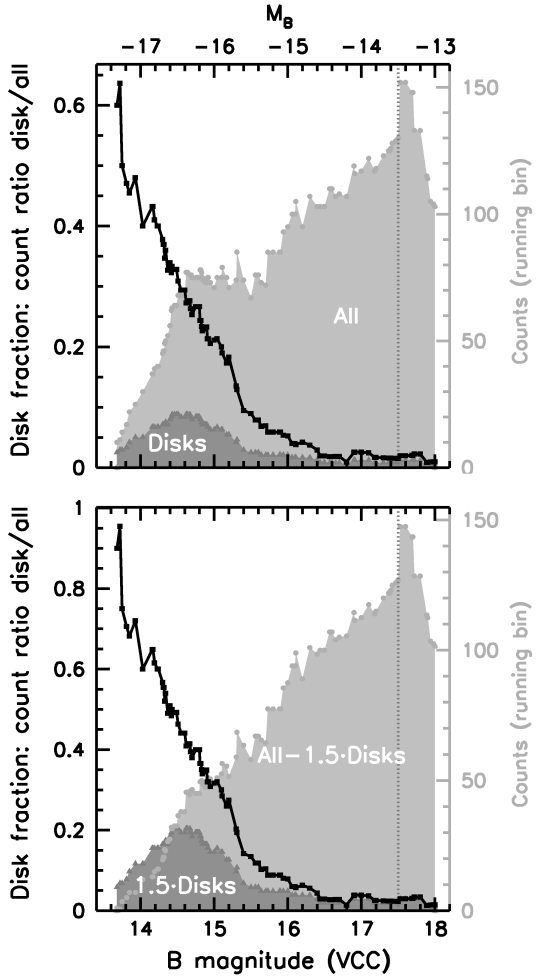

F 2.12. **Luminosity function and disk fraction.** *Upper panel:* Running histogram of the number of all dEs (light grey) and (candidate) dE(di)s (dark grey) with respect to B magnitude as given by the VCC. The bin-width is $1\overset{m}{.}0$, therefore the counts are incomplete for $m_B > 17\overset{m}{.}5$ (vertical dotted line). A bin is calculated at each position of a galaxy in the full sample. The upper x-axis gives absolute magnitude assuming $m - M = 31\overset{m}{.}0$. Only certain cluster members are considered. The ratio of both histograms is the disk fraction and is given as black symbols. *Lower panel:* Similar to the upper panel, but for all dEs minus 1.5 times the number of (candidate) dE(di)s (light grey), for 1.5 times the number of (candidate) dE(di)s (dark grey), and for the disk fraction resulting therefrom (black).

7. D

In the upper panel of Figure 2.12 we show the distribution of dEs and (candidate) dE(di)s with respect to their B magnitude provided by the VCC. For this purpose we present our data as a running histogram with a bin-width of $1\overset{m}{.}0$ (i.e. $\pm 0\overset{m}{.}5$). Only galaxies are considered that are certain cluster members according to Binggeli et al. (1985, 1993), resulting in 414 objects (light grey shaded histogram), containing 36 dE(di)s and candidates (dark grey shaded). The fraction of (candidate) dE(di)s among all dEs is shown as black solid line: it reaches more than 50% for the brightest objects, and then decreases to few percent at $m_B > 16^m$. This 'disk fraction' might be of special interest, since e.g. Binggeli & Cameron (1991) discuss a potential break in dwarf galaxy structure at $M_{B_T} \simeq -16^m$, which corresponds to $m_B = 15\overset{m}{.}7$ given their $m - M = 31\overset{m}{.}7$.

A plateau is seen in the running histogram (the luminosity function) of our full dE sample, the position of which coincides very well with the location of the dE(di)s in the diagram. As a test, we subtracted the dE(di)-counts from those of the full sample, but still a weak bump remains. However,

we need to take into account the fact that we might have missed a significant number of disks in dEs due to the limitations of our data (which are assessed in Section 8). Therefore, we now multiplied the dE(di) counts with 1.5 to account for the missed ones, and subtracted these counts from those of the full sample. Indeed, the plateau disappears (lower panel of Figure 2.12).

These results – independent of any considerations in previous sections – suggest very convincingly that dE(di)s are a different population than dEs with no disk, i.e. both have different origins not related to each other. Taken together with the indications for the disk nature of dE(di)s, evidence accumulates that dE(di)s are not just dwarf ellipticals with embedded disks, but instead constitute a population of disk galaxies different and independent from classical dwarf ellipticals.

In the following, we attempt to estimate the number of disks that are missed by our study, in order to assess whether the above assumption of a factor of 1.5 is realistic. Moreover, we attempt to independently show that the decline of the disk fraction is real, and cannot be just an effect of limited data quality.

8. L

To obtain a realistic estimate for the limitations in detecting disks, we artificially dimmed our objects such that they correspond to dEs that are fainter by one (two) magnitude(s), also taking into account the relation of dE magnitude and radius (Binggeli & Cameron 1991). This was done on the individual images and is described in more detail in Appendix B. The resulting modified images were then co-added like the original data, and unsharp masks were created. The dimmed objects were then treated as if they were real galaxies that have to be searched for disk features, and the same categories (’unambiguous’, ’probable’ etc.) were assigned.

In Figure 2.13, we focus on the galaxies lying within the brightest one-magnitude-interval (solid line, filled circles). When dimmed by 1 magnitude, they result in the histogram given by the dashed line with crosses, and when dimmed by two magnitudes, the resulting histogram is shown by the dot-dashed line with filled triangles. This is illustrating the disk fraction we would *expect* to see at fainter magnitudes *if* the fraction of the brightest one-magnitude-interval of our sample would be constant with magnitude.[2] The obvious mismatch, along with the already strong decrease in disk fraction *within* the brightest one-magnitude-interval itself, suggests that the observed decline in disk fraction is real, and is not due to the limitations of the data. Even if we do not assume the true fraction to be constant, we find down to $m_{\rm B} \approx 16\overset{\rm m}{.}0$ the observed disk fraction to decline much stronger per one-magnitude-interval than what would be expected from artificial dimming (see Appendix C).

However, still a fair part of the decline *is* likely to be caused by the latter effect: the curve for objects dimmed by 1 magnitude lies at about a factor of 1.2 lower than the original one, and the two-magnitude curve is even a factor of two lower. This shows that our above estimate of the true number of dE(di)s being larger by 1.5 than what we observe is a useful estimate for the average fraction of missed objects.

Still, the issue might be more subtle: if the *relative strength* of the disk features was decreasing with magnitude in addition to the S/N of the object *as a whole*, the estimate from artificially dimming the galaxies would be somewhat too high. While several of the disk features of the artificially dimmed galaxies would still be strong enough to be seen, some of the true observed ones would not. We examine this possibility in Appendix D, and find that indeed somewhat more dE(di)s than estimated above might be missed at fainter magnitudes due to data limitations. However, if the true disk fraction were to decrease to zero this effect would be of minor relevance. Although we are not able to give an accurate estimate of the true number fraction of dE(di)s, we point out again that our analysis is consistent with the approximation of multiplying the disk fraction with 1.5 in the lower panel of Figure 2.12. A significantly larger factor can be excluded following the argument given in Section 6.2:

[2] Here we neglect the fact that there is already a large decrease in disk fraction *within* the brightest one-magnitude-interval – however, a certain interval width is necessary in order to still have a fair number of dE(di)s left among the two-magnitude-dimmed dEs.

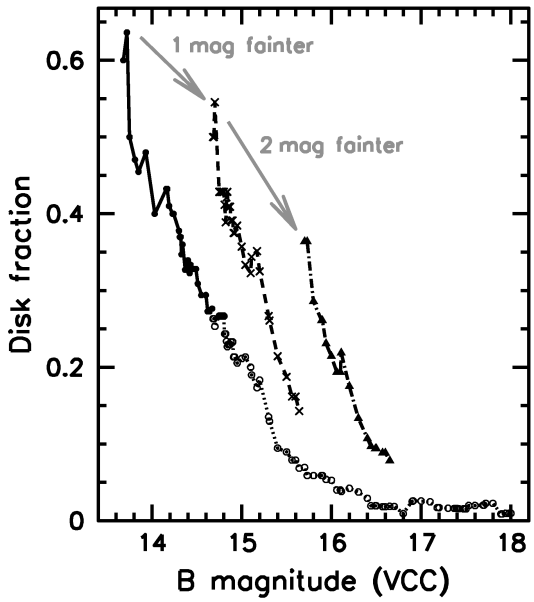

F 2.13. **Effect of S/N on the disk fraction.** *Upper panel:* Running histogram of the disk fraction as given in the upper panel of Figure 2.12 (solid and dashed line with circles). The brightest one-magnitude-interval is shown as solid line with filled circles, changing to a dotted line with open circles outside of the interval. When the dE(di)s in this interval are dimmed (see text) by 1 magnitude, the resulting disk fraction is given by the dashed line with crosses. A dimming by 2 magnitudes results in the dotted-dashed line with triangles. A histogram bin is calculated at each position of a galaxy in the full sample.

the flattening distribution of the brightest one-(two-)magnitude-interval of our sample is inconsistent with all bright dEs being disk galaxies and instead requires a significant number of objects to be spheroids.

9. S

It is well known that the projected spatial distribution of different morphological types of galaxies differs significantly (the so-called morphology-density relation, Dressler 1980). Therefore it appears interesting to examine the distribution of dE(di)s and dEs where no disk was found and compare it to other galaxy types. Those projected spatial distributions are shown in Figure 2.14, along with the distributions for giant ellipticals (Es), for Es and giant S0s together, for spiral galaxies, and for irregulars for comparison. Positions are taken from the VCC by use of the VizieR database (Ochsenbein et al. 2000). Only certain cluster members are considered, and intermediate or uncertain classifications between the types are excluded[3] Clearly, dE(di)s show the least clustering of all types, somewhat similar to the distribution of irregulars with $\delta > 10°$.

For a more quantitative analysis, we show the cumulative distribution of each type of galaxy with respect to the distance from the cluster center. Since there is no unique definition for the latter, we decided to choose a point such that the radius of a circle enclosing all dE(di)s is minimized (Figure 2.1). For this purpose we use a 'corrected right ascension', which we define as

$$\alpha_{corr} = (\alpha - \alpha_{center}) \cdot \cos(\delta) + \alpha_{center} \quad , \tag{2}$$

so that α_{corr} is measured in true degrees. We choose 'our' center to lie at

$$\alpha_{center} = \alpha_{M87} - 0\overset{\circ}{.}15, \quad \delta_{center} = \delta_{M87} - 0\overset{\circ}{.}85 \tag{3}$$

[3] For example, a galaxy classified as 'E/S0' is excluded from the sample of Es, but included in the combined sample of Es and S0s.

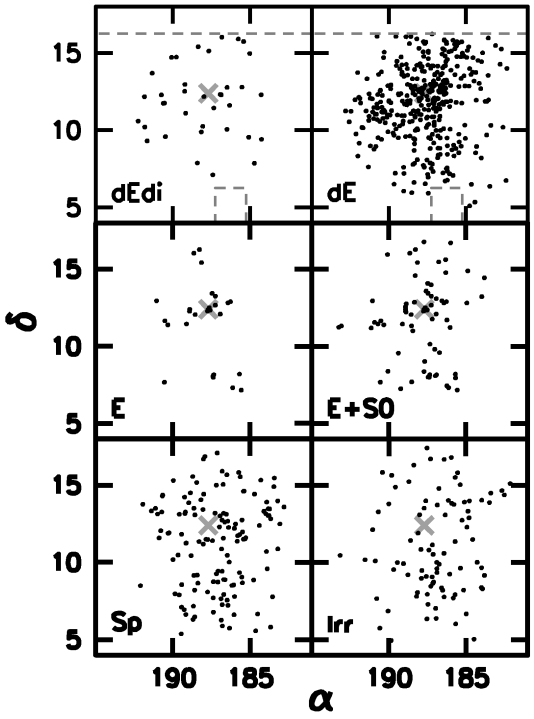

F 2.14. **Distribution of morphological types within the cluster.** For various types of galaxy (dE(di)s, dEs with no disk features, Es, Es+S0s, spirals, and irregulars) the projected spatial distribution is shown. Coordinates are given for J2000. Only certain cluster members are considered. The position of M87 is shown as grey cross. In the upper panels, boundaries of the SDSS coverage are shown as grey dashed lines.

i.e. going from M87 slightly towards M86 and M49. Interestingly, this circle at the same time encloses exactly all the giant ellipticals. For all other types, we only consider galaxies up to the maximum radius of the dE(di)s, in order to properly compare their clustering properties *within* that area. The fact that other galaxy types extend slightly further outwards might have physical significance, but could also be just due to the relatively small number of dE(di)s as compared to other types. Also, a part of it is due to the boundaries of the SDSS DR4 coverage, indicated with dashed grey lines in the upper panels of Figure 2.14.

We show the cumulative distributions in Figure 2.15. Along with the distribution for different morphological types, we show the expected distribution for an isothermal sphere ($\rho(r) \sim r^{-2}$) in the upper panel, and for constant density ($\rho(r) = \text{const.}$) in the lower panel, where $\rho(r)$ denotes the true volume density, not the projected surface density. This is done by populating a (three-dimensional) sphere at the distance of the Virgo cluster (taken to be $d = 15.85$ Mpc, i.e. $m - M = 31\overset{\text{m}}{.}0$) with the same number of objects as the number of dE(di)s, and then 'observing' the projected distribution of this sphere. Vertical intervals containing all but ±15.87% ($\equiv 1\,\sigma$) of Monte-Carlo-simulated values (darker grey) and all but ±2.27% ($\equiv 2\,\sigma$, lighter grey) are shown. Although a sphere is clearly not an ideal representation of the dynamically young and unrelaxed Virgo cluster, this simple model is intended to give at least a rough idea of the actual density distribution of the various galaxy classes.

The well-known difference in the distribution of giant ellipticals and spirals or irregulars is clearly visible, and serves as guidance for the question of what constitutes a *significant* difference between two galaxy types in the diagram. The dEs where no disks were found roughly follow the distribution of giant Es and S0s, i.e. they are less centrally clustered than the Es alone but more strongly than spirals and irregulars. In contrast, dE(di)s lie clearly below this distribution, and for most of the sample they show even less clustering than spirals and irregulars, confirming the impression given by Figure 2.14. While giant Es tend towards the isothermal sphere and spirals and irregulars more or

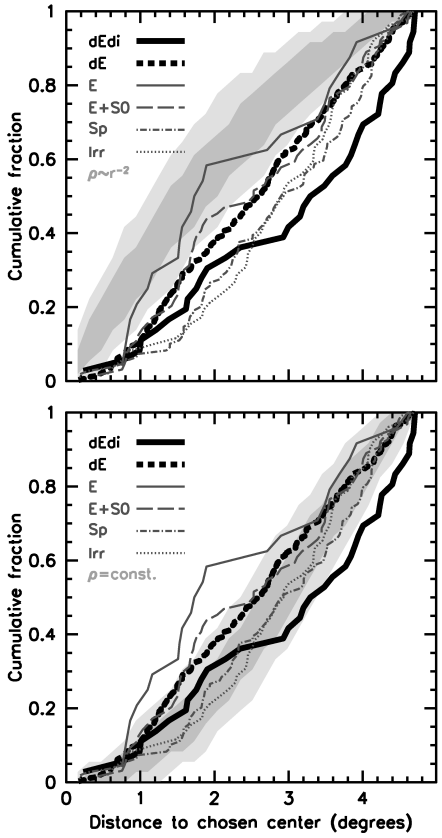

F 2.15. **Radial distribution of morphological types.** Both panels show the cumulative distribution of the angular distances of galaxies from our chosen cluster center (see text). Only certain cluster members are considered, and all galaxy types are only considered up to the maximum distance of the dE(di)s. Various line types give the cumulative distributions for dE(di)s, dEs with no disk features, Es, Es+S0s, spirals, and irregulars, as labelled in the figure. In the upper panel, Monte-Carlo-simulations were performed to yield the expected distribution for an isothermal sphere potential (i.e. $\rho \sim r^{-2}$) for a total number of 36 objects, i.e. the number of (candidate) dE(di)s. For the simulation, a distance to the Virgo cluster center of 15.85 Mpc was adopted (corresponding to $m - M = 31$), resulting in an angular scale of 0.28 Mpc/°. The simulated objects populate a sphere with a physical radius of 1.4 Mpc, i.e. corresponding to the angular value of 5.°0 for the circle in Figure 2.1. The resulting distribution is shown as grey areas that enclose vertical intervals around the median, containing all but ±15.87% of simulated values ($\equiv 1\,\sigma$, darker grey) and all but ±2.27% ($\equiv 2\,\sigma$, lighter grey). In the lower panel, analogous Monte-Carlo-simulations were done for a constant galaxy density. Note that 1(2)-sigma areas are only valid for a comparison with the dE(di)s, not with other types, since the number of galaxies is different for the latter.

less follow the distribution for constant volume density, dE(di)s even lie beyond the latter – a clear sign for them being not yet virialized, and thus being a population that has experienced fairly recent cluster infall.

For the sake of completeness, we also show the resulting distributions when M87 is chosen as cluster center instead (Figure 2.16). The difference between dE(di)s and dEs is now slightly less pronounced, but also it now varies somewhat less with radius than before. Here the dE(di)s follow closely the distribution of spirals, and fall within the 1-sigma area of the theoretical distribution for constant volume density – note, however, that a sphere around M87 is clearly no good representation of the Virgo cluster's shape. In contrast to the dE(di)s, dEs where no disk features were found approach the distribution of E+S0s, and at larger distances reach the distribution of the Es alone.

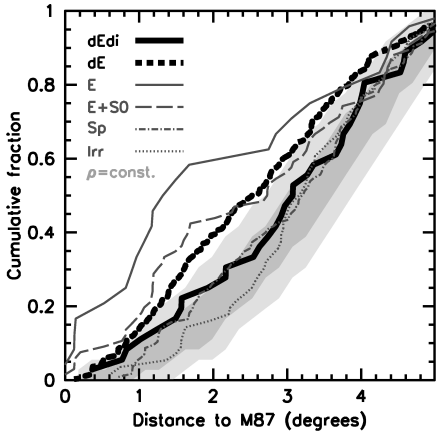

F 2.16. **Radial distribution with respect to M87.** Same as in Figure 2.15, but now adopting M87 as cluster center.

10. D

It is a long-standing question how early-type dwarf galaxies form, and whether there is more than one formation channel producing them. Current theories include ram-pressure stripping, galaxy harassment, or in-situ formation. However, for a proper theoretical approach of dE formation, first the characteristics and possible subpopulations of the dE class need to be fully understood and unveiled from the observational side. While the definition of the dS0 class by Binggeli et al. (1985) implied a disk nature of these objects, the fairly diverse classification criteria had to remain suggestive but not compelling for dS0s being disk galaxies. The discovery of disk features in a handful of dEs had not yet been succeeded by a systematic, quantitative study, and could thus not provide significant input for models of dE formation.

Moreover, kinematics – which might provide further insight into the presence of disks – are well studied only for a relatively small sample of dEs. With the SDSS data at hand, we performed for the first time a systematic search for disk features in an almost-complete sample of dEs down to $m_B \leq 18\overset{m}{.}0$, and found 41 out of 476 objects to show (possible, probable) disk features. In the light of the diversity of the early-type dwarfs, one of our primary and most important results is that dE(di)s most likely constitute a different galaxy population than dEs where no disk features are found: the bump in the luminosity function of dEs (Figure 2.12) is highly unlikely to be an intrinsic characteristic of just a single population, and it is nicely explained by the superposition of dE(di)s and dEs with no disk features. Therefore, at least two different formation scenarios appear to be required: one for each dEs with and without disk features.

When the first observations of spiral structure in dEs were made, galaxy harassment seemed to provide a simple explanation for the apparently embedded disks in dwarf ellipticals: Mastropietro et al. (2005) showed that the progenitor galaxy's disk need not be completely destroyed during the process of transformation, but part of it is left over inside the newly formed dwarf. However, we point out a main problem with this scenario: how could the observed *well-defined, early-type* spiral-arm structure of dE(di)s be reconciled with them having *late-type* progenitor spirals with their typically flocculent arm structure? Figure 2.8 directly compares the pitch angle of our objects to that of Scd and Sd galaxies in the diagram - and shows an obvious mismatch. If one assumes a relatively weak spiral structure for the late-type progenitor that would quickly disappear after star formation ceases, one might conclude that the above harassment scenario could still be valid, provided that the dE(di) spiral structure is purely of tidal origin, as e.g. suggested by Jerjen et al. (2000). The above question then changes into asking whether such well-defined spiral arms can at all be created through a process like harassment, and what parameters determine their appearance. To confirm that we are not looking at spiral structure traced by regions of star formation, we examined near-infrared H-band images for

VCC 0308 and VCC 0856 which we obtained through the ESO/ST-ECF Science Archive facility.[4] These images show the very same spiral structure as the optical data, consistent with what would be expected for grand-design, early-type spiral arms. A detailed examination of the colour properties of the spiral structure will be presented in a future paper.

Even without considering a specific formation theory, our data also allow us to address the question of whether dE(di)s are genuine disk galaxies or whether they are spheroids hosting a disk. Our distribution of axial ratios for the *disks* (i.e. where we measured the disk features, not the galaxies as a whole) agrees well with the expected distribution assuming an intrinsic axial ratio of 0.25 (left panel of Figure 2.10), confirming our general approach to finding disk features in dEs. More importantly, also the distribution of axial ratios of the *galaxies* where disk features were found is nicely consistent with the assumption of their being disk galaxies with an intrinsic axial ratio of 0.35 (right panel of Figure 2.10). This distribution significantly differs from the distribution of dEs with no disk features, the latter being consistent with a distribution of genuine spheroids. We do not see how this could be reconciled with the assumption that dE(di)s themselves are spheroids – instead, we take these results as compelling indication for dE(di)s being disk galaxies, represented by the edge-on view of VCC 1304 (third row of Figure 2.5).

Could this population of disk galaxies be simply an extension of their giant counterparts? The deduced intrinsic thickness of dE(di)s (0.35) agrees with the corresponding value for giant Sa galaxies as given by Fouqué et al. (1990) (0.37 for 'S0/Sa', 0.33 for 'Sa'; Schröder 1995), and the measured pitch angles best agree with Hubble type Sab/Sb (Figure 2.8). The dwarf-like S0/Sa galaxies presented in Section 5.2 could in fact bridge the gap from dE(di)s to giant disk galaxies. Here, the presence or absence of a 'classical' bulge can distinguish between what would be called a giant or a dwarf galaxy. However, early-type dwarfs are rare in the field environment, while early-type spiral galaxies are preferentially found in the field. This fundamental observation provides evidence against a close relation of dE(di)s and early-type spirals.

The projected spatial distribution of dE(di)s within the Virgo cluster differs significantly from dEs with no disk features, and implies that the population of dE(di)s is not virialized yet. Thus, if dE(di)s would be the result of a morphological transformation, this should have occured recently. Any spiral structure of the late-type progenitor galaxies would have had to be destroyed during the process, since the spiral arm characteristics of the dE(di)s are incompatible with being remainders from Sc/Sd spiral galaxies. While a pure star formation origin of the spiral arms is unlikely (see above), they might originate from the recent galaxy-galaxy interaction that triggered the transformation process. Since such spiral structure would quickly disappear after the interaction ended, one would expect the dE(di)s to still show structural distortions, i.e. to be less homogeneous in appearance. Moreover, a significant amount of tidal debris should still be present around them. At least the latter issue could be settled observationally with dedicated deep imaging of dE(di)s and their vicinity.

Even before the discovery of the first spiral structure within a dE by Jerjen et al. (2000), it was obvious from the existence of a dS0 class that treating all early-type dwarfs as one single population of galaxies always bore the risk of mixing objects that might have had different evolutionary histories. With our systematic search for disk features, we have now provided several strong indications that early-type dwarfs do indeed consist of two distinct populations of galaxies. Therefore, with our results at hand, we strongly recommend that those objects identified by us as (candidate) dE(di)s be considered separately from the rest of dEs in any future study of early-type dwarfs, like e.g. a study of dE colours. Furthermore, one should keep in mind that a significant fraction of the brighter dEs where we did not *find* any disk features might still *be* dE(di)s – this possible incompleteness could fake systematic differences between brighter and fainter dEs. We also suggest to separately consider objects where we did not find disk features but that have been classified as dS0 in the VCC, since our results confirm that these also differ from 'ordinary' dwarf ellipticals. As a technical recommendation, we advise caution on the interpretation of substructure that is seen in unsharp mask images created

[4] Observations made with ESO/NTT at the La Silla Observatory under programme ID 64.N-0288.

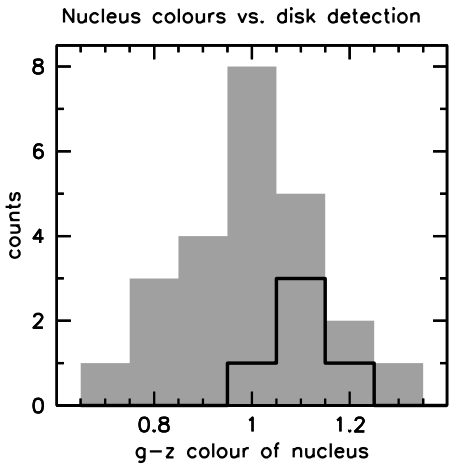

F 2.17. **Nucleus colours of dE(di)s.** Histogram of g-z colours of dE nuclei (grey) as derived by Strader et al. (2006). Five of these objects are dE(di)s; their nucleus colours are shown as black histogram.

with *isotropic* smoothing of a *non-circular* object: as illustrated in Figure 2.3, this can lead to artificial elongated features similar to an edge-on disk.

Now that the separation between dEs and dE(di)s has been established, their properties can be analyzed. Given the disk nature of the dE(di)s, a correlation with kinematical studies of early-type dwarfs is an obvious thing to do. Such a correlation has first been investigated by Geha et al. (2003) who found that two out of three rotating dEs show disk features, yet two out of four non-rotating dEs have weak disk substructure as well. Without going into the details of the kinematical analyses, we compiled results from several studies that state whether or not a dE shows significant rotation (van Zee et al. 2004b; Geha et al. 2003; Simien & Prugniel 2002a). Note that these studies differ in their data properties, their maximum radius for sampling the rotation curve, and their criteria for significant rotation. 18 out of 29 galaxies are found to be not rotationally supported, i.e. they show no or too slow rotation as compared to the observed velocity dispersion. 4 of these objects (22%) are (candidate) dE(di)s. However, it needs to be stressed that rotation curves are only sampled out to about the half-light radius, which might not be enough for definite statements about rotational support. 3 of those 4 dE(di)s do show significant rotation, but not enough to qualify for being rotationally supported. Of the 11 galaxies that were found to be rotationally supported, 6 (55%) are (candidate) dE(di)s. There is thus a tendency for dE(di)s to be rotationally supported systems, as one would expect for disk galaxies. The number statistics are consistent with our rough estimate of a third of the dE(di)s being missed in our study when assuming that most or all of them are rotationally supported.

Given the different spatial distribution of dE(di)s and dEs within the cluster, a further issue of interest would of course be their distribution of heliocentric velocities. These are available for 31 dE(di)s and 162 dEs where no disks were found. However, the two distributions do not differ significantly. Since the true threedimensional locations of our galaxies within the cluster are not known, let alone the exact threedimensional structure of the cluster itself, unfortunately no useful conclusion can be drawn here.

To demonstrate how our recommended separation of dE(di)s and the rest can be applied to other studies of early-type dwarfs, we show in Figure 2.17 the colours of dE nuclei derived by Strader et al. (2006): five objects of this sample are identified by us as dE(di)s, and show redder nucleus colours than the bulk of dEs. To obtain a clearer relation, it would be desirable to further pin down the possible disk nature of the remaining dEs where we could not find disk features. This calls for a larger sample of kinematically studied dEs as well as for deeper images of higher resolution to detect further substructure, so that more quantitative input for theories of dE and dE(di) formation can eventually be provided.

Acknowledgements

We gratefully acknowledge support by the Swiss National Science Foundation through grant number 200020-105260. We thank the referee for constructive suggestions. T.L. would like to thank Victor Debattista for repeatedly affirming that dwarf galaxies are *interesting. This study is based on publicly available data from the SDSS.*

A

A. Residual image optimization

In the residual images obtained in Section 3.3, the flux level in between the spiral arms is negative: when fitting ellipses, the average flux value of each elliptical isophote is affected by the spiral arms and thus comes out slightly too high (panel A of Figure 2.18). This results in negative flux values when the model is subtracted from the original image (panel B). We construct optimized residual images through the following iterative procedure. Where the initial residual image has negative flux values, its flux is set to zero, otherwise it is left unchanged (panel C). The resulting image is then subtracted from the original galaxy image (panel D), and a new residual image is obtained like before by fitting ellipses, constructing a new galaxy model, and subtracting it from the original image (panel E). This is repeated nine times iteratively, so that the final (tenth) residual image has reached (or come close to) a flux level of zero in between the spiral arms (panel F). A slight variation of this procedure is to smooth the residual image with a 3×3 pixel median filter each time before the negative flux values are set to zero. It turns out that the final image of the latter version still has a slightly negative overall flux level, while the version without smoothing yields a slightly positive (i.e. too high) overall value in the residual image. We therefore use the strength measurement from the version with smoothing as lower limit, and the one without smoothing as upper limit.

B. Artificial dimming of the galaxies

In order to artificially dim our objects by 1 (2) magnitudes, first the object size was decreased by a factor of 1.2 per magnitude with *IRAF/magnify*, preserving the total flux. This follows the relation of magnitude and radius of the dEs (Binggeli & Cameron 1991): on average, the radius decreases with a roughly a factor of 1.2 per magnitude. Since this demagnification also affects the PSF, the image was then convolved with a (normalized) Moffat kernel of proper size so as to approximately reproduce the original SDSS PSF (taken to be 1 FWHM = 4 pix; Stoughton et al. 2002). We then added noise to the image, with a σ larger by 2.51 (6.56) compared to the original noise, thereby simulating the S/N of the 1 (2) magnitude fainter object. To increase the noise σ by 1 magnitude, one would actually need to add noise with $\sigma' = \sqrt{2.51^2 - 1^2} \cdot \sigma = 2.30\,\sigma$. However, since the original noise has already been weakened by demagnifying the image, we chose to use $\sigma' = 2.51\,\sigma$ as a conservative approximation instead.

C. Effect of S/N on the disk fraction

In Figure 2.19 we show a running histogram of the observed disk fraction (solid line with filled circles) and of the fraction obtained after dimming all objects by 1 magnitude (dashed line with crosses). The original disk fraction lies clearly below the shifted one until the region where both become very small and are affected by small number statistics. It is important to point out that Figure 2.19 does *not* show how many dE(di)s would be detected assuming a constant true disk fraction. Instead, since all objects are dimmed by an equal amount (namely 1 magnitude), it shows the disk fraction that we would expect to find at a magnitude m when starting from the observed fraction at $m - 1^{\mathrm{m}}$ and artificially dimming the objects there. Thus, any difference between the observed value at $m - 1^{\mathrm{m}}$ and the 'expected' value at m is due to data limitations only. This is symbolized by the arrows in the figure. Consequently, if the observed decline from $m - 1^{\mathrm{m}}$ to m is stronger than this 'expected' one, at least part of it has to be real and be not only due to data limitations. The ratio between the two curves thus tells us how much stronger the observed decline *per one-magnitude-interval* is compared to what artificial dimming of the galaxies would predict. We plot this ratio in Figure 2.19 as grey solid line. Until $m_{\mathrm{B}} \approx 16\overset{\mathrm{m}}{.}0$ – where the number of dE(di)s becomes very small – for each one-magnitude-step the observed disk fraction declines a factor of 1.5-2.2 stronger than the 'expected' one from limitations of our data only. This clearly shows that the decline of the disk fraction is real.

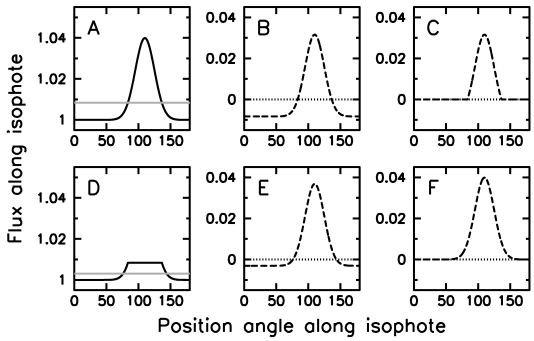

F 2.18. **Residual image optimization.** Sketch of the iterative method for improving the spiral arm residual image. Each panel shows the flux distribution along an elliptical isophote, i.e. with respect to position angle. The isophote is represented by a constant flux value superposed by a crossing spiral arm modeled by a Gaussian. See text for the details of the method. Panel A shows the initial flux as solid line, with the average flux value given as grey line. Panel B shows the residual flux as dashed line, with the zero value given as dotted line. Panel C results from B when all negative values are set to zero. Panel D is obtained by subtracting panel C from A, with the new average flux value given as grey line. This value is subtracted from the original flux and results in the residual flux given in panel E. Panel F shows the final residual flux after 9 iterations.

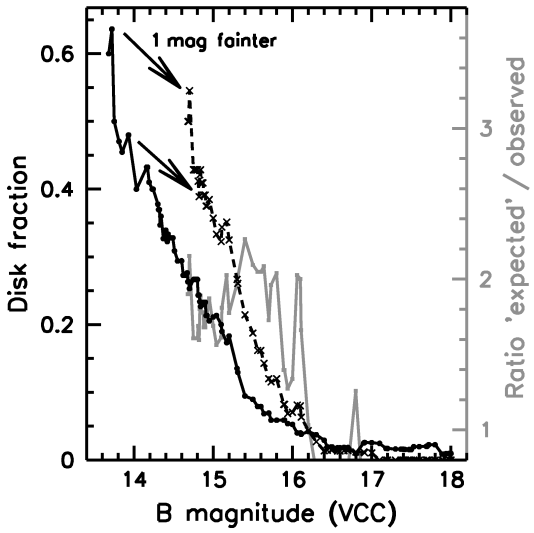

F 2.19. **Decline of the disk fraction.** Running histogram of the disk fraction as given in the upper panel of Figure 2.12 (solid line with circles). When all dE(di)s are dimmed by 1 magnitude (see text), the resulting disk fraction is given by the dashed line with crosses. A histogram bin is calculated at each position of a galaxy in the full sample. The grey line gives the ratio of both running histograms, and illustrates how much stronger the observed disk fraction declines per one-magnitude-interval than the 'expected' fraction does from artificial dimming only.

D. Effect of S/N on the flattening distribution of the disks

Apparent axial ratios of disk features were not only measured on the original images, but also on those where the galaxies had been artificially dimmed, in order to reveal potential changes in the flattening distribution with magnitude. In the upper panel of Figure 2.20 we compare the distribution of disk axial ratios for both the observed (black) and the artificially dimmed (grey) galaxies that lie within the brightest one-magnitude-interval of our sample. As in Figure 2.10, solid lines are derived from lower limits of the axial ratios, dashed lines from upper limits, depending on the interpretation of

an elongated feature as a bar or as an edge-on disk. Both curves are normalized to an area of 1. They show a tendency for the dimmed objects towards lower axial ratios, indicating that the (artificial) dimming of objects might slightly prefer disks of certain inclinations over others. However, the distribution of axial ratios for the galaxies of the *observed* second-brightest one-magnitude-interval is much more clearly skewed towards smaller axial ratios, i.e. larger inclinations (solid line in the lower panel of Figure 2.20). While the upper panel suggests that part of this is due to the effect of the S/N on the detectability of features like spiral arms, it might also be that such features are intrinsically weaker – or not even present – in fainter objects. For example, the observed second-brightest one-magnitude-interval does not contain objects that look like the close-to-face-on spirals in all of VCC 0308, VCC 0490, and VCC 0856, although it does contain galaxies with weaker spiral features that have a larger inclination. Note, however, that the black histogram in the upper panel consists of 16 objects, and both the grey histogram and the black histogram in the lower panel consist of only 13 objects. Therefore, the axial ratio distributions could at least to some extent be affected by small number statistics. We emphasize that the above effects on the axial ratio of the *disk* features need not go hand in hand with the axial ratios of the *galaxies*: as an example, the weak spiral arms in VCC 1896 are not seen anymore when the galaxy is dimmed by one magnitude. One could then confuse the bar with being an inclined disk and thus measure a much smaller axial ratio of the disk feature, while the galaxy's axial ratio is the same in both cases.

E. Objects where no disk features were found

VCC numbers of objects where no substructure was found:
0011, 0029, 0033, 0050, 0061, 0065, 0068, 0070, 0082, 0091, 0096, 0106, 0108, 0109, 0115, 0118, 0127, 0158, 0173, 0178, 0200, 0208, 0227, 0230, 0235, 0236, 0244, 0261, 0273, 0287, 0292, 0294, 0299, 0303, 0317, 0319, 0321, 0330, 0335, 0346, 0361, 0372, 0388, 0390, 0394, 0396, 0401, 0403, 0418, 0421, 0436, 0439, 0440, 0444, 0452, 0454, 0458, 0461, 0466, 0499, 0503, 0504, 0510, 0525, 0539, 0542, 0543, 0545, 0554, 0558, 0560, 0561, 0587, 0592, 0594, 0600, 0611, 0622, 0632, 0634, 0652, 0653, 0668, 0674, 0684, 0687, 0695, 0706, 0711, 0723, 0725, 0745, 0746, 0747, 0748, 0750, 0753, 0755, 0756, 0760, 0761, 0762, 0765, 0769, 0775, 0777, 0779, 0786, 0790, 0791, 0795, 0803, 0808, 0810, 0812, 0815, 0816, 0817, 0820, 0823, 0824, 0833, 0838, 0839, 0840, 0846, 0855, 0861, 0862, 0863, 0871, 0872, 0877, 0878, 0882, 0896, 0916, 0917, 0920, 0926, 0928, 0930, 0931, 0933, 0936, 0940, 0949, 0953, 0965, 0972, 0974, 0976, 0977, 0983, 0991, 0992, 0997, 1005, 1028, 1034, 1039, 1040, 1044, 1059, 1064, 1065, 1069, 1073, 1075, 1076, 1079, 1087, 1089, 1092, 1093, 1099, 1101, 1104, 1105, 1107, 1111, 1115, 1119, 1120, 1122, 1123, 1124, 1129, 1132, 1137, 1149, 1151, 1153, 1163, 1164, 1167, 1172, 1173, 1185, 1191, 1198, 1207, 1209, 1210, 1212, 1213, 1218, 1222, 1223, 1225, 1228, 1235, 1238, 1239, 1240, 1246, 1254, 1261, 1264, 1268, 1296, 1298, 1302, 1307, 1308, 1311, 1314, 1317, 1323, 1333, 1337, 1348, 1351, 1352, 1353, 1355, 1366, 1369, 1373, 1384, 1386, 1389, 1396, 1399, 1400, 1402, 1407, 1414, 1417, 1418, 1420, 1430, 1431, 1432, 1438, 1441, 1443, 1446, 1449, 1451, 1453, 1464, 1472, 1481, 1482, 1488, 1489, 1491, 1495, 1496, 1498, 1503, 1509, 1517, 1518, 1519, 1523, 1528, 1531, 1533, 1539, 1549, 1553, 1561, 1563, 1565, 1571, 1573, 1577, 1599, 1601, 1603, 1604, 1606, 1609, 1616, 1622, 1629, 1642, 1643, 1647, 1649, 1650, 1651, 1652, 1657, 1658, 1661, 1663, 1669, 1674, 1677, 1682, 1683, 1687, 1688, 1689, 1702, 1704, 1710, 1711, 1717, 1719, 1729, 1733, 1740, 1745, 1755, 1761, 1762, 1764, 1767, 1773, 1785, 1792, 1794, 1796, 1803, 1806, 1812, 1815, 1826, 1828, 1829, 1831, 1839, 1843, 1857, 1861, 1866, 1867, 1870, 1876, 1879, 1881, 1886, 1887, 1890, 1891, 1893, 1895, 1897, 1901, 1909, 1912, 1915, 1917, 1919, 1928, 1934, 1936, 1942, 1945, 1948, 1950, 1951, 1958, 1964, 1966, 1967, 1971, 1980, 1982, 1983, 1991, 1995, 2004, 2008, 2011, 2012, 2014, 2017, 2028, 2032, 2043, 2049, 2051, 2054, 2056, 2061, 2063, 2074, 2078, 2081, 2083, 2088.

VCC numbers of objects where substructure other than a disk was found (see Section 4.1):
0009, 0021, 0046, 0170, 0209, 0281, 0288, 0338, 0501, 0636, 0781, 0870, 0929, 0951, 0962, 1078, 1288, 1334, 1370, 1395, 1457, 1501, 1512, 1567, 1617, 1668, 1715, 1743, 2045.

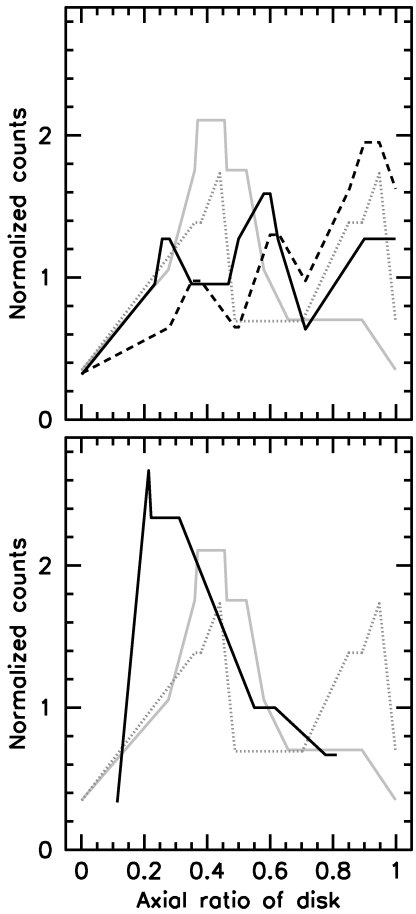

F 2.20. **Effect of S/N on the flattening distribution.** *Upper panel:* Distribution of axial ratio measurements of disk features as illustrated in Figure 2.9, but this time only for the galaxies in the brightest one-magnitude-interval. The black lines show the running histogram of the original measurements, while the grey lines give the axial ratios measured for the disk features after artificially dimming the galaxies by 1 magnitude. A bin is calculated at each data point of each curve with a bin-width of 0.2, and the counts are normalized to an area of 1 under the curve. *Lower panel:* Same as above, but here we compare the observed *second-brightest* one-magnitude-interval (black) to the *brightest* interval dimmed by 1 magnitude (grey, same as in the upper panel).

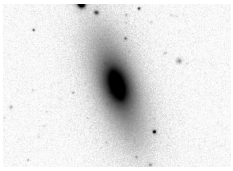

CHAPTER 3

B : ?

"Dwarfs are really lousy at turning gas into stars!"
Marla Geha

Despite the common picture of an early-type dwarf (dE) as a quiescent galaxy with no star formation and little gas, we identify 23 dEs that have blue central colours caused by recent or ongoing star formation in our sample of 476 Virgo cluster dEs. In addition, 14 objects that were mostly classified as (candidate) BCDs have similar properties. Among the certain cluster members, the dEs with blue centers reach a fraction of more than 15% of the dE population at brighter ($m_B \leq 16^m$) magnitudes. A spectral analysis of the centers of 16 galaxies reveals in all cases an underlying old population that dominates the mass, with $M_{old} \geq 90\%$ for all but one object. Therefore the majority of these galaxies will appear like ordinary dEs within ~ one Gigayear or less after the last episode of star formation. Their overall gas content is less than that of dwarf irregular galaxies, but higher than that of ordinary dEs. Their flattening distribution suggests the shape of a thick disk, similar to what has been found for dEs with disk features in Chapter 2. Their projected spatial distribution shows no central clustering, and their distribution with local projected density follows that of irregular galaxies, indicative of an unrelaxed population. This is corroborated by their velocity distribution, which displays two side peaks characteristic of recent infall. We discuss possible formation mechanisms (ram-pressure stripping, tidally induced star formation, harassment) that might be able to explain both the disk shape and the central star formation of the dEs with blue centers.

This study was done together with Katharina Glatt, Pieter Westera, and Eva K. Grebel.
It has been published in The Astronomical Journal (2006, vol. 132, p. 2432).

1. I

Early-type dwarf galaxies are the most numerous type of galaxy in clusters, suggesting that the vigorous forces acting within a cluster environment might actually be creating them. At least theoretically, this could come about via a morphological transformation of infalling galaxies, like e.g. ram-pressure stripping of irregular galaxies (Gunn & Gott 1972), or so-called harassment of late-type spirals (Moore et al. 1996). While these scenarios would in principle also be able to explain the famous morphology-density relation (e.g. Dressler 1980), unambiguous observational proofs are difficult to obtain. Early-type dwarfs are characterized by their smooth, regular appearance, while any possible progenitor galaxy probably displays a different overall structure, before a morphological transformation occurs. Moreover, early-type dwarfs themselves are not a homogeneous class of objects. In addition to the classical dwarf ellipticals, Sandage & Binggeli (1984) introduced the class of dwarf S0 (dS0) galaxies, which were conjectured to have disk components, based on indications like high flattening or a bulge-disk-like profile (Binggeli & Cameron 1991). Following up on the discovery of spiral structure in an early-type dwarf (Jerjen et al. 2000) and on similar other discoveries, we identified 41 Virgo cluster early-type dwarfs with disk features in Lisker et al. (2006b, Chapter 2), and argued that they constitute a population of disk-shaped objects. Furthermore, nucleated and non-nucleated dwarf ellipticals show significantly different clustering properties (Binggeli et al. 1987) and flattening distributions (Ryden & Terndrup 1994; Binggeli & Popescu 1995).

Aside from this structural heterogeneity, colour differences have been reported as well (Rakos & Schombert 2004; Lisker et al. 2005), hinting at a range of stellar populations in early-type dwarfs. While the classical dwarf ellipticals are typically considered not to have recent or ongoing star formation and no significant gas or dust content (e.g. Grebel 2001; Conselice et al. 2003), the well known Local Group galaxy NGC 205 constitutes a prominent example for an early-type dwarf that does exhibit central star formation, gas, and dust (Hodge 1973). More examples are NGC 185 (Hodge 1963) and the apparently isolated galaxy IC 225 (Gu et al. 2006). Furthermore, Conselice et al. (2003) reported a 15% HI detection rate for early-type dwarfs in the Virgo cluster. All these objects are morphologically early-type dwarfs, but form a heterogeneous family of objects, which we assign the common abbreviation “dE”, thereby including galaxies classified as dwarf elliptical or as dS0.

Based on the general idea of gas removal due to effects like ram-pressure stripping, numerous observational studies have focused on comparing the properties of gas-rich dwarf irregular (dIrr) galaxies and gas-poor dEs and dwarf spheroidals (dSphs), attempting to confirm or reject a possible evolutionary relation between them. Thuan (1985) found in his study of optical–near-infrared colours the metallicity ranges of dIrrs and Virgo dEs to be “mutually exclusive”. In their spectroscopic analysis of oxygen abundances of planetary nebulae in Local Group dEs and dSphs, Richer et al. (1998) also found a significant offset to the respective abundances of dIrrs. Similarly, Grebel et al. (2003) recently showed for the Local Group that this metallicity difference exists even when considering only the respective old stellar populations of dIrrs and dSphs, indicative of more intense star formation and enrichment in dSphs. Thuan (1985) and Binggeli (1985) also noted that many Virgo dEs are nucleated, while none of the dIrrs are. Bothun et al. (1986) concluded that Virgo dIrrs would have to fade by $\sim 1\overset{\mathrm{m}}{.}5$ in B to fall into the optical–near-infrared colour range of dEs. However, the bulk of faded dIrrs would then have an effective surface brightness $\mu_{\mathrm{B,e}} > 25$ mag/arcsec^2, substantially lower than the observed values of dEs.

Despite these counter-arguments, potential dIrr/dE “transition types” have frequently been discussed (e.g. Ferguson & Binggeli 1994; Johnson et al. 1997; Knezek et al. 1999). Recently, van Zee et al. (2004b) pointed out the “remarkable commonality” between dEs and dIrrs with respect to their surface brightness distributions and metallicity-luminosity relations. These authors found significant rotation in several bright dEs, upon which they base their discussion about the possibility that these very dEs may have formed via ram-pressure stripping of dIrrs. While van Zee et al. (2004b) admitted that dEs (in Virgo) might actually form through various processes, they argued that every dE must have been gas-rich and star-forming in the past, and would thus inevitably have been classified as dIrr.

However, these properties also apply to blue compact dwarf (BCD) galaxies, which have often been discussed in the literature as potential dE progenitors.

An important difference between dIrrs and BCDs was highlighted by Bothun et al. (1986), who characterized dIrrs as an "odd combination of rather blue colours, yet quite low surface brightness," indicative of a low surface mass density. In contrast, BCDs have a much higher surface brightness, suggesting a higher surface mass density, since they are not bluer than the dIrrs. Whether or not BCDs could indeed be the gas-rich, star-forming progenitors of dEs has been discussed controversially (e.g. Bothun et al. 1986; Drinkwater et al. 1996; Guzman et al. 1996; Papaderos et al. 1996). A glance at the colour images[1] of Virgo cluster galaxies that were classified as (candidate) BCDs reveals what might be one reason for this controversy: these objects do not constitute a homogeneous class, but they vary strongly in size, (ir)regularity, and the fraction of area dominated by blue light with respect to the total area of the galaxy. It might thus be more promising to simply look for plausible dE progenitors among the BCDs, instead of attempting to draw conclusions about this class as a whole.

Interestingly, Bothun et al. (1986) mentioned that the BCDs in their sample look similar to NGC 205. Could dEs with central star formation thus bridge the evolutionary gap from quiescent dEs to potentially star-bursting progenitors? To our knowledge, Vigroux et al. (1984) were the first to identify a central star formation region in a dwarf elliptical outside the Local Group. Recently, Gu et al. (2006) presented a similar dE with ongoing star formation in its center. In Chapter 2, we identified nine Virgo early-type dwarfs with central irregularities likely to be caused by dust or gas, and found that all of them have a blue center. In the present study, we follow up on these objects, and systematically search the Virgo cluster for such dEs with blue centers. This is made possible by the publicly available data of the Sloan Digital Sky Survey (SDSS) Data Release 4 (DR4, Adelman-McCarthy et al. 2006) which covers almost the whole Virgo cluster with multiband optical imaging and partly with spectroscopy. Our data and sample are described in Sections 2 and 3, respectively. Results from image analysis are presented in Section 4, followed by the spectral analysis in Section 5. Section 6 focuses on the gas content of our galaxies. The systematic properties of dEs with blue centers are given in Section 7. Their evolutionary role is discussed in Section 8, followed by a summary and outlook in Section 9.

2. D

2.1. SDSS imaging

The SDSS DR4 covers all galaxies listed in the Virgo Cluster Catalog (VCC, Binggeli et al. 1985) with a declination of $\delta \lesssim 16\overset{\circ}{.}25$, except for an approximately $2^\circ \times 2\overset{\circ}{.}5$ area at $\alpha \approx 186\overset{\circ}{.}2$, $\delta \approx +5\overset{\circ}{.}0$. It provides reduced and calibrated images taken in the u, g, r, i, and z bands with an effective exposure time of 54s in each band (see also Stoughton et al. 2002). The pixel scale of $0\overset{\prime\prime}{.}396$ corresponds to a physical size of 30pc when adopting a Virgo cluster distance of $d = 15.85$ Mpc, i.e. a distance modulus $m - M = 31\overset{\mathrm{m}}{.}0$ (see e.g. Ferrarese et al. 2000), which we use throughout. The SDSS imaging camera (Gunn et al. 1998) takes data in drift-scanning mode nearly simultaneously in the five photometric bands, and thus combines very homogeneous multicolour photometry with large area coverage, good resolution, and sufficient depth to enable a systematic analysis of early-type dwarfs. The images have an absolute astrometric accuracy of RMS$\leq 0\overset{\prime\prime}{.}1$ per coordinate, and a relative accuracy between the r band and each of the other bands of less than 0.1 pixels (Pier et al. 2003). They can thus easily be aligned using their astrometric calibration and need not be registered manually. The RMS of the noise per pixel corresponds to a surface brightness of approximately 24.2mag/arcsec^2 in the u-band, 24.7 in g, 24.4 in r, 23.9 in i, and 22.4 in z. The typical total signal-to-noise ratio (S/N) of a bright dE ($m_\mathrm{B} \approx 14^\mathrm{m}$) amounts to about 1000 in the r-band within an aperture radius of approximately two half-light radii. For a faint dE ($m_\mathrm{B} \approx 18^\mathrm{m}$) this value is typically about

[1] Using the Sloan Digital Sky Survey Image List Tool, http://cas.sdss.org/astro/en/tools/chart/list.asp, Authors: J. Gray, A. Szalay, M. Nieto-Santisteban, and T. Budavari

50. While the S/N in the g and i-band is similar to the above value, it is several times lower in the z-band and more than ten times lower in the u-band. Therefore u and z will not be used in the following analysis.

The SDSS provides photometric measurements for our galaxies, but we found these to be incorrect in many cases (Lisker et al. 2005). The SDSS photometric pipeline significantly overestimates the local sky flux around the Virgo dEs due to their large apparent sizes and low surface brightness outskirts. This affects the measurement of isophotal and Petrosian radii, the profile fits, and subsequently the calculation of total magnitudes, which can be wrong by up to $0\overset{\mathrm{m}}{.}5$. Therefore, we use *B* magnitudes from the VCC throughout this study, and defer calculation of total magnitudes from SDSS data to a more detailed photometric study of the Virgo dEs.

2.2. SDSS spectroscopy

The centers of several galaxies are also covered by the SDSS spectroscopic survey, which provides fiber spectra with a wavelength coverage of 3800 – 9200 Å and a resolution of 1800 or larger. The spectra are binned in logarithmic wavelength, such that the wavelength interval of one pixel along the dispersion axis corresponds to a constant velocity interval of 69 km s^{-1} (York et al. 2000). The fiber diameter corresponds to an angular size of 3″, which translates into 231pc at a distance $d = 15.85$ Mpc. Typical half-light radii of the brighter dEs range from $\sim 10''$ to $\sim 25''$ (Binggeli & Cameron 1991), or from 0.8 to 1.9 kpc. *Therefore, spectral information is only available for the very central region of the dEs.*

2.3. Radial velocities

Heliocentric velocities are available for 198 dEs of our sample of 414 dEs from Chapter 2 that are listed as certain Virgo cluster members in Binggeli et al. (1985) and Binggeli et al. (1993). Velocities were taken from the NASA/IPAC Extragalactic Database (NED), originally provided by the SDSS and by the following studies: Binggeli et al. (1985); de Vaucouleurs et al. (1991); Strauss et al. (1992); Binggeli et al. (1993); Young & Currie (1995); Drinkwater et al. (1996); Grogin et al. (1998); Falco et al. (1999); Gavazzi et al. (2000); van Driel et al. (2000); Conselice et al. (2001); Simien & Prugniel (2002b); Caldwell et al. (2003); Geha et al. (2003); Gavazzi et al. (2004).

Four of these galaxies, however, have velocities above 6000 km s^{-1} from recent data (SDSS and Conselice et al. 2001). Since the velocities of known Virgo cluster members are lower by more than a factor of two, we change the membership status of these galaxies (VCC 0401, VCC 0838, VCC 1111, VCC 1517) to "possible member". This leaves us with a subsample of 194 dEs that are certain cluster members and for which radial velocity measurements are available.

3. S

3.1. Sample selection

In Chapter 2, we put together a sample of Virgo cluster dEs that comprises all dEs with $m_B \leq 18\overset{\mathrm{m}}{.}0$ that are listed in the VCC, that are covered by the SDSS, and that are certain or possible cluster members according to Binggeli et al. (1985) and Binggeli et al. (1993). While objects with uncertainties were initially included, we then excluded all galaxies that appeared to be possible dwarf irregulars due to asymmetric shapes. Objects classified as "dE/dIrr" were not included. 25 galaxies classified as (candidate) dE in the VCC are not covered by the SDSS DR4. The resulting sample comprises 476 early-type dwarfs, 410 of which are certain cluster members (see Section 2.3). Note that our magnitude limit of $m_B \leq 18\overset{\mathrm{m}}{.}0$ corresponds to the magnitude up to which the VCC was found to be complete (Binggeli et al. 1985). With a distance modulus of $m - M = 31\overset{\mathrm{m}}{.}0$, this translates into $M_B \leq -13\overset{\mathrm{m}}{.}0$.

In this sample, we identified several dEs with irregular or clumpy central features likely caused by gas and dust (cf. Figure 6 of Chapter 2). By dividing the background-subtracted aligned g and i-band images provided by Chapter 2, we obtain colour maps that are not calibrated, yet are useful to look for significant colour gradients. Most of the objects just described have a central region whose colour is clearly bluer than that of the rest of the galaxy, similar to the dE recently presented by Gu et al. (2006). Using these colour maps, we visually searched all 476 early-type dwarf galaxies that were presented in Chapter 2 for such a blue center. As a complementary check we then examined the radial $g - i$ colour profiles (Section 4.1) of the thus selected galaxies to confirm the presence of a clear colour gradient.

23 out of 476 dEs (16/410 certain cluster members) entered our working sample of galaxies with blue centers (Figures 3.1, 3.2, and 3.3). We shall term these objects "dE(bc)s" hereafter. Note that the presence of *weak* colour gradients (either negative or positive) in dEs has been reported in the literature (e.g. Gavazzi et al. 2005). Such objects are not the focus of this study; we rather aim at dEs with a blue center, i.e. a significant positive gradient. The distinction between a weak and a significant gradient might appear somewhat arbitrary; however, a detailed and quantitative study of colour gradients of our full dE sample is beyond the scope of this study and will be presented elsewhere. The weakest gradient visually selected by us is that of VCC 0308, with a colour difference of $0\overset{\mathrm{m}}{.}1$ between inner and outer regions (see Figure 3.2).

We point out that the dE(bc)s were morphologically classified as dwarf ellipticals or dS0s by Sandage & Binggeli (1984), and were confirmed as early-type dwarfs in Chapter 2. While Ferrarese et al. (2006) suggest to reclassify four dE(bc)s as dE/dIrr based on their blue central colours and irregular isophotal shapes in the center, we do not use colour as a criterion for *morphological* classification. The *central* irregularities are the reason for which they were assigned to the class dS0 (Binggeli & Cameron 1991), but their overall appearance is smooth and regular, as can be seen from the combined images (Figures 3.1 to 3.3). Complementary to these, we show isophotal contours of the dE(bc)s in Figure 3.4 (see Section 4.1). There, the central irregularities in several dE(bc)s can be seen, which are also revealed by the unsharp mask images. Outside of the central region, though, the isophotes are regularly shaped, confirming the early-type dwarf morphology of these galaxies.

Our preselection of dEs relies on the classification given in the VCC, and on the subsequent examination of the combined images in Chapter 2. However, the intial selection was based on photographic plates, which are most sensitive to the blue light. Therefore, if the colour distribution of a candidate dE(bc) would be quite asymmetric or if the blue central region would make up a rather large fraction of the total light, this galaxy might not have been classified as dE in the first place.[2] We thus decided to use the colour-combined images provided by the SDSS Image List Tool[3] to search all objects classified as irregular galaxy or as blue compact dwarf (BCD; including candidates) for galaxies that look similar to the dE(bc)s, i.e., that have a regular outer shape and a colour similar to the dEs, while having a blue inner region. We found 12 such objects (10 certain cluster members). Furthermore, two galaxies classified as E/S0 with magnitudes similar to the brighter dEs show the same appearance; both are certain cluster members. Images and colour profiles of these additional galaxies are presented in Figures 3.5 and 3.6, and their isophotal contours are shown in Figure 3.7.

To ensure that we are not mixing different types of galaxies, we shall use separate samples of objects in the course of our study: the *main sample* comprising the 23 galaxies classified as dE that have a blue center, and an *additional sample* comprising the 14 galaxies classified other than dE that are similar in appearance to the dE(bc)s. Table 3.1 lists our selected objects along with their classification.

[2] Note that the dE(bc)s identified above were classified as dE *despite* their having been observed in blue light, in which the light of young stars – if present – dominates.

[3] http://cas.sdss.org/astro/en/tools/chart/list.asp, Authors: J. Gray, A. Szalay, M. Nieto-Santisteban, and T. Budavari

T 3.1. **Early-type dwarfs with blue centers.** Cluster membership (column "Mem.") is provided by Binggeli et al. (1985, 1993): M = certain cluster member, P = possible member. Classification as in the VCC, except for VCC 1488 which has been reclassified as probable dE by Geha et al. (2003) (former class E6:). VCC 1175 belongs to the M32-like compact ellipticals (Binggeli et al. 1985). Notes in the last column are as follows: D = disk identified in Chapter 2, D1s = certain disk with spiral arms, D2 = probable disk, D3 = possible disk. S = useful spectrum available. H$\alpha\beta$ = spectrum displays Balmer line emission; Hα = spectrum displays only Hα emission. *Hα lit.* = Hα detection reported by Boselli et al. (2002). Only given if Hα is not detected in the SDSS spectrum, or if no spectrum was available. Units of right ascension are hours, minutes, and seconds, and units of declination are degrees, arcminutes, and arcseconds.

VCC	α_{J2000}	δ_{J2000}	M	.	m_B	C	N
Main sample							
0021	$12^h10^m23\overset{s}{.}2$	+10°11′19″	M		14.75	dS0(4)	
0046	12 12 11.0	+12 53 37	P		17.00	dE3?	S
0170	12 15 56.3	+14 26 00	M		14.86	dS0 pec:	
0173	12 16 00.4	+08 12 08	M		15.00	dS0(1)?	
0218	12 17 05.4	+12 17 22	M		14.88	dS0(8),N:	D2
0278	12 18 14.4	+06 36 14	P		15.10	dS0,Npec	D1s
0281	12 18 15.2	+13 44 58	M		15.30	dS0 or BCD	S, H$\alpha\beta$
0308	12 18 50.9	+07 51 43	M		14.30	d:$S0_1$(0),N:	D1s
0636	12 23 21.3	+15 52 06	P		16.44	dE0,N or $S0_1$(0)	
0674	12 23 52.6	+13 52 58	M		18.00	dE0,N	
0781	12 25 15.2	+12 42 53	M		14.46	$dS0_3$(5),N:	S, Hα
0870	12 26 05.4	+11 48 43	M		14.68	dS0(5),N	S, H$\alpha\beta$
0951	12 26 54.4	+11 39 50	M		14.23	dE2 pec,N or dS0(2),N	S, Hα
0953	12 26 54.8	+13 33 58	P		15.70	dE5?,Npec?	S
1078	12 28 11.4	+09 45 38	P		15.30	dE5 pec?	S, Hα
1488	12 33 13.5	+09 23 51	M		14.76	dE:	S; *Hα lit.*
1501	12 33 24.7	+08 41 27	M		15.10	dS0?	
1512	12 33 34.6	+11 15 43	M		15.73	dS0 pec	
1617	12 35 30.9	+06 20 01	P		15.00	d:S0(4) pec?	
1684	12 36 39.4	+11 06 07	M		14.87	dS0(8):	S, Hα; D3
1715	12 37 28.5	+08 47 40	P		16.20	dE0 pec?	
1779	12 39 04.7	+14 43 52	M		14.83	dS0(6):	D3
1912	12 42 09.1	+12 35 48	M		14.16	dS0(8),N	
Additional sample							
0024	12 10 35.7	+11 45 39	M		14.95	BCD	S, H$\alpha\beta$
0135	12 15 06.9	+12 00 59	M		14.81	S pec / BCD	S, H$\alpha\beta$
0334	12 19 14.2	+13 52 57	M		16.20	BCD	
0340	12 19 22.1	+05 54 38	P		14.43	BCD or merger	S, H$\alpha\beta$
0446	12 20 57.9	+06 20 21	M		15.50	Im / BCD:	
0841	12 25 47.6	+14 57 07	M		16.70	BCD	
0890	12 26 21.6	+06 40 11	P		16.00	BCD?	
1175	12 29 18.5	+10 08 13	M		15.10	E5 / $S0_1$(5)	S, H$\alpha\beta$; M32
1273	12 30 17.0	+09 05 07	M		15.25	ImIII:	S, H$\alpha\beta$
1437	12 32 33.5	+09 10 25	M		15.70	BCD	S, H$\alpha\beta$
1499	12 33 20.2	+12 51 04	M		14.58	E3 pec or S0	S
1955	12 43 07.6	+12 03 00	M		14.12	S pec / BCD	*Hα lit.*
2007	12 44 47.5	+08 06 25	M		15.20	ImIII / BCD:	*Hα lit.*
2033	12 46 04.4	+08 28 34	M		14.65	BCD	*Hα lit.*

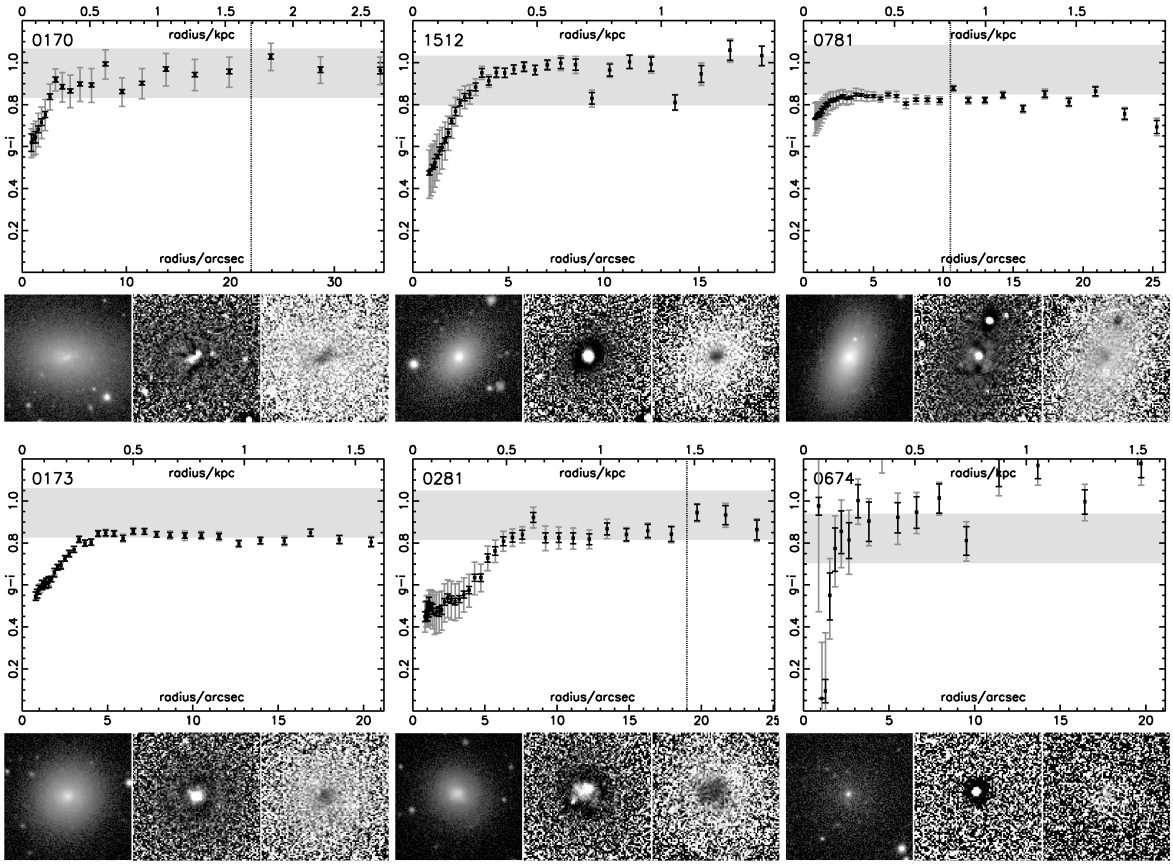

F 3.1. **Early-type dwarfs with blue centers.** For each galaxy, the radial $g - i$ colour profile is shown (top panel; radius= $\sqrt{ab}$), along with the combined image (bottom left), the unsharp mask created with a Gaussian filter with $\sigma = 4$ pixels (bottom center), and the $g - i$ colour map (bottom right). The combined images have a horizontal scale of 70″, or 5.4 kpc with $d = 15.85$ Mpc, while the scales of unsharp masks and colour maps are only half as large. A legend showing the grey scales of the colour maps is given in Figure 3.3. The galaxies are sorted such that those with a relatively constant outer colour and an abruptly starting, steep gradient come first, while those with a gradual colour change come last (in Figure 3.3). The sorting has been done visually, without any quantitative basis. The black error bars in the colour profiles give the uncertainty calculated from the S/N only, whereas the grey error bars represent the *azimuthal* variation of the colour at the respective radius. Since the latter includes S/N-effects, the grey error bars are always larger than the black ones. The vertical dotted line denotes the half-light radius – if available – as given by Binggeli & Cameron (1993). The profiles are shown up to the estimated radius from Binggeli et al. (1985), at $\mu_B \approx 25.5$ mag/arcsec^2. The grey-shaded areas enclose the 2-σ-range of the colours of "ordinary" dEs (i.e. without a blue center) at the respective magnitude, as derived from Lisker et al. (2005). See text for details. For VCC 0674, the steps between each point are twice as large as for the other galaxies, due to its low S/N.

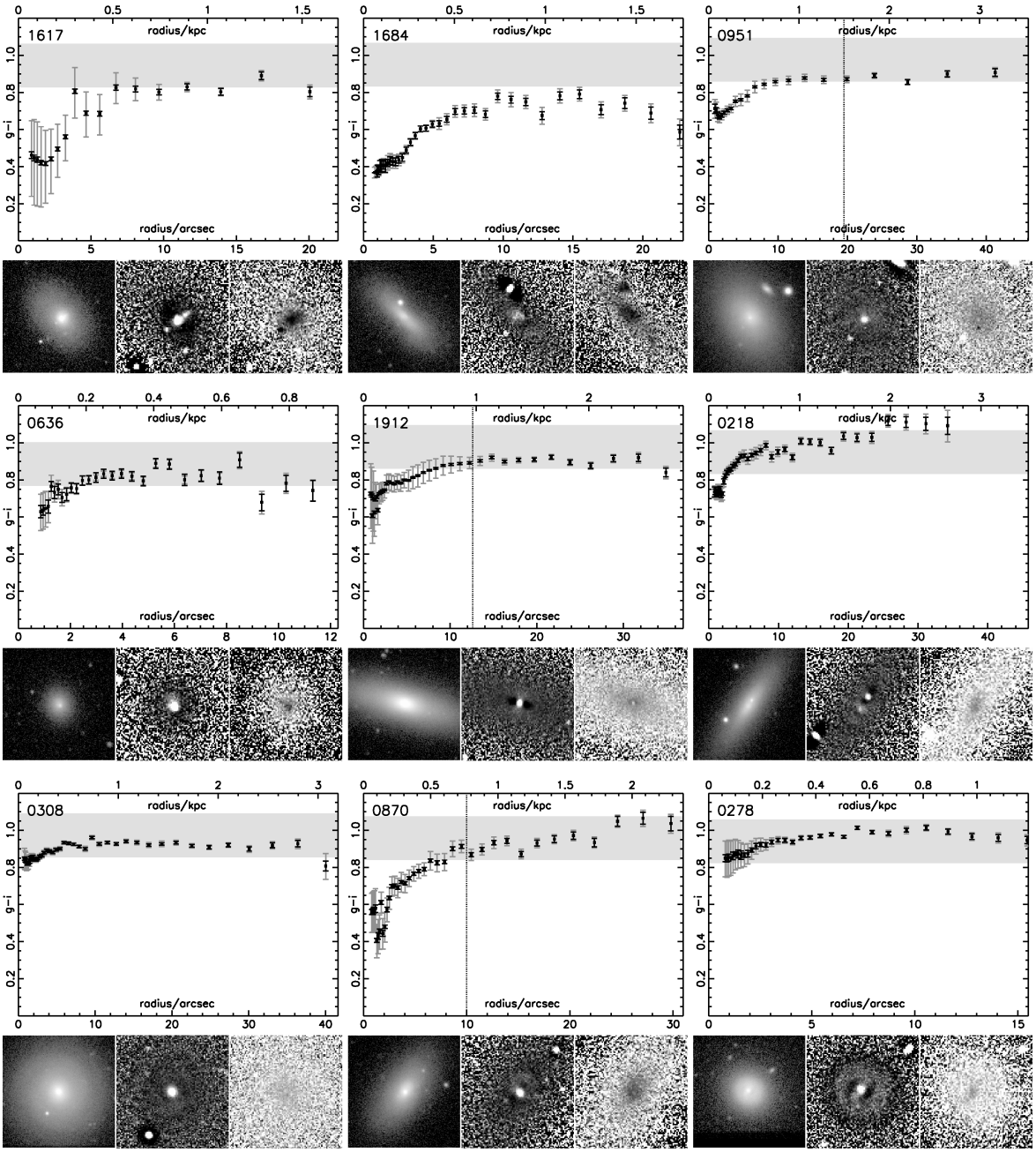

F 3.2. **Early-type dwarfs with blue centers.** Continued from Figure 3.1.

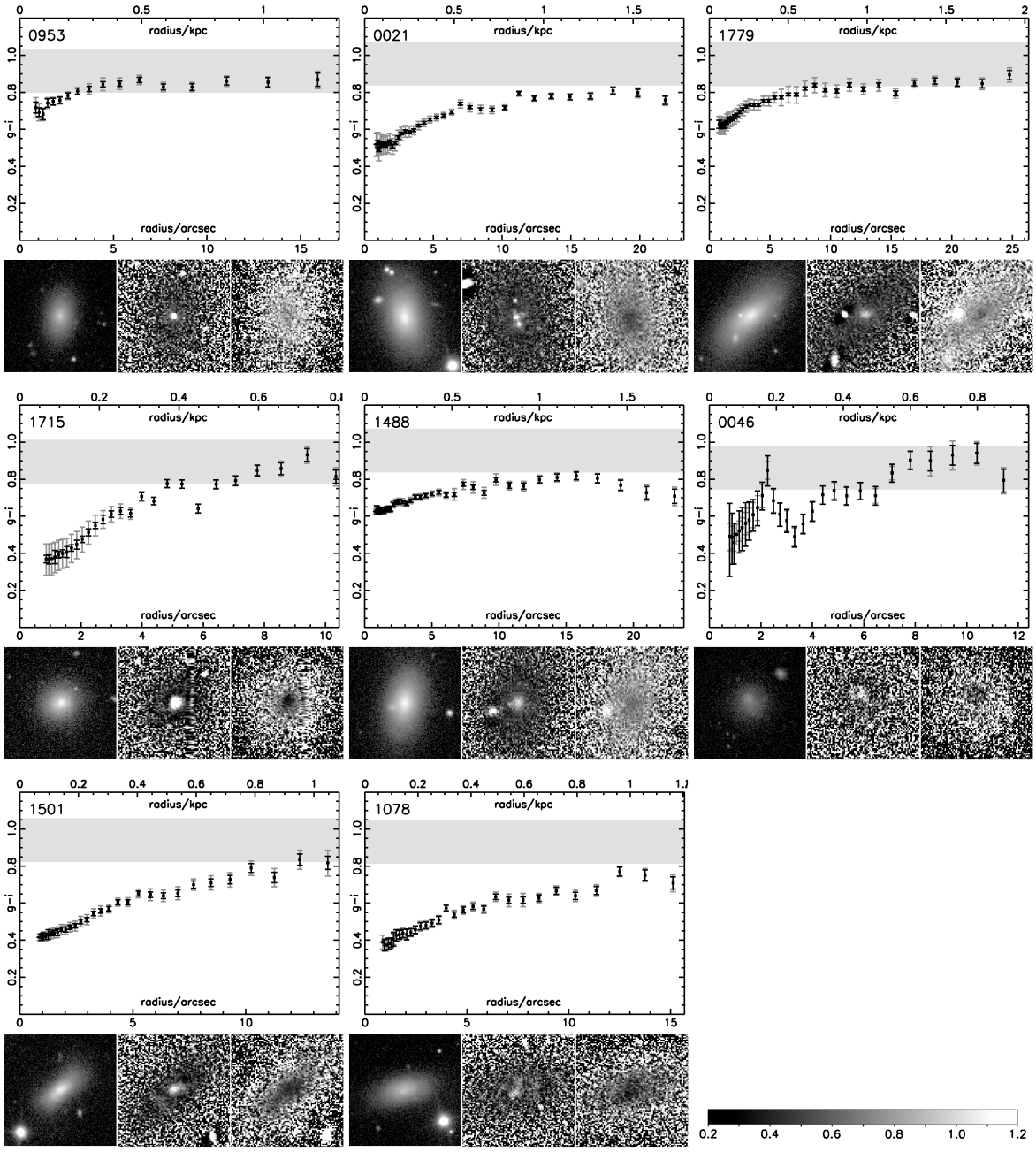

F 3.3. **Early-type dwarfs with blue centers.** Continued from Figure 3.2. The bar in the bottom right panel indicates the grey scale used for the colour maps.

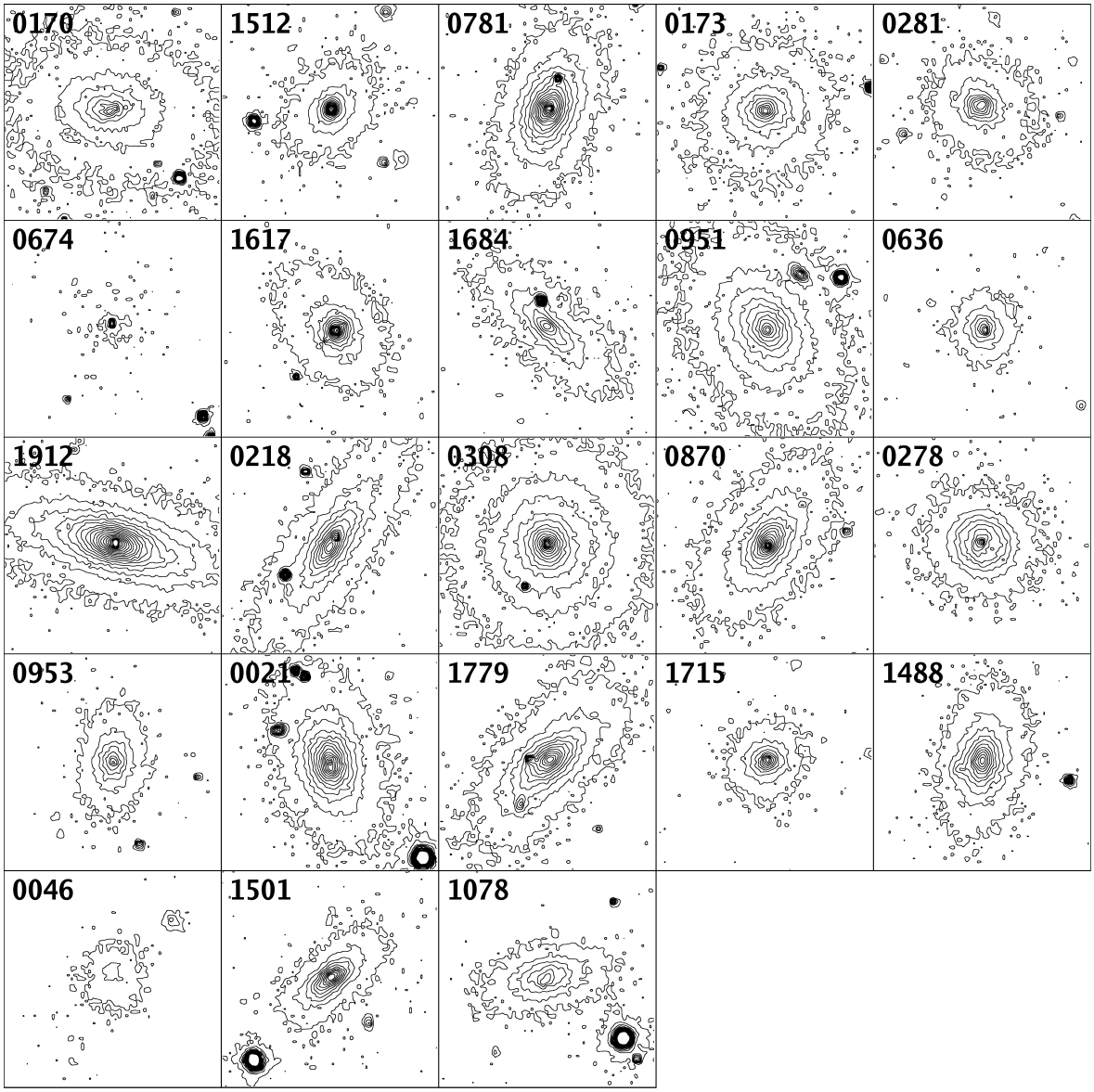

F 3.4. **Isophotal contours of the dE(bc)s.** The galaxies are shown in the same order as in Figures 3.1 to 3.3. Contour diagrams were produced with *IRAF*/*newcont* on the combined images. The outermost contour lies at a level of three times the noise RMS, which was measured for each image separately. Contours are then displayed for 15 logarithmic steps up to 300 times the RMS.

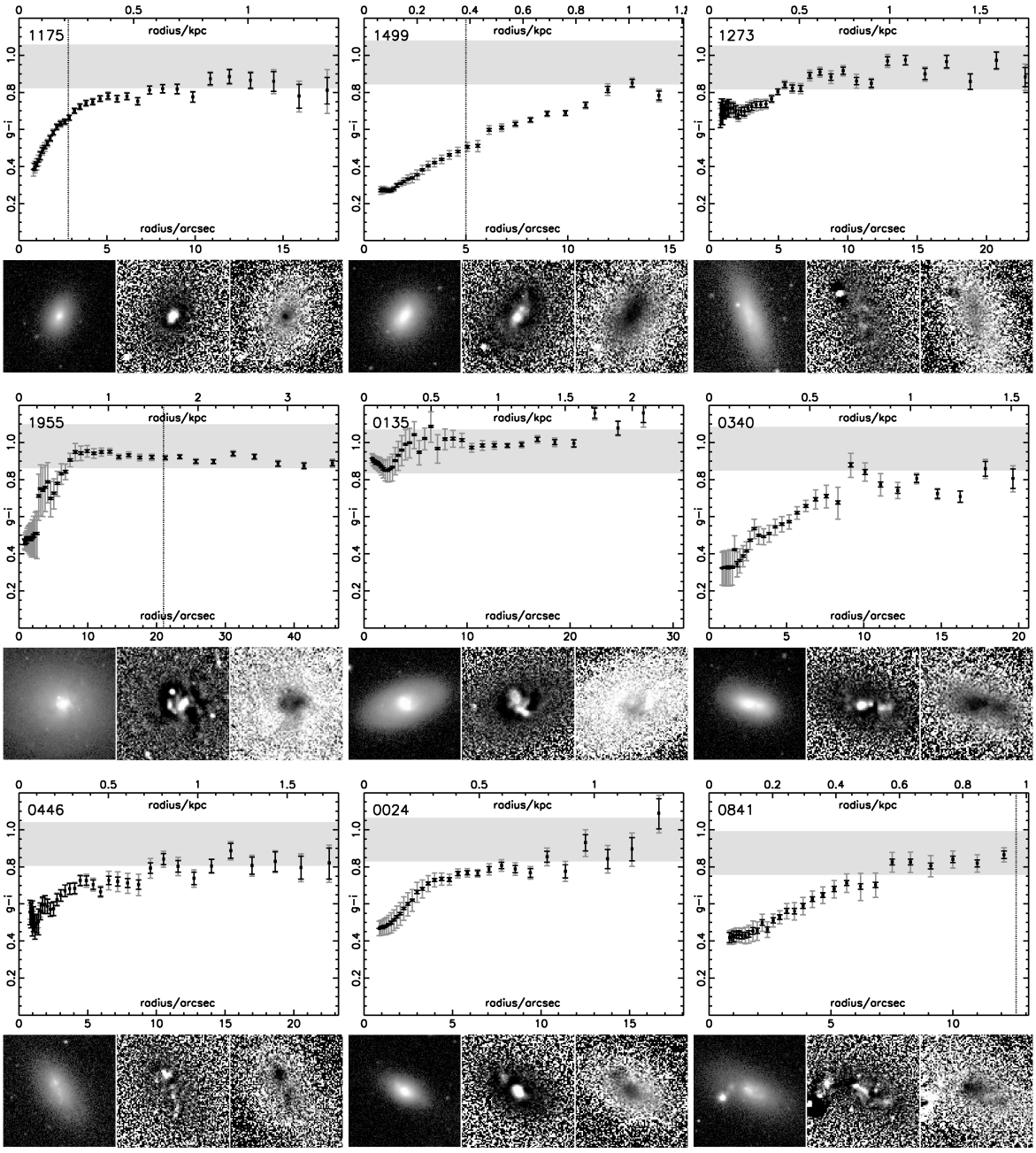

F 3.5. **Galaxies similar to the dE(bc)s.** Like Figure 3.1, but for the galaxies of the additional sample, which were not classified as dEs but were chosen by us as being similar. The two top left galaxies were classified as E or S0; the top right galaxy as irregular. All other objects here and in Figure 3.6 were classified as (candidate) BCDs, and are sorted according to the shape of the colour gradient, analogous to Figures 3.1 to 3.3.

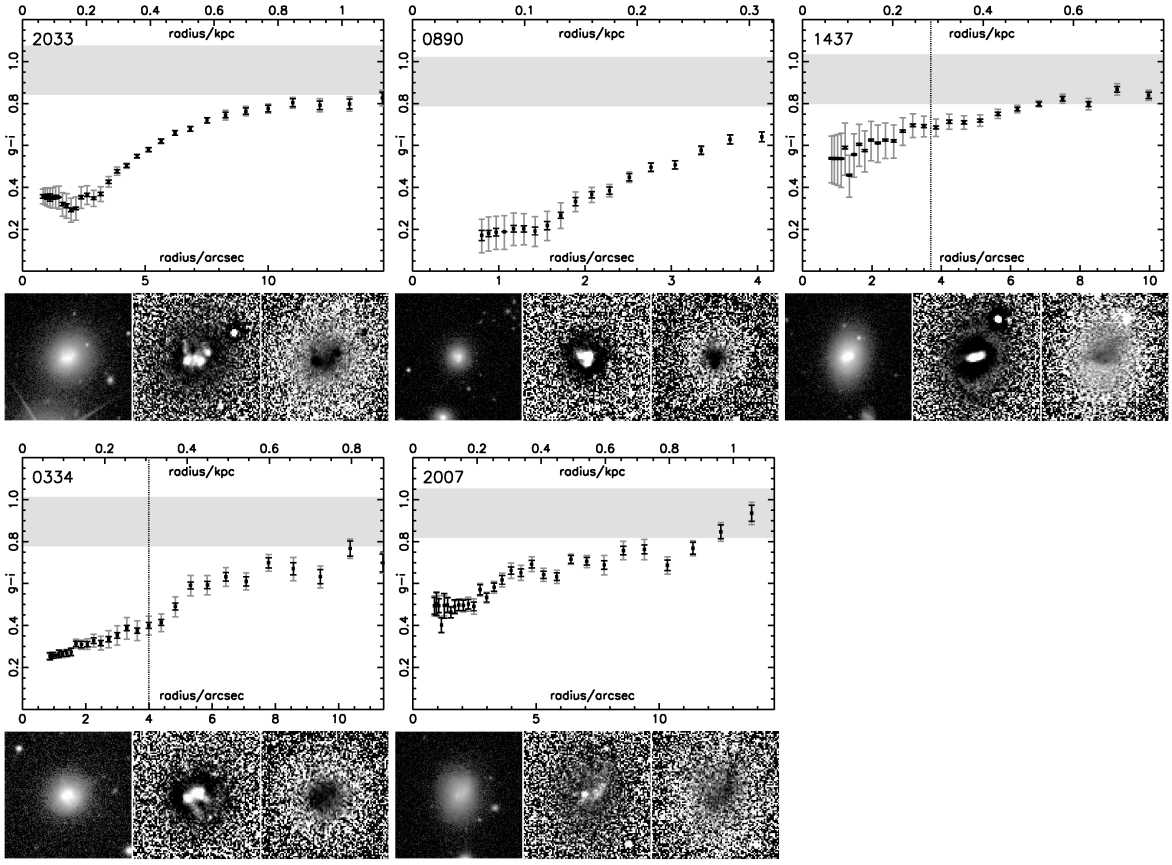

F 3.6. **Galaxies similar to the dE(bc)s.** Continued from Figure 3.5.

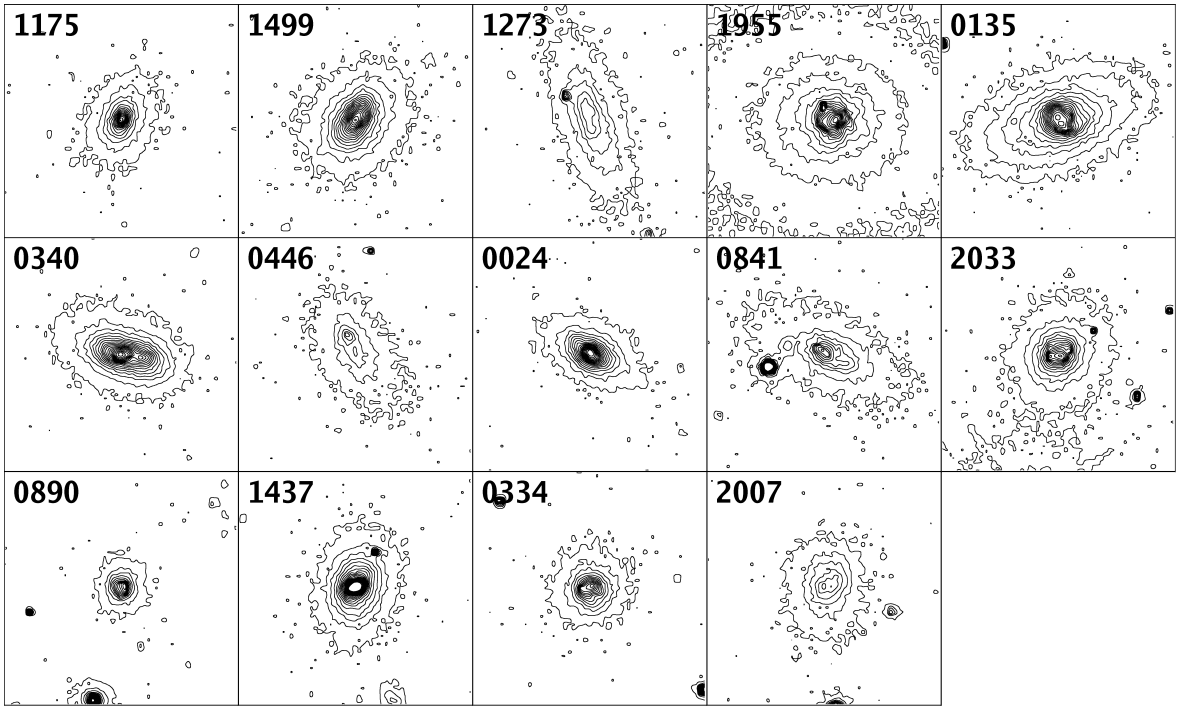

F 3.7. **Isophotal contours of the additional sample.** Like Figure 3.4, but for the galaxies of the additional sample, shown in the same order as in Figures 3.5 and 3.6.

3.2. Presence of disks

In Chapter 2 we presented a systematic search for disk features in Virgo cluster dEs, which we detected in 41 out of 476 objects (including candidates). We showed that these galaxies – termed dE(di)s – are not simply dwarf ellipticals that just have an embedded disk component, but appear to be instead a population of genuine disk galaxies, i.e. flat oblate objects. Amongst the 23 dE(bc)s of our main sample, five are (candidate) dE(di)s, or 4 out of 16 if only certain cluster members are counted. The fraction of dE(di)s among the full dE sample is roughly about 25% at the median B magnitude of the dE(bc)s ($14\overset{m}{.}86$, again counting only certain cluster members). In a randomly chosen sample of 16 dEs we would thus expect to find 4 dE(di)s, which equals our observed number. Two galaxies in the additional sample also show possible disk features (VCC 0135: possibly spiral arms, VCC 1437: possibly spiral arms and a bar). Both are certain cluster members, so the number of 2 out of 10 objects with disks is again consistent with the above fractions. A detailed comparison of the properties of dE(bc)s, dE(di)s, and ordinary dEs is presented in Section 7.

4. I

4.1. Techniques

The study presented in Chapter 2 provides us with background-subtracted, aligned g, r, and i-band images, a combined image, unsharp masks, and an elliptical aperture for each object. A detailed description can be found in Chapter 2. Briefly, combined images were obtained by co-adding the g, r, and i-band images to increase the S/N. From these we produced unsharp masks with various kernel sizes (using *IRAF*[4]*/gauss*; Tody 1993), as well as isophotal contour diagrams (using *IRAF*/*newcont*). An elliptical aperture for each galaxy was determined by performing ellipse fits with *IRAF*/*ellipse* on the combined image, and then choosing by eye one of the outer elliptical isophotes to trace best the outer shape of the galaxy. This isophote was usually between 1 and 2 half-light radii.

The SDSS flux calibration was applied to the aligned g and i-band images for each source, following the instructions on the SDSS webpage[5]. These images were then divided by each other, converted into magnitudes, and corrected for Galactic extinction (Schlegel et al. 1998), yielding proper $g - i$ colour maps. From the same images we obtained radial intensity profiles by azimuthally averaging over elliptical annuli with *IRAF*/*ellipse*. We used geometric steps (i.e., steps that increase by a constant factor) and a fixed position angle, ellipticity, center, and semi-major axis. The ratio of the g and i-band fluxes was then converted into magnitudes, yielding radial $g - i$ colour profiles, where radius is calculated from semi-major (a) and semi-minor axis (b) as $\sqrt{ab}$. Disturbing foreground stars and background galaxies were masked prior to profile calculation.

4.2. Results from the image analysis

In Figures 3.1 to 3.6 we present for each galaxy the radial colour profile, the combined image, the unsharp mask created with a Gaussian filter with $\sigma = 4$ pixels, and the colour map. The colour profiles contain two types of errors: the black error bars give the uncertainty calculated from the S/N only, whereas the grey error bars represent the *azimuthal* variation of the colour at the respective radius (which, of course, includes S/N-effects). A colour distribution that is not symmetric with respect to the galaxy center (e.g. in VCC 1617, see Figure 3.2) or is somewhat irregular (e.g. in VCC 0170, see Figure 3.1) leads to an azimuthal variation of colour significantly larger than the uncertainty from S/N only.

In many cases the unsharp masks reveal central irregularities likely caused by gas and dust features or by asymmetric star forming regions. On average, the central irregularities are stronger and

[4] IRAF is distributed by the National Optical Astronomy Observatories, which are operated by the Association of Universities for Research in Astronomy, Inc., under cooperative agreement with the National Science Foundation.

[5] http://www.sdss.org/dr5/algorithms/fluxcal.html

the blue central regions are larger for galaxies of the additional sample as compared to those of main sample.

Obviously, some galaxies have a relatively constant outer colour and abruptly start to become bluer when going inwards (e.g. VCC 0173), while others display a gradual colour change from the outer regions to the center (e.g. VCC 1501). Although it is not always unambiguous which of the two cases applies to an object, we attempted to sort the dE(bc)s in Figures 3.1 to 3.3, as well as the (candidate) BCDs of the additional sample in Figures 3.5 and 3.6, according to the colour profile shape: starting with those that have a constant outer colour until a steep gradient sets in abruptly, to those with a smooth gradient. We found no correlations of this profile shape with either magnitude, radius, or surface brightness.

In order to compare the $g-i$ colours of the dE(bc)s with those of "ordinary" dEs, we make use of the colours computed by Lisker et al. (2005) for 228 galaxies of our full dE sample, excluding dE(bc)s. Those colours were derived from aperture photometry on the SDSS images, using circular apertures with a radius equalling the half-light radius. We performed a linear fit to the colour-magnitude relation of B magnitude versus $g-i$ colour, yielding an average dE colour for each magnitude with a standard deviation of $0\overset{\mathrm{m}}{.}06$. These values are shown in Figures 3.1 to 3.6 for each galaxy: the grey shaded bands enclose the 2-σ range of colour at each galaxy's magnitude. For most galaxies, the outer colour is still bluer than the typical dE colour; for several objects it is even bluer than the 2-σ range. Note that the above fit has been performed on dE colours computed *within* the half-light radius; however, no strong gradient is to be expected since all dE(bc)s have been excluded from the fit. Thus, the relatively blue outer colours of the dE(bc)s could hint at a younger age of the dE(bc)s as a whole, a lower metallicity, or a shorter time since the last star formation activity in the outer regions as compared to ordinary dEs. A spectroscopic examination of the stellar content of the dE(bc)s is possible at least for the centers of several galaxies, as presented in the following section.

5. S

In order to explore the stellar content of our objects, we examine integrated spectra from the SDSS DR4 as described in Section 2.2. These are taken with fibers of a diameter of 3″, corresponding to a physical size of 231 pc at a distance $d = 15.85$ Mpc. 10 such spectra are available for the main dE(bc) sample, one of which (VCC 0046) proved too noisy for a stellar population analysis. Seven spectra are available for the additional sample. These 16 galaxies are labelled in the last column of Table 3.1 with "S". Six dE(bc)s of the main sample and six galaxies of the additional sample display Balmer line emission (see Table 3.1). One more dE(bc) of the main sample and three galaxies of the additional sample are detected in the Hα imaging study of Boselli et al. (2002). This is a clear indication for ongoing star formation in the dE(bc)s. We note that the overall emission line strengths are larger for objects of the additional sample than for those of the main sample.

We determine the stellar content using a population synthesis method, described in Cuisinier et al. (2006), wherein the spectra are fitted to synthetic composite stellar populations' spectra. Similar methods have already been employed by Cid Fernandes et al. (2003), Kong et al. (2003), Westera et al. (2004), and Gu et al. (2006); the latter describe a dE with blue center very similar to our objects.

5.1. Synthetic stellar populations

The synthetic composite stellar populations were composed using simple stellar population (SSP) spectra from three different libraries of SSPs. The first SSP library (hereafter the "BC99" library) was produced using the Bruzual and Charlot 2000 Galaxy Isochrone Spectral Synthesis Evolution Library (GISSEL) code (Charlot & Bruzual 1991; Bruzual & Charlot 1993, 2000), implementing the Padova 2000 isochrones (Girardi et al. 2000) combined with the BaSeL 3.1 "Padova 2000" stellar library (Westera et al. 2002; Westera 2001). The second SSP library, "Starburst", consists of spectra from the STARBURST99 data package (Leitherer et al. 1999) including nebular continuum emission

T 3.2. **Wavelength ranges that were not used for the spectral fit.**

range (Å)	"contamination" source
3885-3900	H8
3965-3980	Hϵ+[NeIII]3967
4100-4110	Hδ
4335-4345	Hγ+[OIII]4363
4855-4870	Hβ
4955-4965	[OIII]4959
5000-5015	[OIII]5007
5535-5590	telluric lines
5860-5905	HeI 5876
6245-6320	[OI]6300+[SIII]6312
6520-6600	Hα+[NII]
6700-6740	[SII]6717+6731
7130-7145	[ArIII]7136
7560-7600	telluric lines
7700-8100	telluric lines
8250-8480	telluric lines

(Figure 1 on the STARBURST99 web site, http://www.stsci.edu/science/starburst99/). It implements the BaSeL 2.2 library (Lejeune et al. 1997, 1998), and for stars with strong mass loss it also takes into account extended model atmospheres by Schmutz et al. (1992), combined with the Geneva isochrones (Meynet et al. 1994; Schaller et al. 1992; Schaerer et al. 1993a,b; Charbonnel et al. 1993). For old populations, the "BC99" spectrum was used, since the Starburst99 data package only contains spectra up to 900 Myr. Additionally to these two libraries, we also used a library with higher spectral resolution, "BC03", produced by employing the 2003 version of the GISSEL code (Bruzual & Charlot 2003) and the Padova 1995 isochrones (Fagotto et al. 1994; Girardi et al. 1996) combined with the STELIB (Le Borgne et al. 2003) stellar library. The nebular continuum emission was also added to the spectra in the "BC99" and "BC03" libraries, in the same way as described by Leitherer et al. (1999).

5.2. Fit to model spectra: procedure

The spectra cover a wavelength range of around 3820 Å to 9200 Å, but the wavelength region above 8570 Å is too much affected by telluric lines, so we fit the full spectra from 3820 Å to 8570 Å, except for those various parts of the spectra showing "contamination" from different emission and/or telluric line sources. Table 3.2 lists all the regions that were omitted.

We corrected the spectra for redshift and for Galactic foreground extinction using the values from Schlegel et al. (1998) and the extinction law of Fluks et al. (1994). In the eight cases with Hα and Hβ emission we also corrected for internal gas extinction, again using the Fluks et al. extinction law. The extinction constants $E(B-V) = A_V/3.266$ were estimated from the $H\alpha/H\beta$ Balmer decrements following Torres-Peimbert et al. (1989), adopting intrinsic ratios of the emission line fluxes $I_{H\alpha}/I_{H\beta} = 2.87$ (Osterbrock 1989). In order to properly determine the emission line strengths, we first had to remove the contribution from the absorption lines of the underlying stellar populations. This was done by making a first fit to the spectra employing the method described in the following paragraph, using the highest resolution library ("BC03", see above), and then subtracting the best fit spectra from the observed spectra as illustrated in Figure 3.8. The so found values for $E(B-V)$ were multiplied by a factor of 0.44 to correct for systematic differential extinction between the stellar populations and the gas (Calzetti et al. 2000). In the cases where the spectrum displays only Hα but no Hβ emission,

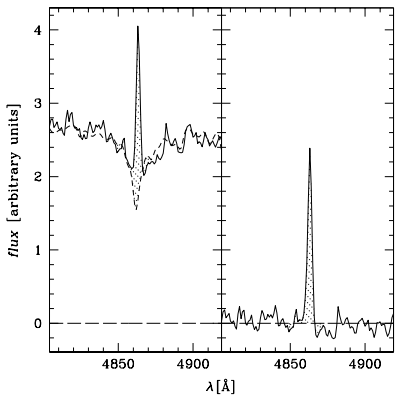

F 3.8. **Emission line strength.** Illustration of how the Hβ emission line strength was measured for the example of VCC 0870. In the left panel, the solid line represents the observed spectrum, whereas the short-dashed line shows the best fit using the "BC03" SSP library. The shaded region between these two lines shows the area used to calculate the emission line strength. The right panel shows the emission line after subtracting the (rebinned) best fit. The shaded area corresponds to the shaded area between spectrum and best fit from the left panel.

we assume the internal extinction to be negligible: in all of these spectra the emission is much weaker than in the cases with both Hα and Hβ emission, in which the lowest value for $E(B-V)$ is already close to zero ($E(B-V) = 0.02$). The average value for internal extinction of the eight galaxies with Hα and Hβ emission is $E(B-V) = 0.10$. Note that the problem of apparent truncation of strong emission lines in SDSS spectra reported by Kniazev et al. (2004) does not occur in any of our spectra.

We modelled the actual population as being composed of an old ($\geq$ 1 Gyr), an intermediate-age (10 Myr to 1 Gyr), and a young ($<$ 10 Myr) stellar population. While there is no standard definition for this age terminology, these age ranges are chosen to reflect the significant changes in the spectrum of an SSP with increasing age. Similar values were used e.g. by Cid Fernandes et al. (2003); Maraston (2005); Gu et al. (2006). The characteristics and free parameters of the three populations are summarized in Table 3.3. In order to confine the parameter space to as few dimensions as possible and to focus on the relative fractions of the populations, we fixed the age of the old population at 5 Gyr, and the metallicity of all populations at [Fe/H] = -0.3. These values equal the best-fitting mean age and metallicity found by Geha et al. (2003) in a study of Lick/IDS absorption line indices for dEs. Moreover, the spectra of SSPs of various ages do not differ much at ages of several Gyr and above (e.g. Bruzual & Charlot 2003).

The best fitting population was found by a χ^2 algorithm. In order to be able to calculate the χ^2 estimator, the observed and theoretical spectra have to be on the same wavelength grid (at least in the range used for the fit). This was done by rebinning the observed spectra to the resolution of the theoretical spectra using a gaussian kernel function with a full width at half maximum (FWHM) corresponding to the resolution of the theoretical spectra (20 Å for "BC99" and "Starburst", and 1 Å for "BC03"). The same was done with the "signal-to-noise spectra", i.e. the S/N as a function of wavelength provided along with the actual spectra. The χ^2 estimator was calculated with wavelength-dependent weighting, giving higher weight to the regions with a higher S/N. Figure 3.9 shows an example of an observed spectrum and the resulting composite model spectra, as well as the individual spectra of the three assumed subpopulations.

5.3. Fit to model spectra: results

The best fitting population parameters for the fits with the different libraries can be found in columns 2 to 6 of Tables 3.4 to 3.6. In all dE(bc)s of the main sample, and all but one (VCC 1499) of the additional sample, the old population makes up 90 % or more of the total mass, even though

T 3.3. **Possible values of the population parameters.** The young population is denoted by index *y*, the intermediate-age one by *i* and the old one by *o*. M_x is the mass fraction of the respective population.

parameter	possible values
$(M_y + M_i):M_o$	0:1, 1:100, 1:30, 1:10, 1:3, 1:1, 3:1, 10:1, 1:0
$M_y:M_i$	0:1, 1:30, 1:10, 1:3, 1:1, 3:1, 10:1, 30:1, 1:0
age_y	1, 2, 3, 4, 5, 6, 7, 8, 9 Myr
age_i	10, 20, 50, 100, 200, 500 Myr
age_o	fixed at 5 Gyr
$[Fe/H]_y$	fixed at -0.3
$[Fe/H]_i$	fixed at -0.3
$[Fe/H]_o$	fixed at -0.3

T 3.4. **Best fitting parameters using the "BC99" library.** M_y and age_y give the mass fraction and age of the young population, respectively. M_i and age_i are the same parameters for the intermediate-age population. The age of the old population was fixed at 5 Gyr; M_o gives its resulting mass fraction.

VCC	M_y	age_y	M_i	age_i	M_o
Main sample					
0021	0.0029	9 Myr	0.0880	509 Myr	0.9091
0281	0.0029	1 Myr	0.0293	203 Myr	0.9677
0781	0.0003	2 Myr	0.0096	203 Myr	0.9901
0870	0.0029	7 Myr	0.0293	102 Myr	0.9677
0951	0.0010	1 Myr	0.0312	203 Myr	0.9677
0953	0.0010	7 Myr	0.0312	509 Myr	0.9677
1078	0.0029	1 Myr	0.0880	509 Myr	0.9091
1488	0.0010	7 Myr	0.0312	203 Myr	0.9677
1684	0.0000	-	0.0909	203 Myr	0.9091
Additional sample					
0024	0.0029	1 Myr	0.0293	102 Myr	0.9677
0135	0.0010	3 Myr	0.0312	102 Myr	0.9677
0340	0.0074	1 Myr	0.0025	509 Myr	0.9901
1175	0.0050	1 Myr	0.0050	509 Myr	0.9901
1273	0.0025	2 Myr	0.0074	203 Myr	0.9901
1437	0.0161	8 Myr	0.0161	50 Myr	0.9677
1499	0.0081	9 Myr	0.2419	509 Myr	0.7500

its contribution to the total light is rather small (spectra f_o in Figure 3.9). The young population, on the other hand, usually contributes less than 1 % to the mass, but often dominates the light (f_y in Figure 3.9), whereas the intermediate-age population usually makes up a few percent of the stellar mass. However, all three populations are doubtlessly present, from which we conclude that these galaxies have been forming stars until the present day. We remind the reader again that the spectra cover only the very central part of our objects and do not allow us to draw direct conclusions about the surrounding regions.

T 3.5. **Best fitting parameters using the "Starburst" library.** Same as Table 3.4, but for the "Starburst" library.

VCC	M_y	age_y	M_i	age_i	M_o
Main sample					
0021	0.0083	8 Myr	0.0826	500 Myr	0.9091
0281	0.0029	1 Myr	0.0293	200 Myr	0.9677
0781	0.0003	8 Myr	0.0096	100 Myr	0.9901
0870	0.0227	8 Myr	0.2273	500 Myr	0.7500
0951	0.0029	9 Myr	0.0880	500 Myr	0.9091
0953	0.0025	8 Myr	0.0074	100 Myr	0.9901
1078	0.0083	8 Myr	0.0826	200 Myr	0.9091
1488	0.0029	8 Myr	0.0880	500 Myr	0.9091
1684	0.0029	1 Myr	0.0880	500 Myr	0.9091
Additional sample					
0024	0.0029	5 Myr	0.0293	500 Myr	0.9677
0135	0.0025	5 Myr	0.0074	100 Myr	0.9901
0340	0.0050	1 Myr	0.0050	20 Myr	0.9901
1175	0.0050	1 Myr	0.0050	500 Myr	0.9901
1273	0.0025	2 Myr	0.0074	200 Myr	0.9901
1437	0.0083	1 Myr	0.0826	500 Myr	0.9091
1499	0.0081	8 Myr	0.2419	200 Myr	0.7500

T 3.6. **Best fitting parameters using the "BC03" library.** Same as Table 3.4, but for the "BC03" library.

VCC	M_y	age_y	M_i	age_i	M_o
Main sample					
0021	0.0029	9 Myr	0.0880	509 Myr	0.9091
0281	0.0029	1 Myr	0.0880	509 Myr	0.9091
0781	0.0003	1 Myr	0.0096	203 Myr	0.9901
0870	0.0029	6 Myr	0.0293	203 Myr	0.9677
0951	0.0010	6 Myr	0.0312	203 Myr	0.9677
0953	0.0010	7 Myr	0.0312	509 Myr	0.9677
1078	0.0029	1 Myr	0.0880	509 Myr	0.9091
1488	0.0010	7 Myr	0.0312	203 Myr	0.9677
1684	0.0029	6 Myr	0.0880	509 Myr	0.9091
Additional sample					
0024	0.0029	5 Myr	0.0880	509 Myr	0.9091
0135	0.0010	4 Myr	0.0312	102 Myr	0.9677
0340	0.0029	1 Myr	0.0293	50 Myr	0.9677
1175	0.0029	1 Myr	0.0880	509 Myr	0.9091
1273	0.0025	2 Myr	0.0074	509 Myr	0.9901
1437	0.0029	3 Myr	0.0880	203 Myr	0.9091
1499	0.0081	8 Myr	0.2419	509 Myr	0.7500

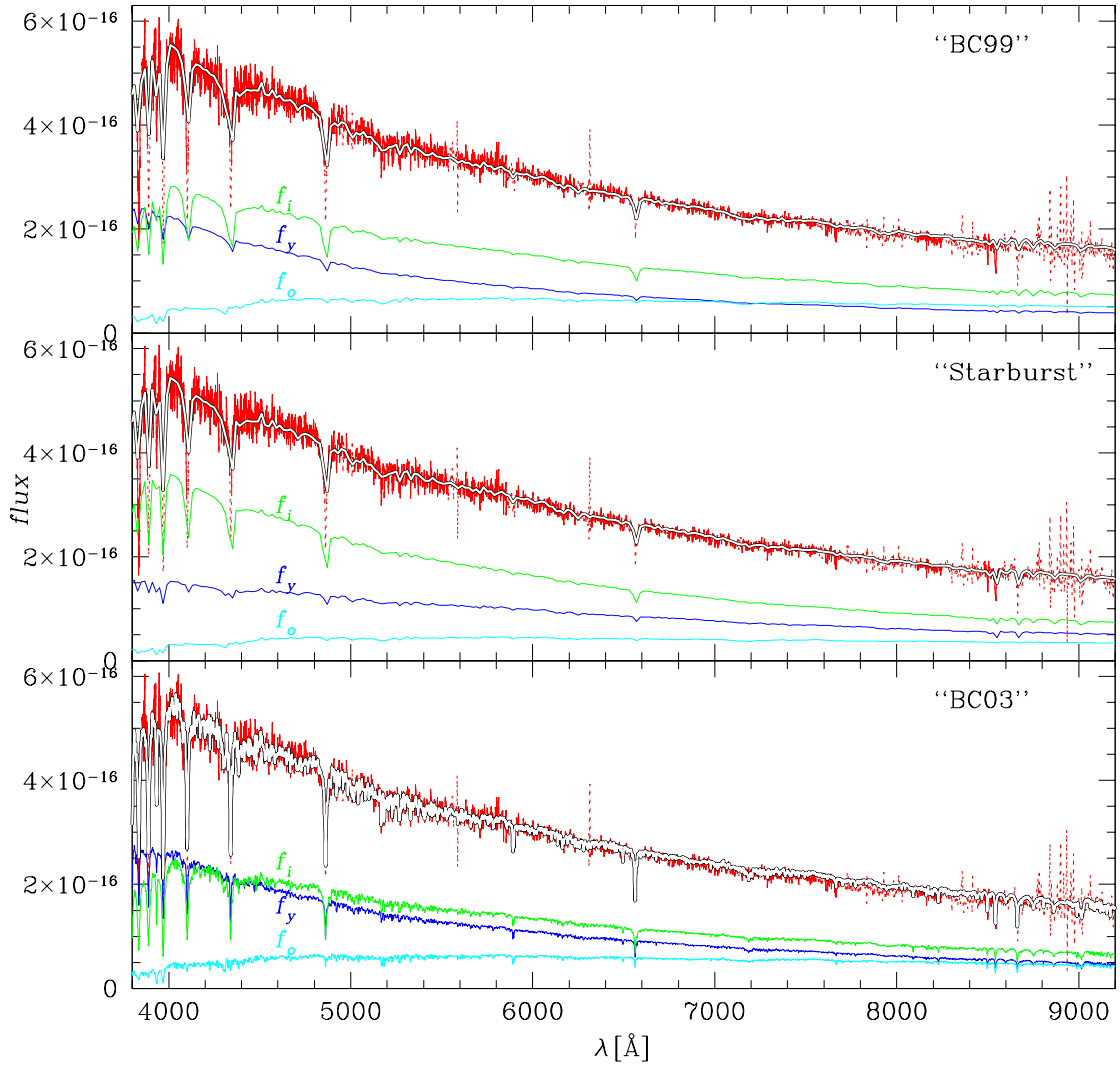

F 3.9. **Example of a "best fit".** The thin (red or dark grey) lines represent the observed spectrum (VCC 1499), the thicker white lines show the best fitting spectra obtained using the different SSP libraries, whereas the lower-level lines show the best fits decomposed into the young (f_y, blue or dark grey), the intermediate-age (f_i, green or medium grey), and the old (f_o, cyan or light grey) populations. Flux is given in erg cm^{-2} s^{-1} Å^{-1}.

Typically, the parameter space of such spectral fits is full of degeneracies. For example, a change of the ratio of the mass fractions of young and intermediate-age population has a similar effect on the composite spectrum as varying one of the ages of these populations. Therefore, the parameter values given in Tables 3.4 to 3.6 for *individual* galaxies should be taken with a grain of salt. However, the excellent agreement between the solutions found with the different libraries, and the similarities in the solutions for the different galaxies, suggest that the *general* trends in the derived parameters reflect the real properties of the dE(bc)s, within the simplified framework of our three-population models. We emphasize that our approach of approximating the SDSS spectra with synthetic populations composed of three SSPs is not meant to represent the detailed star formation history of our target galaxies, but only to demonstrate the range of ages during which star formation must have occured. Whether stars

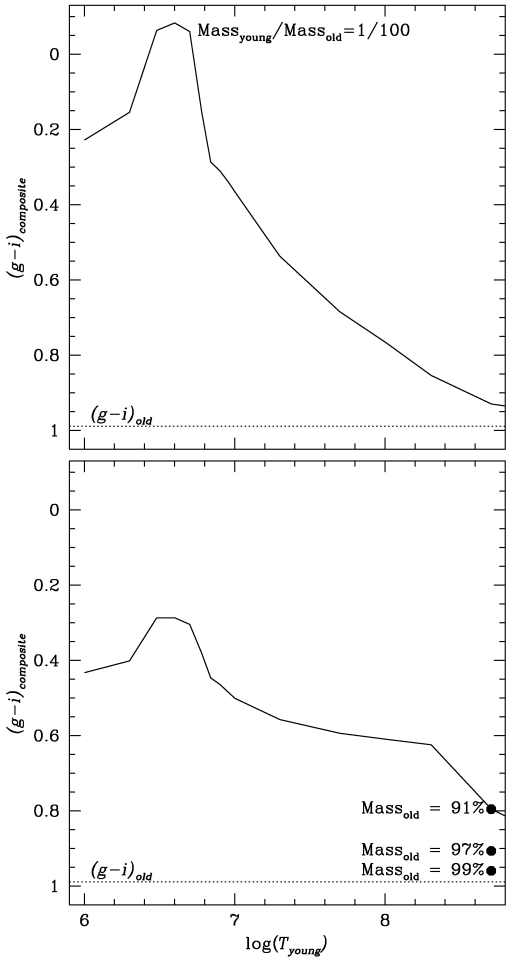

F 3.10. **Colour evolution of an ageing population.** Evolution of $g - i$ colour of different composite stellar populations. The age of the old population is fixed at 5 Gyr, and the metallicity of all populations is fixed at [Fe/H] = −0.3. *Upper panel:* Composite population made out of a young and an old population. The young population makes up 1% of the total mass. *Lower panel:* Composite population made out of a young, an intermediate-age, and an old population, similar to the best fit results derived for the dE(bc)s. The upper curve represents a population with $(M_y + M_i)$:M_o = 1:10, M_y:M_i = 1:30, with $M_{y,i,o}$ denoting the mass fractions of young, intermediate-age, and old population, respectively. The intermediate-age population is chosen to be ∼500 Myr older than the young one. The big black dots mark the colour of this mixture after 500 Myr, as well as that of two other mixtures: {$(M_y + M_i)$:M_o = 1:30, M_y:M_i = 1:30} (middle dot), and {$(M_y + M_i)$:M_o = 1:100, M_y:M_i = 1:10} (lower dot).

were formed by short starbursts or by extended episodes of star formation can typically not be decided for galaxies only observable in integrated light (e.g. Lilly & Fritze-v. Alvensleben 2003).

5.4. Evolution of $g - i$ colour

Finally, we would like to know for how long after the last star formation phase integrated spectral properties can be distinguished from the ones of a pure old population. We focus on the $g - i$ colour since it was used for the actual selection of our objects. For this purpose, we produced synthetic composite populations using the three SSP libraries, and calculated the total $g - i$ colour as a function of the age of the youngest partial population as these composite populations evolve.

The simplest case is that of two populations: a young one turning into an intermediate-age one, on top of the old one. If we assume the mass of the young population to have one hundredth of the mass of the old one, the colour of the mixture evolves as shown by the solid line in the upper panel of Figure 3.10. In this scenario, it takes a few 100 Myr until the $g - i$ colour of the composite population differs by less than $0\overset{\text{m}}{.}1$ from a pure old population (shown by the dotted line), and thus becomes difficult to distinguish from the latter. The colours shown in Figure 3.10 are the ones using the "BC99" library, but the results hold true for all three libraries.

Now we take instead a composite population like one of the typical solutions from Tables 3.4 to 3.6, that is, $(M_y + M_i):M_o$ = 1:10, $M_y:M_i$ = 1:30, the intermediate-age population being around 500 Myr older than the young one. $M_{y,i,o}$ denotes the mass fractions of young, intermediate-age, and old population, respectively. The colour of this mixture evolves like the solid line in the lower panel of Figure 3.10. Again, the dotted line shows the colour of only an old population. In this scenario, the mixture is still distinguishable from a pure old population 500 Myr after the birth of the youngest one. However, this parameter combination is the one with the smallest mass fraction of the old population among the results for the main sample. By using the values of the other typical solutions from Tables 3.4 to 3.6, $(M_y + M_i):M_o$ = 1:30, $M_y:M_i$ = 1:30, or $(M_y + M_i):M_o$ = 1:100, $M_y:M_i$ = 1:10, the $g - i$ colour after 500 Myr is much more similar to the pure old population colour (big black dots in the lower panel of Figure 3.10). Therefore, after the end of star formation it will take less than ∼ a Gigayear for the (strong) colour gradient to disappear, and in many cases only ∼ half a Gigayear depending on the mass fraction of the young and intermediate-age population. This also demonstrates the need for a thorough study of both strong *and* weak colour gradients in early-type dwarfs, in order to draw conclusions about evolutionary histories. Whether or not star formation will cease soon, or has ceased already in some objects, depends on the amount (and state) of leftover gas, which is the subject of the following section.

6. G

Dwarf elliptical galaxies are commonly considered to be systems that have lost their (cold) gas (e.g. Ferguson & Binggeli 1994; Conselice et al. 2003). On the other hand, Conselice et al. (2003) reported "credible" HI detections for seven[6] Virgo dEs from their own study as well as from other literature, translating into a 15% HI detection rate for dEs. The GOLDMine database (Gavazzi et al. 2003) reports detections for six more early-type dwarfs.[7] From the SDSS spectra presented above, we know that the dE(bc)s show clear signs of either ongoing or very recent star formation, suggesting the presence of a certain amount of gas. It would thus be interesting to know whether we can expect more episodes of star formation in the near future – requiring a significant cold gas content – or whether star formation is likely to cease soon due to the lack of leftover gas.

Two dE(bc)s of the main sample are detected in HI, while for 8 others, at least upper limits are available. Ten objects of the additional sample are detected in HI, and upper limits are available for three further galaxies. See Table 3.7 for HI masses and upper limits on our objects, along with the corresponding references to the literature. Two objects have values from more than one publication; these agree well within the errors.

We now seek to derive an estimate for the ratio of the gas mass to the total baryonic mass, $M_{\rm HI}/M_{\rm bary}$. For this purpose we use V-band mass-to-light ratios between 3 and 6, as given by Geha et al. (2003), and assume no dark matter content, again following Geha et al. (2003). We calculate the total V-band absolute magnitude from the g and i-band flux within an elliptical aperture with 1.5 times the estimated semi-major axis from Binggeli et al. (1985) (at $\sim \mu_{\rm B}$ = 25.5 mag/arcsec^2), using

[6] Two of these, however, were not classified as early-type dwarf in the VCC, and appear to us as at least doubtful dE candidates from visual inspection of the SDSS images.

[7] Three of these (VCC 0170, VCC 0227, VCC 0281) are listed as S0 or late-type spiral in the NASA/IPAC Extragalactic Database (NED) and similar in Gavazzi et al. (2005) who reported their HI detections, although they were classified as early-type dwarf in the VCC and confirmed as such in Chapter 2.

T 3.7. **HI detections.** HI masses and upper limits are given for our adopted Virgo cluster distance of $d = 15.85$ Mpc. In columns 3 to 5 we list the ratios of the gas mass to the total baryonic mass, using different mass-to-light ratios as given in the column header; for details see text. References for the HI detections: 1. GOLDMine database (Gavazzi et al. 2003, http://goldmine.mib.infn.it/); 2. Gavazzi et al. (2005); 3. Huchtmeier & Richter (1989); 4. Huchtmeier & Richter (1986).

VCC	$log\left(\frac{M_{\rm HI}}{M_\odot}\right)$	$\frac{M_{\rm HI}}{M_{\rm bary}}(\frac{M}{L}=3)$	$\frac{M_{\rm HI}}{M_{\rm bary}}(\frac{M}{L}=4.5)$	$\frac{M_{\rm HI}}{M_{\rm bary}}(\frac{M}{L}=6)$	Reference
Main sample					
0021	<7.78	<0.048	<0.032	<0.024	1
0170	7.39	0.014	0.009	0.007	2
0281	7.52	0.055	0.037	0.028	2
	7.74				3
0308	<7.92	<0.094	<0.065	<0.049	1
0781	<7.42	<0.055	<0.038	<0.028	1
0951	<6.84	<0.003	<0.002	<0.001	1
0953	<6.54	<0.009	<0.006	<0.004	1
1488	<8.27	<0.134	<0.093	<0.072	1
1779	<7.72	<0.041	<0.027	<0.021	1
1912	<7.44	<0.031	<0.021	<0.016	1
Additional sample					
0024	8.90	0.546	0.445	0.376	2
0135	<7.13	<0.009	<0.006	<0.004	2
	≤7.74				3
0334	7.89	0.339	0.255	0.204	2
0340	8.76	0.547	0.446	0.377	2
0446	7.62	0.284	0.209	0.166	2
0841	7.55	0.270	0.198	0.156	2
0890	7.27	0.106	0.073	0.056	2
1273	<7.10	<0.064	<0.044	<0.033	2
	≤7.54				3
1437	8.17	0.311	0.232	0.184	2
1499	<8.53	<0.256	<0.186	<0.147	4
1955	7.66	0.047	0.032	0.024	2
2007	7.31	0.218	0.157	0.122	2
	7.44				3
2033	7.39	0.045	0.031	0.023	2

the transformation of Smith et al. (2002). The resulting gas-to-baryonic mass fractions or upper limits for mass-to-light ratios of 3, 4.5, and 6 are listed in Table 3.7.

Of the dE(bc)s in the main sample, three objects have a very low gas content, with $M_{\rm HI}/M_{\rm bary}$ values of 1% or below (VCC 0170, VCC 0951, VCC 0953). Of the remaining galaxies, one has an HI content with a resulting fraction of 3 – 6% (depending on the adopted mass-to-light ratio). The others have upper limits of several percent, up to 7 – 13% for VCC 1488. In contrast, most of the galaxies in the additional sample have a much higher gas fraction. Of the 10 detected galaxies, 7 reach up to more than 10%, with values up to 38 – 55%. However, for one object (VCC 0135) the upper limit lies below 1%.

A comparison with average HI-to-total mass ratios for Local Group dwarf galaxies shows that at least some dE(bc)s of the main sample have a larger gas fraction than the 0.2 ± 0.4% of an ordinary dE, while it is mostly lower than the 30 ± 24% of dwarf irregulars (Conselice et al. 2003). If the

detected gas was centrally concentrated, at least some of the dE(bc)s of the main sample might still continue to form stars there for a significant amount of time. In contrast, most objects of the additional sample fall in the range of the Local Group dIrrs, suggesting that a longer duration of star formation is possible. See Section 8 for a further discussion.

7. S

We have shown so far that the dE(bc)s, which were classified morphologically as early-type dwarfs, are dominated by an old stellar population. Given their moderate amount of cold gas and the lack of any (significant) star formation activity beyond their central regions, the dE(bc)s will evolve into ordinary-looking dEs in the future. However, up to this point we have mainly focused on the appearance and the composition of the dE(bc)s, but we have not yet compared the statistical properties of the sample of dE(bc)s with those of the sample of dEs and dE(di)s (dEs with disks, see Section 3.2). As demonstrated in Chapter 2, the luminosity function, the projected spatial distribution, and the flattening distribution are important tools to investigate differences between types of galaxies, and to judge whether or not they constitute separate populations. We present and analyze these distributions for the dE(bc)s in the following subsections.

7.1. Luminosity function

Figure 3.11 shows the distribution of dE(bc)s, dE(di)s, and the remaining dEs with respect to their B magnitude provided by the VCC. With the assumption that all galaxies are located at roughly the same distance from us, this distribution represents their luminosity function. Our data are presented as a running histogram with a bin-width of $1\overset{\mathrm{m}}{.}0$ (i.e. $\pm 0\overset{\mathrm{m}}{.}5$). Only galaxies with certain cluster membership are taken into account, i.e. 16 dE(bc)s in the main sample whose distribution is given by the dark grey shaded area. The dE(di)s are represented by the medium grey shaded area, and the full dE sample with dE(bc)s and dE(di)s excluded is given by the light grey shaded area. The fraction of dE(bc)s among the full dE sample is shown as black line. The white line shows the distribution of the 12 certain cluster members of the additional sample, which by construction are not included in the dE sample.

The luminosity function of the full dE sample is given as grey dashed line. It has a conspicuous bump at brighter magnitudes, which we explained in Chapter 2 with the superposition of dE(di)s and ordinary dEs, implying that they were two different populations of objects. However, as can be seen in the figure, this bump might at least partly be explained by the superposition of dE(bc)s, dE(di)s, and the remaining dEs. On the other hand, it has been shown in Chapter 2 that we missed ~50% of dE(di)s due to issues of signal-to-noise. Therefore we now subtracted the dE(bc)s and 1.5 times the number of dE(di)s from the full sample as a further test (not shown). Still, there is no obvious over-subtraction of the bump (which would result in a dip), so the data are consistent with the estimated number of missed dE(di)s.

The fraction of dE(bc)s among all dEs reaches up to more than 15% for the main sample at brighter magnitudes, and declines to almost zero at $m_{\mathrm{B}} \gtrsim 16^{\mathrm{m}}$. Thus the dE(bc)s are not a negligible population of objects, but instead constitute a significant fraction of the bright dEs. To investigate whether the decline of the dE(bc) fraction at fainter magnitudes is real or whether it is due to S/N effects, we artificially dimmed all 11 dE(bc)s of the main sample with $14^{\mathrm{m}} \leq m_{\mathrm{B}} < 15^{\mathrm{m}}$ by 1 and 2 magnitudes. This was done by adding Gaussian noise to the images such that the RMS of the total noise was increased by 1 and 2 magnitudes. Colour maps and radial colour profiles were then constructed as described above, and were examined for whether they would have been selected as dE(bc)s by us. When dimmed by 1 magnitude, 9 of the 11 objects would still have been selected, whereas at 2 magnitudes fainter only 5 would have been recognized as dE(bc)s. Thus, if the *true* dE(bc) fraction would be constant at 17% (the average value within the interval $14^{\mathrm{m}} \leq m_{\mathrm{B}} < 15^{\mathrm{m}}$) independent of magnitude, we would expect to *observe* a fraction of 14% at magnitudes between

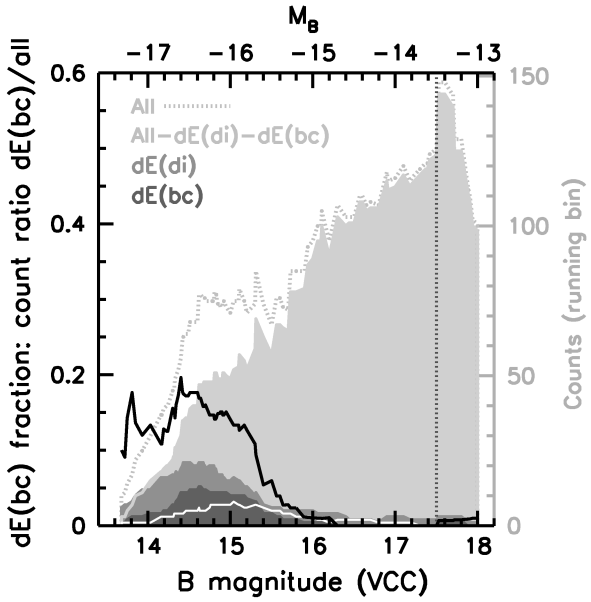

F 3.11. **Luminosity function.** Running histogram of the number of galaxies (right y-axis) with respect to B magnitude as given by the VCC. Shown are dE(bc)s of the main sample (dark grey area), dE(di)s (medium grey area), all dEs excluding both dE(di)s and dE(bc)s (light grey area), and all dEs (light grey dashed line). Galaxies of the additional sample – which by construction are not included in the dE sample – are represented by the white line. The bin-width is $1\overset{m}{.}0$, therefore the counts are incomplete for $m_B > 17\overset{m}{.}5$ (vertical dotted line). A bin is calculated at each position of a galaxy in the full sample. Only galaxies with certain cluster membership are taken into account. The fraction of dE(bc)s – the ratio of the dE(bc) histogram to the histogram of all dEs – is given as black line (left y-axis applies). The upper x-axis gives absolute magnitudes assuming $m - M = 31\overset{m}{.}0$.

$15^m \leq m_B < 16^m$, and 8% between $16^m \leq m_B < 17^m$. Within these magnitude ranges, we should thus find 9.4 ± 2.8 and 8.2 ± 2.8 dE(bc)s, respectively, for a binomial distribution. However, we found only 4 and 0 dE(bc)s, which lies within 1.9 and 3.0 standard deviations, respectively. It is thus very likely that the decline of the number fraction of dE(bc)s is real.

Since we are using B band magnitudes, it is an obvious question how much fainter the dE(bc)s will become after their star formation has ceased. From our spectral analysis, we expect a decrease of the B band flux *of the central* $3''$ to one third of the current flux (median value: 0.32) for the main sample dE(bc)s. To obtain this estimate we compared the total spectrum of each galaxy with the model spectrum of the old population only, as a conservative estimate. Since our galaxies show a colour gradient (Figures 3.1 to 3.3), which we interpret as a decrease of the fraction of young stars when going outwards, we now assume that the above ratio of faded and current flux linearly increases to 1 up to the B band half-light radius. This leads to an estimated fading of the total galaxy flux in the B band of $0\overset{m}{.}2$ for all dE(bc)s. Therefore, we do not expect significant evolution of the dE(bc) luminosity function after the cessation of star formation.

For the galaxies in the additional sample, Figures 3.5 and 3.6 show that the blue regions are more extended. We therefore assume the linear increase of the ratio of faded and current flux (see above) to extend to two half-light radii. This leads to an estimated fading of $0\overset{m}{.}4 - 0\overset{m}{.}5$. On average, these galaxies are already slightly fainter than the dE(bc)s of the main sample (see Figure 3.11). This difference would thus become more pronounced after their star formation has ceased. On the other hand, one might expect from their gas content that a significant amount of stars could still be formed in these objects, which would counteract the fading to some extent.

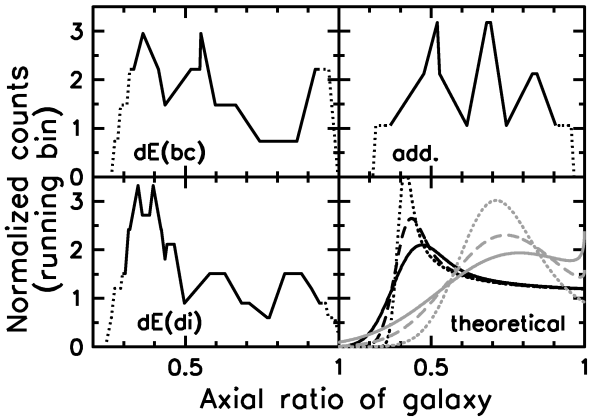

F 3.12. **Flattening distribution.** Distribution of projected axial ratios of the dE(bc)s of the main sample (top left), the galaxies of the additional sample (top right), and the dE(di)s from Chapter 2 (bottom left). The data are shown as running histogram with a bin-width of 0.1. Only galaxies with certain cluster membership are considered. Beyond the last data point on each side, the histograms are plotted with dotted instead of solid lines. The bottom right hand panel shows theoretically expected curves for intrinsic oblate (black) and prolate (grey) shapes, assuming randomly distributed inclinations and intrinsic axial ratios that are described by the following Gaussian distributions: oblate with mean $\mu = 0.4$ and $\sigma = 0.07$ (black solid line), $\sigma = 0.04$ (black dashed line), $\sigma = 0.02$ (black dotted line); prolate with $\mu = 0.65$ and $\sigma = 0.2$ (grey solid line), $\sigma = 0.15$ (grey dashed line), $\sigma = 0.1$ (grey dotted line).

7.2. Flattening distribution

The flattening distribution of the dE(bc)s is presented in Figure 3.12, along with that of the dE(di)s from Chapter 2. The axial ratios were derived from the elliptical apertures provided by Chapter 2 (see Section 4.1). Again, only galaxies with certain cluster membership are considered. The distributions are presented as running histograms with a binsize of 0.1 (±0.05), normalized to an area of 1. In the bottom right hand panel of the figure, we show various theoretical curves for comparison. We assume randomly distributed inclinations and oblate (black lines) or prolate (grey lines) intrinsic axial ratios. For the oblate case we adopt Gaussian distributions of various widths with a mean axial ratio of 0.4, while for the prolate case a mean value of 0.65 is used.

In Chapter 2, we deduced that dE(di)s are consistent with being flat oblate objects. Here, we find that the dE(bc)s of the main sample are similarly distributed, with slightly larger axial ratios than the dE(di)s. A comparison with the theoretical curves demonstrates that, despite the small sample size, their distribution is hardly consistent with dE(bc)s being spheroidal objects, and instead suggests the shape of a relatively thick disk. The galaxies of the additional sample are rounder, though not spheroidal. This is another point – besides the overall gas content, strength of emission lines, and size of star forming regions – in which the dE(bc)s of the main sample and the additional galaxies are not alike.

7.3. Spatial distribution

In Chapter 2 we found that while ordinary dEs are more strongly clustered towards the Virgo cluster center, dE(di)s basically show no clustering at all, another indication for them being a different population of galaxies. The dE(bc)s of the main sample also show no central clustering (Figure 3.13, upper panel), similar to the dE(di)s. The same applies to the objects of the additional sample (Figure 3.13, lower panel). While the number of dE(bc)s is relatively small and does not allow statistically secure statements, their distribution is hardly consistent with a centrally concentrated population.

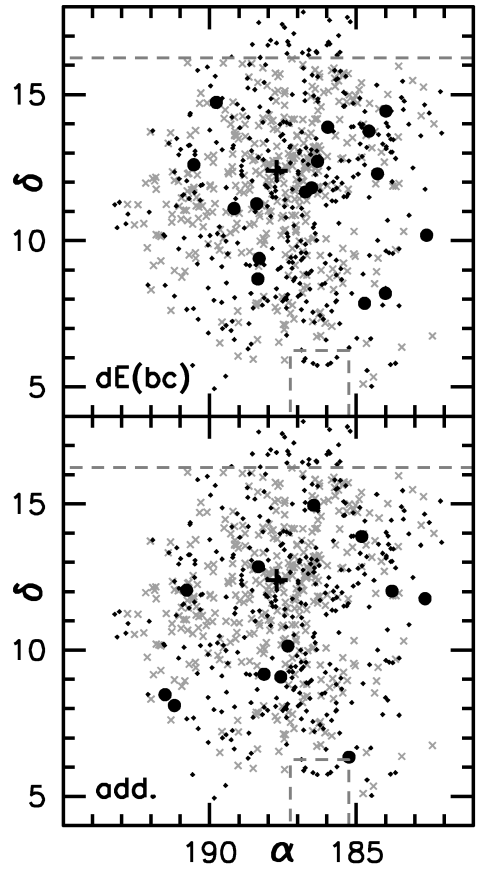

F 3.13. **Distribution within the cluster.** Projected spatial distribution of the dE(bc)s of the main sample (black circles, upper panel) and the galaxies of the additional sample (black circles, lower panel). Coordinates are given for J2000. Grey crosses represent all dEs without blue centers. All other Virgo cluster galaxies with $m_B \leq 18\overset{m}{.}0$ are shown as small black dots. Only galaxies with certain cluster membership are considered. The black cross gives the position of M87. Boundaries of the SDSS coverage are shown as grey dashed lines.

7.4. Morphology-density relation

In Figure 3.14 we present the cumulative distributions of local projected densities – calculated as in Dressler (1980) and Binggeli et al. (1987) – for the dE(bc)s, the galaxies of the additional sample, the dE(di)s, and the remaining, ordinary dEs (upper panel). We also compare these with the distributions of standard Hubble types (lower panel), i.e., with the well-known morphology-density relation.

The dE(bc)s and the objects of the additional sample are preferentially found in regions of moderate to lower density, and are distributed similarly to the irregular galaxies. This implies that they, as a population, are far from being virialized, corroborating the indications from the spatial distribution (Section 7.3). The dE(di)s show a similar distribution, which follows that of the spiral galaxies. Ordinary dEs, though, are preferentially found in higher density regions. Their location in the morphology-density diagram is intermediate between E/S0 galaxies and spirals.

7.5. Velocity distribution

Heliocentric velocities are available for 194 early-type dwarfs of our full dE sample that are certain Virgo cluster members (see Section 2.3). We present these data in Figure 3.15 for the dE(bc)s, the dE(di)s, and the remaining dEs (i.e., dE(bc)s and dE(di)s excluded). Each panel shows a running histogram with a bin-width of 366 km s^{-1}, which corresponds to the semi-interquartile range of all

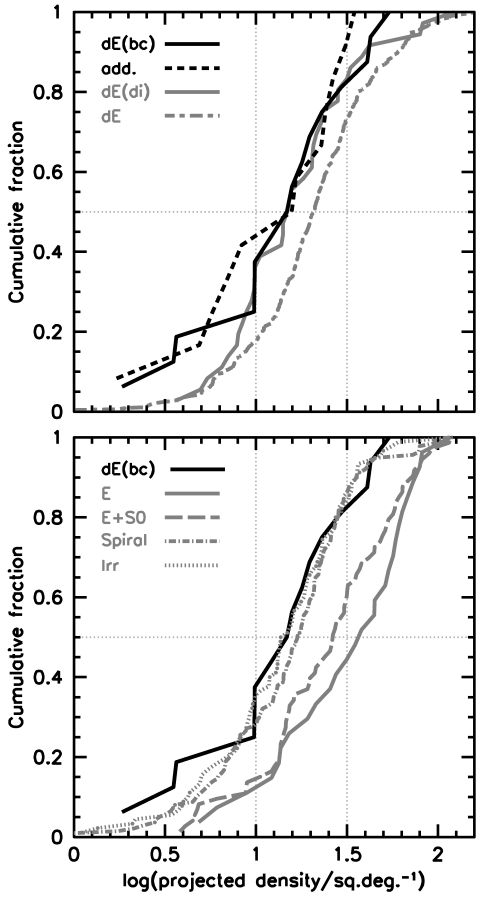

F 3.14. **Morphology vs. density.** Cumulative distribution of local projected densities. Following Dressler (1980) and Binggeli et al. (1987), we define a circular area around each VCC galaxy that includes its ten nearest neighbours (independent of galaxy type), yielding a projected density (number of galaxies per square degree). Only galaxies with certain cluster membership are taken into account. *Upper panel:* The dE(bc)s of the main sample (solid black line), the galaxies of the additional sample (dashed black line), the dE(di)s from Chapter 2 (solid grey line), and ordinary dEs (excluding dE(bc)s and dE(di)s, dashed grey line). *Lower panel:* The dE(bc)s of the main sample (solid black line) compared to various Hubble types.

194 velocities. Their median value, $v_{\rm helio}$ = 1248 km s^{-1}, is given as a dotted vertical line in each panel for comparison.

The dE(bc)s of the main sample show a relatively large deviation from the overall median value: their median velocity is only $v_{\rm helio}$ = 802 km s^{-1}. However, since the semi-interquartile range is large ($\Delta v_{\rm helio}$ = 463 km s^{-1}), and since only 15 objects are included in this sample, we cannot state whether this constitutes a significant difference. Instead, it might be more promising to compare the shapes of the distributions. The sample of ordinary dEs shows a close-to-symmetric distribution, which would be expected for a relaxed population. In contrast, the distribution of dE(bc)s and dE(di)s are asymmetric and less smooth. Both display side peaks, indicative of an infalling population (Tully & Shaya 1984; Conselice et al. 2001). This would be consistent with their spatial distribution, which shows no central concentration within the cluster, and with their distribution with local projected density, which follows that of the irregular cluster galaxies.

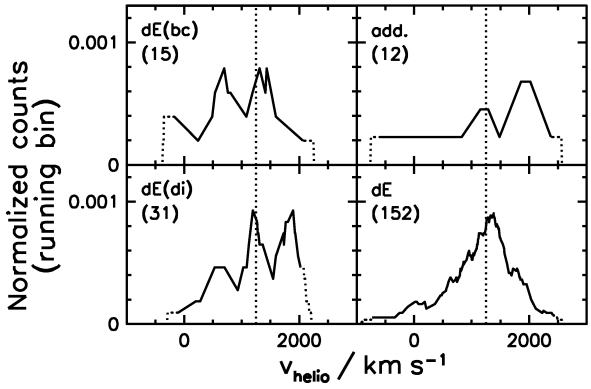

F 3.15. **Velocity distribution.** Distribution of available heliocentric velocities, taken from the NASA/IPAC Extragalactic Database (NED). The dE(bc)s of the main sample are shown in the top left panel, the galaxies of the additional sample in the top right panel, the dE(di)s from Chapter 2 in the bottom left panel, and the remaining dEs (excluding dE(bc)s and dE(di)s) in the bottom right panel. Only galaxies with certain cluster membership are included. The vertical dotted line marks the value of $v_{\rm helio}$ = 1248 km s^{-1}, which is the median value of all 194 available velocities for early-type dwarfs. The data are shown as running histogram with a bin-width of 366km s^{-1}, corresponding to the semi-interquartile range of these 194 velocities. Numbers in brackets are the number of galaxies included in the respective panel. Beyond the last data point on each side, the histograms are plotted with dotted instead of solid lines

8. D

The SDSS enables for the first time a systematic analysis of several hundred dEs in the Virgo cluster with optical imaging and partly with spectroscopy. These data provide the basis for our studies, which aim at disentangling the various subpopulations of early-type dwarfs and uncovering their evolutionary histories. In Chapter 2, we found that dEs with disk features (dE(di)s) constitute a disk-shaped, unrelaxed dE population that is clearly different from classical dwarf ellipticals. In the current study, we focus on another conspicuous feature that is common to several dEs: a blue center caused by recent or ongoing central star formation. We have shown that these dE(bc)s constitute a significant fraction (more than 15%) of bright dEs in the Virgo cluster. This number declines to almost zero beyond $m_{\rm B} > 16$, which is most likely a real decline and is not mainly due to signal-to-noise effects.

Two dE(bc)s of the main sample are detected in HI, with gas-to-baryonic mass fractions of 1% and 3 – 6%, respectively. These values and the upper limits for several other dE(bc)s suggest an average gas content larger than that of ordinary dEs, but lower than that of dwarf irregulars. Note that we do not know where in the galaxies the gas is located: if it were concentrated in the central region, it would probably be able to fuel star formation for a longer time than if the gas were distributed homogeneously.

As soon as star formation has ceased, each dE(bc)'s colour – which provided the basis of its selection – will become indistinguishable from that of an ordinary dE within ∼ a Gigayear or less (see Section 5.4). However, the statistical properties of the dE(bc) *population* are unlike those of ordinary dEs: the projected spatial distribution and the flattening distribution of the dE(bc)s are similar to those of the dE(di)s and are different from those of dEs that have no blue centers or disk features. Both the dE(bc) and dE(di) population show no central clustering, which, along with the side-peaks of their velocity distributions, hints towards fairly recent infall. How long ago this infall could have taken place depends on relaxation timescales. Conselice et al. (2001) derived a two-body relaxation time for the Virgo dEs of much more than a Hubble time. Even violent relaxation, which might only apply for the case of merging groups or subclusters, would take at least a few crossing times $t_{\rm cr}$, with $t_{\rm cr} \approx 1.7$ Gyr for the Virgo cluster (Boselli & Gavazzi 2006). Thus, a dE population built out of

infalling galaxies remains in an unrelaxed, non-virialized state for many Gyr. We conclude that the dE(bc)s most likely formed through infall of progenitor galaxies.

The shape of the dE(bc)s, as deduced from their flattening distribution, is hardly consistent with their being spheroidal objects, and instead implies that the dE(bc)s are rather thick disks, i.e. oblate-shaped objects with intrinsic axial ratios around ~0.4. This is only somewhat thicker than the dE(di)s, for which we derived an axial ratio of ~0.35 in Chapter 2. How could these disk-shaped dEs be produced?

8.1. Formation scenarios

In the galaxy harassment scenario (Moore et al. 1996), an infalling late-type disk galaxy gets transformed into a dE through high-speed encounters with massive cluster galaxies. This obviously leads to an increase in the axial ratio during the transformation process, since a disk is converted into a spheroid. However, a thick stellar disk may survive and lead to lenticular systems (Moore et al. 1996; Mastropietro et al. 2005). These may form a bar and spiral features, and retain them for some time, depending on the tidal heating of the galaxy (Mastropietro et al. 2005). Galaxy harassment thus appears to be a plausible scenario to explain the formation of disk-shaped dEs, and of dE(di)s in particular. Moreover, it predicts gas to be funneled to the center and form a density excess there (Moore et al. 1998). While Moore et al. compare this to the presence of a nucleus in many dEs, they admit that their simulations "were not designed to probe the inner 200 pc". The radii of many of the blue central regions of the dE(bc)s are only slightly larger than this value (see Figures 3.1 to 3.3); consequently, the central gas density excess could well explain the blue centers. The harassment scenario thus describes a possible evolution of an infalling late-type disk galaxy to a dE(bc) and to a dE(di).

Another mechanism to form disk-shaped dEs could be ram-pressure stripping (e.g. Gunn & Gott 1972) of dwarf irregulars. Depending on galaxy mass, the gas might be significantly removed except around the central region (Mori & Burkert 2000), which would seem to be consistent with the central star formation of the dE(bc)s. As shown by van Zee et al. (2004b), several dEs have significant rotation, and could thus be the descendants of dIrrs, which are also known to be mostly rotationally supported, at least at the luminosities considered here. However, apart from the problems with this scenario discussed in Section 1, like the metallicity offset between dEs and dIrrs or the too strong fading of dIrrs, the flattening distribution of dIrrs shown by Binggeli & Popescu (1995) is not quite like that of our dE(bc)s. Instead, dIrrs have a (primary) axial ratio $\geq$0.5. On the other hand, significant mass loss due to stripped gas would be expected to affect also the *stellar* configuration of the galaxies and could thus possibly account for the difference.

As outlined in Section 1, several studies claimed that BCDs might be progenitors of dEs. Their flattening distribution, as analyzed by Binggeli & Popescu (1995), is somewhat more like that of our dE(bc)s, though still slightly rounder. These BCDs behave similarly to the galaxies of our additional sample – which were mostly classified as (candidate) BCDs, but were selected only if their appearance was similar to the dE(bc)s. Overall, they have more extended blue regions, stronger emission lines, and clearly a higher gas content than the dE(bc)s of the main sample. They are also dominated by an underlying old population – only one out of seven has $M_{\rm old} < 90\%$ – and they have fairly regular outer shapes. Their spatial distribution also hints at an unrelaxed population, and their velocity distribution is asymmetric.

Tidally induced star formation in dIrrs (Davies & Phillipps 1988) might be able to link BCDs and dEs, and could at the same time overcome the problems of the ram-pressure stripping scenario. The initially lower metallicity and surface brightness of a dIrr are increased by several bursts of star formation, during which the galaxy appears as blue compact dwarf (BCD). After that, it fades to become a dE. The last star formation burst might occur in the central region of the dwarf (Davies & Phillipps 1988), consistent with the appearance of the dE(bc)s.

8.2. Presence of nuclei

Many late-type spirals – which act as dE progenitors in the harassment scenario – host a compact nucleus (e.g. Böker et al. 2004). If the nucleus survives the morphological transformation, it would become the nucleus of the resulting dE(bc) or dE(di). A second scenario for nucleus formation in dEs is late star formation out of central gas (e.g. Oh & Lin 2000), which in principle might be taking place in the centers of the dE(bc)s.

The fraction of nucleated galaxies among the dE(bc)s is 7/16 (44%), which is based on the VCC classification and has been verified by us through visual inspection of images and unsharp masks. We find one more dE(bc) to have "multiple nuclei" (VCC 0021), and one to have a possible nucleus (VCC 1512). If those two objects were counted as being nucleated, the fraction would increase to 56%. Among the dE(di)s, 26 out of 36 galaxies are nucleated (72%). Ordinary dEs (i.e. excluding dE(bc)s and dE(di)s) have a nucleated fraction of also 72% among the brighter objects ($m_B \leq 16^m$), which is the magnitude range of most dE(di)s and of all but one dE(bc). If we assumed a 72% nucleated fraction for the dE(bc)s as well, we would expect to find 11.5 nucleated dE(bc)s among our 16 objects, with a standard deviation $\sigma = 1.8$. Our observed number thus lies within 1.4σ of the expected value if dE(bc)s had the same nucleated fraction as dEs and dE(di)s, and if the two uncertain objects were counted as nucleated. Thus, there is no significant difference between dE(bc)s, dE(di)s, and the other dEs with respect to the presence or absence of a nucleus. Still, the somewhat smaller number of nuclei in dE(bc)s could be a hint that nuclei are indeed forming in their centers. Of the galaxies in the additional sample, none displays a nucleus, but the significant amount of central gas and dust might leave the possibility of a hidden nucleus, or of a nucleus just being formed.

We point out that the ACS Virgo Cluster Survey (Côté et al. 2004) found a much higher frequency of compact stellar nuclei in early-type galaxies than Binggeli et al. (1985) did, primarily due to the much higher resolution of space-based studies as compared to ground-based ones (Côté 2005). However, if we took into account these results, a dE classified as nucleated in the VCC would then simply be termed *a dE with a nucleus bright enough to have been detected by Binggeli et al. (1985)*.

8.3. Presence of dE(bc)s in less dense environments

Early-type dwarfs with blue centers are not only present in the Virgo cluster. NGC 205, with its central region of young stars and central dust clouds (Hodge 1973), is a well known local example of what we term a dE(bc); the same applies to NGC 185 (Hodge 1963). On the one hand, NGC 205 might be considered as special case due to its clear signs of tidal interaction with M 31 (Mateo 1998). On the other hand, tidal interaction might not be something special but instead something very common and even required for the formation of dEs, and of dE(bc)s in particular. While galaxy harassment is negligible in groups (Mayer et al. 2001a), a similar mechanism is provided there by the so-called tidal stirring scenario (Mayer et al. 2001b), in which a dIrr that suffers repeated tidal shocks is transformed into a dE or a dSph. In this model, the galaxies with higher surface brightness can reach a central gas density excess like what was described above for harassment. Tidal stirring might thus provide a consistent explanation for dE(bc)s in groups.

Contrary to the above interpretation of NGC 185 and NGC 205 as possible result of tidal stirring, Gu et al. (2006) recently presented an apparently isolated dwarf elliptical with a blue center (IC 225) at a distance of 20.6 Mpc. Its spectrum displays Balmer line emission, and based on its appearance it would doubtlessly enter our dE(bc) sample. The authors based their conclusion about the galaxy's isolation on their failure to find a potential companion within 30 arcmin, using the NED. This angular search radius corresponds to 180 kpc at their given distance. We increased the search radius, and found the small galaxy group USGC U124 (Ramella et al. 2002) to lie at the same distance as IC 225 (within 25 km s^{-1} in radial velocity), and at an angular separation of 145 arcmin, or 870 kpc. The brightest group member (NGC 0936) is an early-type spiral galaxy with $M_B \approx -20.5$. Since 870 kpc would seem a rather large distance for IC 225 to be a bound companion, we test whether a single interaction could have occured in the past. As an example, if the relative velocity was 100 km s^{-1},

the encounter would have occured 8.5 Gyr ago, much too long for the current star formation to have been triggered by it.

While the tidal forces of smaller galaxies closer to IC 225 could possibly affect the galaxy's gas distribution, Brosch et al. (2004) argued that tidal interactions might not be necessary for activating star formation, and that instead, the dynamics of gas masses in a dark matter gravitational potential could be the primary trigger. Nevertheless, the main problem would be to explain how an *isolated dE* could have formed at all. Therefore, if IC 225 is indeed a truly isolated galaxy, one has to think of other mechanisms for dE formation than the ones we have discussed. It also demonstrates along with NGC 185 and NGC 205 that central star formation does not only occur in cluster dEs, and that, consequently, the mechanisms for dE formation might be similar in different environments. In fact, in the Local Group, where we can study galaxies at the highest angular resolution, many dSphs show star formation histories that extend over many Gyr. In all of these cases, the younger populations are more centrally concentrated than the old ones (Harbeck et al. 2001). Apart from interactions, this may also be a consequence of longer-lived gas reservoirs at the centers of these galaxies' potential wells.

Finally, we caution against calling the dE(bc)s "dE/dIrr transition types": this would suggest that every dE(bc) has a dIrr progenitor, which might not be the case as discussed above. Similarly, Grebel et al. (2003) argued for Local Group dwarfs that the so-called dIrr/dSph transition types are plausible progenitors of dSphs, while dIrrs themselves seem less likely.

9. S

We have presented a study of Virgo cluster early-type dwarf galaxies (dEs) with central star forming regions, based on photometric and spectroscopic data from the SDSS DR4. These "dE(bc)s" are not rare objects, but they reach a fraction of more than 15% among the bright ($m_B < 16$) dEs. Their spatial distribution and their distribution with local projected density suggest that they are an unrelaxed population. Their flattening distribution is consistent with them being disk-shaped objects like the dEs with disk substructure (dE(di)s) identified in Chapter 2. Even in the very center, where their colours are bluest, 90% or more of their mass belongs to an old stellar population. Thus, they will appear like ordinary dEs within about one Gigayear after the end of their star formation. The gas content of the dE(bc)s is lower than in dwarf irregulars, but probably somewhat higher than in classical dEs, implying that at least in some dE(bc)s star formation might still continue for some time. Plausible formation mechanisms that could explain both the disk shape and the central star formation of the dE(bc)s are galaxy harassment (Moore et al. 1996), which describes the transformation of infalling late-type disk galaxies into dEs, tidally induced star formation in dIrrs (Davies & Phillipps 1988), and possibly also ram-pressure stripping (Gunn & Gott 1972) of dIrrs and star formation induced by gas compression due to ram pressure.

We have started our studies of Virgo early-type dwarfs by describing two sorts of dEs with "special features", i.e., dEs with a blue center (this study) and dEs with disk substructure (Chapter 2). It is important to stress that we are not looking at one single population of dEs, with those features just being some extra "flavour", but that these dE subtypes constitute populations with distinct properties that differ from the rest of dEs. To complicate the issue even more, ordinary dEs (i.e., exluding dE(bc)s and dE(di)s) are probably not a homogeneous population either, since e.g. the clustering properties of nucleated and non-nucleated dEs differ significantly (Binggeli et al. 1987). Whether or not all of these dE subtypes simply reflect different evolutionary stages of one single class of galaxy, or whether they are indeed different classes of early-type dwarfs, will be discussed in detail in Chapter 4.

Acknowledgements

It is a pleasure to thank B. Binggeli for many fruitful discussions and a careful reading of the manuscript. We thank the referee for useful comments that helped us improve the paper. We gratefully acknowledge support by the Swiss National Science Foundation through grants number 200020-105260, 200020-105535, and 200021-109616. We thank J. Gallagher for stimulating discussions. This study is based on publicly available data from the SDSS and the GOLDMine Database.

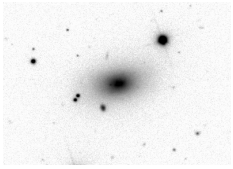

CHAPTER 4

A : -

"Subpopulation is a group which is basically an array of Individuals."
From http://cs1.gmu.edu/~eclab/

From a quantitative analysis of 413 Virgo cluster early-type dwarf galaxies (dEs) with Sloan Digital Sky Survey imaging data, we find that the dE class can be divided into multiple subpopulations that differ significantly in their morphology and clustering properties. Three dE subclasses are shaped like thick disks and show no central clustering: (1) dEs with disk features like spiral arms or bars, (2) dEs with central star formation, and (3) ordinary, bright dEs that have no or only a weak nucleus. These populations probably formed from infalling progenitor galaxies. In contrast, ordinary nucleated dEs follow the picture of classical dwarf elliptical galaxies in that they are spheroidal objects and are centrally clustered like E and S0 galaxies, indicating that they have resided in the cluster since a long time, or were formed along with it. These results define a morphology-density relation within *the dE class. We find that the difference in the clustering properties of nucleated dEs and dEs with no or only a weak nucleus is not caused by selection biases, as opposed to previously reported suggestions. The correlation between surface brightness and observed axial ratio favors oblate shapes for all subclasses, but our derivation of intrinsic axial ratios indicates the presence of at least some triaxiality. We discuss possible interrelations and formation mechanisms (ram-pressure stripping, tidally induced star formation, harassment) of these dE subpopulations.*

This study was done together with Eva K. Grebel, Bruno Binggeli, and Katharina Glatt.
It is accepted for publication in The Astrophysical Journal.

1. I

As the most numerous type of galaxy in clusters, early-type dwarf galaxies are ideal probes to study the physical processes that govern galaxy formation and evolution in environments of different density. The pronounced morphology-density relation (e.g., Dressler 1980; Binggeli et al. 1987) suggests that early-type dwarfs were either formed mainly in high-density environments, or originate from galaxies that fell into a cluster and were morphologically transformed. However, the actual formation mechanisms are still a matter of debate (see Jerjen & Binggeli 2005, and references therein). Most of the proposed scenarios are based on the vigorous forces acting within a cluster environment, like ram-pressure stripping (Gunn & Gott 1972) of dwarf irregular (dIrr) galaxies (e.g., van Zee et al. 2004b), tidally induced star formation in dIrrs (Davies & Phillipps 1988), or so-called harassment (Moore et al. 1996) of infalling late-type spirals through close encounters with massive cluster members.

Early-type dwarfs form a rather heterogeneous class of objects. In addition to the classical dwarf ellipticals, Sandage & Binggeli (1984) introduced the class of dwarf S0 (dS0) galaxies, which were conjectured to have disk components, based on signatures like high flattening or a bulge+disk-like profile (Binggeli & Cameron 1991). The identification of spiral substructure then provided the first direct proof for a disk in an early-type dwarf (Jerjen et al. 2000), which, however, had not been classified as dS0 but as dwarf elliptical. Inspired by similar discoveries (e.g., Barazza et al. 2002; Graham et al. 2003; De Rijcke et al. 2003), we performed a search for disk features in 410 Virgo cluster early-type dwarfs (Lisker et al. 2006b, Chapter 2). We thereby included galaxies classified as dwarf elliptical and as dS0 to avoid any preselection bias, and assigned them the common abbreviation "dE", which we adopt for this study as well. We identified disk features in 36 dEs, and argued that they constitute an unrelaxed population of disk-shaped galaxies different from the classical dwarf ellipticals (Chapter 2).

But the dE class shows yet more diversity: nucleated and non-nucleated dEs have different clustering properties (van den Bergh 1986; Ferguson & Sandage 1989), their flattening distributions differ (Binggeli & Cameron 1991; Ryden & Terndrup 1994; Binggeli & Popescu 1995), and colour differences were reported as well (Rakos & Schombert 2004; Lisker et al. 2005). Moreover, several of the bright dEs display blue central regions caused by recent or ongoing star formation (Lisker et al. 2006c, Chapter 3), and also differ in their spatial and flattening distributions from the bulk of dEs. Thus, prior to discussing possible formation mechanisms, we need to systematically disentangle the various dE subclasses observationally. This is the purpose of this study.

2. S

While our dE sample selection was already described in Chapters 2 and 3, these studies were still based on the Data Release 4 of the Sloan Digital Sky Survey (SDSS; Adelman-McCarthy et al. 2006). Since we are now using the full SDSS Data Release 5 (DR5, Adelman-McCarthy et al. 2007) dataset, we provide here a detailed, updated description of our selection.

2.1. Selection process

The Virgo Cluster Catalog (VCC, Binggeli et al. 1985), along with revised classifications from Barazza et al. (2002, VCC 1422), Barazza et al. (2003, VCC 0850), and Geha et al. (2003, VCC 1488), contains 1197 galaxies classified "dE" or "dS0", including candidates, that are certain or possible cluster members according to Binggeli et al. (1985), Binggeli et al. (1993), and Chapter 3. 552 of these fall within our chosen limit in apparent B magnitude from the VCC of $m_B \leq 18\overset{m}{.}0$ (see Chapter 2). This is the same magnitude limit up to which the VCC was found to be complete (Binggeli et al. 1985). When adopting a Virgo cluster distance of $d = 15.85$ Mpc, i.e., a distance modulus $m - M = 31\overset{m}{.}0$

(see, e.g., Ferrarese et al. 2000), which we use throughout, this corresponds roughly to a limit in absolute magnitude of $M_B \leq -13.^m0$.

Six galaxies are not covered by the SDSS. While we initially included objects with uncertain classification (e.g., "dE?"), we then excluded all 50 galaxies that appeared to be possible dwarf irregulars from visual inspection of the co-added SDSS *g*,r, and *i* images (see Chapter 2), or were classified as "dE/Im". Three more objects (VCC 0184, VCC 0211, and VCC 1941) were excluded because they appear to be probable background spirals. Finally, VCC 1667 could not be classified properly, since it is significantly blended with multiple other galaxies. This leads to a final dE sample of 492 certain or possible cluster members, containing 426 certain cluster members on which we focus in the present study.

2.2. Presence of nuclei

While our classification of nucleated and non-nucleated dEs relies on the VCC, it is known from HST observations that many apparently non-nucleated dEs actually host a faint nucleus hardly detectable with ground-based imaging (Côté et al. 2006, also see Lotz et al. 2004b). A direct comparison of the VCC classification with the results from Côté et al. (2006) shows that, as a rough rule of thumb, the detection of dE nuclei in the VCC becomes incomplete for nucleus magnitudes that are fainter than the respective value of the host galaxy's central surface brightness, measured within a radius $r = 0.1''$ (Figure 4.1). Our non-nucleated dEs could thus be more appropriately termed *dEs without a nucleus of significant relative brightness* as compared to the underlying light of the galaxy's center. In fact, Grant et al. (2005) suggested that dEs classified as nucleated and non-nucleated might actually form a continuum of dEs with respect to relative nucleus brightness. Therefore, the VCC classification basically translates into probing opposite sides of this continuum — and this is exactly what makes it useful for our study of dE subclasses. If the relative brightness of a nucleus depends on its host galaxy's evolutionary history, then one might expect nucleated and "VCC-non-nucleated" dEs to exhibit different population properties.

3. D

The SDSS DR5 covers all VCC galaxies except for an approximately $2^\circ \times 2.^\circ5$ area at $\alpha \approx 186.^\circ2$, $\delta \approx +5.^\circ0$. It provides reduced images taken in the *u*, *g*, *r*, *i*, and *z* bands with an effective exposure time of 54s in each band (see also Stoughton et al. 2002), as well as the necessary parameters to flux calibrate them. The pixel scale of $0.''396$ corresponds to a physical size of 30 pc at our adopted Virgo cluster distance of $d = 15.85$ Mpc. The SDSS imaging camera (Gunn et al. 1998) takes data in drift-scanning mode nearly simultaneously in the five photometric bands, and thus combines very homogeneous multicolour photometry with large area coverage and sufficient depth to enable a systematic analysis of dEs. The images have an absolute astrometric accuracy of RMS$\leq 0.''1$ per coordinate, and a relative accuracy between the *r* band and each of the other bands of less than 0.1 pixels (Pier et al. 2003). They can thus easily be aligned using their astrometric calibration and need not be registered manually.

The RMS of the noise per pixel corresponds to a surface brightness of approximately 24.2 mag arcsec^{-2} in the u-band, 24.7 in *g*, 24.4 in *r*, 23.9 in *i*, and 22.4 in z. The typical total signal-to-noise ratio (S/N) of a bright dE ($m_{B,VCC} \approx 14^m$) amounts to about 1000 in the r-band within an aperture radius of approximately two half-light radii. For a faint dE ($m_B \approx 18^m$) this value is typically about 50. While the S/N in the *g* and i-band is similar, it is several times lower in the z-band and more than ten times lower in the u-band.

The SDSS provides photometric measurements for our galaxies, but we found these to be incorrect in many cases (Lisker et al. 2005). The SDSS photometric pipeline significantly overestimates the local sky flux around the Virgo dEs due to their large apparent sizes and low surface brightness outskirts. This affects the derivation of isophotal and Petrosian radii, the profile fits, and subsequently

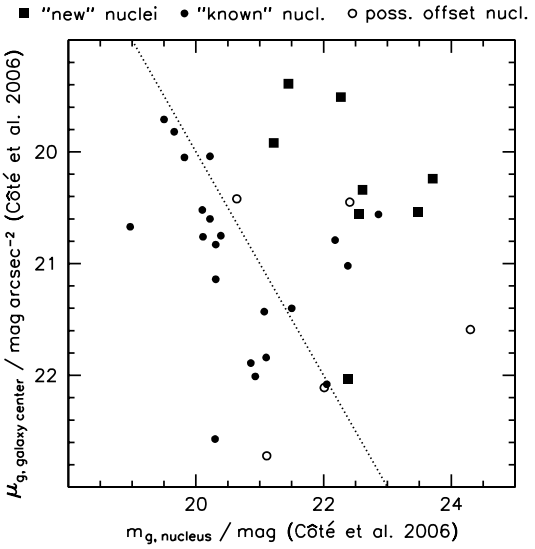

F 4.1. **Nucleus detection limits.** Shown are central surface brightnesses and nucleus magnitudes in *g*, both from Côté et al. (2006), for 34 of the 36 VCC dEs of their sample (VCC 1512 has no nucleus, and for VCC 1743 no values could be derived). Objects where Côté et al. (2006) identified "new" nuclei, i.e., that are listed as non-nucleated or only possibly nucleated in the VCC, are shown as filled squares. Objects that might have an offset nucleus according to Côté et al. (2006) and that are listed as non-nucleated in the VCC are shown as open circles. Objects classified as nucleated in both Côté et al. (2006) and the VCC (including class "N:") are represented by the filled circles. The dotted line follows equal values of central surface brightness (in mag arcsec^{-2}) and nucleus magnitude (in mag).

the calculation of total magnitudes, which can be wrong by up to $0\overset{m}{.}5$. For this reason, we used *B* magnitudes from the VCC throughout Chapters 2 and 3. In the meantime, we had performed our own structural and photometric measurements (see Section 4), which we shall use here as well as in the following chapters. Still, when we refer to *B* magnitudes, these were adopted from the VCC.

Heliocentric velocities for part of the sample are provided by the NASA/IPAC Extragalactic Database (NED; also see Chapter 3 for more detailed references).

4. I

4.1. Sky subtraction

The sky level on the SDSS images can vary by some tenths of the noise level across an image. For a proper determination of Petrosian radii of the dEs (see Section 4.3) despite their low surface brightness outskirts, it is thus not always sufficient to subtract only a single sky flux value from each SDSS image. Therefore, we performed sky subtraction through the following procedure. First, we constructed object masks for each SDSS image from the so-called segmentation images of the Source Extractor software (Bertin & Arnouts 1996) by expanding these through smoothing with a Gaussian filter (using *IRAF*[1], Tody 1993). A preliminary sky level was then determined for each image as the median of all unmasked pixels, clipped three times iteratively at 3σ. In order to reach a higher S/N than that of the individual images, we then produced a co-added image by summing the (weighted) *g*, *r*, and i-band images as described in Chapter 2. We then obtained an improved object mask from the co-added image and used this to refine our sky level measurement.

[1] IRAF is distributed by the National Optical Astronomy Observatories, which are operated by the Association of Universities for Research in Astronomy, Inc., under cooperative agreement with the National Science Foundation.

Finally, the sky flux distribution across the image was determined by computing the average flux – clipped five times iteratively at 3σ – of all unmasked pixels in 201×201 pixel boxes, centered every 40 pixels. This grid of values can be stored as a 52×38 pixel "sky image". Pixels in this sky image that did not contain useful values due to too many masked pixels in the parent image were linearly interpolated using *IRAF/fixpix*. We then applied a 3×3 pixel median filter to the sky image, expanded it to match its parent SDSS image's size (using *IRAF/magnify* with linear interpolation), and subtracted it from the latter. This yields the final *u*, *g*, *r*, *i*, and *z* images.

We point out that there is, to our knowledge, no general agreement or recipe as to whether to use, e.g., the clipped mean, the median, the clipped median, or the mode, for determination of the sky level. However, it is advisable that the chosen approach be reconciled with the image measurements to be performed, which in our case is the derivation of Petrosian radii (see Section 4.3). Since the latter is based on the *average* flux within given annuli, we chose to use the clipped *average* flux of all unmasked pixels for our sky level measurement. This guarantees that the resulting flux level in each image is zero as "seen" by the Petrosian radius calculation.[2]

4.2. Calibration and extraction

We calibrated the sky subtracted SDSS images using the provided flux calibration information (photometric zeropoint and airmass correction). We also corrected for the reported[3] SDSS zeropoint offsets in the *u* and *z* bands from the AB system (Oke & Gunn 1983). However, before working with the images, it is advantageous to put together adjacent images: a number of galaxies partly extend beyond the image edges and reappear on the corresponding neighbouring image. Bright dEs typically have apparent diameters of 300 pixels or more, which is rather large compared to the SDSS image size of 2048×1489 pixels. The SDSS astrometric calibration allows us to accurately put together adjacent images, which we did before extracting an 801×801 pixel cutout image for each galaxy. These cutout images were then corrected for Galactic extinction, using one value per image, calculated with the dust maps and corresponding software[4] of Schlegel et al. (1998). From the *g*, *r*, and *i* cutout image we produced a final co-added image for each galaxy.

4.3. Morphology

We perform an iterative process of determining shape and total flux for each galaxy, as described below. Throughout this process, we mask disturbing foreground or background objects, i.e., we do not consider masked pixels in any calculation. We start with deriving the Petrosian radius (Petrosian 1976), as defined by Stoughton et al. (2002), on the co-added image. Using a circular aperture with one Petrosian radius, we then find the center of the galaxy's image by iteratively searching for the minimum asymmetry, following Conselice et al. (2000). The asymmetry *A* is calculated as

$$A = \frac{\sum_i |f_i - f_{i,180}|}{\sum_i |f_i|}, \tag{4}$$

where f_i is the flux value of the i-th pixel, and $f_{i,180}$ is the flux value of the corresponding pixel in the 180-degree rotated image.

The asymmetry is computed using an initially guessed central position (from Chapter 2 for objects in the SDSS DR4, and from visual examination for objects in DR5, using SAOImage DS9, Joye & Mandel 2003), as well as for using the surrounding eight positions in a 3×3 grid as center. If one

[2] The reason why such considerations are at all necessary is the same as that for which the SDSS pipeline overestimated the local sky flux: the Virgo dEs are large in apparent size and cover 10^4 to 10^5 pixels, but their low surface brightness outskirts cause a large number of these pixels to have S/N< 1. Thus, a wrong sky level estimate of the order of just a few tenths of the noise level can have a large effect in total.

[3] see http://www.sdss.org/dr5/algorithms/fluxcal.html

[4] provided at http://www.astro.princeton.edu/~schlegel/dust/data/

of the surrounding positions yields a lower asymmetry, it is adopted as new central position. This process is repeated until convergence. We perform two of these "asymmetry centerings": a first one with a step size of 1 pixel, and a second one with a step size of 0.3 pixels. The initial and final value typically differ by less than a pixel.

We then compute the parameters defining an elliptical aperture (axial ratio and position angle) from the image moments (Abraham et al. 1994), and derive a "Petrosian semimajor axis" (hereafter "Petrosian SMA", $a_{\rm p}$), i.e., we use ellipses instead of circles in the calculation of the Petrosian radius (see, e.g., Lotz et al. 2004a). Within this elliptical aperture with a semimajor axis a of $1a_{\rm p}$, we perform another iteration to re-derive the elliptical shape parameters from the image moments, and also to re-derive $a_{\rm p}$.

The elliptical shape is then applied to measure the total flux in the r band within an elliptical aperture with $a = 2a_{\rm p}$, which also yields a half-light semimajor axis in r ($a_{\rm hl,r}$). Using this value for $a_{\rm hl,r}$, we go back to the co-added image and fit an ellipse to the isophotal shape of the galaxy at $a = 2\,a_{\rm hl,r}$, using *IRAF/ellipse*. The elliptical annulus used for the isophotal fit ranges from $2^{0.75}a_{\rm hl,r}$ to $2^{1.25}a_{\rm hl,r}$.

This new elliptical shape is now used to derive the final Petrosian semimajor axis on the co-added image, and to subsequently measure again the total flux in the r band within $a = 2\,a_{\rm p}$, yielding the final value for $a_{\rm hl,r}$. The isophotal shape is then measured again at $a = 2\,a_{\rm hl,r}$, yielding the axial ratio that we shall use throughout this study.

Since we masked disturbing foreground or background objects by not considering their pixels, our measured total flux for a given galaxy is always lower than it would be without any such "holes" in the galaxy's image. In order to correct for this effect, we subdivide the final aperture of each galaxy into 20 elliptical annuli of equal width, and assign each masked pixel the average flux value of its respective annulus. This yields our final value for the total r band flux and the corresponding magnitude. The difference to the uncorrected value is typically less than $0\overset{\rm m}{.}1$.

For 13 of our dEs, the derivation of the Petrosian SMA did not converge, due to the fact that these galaxies sit within the light of nearby bright sources. While in some of these cases, it would still be possible to "manually" define an axial ratio for the galaxy, we decided to exclude these objects from our sample, since no reliable r magnitudes can be derived, which are needed for our definitions of dE subclasses in Section 5. This leaves us with a working sample of 413 Virgo cluster dEs.

5. E -

5.1. Subclass definitions

Of our 413 Virgo dEs, 37 display disk features, like spiral arms, bars, or signs of an edge-on disk (Chapter 2, adding VCC 0751 to the objects listed there in order to update to SDSS DR5). We term these objects "dE(di)s", and separate this dE subclass from the ordinary, "featureless" dEs (Figure 4.2). In order to further explore the diversity of the latter, we perform a secondary subdivision into nucleated ("dE(N)") and non-nucleated ("dE(nN)") galaxies, based on the identification of nuclei in the VCC as outlined in Section 2.2. Since a further subdivision of the dE(di)s would lead to statistically insignificant subsamples, we shall instead discuss their nucleated fraction in the text. Finally, since our galaxies span a range of almost $5^{\rm m}$ in r, it appears worth performing a tertiary subdivision into dEs brighter and fainter than the median r brightness of our full sample, namely $m_{\rm r} = 15\overset{\rm m}{.}67$ mag. Moreover, all but three of the dE(di)s are brighter than this value; thus our subdivision allows us to compare them to ordinary dEs of similar luminosities. The percentage of each subsample among our full sample of 413 dEs is given in parentheses in Figure 4.2, whereas the actual number of galaxies contained in each subsample is given in the left column of Figure 4.3.

The subclasses defined so far are based on structural properties only — for *morphological* classification of galaxies, it is not advisable to use colour information. However, in Chapter 3 we identified a significant number of dEs with blue centers (17 galaxies, including VCC 0901 from the SDSS DR5).

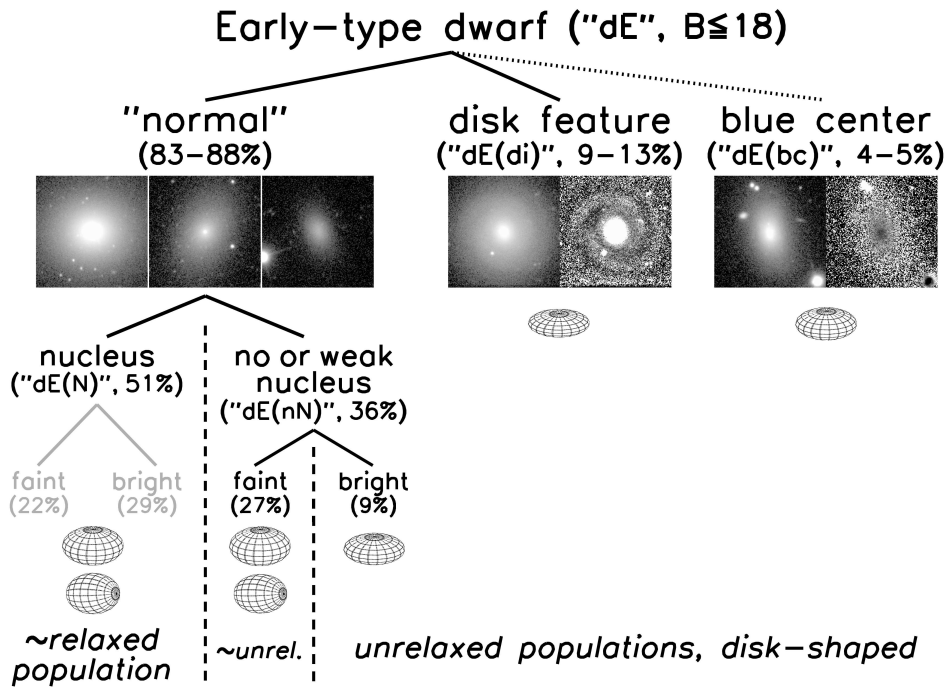

F 4.2. **The zoo of early-type dwarfs.** Our subdivision is shown as tree scheme, along with a 3-D illustration of a typical intrinsic shape, using the median axial ratio from the intrinsic distributions shown in Figure 4.3 (see Section 5.2). We also provide a statement about the inferred dynamical status of each subpopulation, as indicated by their clustering properties: "relaxed" and "unrelaxed" (see Section 5.3). The subdivision of dE(N)s into faint and bright samples is shown in grey colour to reflect the fact that we find them to be not different in their properties (see Section 5). The branch of the dE(bc)s is shown as dotted line only, since these are not a *morphological* subclass (see text). The percentage of each subsample among our 413 Virgo cluster dEs is given in parentheses. For the dE(bc)s and dE(di)s the percentage ranges include corrections for the estimated number of objects missed by our detection techniques (see Chapters 2 and 3). Three sample images are shown for the normal dEs. For the dE(di)s, we show one sample image along with its unsharp mask revealing the spiral substructure. For the dE(bc)s, one sample image is shown along with its $g - i$ colour map revealing the blue center (dark=blue). See text for further details.

These objects, termed "dE(bc)s", exhibit recent or ongoing central star formation, similar to NGC 205 in the Local Group. They were morphologically classified as dwarf ellipticals or dS0s by Sandage & Binggeli (1984), and their regular, early-type morphology was confirmed in Chapter 3; thus, they are not possible irregular galaxies, which we have excluded from our samples here and in the previous chapters. The flattening distribution of the dE(bc)s was found to be incompatible with intrinsically spheroidal objects (Chapter 3), and their distribution with respect to local projected density suggests that they are an unrelaxed population. The latter result is similar to the spatial distribution of Virgo and Fornax dwarfs with early-type morphology that are gas-rich and/or show star formation (Drinkwater et al. 2001; Conselice et al. 2003; Buyle et al. 2005).

While it is not clear a priori that any of the dE subclasses defined above are evolutionary interrelated, each dE(bc) unavoidably evolves into one of the above dE types once star formation ceases and the central colour reddens (Chapter 3). Therefore, and because the dE(bc)s are defined through colour instead of morphological properties, we do not consider them a *morphological* dE subclass.[5]

[5] A *morphological* peculiarity of several dE(bc)s is that they show central irregularities, which are presumably due to gas, dust, and/or star formation, similar to NGC 205. These can be seen, e.g., when constructing unsharp mask images (Chapter 3). However, an attempt to quantify these weak features through image parameters like asymmetry or clumpiness yielded no clear separation from the bulk of dEs. Moreover, not all dE(bc)s display such features.

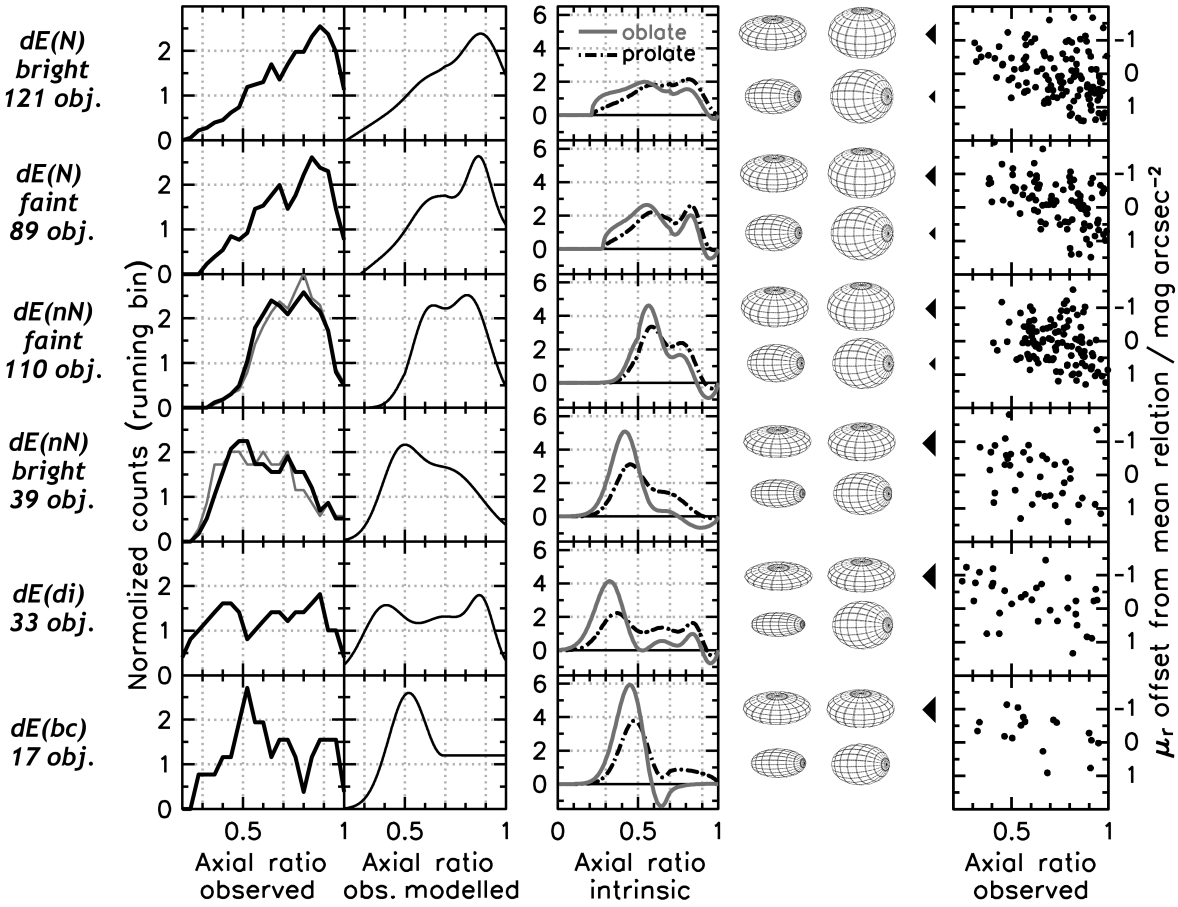

F 4.3. **Deduction of intrinsic shapes.** In the leftmost column, the number of objects in each of our dE subsamples are given. In the second column, we show the distribution of projected axial ratios for each of our dE subsamples. The data are shown as running histogram with a bin width of 0.15, corresponding to one fifth of the range in axial ratio covered by our galaxies. Each curve is sampled in steps of 0.04 (one quarter of the bin width) and normalized to an area of 1. The observed distributions are approximated by analytic functions (see text), shown in the third column. From these, we derive intrinsic axial ratio distributions (fourth column), adopting purely oblate (grey solid line) and purely prolate (black dash-dotted line) shapes. For these distributions, we show in the fifth column 3-D illustrations of the galaxy shapes for the oblate (upper) and prolate (lower) case. For each distribution, we show the shape when using the 25th percentile axial ratio (left) and the 75th percentile axial ratio (right). In the rightmost column, we show for each dE subsample the surface brightness test (see text): we plot the surface brightness offset from the mean relation of r band surface brightness and magnitude against axial ratio. Surface brightness is measured within $a = 2\,a_{\mathrm{hl,r}}$, since axial ratio is measured at the same semimajor axis. The mean relation of surface brightness and magnitude is obtained through a linear least squares fit with one $3\,\sigma$-clipping. The arrows pointing from the surface brightness test diagrams towards the shape illustrations reflect whether the test implies oblate or prolate intrinsic shapes; see text for more details.

On the other hand, their star formation and presence of gas (Chapter 3) might imply that their formation process is not completely finished yet. It thus appears more cautious to separate them from the rest of dEs (see Figure 4.2) in order to not bias the population properties of the other subclasses. In the discussion (Section 7) we try to assess which dE type(s) the dE(bc)s could possibly evolve into. Note that four objects are common to both the dE(di) and the dE(bc) sample. We exclude these from

the sample of dE(di)s, which now comprises 33 galaxies. Table 4.1 lists our dEs along with their subclass.

A similar subdivision of the dE class into bright and faint (non-)nucleated subsamples was performed by Ferguson & Sandage (1989), also with the aim of studying shapes and spatial distributions of the resulting subsamples. Our subdivision is different in two respects: first, Ferguson & Sandage defined all galaxies with $m_B < 17\overset{m}{.}5$ as "bright", whereas our magnitude separation (at $m_r = 15\overset{m}{.}67$) is done at significantly brighter values and divides our full sample into equally sized halves. Second, we have the advantage of excluding dE(di)s and dE(bc)s from the "normal" dEs, thereby obtaining cleaner subsamples, especially for the bright objects: all but three of the dE(di)s are brighter than $m_r = 15\overset{m}{.}67$.

While Ferguson & Sandage (1989) found statistically significant differences in the spatial distributions of their subsamples – with dE(N)s being much more centrally clustered than the bright dE(nN)s – their flattening distributions were only based on eye-estimated axial ratios from photographic plates. These can be uncertain by ~20% (Ferguson & Sandage 1989). With our measured axial ratios from the co-added SDSS images at hand, we therefore present in the following subsection a more detailed and accurate study of the flattening distributions of the different dE subsamples, and attempt to deduce their approximate intrinsic shapes.

5.2. Subclass shapes

From the axial ratio measurements of our galaxies (Section 4.3), we put together the flattening distributions of each dE subsample. These are presented in the second column of Figure 4.3 as running histograms, i.e., at each sampling point we consider the number of objects within a bin of constant width, and normalize the resulting curve to an area of 1. The bin width is 0.15, which we have chosen to be one fifth of the range in axial ratio covered by our galaxies. The sampling step is 0.04 (one quarter of the bin width). The bright and faint dE(N)s, and also the faint dE(nN)s, predominantly have rather round apparent shapes, while the bright dE(nN)s, dE(di)s, and dE(bc)s exhibit a significant fraction of objects with rather flat apparent shapes.

Since the division between bright and faint objects at $m_r = 15\overset{m}{.}67$ is somewhat arbitrary, we test whether the difference between the axial ratio distributions of faint and bright dE(nN)s becomes even more pronounced if a wider magnitude separation is adopted. The grey curves in the respective panels of the second column of Figure 4.3 show the distributions for bright dE(nN)s with $m_r \leq 15\overset{m}{.}67 - 0\overset{m}{.}5$ (23 objects) and for faint dE(nN)s with $m_r \leq 15\overset{m}{.}67 + 0\overset{m}{.}5$ (86 objects). While the faint dE(nN)s basically remain unchanged, the bright dE(nN)s indeed tend slightly towards flatter shapes, but the difference is rather small.

A statistical comparison of the axial ratio distributions of our dE subsamples confirms what is seen in Figure 4.3: a K-S test yields very low probabilities that any of the "flatter" subsamples (bright dE(nN)s, dE(di)s, and dE(bc)s, lower three rows) could stem from the same true distribution function as any of the "rounder" subsamples (bright and faint dE(N)s as well as faint dE(nN)s, upper three rows). This confirms our findings from Chapters 2 and 3 for the dE(di)s and dE(bc)s, respectively. The resulting probabilities from the K-S test for the pairwise comparison of the subsamples are given as percentages in Figure 4.4. Interestingly, the lowest probability of all comparisons is obtained when matching the distributions of bright and faint dE(nN)s: here, the probability of the null hypothesis that they stem from the same underlying distribution function is only 0.10%. Note that the probabilities for the comparison of the "flatter" subsamples with the "rounder" ones increase slightly with decreasing sample size, going from the bright dE(nN)s to the dE(di)s and then to the dE(bc)s. However, the probability for a common underlying distribution of dE(bc)s and the bright and faint dE(N)s is still only 3.8% and 4.6%, respectively.

Is it possible to deduce the distributions of *intrinsic* axial ratios from those of the apparent ones? As discussed in detail by Binggeli & Popescu (1995), the intrinsic shapes can be deduced when assuming that they are purely oblate or purely prolate. The distribution function Ψ of intrinsic axial ratios q can then be derived from the distribution function Φ of observed axial ratios p through (Fall

	dE(N) bright	dE(N) faint	dE(nN) faint	dE(nN) bright	dE(di)	dE(bc)
dE(N) bright		78.18	6.08	0.19	1.31	3.77
dE(N) faint	78.18		58.68	1.19	1.80	4.61
dE(nN) faint	6.08	58.68		0.10	0.24	0.44
dE(nN) bright	0.19	1.19	0.10		36.89	90.25
dE(di)	1.31	1.80	0.24	36.89		61.80
dE(bc)	3.77	4.61	0.44	90.25	61.80	

F 4.4. K-S test results for the comparison of the axial ratio distributions of our dE subsamples. For each pair of distributions we give the probability in percent for the null hypothesis that the two distributions stem from the same underlying distribution function.

& Frenk 1983, eqs. (6) and (9))

$$\Psi(q) = \frac{2}{\pi}\sqrt{1-q^2}\frac{d}{dq}\int_0^q dp \frac{\Phi(p)}{\sqrt{q^2-p^2}} \tag{5}$$

for the oblate case, and

$$\Psi(q) = \frac{2}{\pi}\frac{\sqrt{1-q^2}}{q^2}\frac{d}{dq}\int_0^q dp \frac{p^3\Phi(p)}{\sqrt{q^2-p^2}} \tag{6}$$

for the prolate case. Following Binggeli & Popescu (1995), we first defined adequate analytic functions $\Phi(p)$ that represent the observed distributions, and then evaluated the above equations numerically. The analytic "model functions" are shown in the third column of Figure 4.3; they were constructed from combinations of (skewed) Gaussians with each other and, in some cases, with straight lines. Note that, for the dE(bc)s, we decided not to follow the observed distribution in all detail, since it is drawn from a rather small sample of 17 galaxies, which probably is the cause of the fluctuations seen.

The deduced intrinsic distributions are presented in the fourth column of Figure 4.3, for the oblate (grey lines) and prolate (black dash-dotted lines) case. We also show 3-D illustrations of the galaxy shapes for each distribution (fifth column), using in each case the axial ratio of the 25th percentile (left 3-D plot) and the 75th percentile (right 3-D plot). These results confirm that the bright dE(nN)s, dE(di)s, and dE(bc)s do have lower axial ratios than the bright and faint dE(N)s and the faint dE(nN)s. Furthermore, we point out that the bright and faint dE(N)s span a rather wide range of intrinsic axial ratios, and are, on average, somewhat flatter than what was deduced by Binggeli & Popescu (1995): our median value (see the 3-D illustrations in Figure 4.2) is slightly flatter than E3 for the prolate case, and slightly flatter than E4 for the oblate case.

Can we decide whether the true shapes of our galaxies are more likely to be oblate or to be prolate? For this purpose, we make use of the surface brightness test (Marchant & Olson 1979; Richstone 1979), again following Binggeli & Popescu (1995). If dEs were intrinsically oblate spheroids, galaxies that appear round would be seen face-on and should thus have a lower mean surface brightness than galaxies that appear flat; the latter would be seen edge-on. For the prolate case, the inverse relation should be observed. However, before we can perform this test, we need to take into account the strong correlation of dE surface brightness with magnitude (e.g., Binggeli & Cameron 1991): if, by chance, the few apparently round galaxies in one of our smaller subsamples would happen to be fainter on average than the apparently flat ones, this could introduce an artificial relation of axial ratio with surface brightness. Therefore, instead of directly using surface brightness like earlier studies

T 4.1. **Subclass assignment.** Classification of a dE as nucleated or non-nucleated is provided by the VCC (Binggeli et al. 1985). Of the dEs that do not display disk substructure or a blue center, those with a small uncertainty on the presence of a nucleus ("N:") were included in the nucleated subclass, while those with a larger uncertainty ("N?", "Npec") were not assigned to any subclass (entry "—" as subclass), but were excluded from all comparisons of dE subclasses. Objects VCC 0218, 0308, 1684, and 1779 are dE(bc)s with disk features.

VCC	S	m_r	VCC	S	m_r	VCC	S	m_r
0009	$dE(N)_{bright}$	$12^m.94$	1069	$dE(N)_{bright}$	$15^m.58$	1567	$dE(N)_{bright}$	$13^m.80$
0033	$dE(N)_{bright}$	14.26	1073	$dE(N)_{bright}$	13.19	1649	$dE(N)_{bright}$	14.75
0050	$dE(N)_{bright}$	15.12	1075	$dE(N)_{bright}$	14.01	1661	$dE(N)_{bright}$	14.91
0109	$dE(N)_{bright}$	15.29	1079	$dE(N)_{bright}$	15.67	1669	$dE(N)_{bright}$	15.44
0158	$dE(N)_{bright}$	14.87	1087	$dE(N)_{bright}$	12.59	1674	$dE(N)_{bright}$	15.10
0178	$dE(N)_{bright}$	14.61	1092	$dE(N)_{bright}$	15.64	1711	$dE(N)_{bright}$	15.35
0200	$dE(N)_{bright}$	14.02	1093	$dE(N)_{bright}$	15.53	1755	$dE(N)_{bright}$	14.86
0227	$dE(N)_{bright}$	14.12	1101	$dE(N)_{bright}$	15.11	1773	$dE(N)_{bright}$	15.30
0230	$dE(N)_{bright}$	14.72	1104	$dE(N)_{bright}$	14.51	1796	$dE(N)_{bright}$	15.64
0235	$dE(N)_{bright}$	15.56	1107	$dE(N)_{bright}$	14.56	1803	$dE(N)_{bright}$	14.82
0273	$dE(N)_{bright}$	15.41	1122	$dE(N)_{bright}$	13.96	1826	$dE(N)_{bright}$	14.79
0319	$dE(N)_{bright}$	14.31	1151	$dE(N)_{bright}$	15.54	1828	$dE(N)_{bright}$	14.27
0437	$dE(N)_{bright}$	13.13	1164	$dE(N)_{bright}$	15.24	1861	$dE(N)_{bright}$	13.22
0452	$dE(N)_{bright}$	15.02	1167	$dE(N)_{bright}$	14.15	1876	$dE(N)_{bright}$	14.23
0510	$dE(N)_{bright}$	14.12	1172	$dE(N)_{bright}$	15.32	1881	$dE(N)_{bright}$	15.25
0545	$dE(N)_{bright}$	14.48	1173	$dE(N)_{bright}$	15.28	1886	$dE(N)_{bright}$	14.52
0560	$dE(N)_{bright}$	15.61	1185	$dE(N)_{bright}$	14.44	1897	$dE(N)_{bright}$	13.49
0592	$dE(N)_{bright}$	15.43	1213	$dE(N)_{bright}$	15.49	1909	$dE(N)_{bright}$	15.47
0634	$dE(N)_{bright}$	12.71	1218	$dE(N)_{bright}$	15.09	1919	$dE(N)_{bright}$	15.64
0684	$dE(N)_{bright}$	15.10	1222	$dE(N)_{bright}$	15.20	1936	$dE(N)_{bright}$	14.90
0695	$dE(N)_{bright}$	15.24	1238	$dE(N)_{bright}$	14.49	1942	$dE(N)_{bright}$	15.31
0711	$dE(N)_{bright}$	15.46	1254	$dE(N)_{bright}$	13.92	1945	$dE(N)_{bright}$	13.98
0725	$dE(N)_{bright}$	14.90	1261	$dE(N)_{bright}$	12.62	1991	$dE(N)_{bright}$	14.52
0745	$dE(N)_{bright}$	13.54	1308	$dE(N)_{bright}$	14.59	2012	$dE(N)_{bright}$	13.75
0750	$dE(N)_{bright}$	14.15	1311	$dE(N)_{bright}$	15.09	2045	$dE(N)_{bright}$	14.95
0753	$dE(N)_{bright}$	15.11	1333	$dE(N)_{bright}$	15.65	2049	$dE(N)_{bright}$	15.47
0762	$dE(N)_{bright}$	14.81	1353	$dE(N)_{bright}$	15.58	2083	$dE(N)_{bright}$	14.74
0765	$dE(N)_{bright}$	15.41	1355	$dE(N)_{bright}$	13.50	0029	$dE(N)_{faint}$	16.58
0786	$dE(N)_{bright}$	14.06	1384	$dE(N)_{bright}$	15.38	0330	$dE(N)_{faint}$	15.82
0790	$dE(N)_{bright}$	14.96	1386	$dE(N)_{bright}$	13.80	0372	$dE(N)_{faint}$	17.48
0808	$dE(N)_{bright}$	15.47	1389	$dE(N)_{bright}$	15.11	0394	$dE(N)_{faint}$	16.70
0815	$dE(N)_{bright}$	14.96	1400	$dE(N)_{bright}$	14.86	0503	$dE(N)_{faint}$	16.43
0816	$dE(N)_{bright}$	13.64	1407	$dE(N)_{bright}$	14.14	0505	$dE(N)_{faint}$	16.66
0823	$dE(N)_{bright}$	14.85	1420	$dE(N)_{bright}$	15.48	0539	$dE(N)_{faint}$	15.85
0824	$dE(N)_{bright}$	15.38	1431	$dE(N)_{bright}$	13.37	0554	$dE(N)_{faint}$	16.12
0846	$dE(N)_{bright}$	15.17	1441	$dE(N)_{bright}$	15.38	0632	$dE(N)_{faint}$	16.53
0871	$dE(N)_{bright}$	14.57	1446	$dE(N)_{bright}$	15.03	0706	$dE(N)_{faint}$	16.69
0916	$dE(N)_{bright}$	14.88	1451	$dE(N)_{bright}$	15.26	0746	$dE(N)_{faint}$	17.30
0928	$dE(N)_{bright}$	15.21	1453	$dE(N)_{bright}$	13.25	0747	$dE(N)_{faint}$	16.17
0929	$dE(N)_{bright}$	12.51	1491	$dE(N)_{bright}$	14.11	0755	$dE(N)_{faint}$	15.77
0931	$dE(N)_{bright}$	15.49	1497	$dE(N)_{bright}$	15.03	0756	$dE(N)_{faint}$	16.31
0936	$dE(N)_{bright}$	14.70	1503	$dE(N)_{bright}$	14.38	0779	$dE(N)_{faint}$	16.89
0940	$dE(N)_{bright}$	13.78	1539	$dE(N)_{bright}$	14.88	0795	$dE(N)_{faint}$	16.52
0949	$dE(N)_{bright}$	14.31	1549	$dE(N)_{bright}$	13.85	0810	$dE(N)_{faint}$	15.79
0965	$dE(N)_{bright}$	14.54	1561	$dE(N)_{bright}$	14.97	0812	$dE(N)_{faint}$	15.89
0992	$dE(N)_{bright}$	15.35	1563	$dE(N)_{bright}$	15.45	0855	$dE(N)_{faint}$	16.44
1005	$dE(N)_{bright}$	15.23	1565	$dE(N)_{bright}$	15.62	0877	$dE(N)_{faint}$	16.86

T 4.1. ***Continued.***

VCC	S	m_r	VCC	S	m_r	VCC	S	m_r
0896	dE(N)$_{faint}$	$16^m.66$	1616	dE(N)$_{faint}$	$15^m.79$	2008	dE(nN)$_{bright}$	$14^m.04$
0920	dE(N)$_{faint}$	16.20	1642	dE(N)$_{faint}$	16.58	2028	dE(nN)$_{bright}$	15.61
0933	dE(N)$_{faint}$	15.76	1677	dE(N)$_{faint}$	16.07	2056	dE(nN)$_{bright}$	15.33
0972	dE(N)$_{faint}$	15.78	1683	dE(N)$_{faint}$	15.71	2078	dE(nN)$_{bright}$	15.63
0974	dE(N)$_{faint}$	15.69	1767	dE(N)$_{faint}$	15.68	0011	dE(nN)$_{faint}$	16.15
0977	dE(N)$_{faint}$	17.11	1785	dE(N)$_{faint}$	16.96	0091	dE(nN)$_{faint}$	16.85
0997	dE(N)$_{faint}$	17.04	1794	dE(N)$_{faint}$	16.82	0106	dE(nN)$_{faint}$	17.11
1044	dE(N)$_{faint}$	16.16	1812	dE(N)$_{faint}$	16.64	0127	dE(nN)$_{faint}$	16.49
1059	dE(N)$_{faint}$	17.10	1831	dE(N)$_{faint}$	17.38	0244	dE(nN)$_{faint}$	16.62
1064	dE(N)$_{faint}$	16.44	1879	dE(N)$_{faint}$	16.08	0294	dE(nN)$_{faint}$	17.49
1065	dE(N)$_{faint}$	15.70	1891	dE(N)$_{faint}$	16.16	0299	dE(nN)$_{faint}$	16.22
1076	dE(N)$_{faint}$	16.22	1928	dE(N)$_{faint}$	16.56	0317	dE(nN)$_{faint}$	17.18
1099	dE(N)$_{faint}$	16.74	1951	dE(N)$_{faint}$	15.85	0335	dE(nN)$_{faint}$	16.81
1105	dE(N)$_{faint}$	15.79	1958	dE(N)$_{faint}$	15.99	0361	dE(nN)$_{faint}$	16.58
1115	dE(N)$_{faint}$	16.26	1980	dE(N)$_{faint}$	15.94	0403	dE(nN)$_{faint}$	17.12
1119	dE(N)$_{faint}$	16.29	2014	dE(N)$_{faint}$	16.04	0418	dE(nN)$_{faint}$	16.45
1120	dE(N)$_{faint}$	16.09	2088	dE(N)$_{faint}$	16.24	0421	dE(nN)$_{faint}$	16.65
1123	dE(N)$_{faint}$	15.74	0108	dE(nN)$_{bright}$	15.08	0422	dE(nN)$_{faint}$	16.81
1137	dE(N)$_{faint}$	16.89	0115	dE(nN)$_{bright}$	15.63	0444	dE(nN)$_{faint}$	16.44
1191	dE(N)$_{faint}$	16.64	0118	dE(nN)$_{bright}$	15.41	0454	dE(nN)$_{faint}$	16.97
1207	dE(N)$_{faint}$	16.06	0209	dE(nN)$_{bright}$	14.18	0458	dE(nN)$_{faint}$	15.84
1210	dE(N)$_{faint}$	16.47	0236	dE(nN)$_{bright}$	15.23	0466	dE(nN)$_{faint}$	15.92
1212	dE(N)$_{faint}$	16.05	0261	dE(nN)$_{bright}$	15.31	0499	dE(nN)$_{faint}$	16.89
1225	dE(N)$_{faint}$	16.31	0461	dE(nN)$_{bright}$	15.38	0501	dE(nN)$_{faint}$	16.02
1240	dE(N)$_{faint}$	16.63	0543	dE(nN)$_{bright}$	13.35	0504	dE(nN)$_{faint}$	15.89
1246	dE(N)$_{faint}$	16.84	0551	dE(nN)$_{bright}$	15.17	0561	dE(nN)$_{faint}$	16.73
1264	dE(N)$_{faint}$	15.68	0563	dE(nN)$_{bright}$	14.80	0594	dE(nN)$_{faint}$	16.34
1268	dE(N)$_{faint}$	16.29	0611	dE(nN)$_{bright}$	15.50	0600	dE(nN)$_{faint}$	18.47
1296	dE(N)$_{faint}$	16.18	0794	dE(nN)$_{bright}$	13.88	0622	dE(nN)$_{faint}$	17.65
1302	dE(N)$_{faint}$	16.94	0817	dE(nN)$_{bright}$	13.09	0652	dE(nN)$_{faint}$	16.76
1307	dE(N)$_{faint}$	17.19	0917	dE(nN)$_{bright}$	14.54	0668	dE(nN)$_{faint}$	16.06
1317	dE(N)$_{faint}$	17.25	0982	dE(nN)$_{bright}$	15.26	0687	dE(nN)$_{faint}$	17.31
1366	dE(N)$_{faint}$	16.15	1180	dE(nN)$_{bright}$	15.41	0748	dE(nN)$_{faint}$	16.26
1369	dE(N)$_{faint}$	16.02	1323	dE(nN)$_{bright}$	15.49	0760	dE(nN)$_{faint}$	16.32
1373	dE(N)$_{faint}$	16.67	1334	dE(nN)$_{bright}$	14.69	0761	dE(nN)$_{faint}$	16.33
1396	dE(N)$_{faint}$	16.29	1351	dE(nN)$_{bright}$	14.91	0769	dE(nN)$_{faint}$	16.20
1399	dE(N)$_{faint}$	15.85	1417	dE(nN)$_{bright}$	15.06	0775	dE(nN)$_{faint}$	17.17
1402	dE(N)$_{faint}$	17.27	1528	dE(nN)$_{bright}$	13.67	0777	dE(nN)$_{faint}$	16.61
1418	dE(N)$_{faint}$	16.37	1553	dE(nN)$_{bright}$	15.53	0791	dE(nN)$_{faint}$	16.22
1481	dE(N)$_{faint}$	17.10	1577	dE(nN)$_{bright}$	14.97	0803	dE(nN)$_{faint}$	17.87
1495	dE(N)$_{faint}$	16.69	1647	dE(nN)$_{bright}$	15.14	0839	dE(nN)$_{faint}$	16.80
1496	dE(N)$_{faint}$	17.20	1698	dE(nN)$_{bright}$	15.14	0840	dE(nN)$_{faint}$	17.09
1498	dE(N)$_{faint}$	15.91	1704	dE(nN)$_{bright}$	15.57	0861	dE(nN)$_{faint}$	16.73
1509	dE(N)$_{faint}$	15.77	1743	dE(nN)$_{bright}$	14.65	0863	dE(nN)$_{faint}$	16.73
1519	dE(N)$_{faint}$	16.57	1762	dE(nN)$_{bright}$	15.67	0878	dE(nN)$_{faint}$	16.04
1523	dE(N)$_{faint}$	16.61	1870	dE(nN)$_{bright}$	15.11	0926	dE(nN)$_{faint}$	16.06
1531	dE(N)$_{faint}$	16.62	1890	dE(nN)$_{bright}$	14.06	0962	dE(nN)$_{faint}$	16.07
1533	dE(N)$_{faint}$	16.80	1895	dE(nN)$_{bright}$	14.15	0976	dE(nN)$_{faint}$	16.93
1603	dE(N)$_{faint}$	16.47	1948	dE(nN)$_{bright}$	14.78	1034	dE(nN)$_{faint}$	17.42
1604	dE(N)$_{faint}$	15.99	1982	dE(nN)$_{bright}$	14.68	1039	dE(nN)$_{faint}$	16.29
1606	dE(N)$_{faint}$	16.61	1995	dE(nN)$_{bright}$	14.96	1089	dE(nN)$_{faint}$	16.98
1609	dE(N)$_{faint}$	16.19	2004	dE(nN)$_{bright}$	15.17	1124	dE(nN)$_{faint}$	16.75

T 4.1. ***Continued.***

VCC	S	m_r	VCC	S	m_r	VCC	S	m_r
1129	dE(nN)$_{faint}$	$16^m.87$	1983	dE(nN)$_{faint}$	$16^m.06$	0308	dE(bc)	$13^m.14$
1132	dE(nN)$_{faint}$	15.85	2011	dE(nN)$_{faint}$	16.40	0674	dE(bc)	16.18
1149	dE(nN)$_{faint}$	16.78	2032	dE(nN)$_{faint}$	16.08	0781	dE(bc)	13.90
1153	dE(nN)$_{faint}$	16.51	2043	dE(nN)$_{faint}$	17.07	0870	dE(bc)	14.10
1209	dE(nN)$_{faint}$	16.55	2051	dE(nN)$_{faint}$	16.54	0901	dE(bc)	16.49
1223	dE(nN)$_{faint}$	15.74	2054	dE(nN)$_{faint}$	15.76	0951	dE(bc)	13.35
1224	dE(nN)$_{faint}$	16.52	2061	dE(nN)$_{faint}$	16.68	1488	dE(bc)	14.12
1235	dE(nN)$_{faint}$	16.75	2063	dE(nN)$_{faint}$	16.54	1501	dE(bc)	14.90
1288	dE(nN)$_{faint}$	16.40	2074	dE(nN)$_{faint}$	16.58	1512	dE(bc)	14.82
1298	dE(nN)$_{faint}$	16.97	2081	dE(nN)$_{faint}$	16.17	1684	dE(bc)	14.45
1314	dE(nN)$_{faint}$	16.12	0535	—	15.69	1779	dE(bc)	14.01
1337	dE(nN)$_{faint}$	16.66	1348	—	14.15	1912	dE(bc)	13.26
1352	dE(nN)$_{faint}$	16.33	1489	—	15.07			
1370	dE(nN)$_{faint}$	16.57	1857	—	13.92			
1432	dE(nN)$_{faint}$	16.43	0216	dE(di)	14.31			
1438	dE(nN)$_{faint}$	16.69	0389	dE(di)	13.09			
1449	dE(nN)$_{faint}$	16.86	0407	dE(di)	13.74			
1464	dE(nN)$_{faint}$	16.73	0490	dE(di)	13.00			
1472	dE(nN)$_{faint}$	17.52	0523	dE(di)	12.52			
1482	dE(nN)$_{faint}$	17.07	0608	dE(di)	13.56			
1518	dE(nN)$_{faint}$	17.82	0751	dE(di)	13.74			
1543	dE(nN)$_{faint}$	16.99	0788	dE(di)	15.33			
1573	dE(nN)$_{faint}$	15.68	0854	dE(di)	16.71			
1599	dE(nN)$_{faint}$	16.68	0856	dE(di)	13.38			
1601	dE(nN)$_{faint}$	16.18	0990	dE(di)	13.70			
1622	dE(nN)$_{faint}$	16.82	1010	dE(di)	12.72			
1629	dE(nN)$_{faint}$	16.75	1036	dE(di)	12.94			
1650	dE(nN)$_{faint}$	16.32	1183	dE(di)	13.27			
1651	dE(nN)$_{faint}$	16.33	1204	dE(di)	15.35			
1652	dE(nN)$_{faint}$	16.07	1304	dE(di)	14.23			
1657	dE(nN)$_{faint}$	16.40	1392	dE(di)	13.84			
1658	dE(nN)$_{faint}$	15.82	1422	dE(di)	12.78			
1663	dE(nN)$_{faint}$	16.56	1444	dE(di)	15.04			
1682	dE(nN)$_{faint}$	16.24	1505	dE(di)	17.03			
1688	dE(nN)$_{faint}$	15.93	1514	dE(di)	14.40			
1689	dE(nN)$_{faint}$	16.44	1691	dE(di)	16.92			
1702	dE(nN)$_{faint}$	16.51	1695	dE(di)	13.46			
1717	dE(nN)$_{faint}$	15.80	1836	dE(di)	13.66			
1719	dE(nN)$_{faint}$	17.55	1896	dE(di)	14.07			
1729	dE(nN)$_{faint}$	17.76	1910	dE(di)	13.23			
1733	dE(nN)$_{faint}$	16.59	1921	dE(di)	14.37			
1740	dE(nN)$_{faint}$	16.64	1949	dE(di)	13.08			
1745	dE(nN)$_{faint}$	16.28	2019	dE(di)	13.56			
1764	dE(nN)$_{faint}$	15.96	2042	dE(di)	13.58			
1792	dE(nN)$_{faint}$	16.99	2048	dE(di)	12.99			
1815	dE(nN)$_{faint}$	16.64	2050	dE(di)	14.36			
1843	dE(nN)$_{faint}$	16.64	2080	dE(di)	14.96			
1867	dE(nN)$_{faint}$	16.62	0021	dE(bc)	14.08			
1915	dE(nN)$_{faint}$	16.09	0170	dE(bc)	13.50			
1950	dE(nN)$_{faint}$	15.67	0173	dE(bc)	14.21			
1964	dE(nN)$_{faint}$	17.23	0218	dE(bc)	14.00			
1971	dE(nN)$_{faint}$	15.69	0281	dE(bc)	14.77			

did, we use the surface brightness *offset* from the mean relation of surface brightness and magnitude. We plot these values, measured in the r band within $a = 2\,a_{\rm hl,r}$, against axial ratio (measured at the same semimajor axis, see Section 4.3) for each dE subsample, shown in the rightmost column of Figure 4.3. For all subsamples, a positive correlation of surface brightness offset with axial ratio can be seen, favoring the oblate model in agreement with earlier studies (e.g., Marchant & Olson 1979; Richstone 1979; Binggeli & Popescu 1995). For the "rounder" subsamples (top three rows), some additional contribution by prolate objects might be "hidden" within the rather large scatter of surface brightness offsets at larger axial ratios. We denote these results in Figure 4.3 by the arrows pointing from the surface brightness test diagram towards the favored intrinsic galaxy shapes. The arrow size represents the implied contribution from intrinsically prolate and oblate objects. Among the "flatter" subsamples (lower three rows), for which the oblate case is favored, the dE(di)s have the lowest axial ratios, with a median value of 0.33 (bright dE(nN)s: 0.42, dE(bc)s: 0.44). The galaxies in these subsamples are thus most likely shaped like thick disks.

The above considerations needed to be restricted to purely oblate and purely prolate shapes. However, for all subsamples, a small part of the deduced (and favored) intrinsic oblate distribution becomes negative at large axial ratios, trying to account for the low number of apparently round objects. This implies that most of the galaxies might actually have triaxial shapes, in accordance with the conclusions of Binggeli & Popescu (1995).

5.3. Subclass distribution within the cluster

While it has been known since long that nucleated and non-nucleated dEs have different clustering properties (e.g., van den Bergh 1986; Ferguson & Sandage 1989), this statement has been challenged by Côté et al. (2006), who conjectured that it might just be the result of a selection bias in the VCC. It therefore appears worth to perform a quantitative comparison of the distributions of our dE subsamples within the cluster, and to then proceed with testing the issues raised by Côté et al. (2006) in detail.

The projected spatial distributions of our subsamples are shown in the middle column of Fig 4.5. While both bright and faint dE(N)s exhibit a rather strong central clustering, the faint dE(nN)s appear to be only moderately clustered, and the dE(di)s and dE(bc)s show basically no central clustering. The bright dE(nN)s even seem to be preferentially located in the outskirts of the cluster.

To put the above on a more quantitative basis, we present in Figure 4.6 the cumulative distribution of each of our subsamples with respect to local projected density. Following Dressler (1980) and Binggeli et al. (1987), we define the latter for each galaxy as the number of objects per square degree within a circle that includes the ten nearest neighbours, independent of galaxy type. Only certain cluster members are considered. For comparison, we also show the same distributions for different Hubble types (Figure 4.6, inset), i.e., for the rather strongly centrally clustered giant early-type galaxies, as well as for the weakly clustered and probably infalling spiral and irregular galaxies (e.g., Binggeli et al. 1987).

As a confirmation of the impression from the spatial distribution, the bright dE(nN)s are preferentially found in regions of moderate to lower density, similar to (and at even slightly lower densities than) the distribution of irregular galaxies, in accordance with the findings of Ferguson & Sandage (1989). This implies that they, as a population, are far from being virialized. The densities then increase slightly going from the bright dE(nN)s to the dE(bc)s, dE(di)s, and the faint dE(nN)s, in this order. Still, all of these are distributed similarly to the irregular and spiral galaxies in the cluster, again implying that they are unrelaxed or at least largely unrelaxed galaxy populations, and confirming the impression from their projected spatial distribution. In contrast, both bright and faint dE(N)s are located at larger densities, and display a distribution comparable to the E and S0 galaxies, in agreement with the results of Ferguson & Sandage (1989). This would suggest that they are a largely relaxed or at least partially relaxed population. Note, however, that the Es *alone* (without the S0s) are located at still higher densities. Conselice et al. (2001) pointed out that only the Es appear to be a relaxed

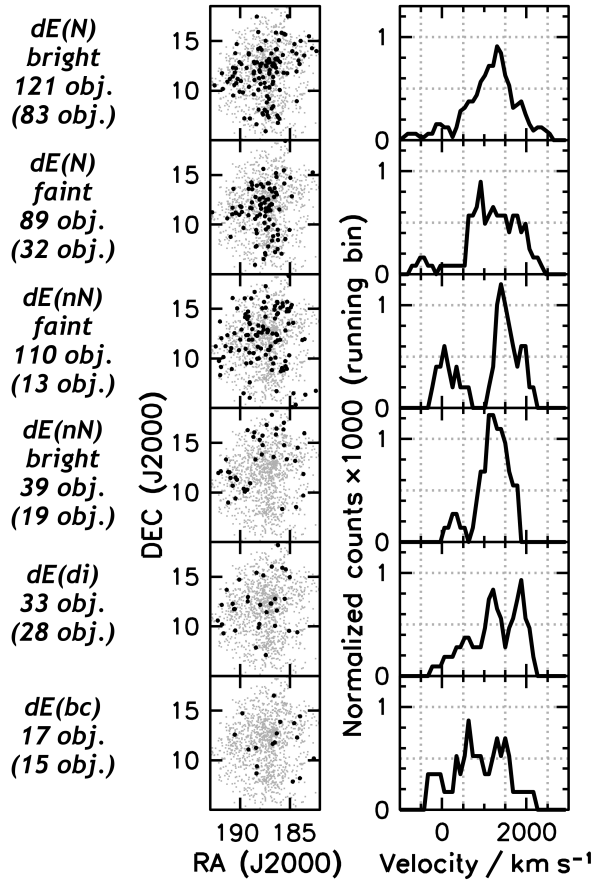

F 4.5. **Spatial and velocity distribution.** In the left column, the number of objects in each of our dE subsamples are given. Numbers in parentheses apply to those dEs for which heliocentric velocities are available. The middle column shows the projected distribution of the dE subsamples (black dots) within the cluster. All Virgo cluster member galaxies are shown as small grey dots. The right column shows the velocity distributions of the dE subsamples. The data are shown as running histogram with a bin width of 384 km/s, corresponding to the semi-interquartile range of the total 193 velocities. Each curve is sampled in steps of 96 km/s (one quarter of the bin width) and normalized to an area of 1.

galaxy population, while all others, including the S0s, are not — thus, the dE(N)s presumably are not fully relaxed either.

We performed statistical pairwise comparisons of the distributions of our dE subsamples with respect to density, similar as for the axial ratios in Section 5.2. The K-S test probabilities for the null hypothesis that two observed distributions stem from the same underlying distribution are given as percentages in Figure 4.7. Even though the faint dE(nN)s are, among the "lower-density" subsamples, closest to the bright and faint dE(N)s, their probability for having the same underlying distribution is 0.08 and 0.07%, respectively. These probabilities are higher for the dE(di)s and dE(bc)s: although they are located at even lower densities, their rather small sample sizes let the probability increase as compared to that of the faint dE(nN)s. Finally, the bright dE(nN)s are located at such low densities that their K-S test comparison with the dE(N)s yields a probability of 0.00%, and that even the comparison with the faint dE(nN)s only yields a probability of 3.7% for them having the same true distribution. Given the morphological differences between the subsamples, as deduced in Section 5.2, Figure 4.6 basically shows a morphology-density relation *within* the dE class.

This view appears to be corroborated by the distributions of heliocentric velocities (right column of Figure 4.5) of the dE subsamples: that of the bright dE(N)s has a single peak and is fairly symmetric, while especially the faint dE(nN)s, dE(di)s, and dE(bc)s display rather asymmetric distributions

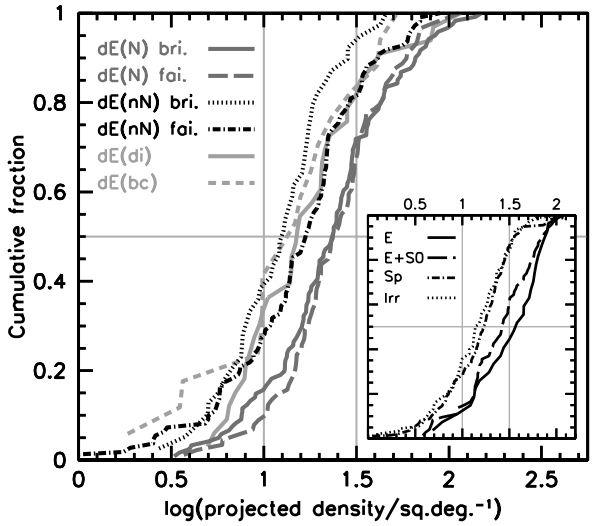

F 4.6. **Morphology vs. density.** Cumulative distribution of local projected densities of our dE subsamples, and of Hubble types (inset). Following Dressler (1980) and Binggeli et al. (1987), we define a circular area around each galaxy that includes its ten nearest neighbours (independent of galaxy type), yielding a projected density (number of galaxies per square degree).

	dE(N) bright	dE(N) faint	dE(nN) faint	dE(nN) bright	dE(di)	dE(bc)
dE(N) bright		73.94	0.08	0.00	5.49	11.30
dE(N) faint	73.94		0.07	0.00	1.51	4.35
dE(nN) faint	0.08	0.07		3.66	88.86	85.42
dE(nN) bright	0.00	0.00	3.66		20.19	79.16
dE(di)	5.49	1.51	88.86	20.19		83.95
dE(bc)	11.30	4.35	85.42	79.16	83.95	

F 4.7. K-S test results for the comparison of the distributions of our dE subsamples with respect to local projected density. For each pair of distributions we give the probability in percent for the null hypothesis that the two distributions stem from the same underlying distribution function.

with multiple peaks. The latter could be interpreted as being a signature of infalling populations (Tully & Shaya 1984; Conselice et al. 2001). However, the differences between these velocity distributions are not or only marginally significant — the "most different" pair of distributions according to the K-S test are the bright dE(nN)s and the dE(bc)s, which have a probability of 6.6% for the null hypothesis. The main issue here are the small sample sizes: only a fraction of the galaxies of each subsample has measured velocities (numbers are given in parentheses in the left column of Figure 4.5), which are available from the NED for 193 of our 413 dEs, and, e.g., for only 19 of our 39 bright dE(nN)s. Similarly, measurements of the skew or kurtosis of the distributions do not yield values that differ significantly from zero. We can thus only state that the rather asymmetric, multi-peaked distributions of the faint dE(nN)s, the dE(di)s, and the dE(bc)s would be consistent with our above conclusion that

they are mostly unrelaxed populations, but that more velocity data is needed to perform a reliable quantitative comparison of velocity distributions.

5.4. Remarks on possible selection biases

The different spatial distribution of dE(N)s and dE(nN)s was long considered a fundamental and well-founded observation, but has recently been questioned by Côté et al. (2006). These authors argued that galaxies with high central surface brightness (HSB, with $\mu_{\mathrm{g,central}} \lesssim 20$ mag arcsec^{-2} or $B \lesssim 14\overset{\mathrm{m}}{.}55$) would have been preferentially classified as non-nucleated in the VCC, which may have led to a selection bias in the VCC that artificially relates spatial distribution to nucleus presence. We test this conjecture by considering the following points:

(1) If the dE(nN)s were objects in which nuclei have preferentially gone undetected due to a too high central surface brightness, the dE(nN)s' surface brightnesses should, on average, be significantly higher than those of the dE(N)s. However, the mean surface brightness in *r* within the half-light aperture has very similar median values for the bright dE(nN)s (μ_r = 22.65 mag arcsec^{-2}) and the bright dE(N)s (μ_r = 22.63 mag arcsec^{-2}), which makes such a bias unlikely. Furthermore, the distributions of surface brightnesses of the two subsamples are similar — a K-S test yields a probability of 84% for the null hypothesis that they stem from the same underlying distribution. Certainly, measurements of the very central surface brightness, which are possible only with high-resolution observations, would provide a more direct argument here. However, since both nucleated and non-nucleated dEs within a given magnitude range have similar surface brightness profiles (Binggeli & Cameron 1991), their effective surface brightness and central surface brightness are closely correlated.

(2) Only one single galaxy among our 39 bright dE(nN)s (2.5%) is bright enough to fall among Côté et al.'s definition of a HSB dE. In contrast, 14 of our 121 bright dE(N)s (12%) would qualify as HSB dE. Therefore, it appears highly unlikely that a significant number of dE(nN)s possess nuclei *with similar relative brightnesses as those of the dE(N)s* that were not detected by Binggeli et al. (1985).

(3) None of the dEs in Côté et al.'s own sample that were previously classified as non-nucleated, but have now been found to host a weak nucleus, actually are HSB dEs.

(4) Since we are interested in the distributions of our subsamples with respect to density in the cluster, we translate Côté et al.'s conjecture about the *spatial* distribution of the dEs into one about the distribution with respect to *density*: if the different density distributions of bright dE(N)s and dE(nN)s (see above) would primarily be caused by a surface brightness selection effect, a significantly larger fraction of the high surface brightness objects should be located at lower densities as compared to the lower surface brightness objects. To test for this possible bias, we plot the mean *r* band surface brightness within the half-light aperture against local projected density for the combined sample of bright dE(N)s and dE(nN)s (Figure 4.8). No correlation is seen, ruling out that such a bias is present in our data.

We point out that it might of course still be the case that most of the dE(nN)s host *weak* nuclei that are below the VCC detection limit, as discussed in Section 2.2. However, what is at stake here is the question whether a significant number of dE(nN)s should already have been classified as dE(N)s *by the VCC*, and whether this could account for the population differences that we find. The above arguments clearly rule out such a bias. We can thus conclude that the bright dE(N)s and dE(nN)s are indeed distinct dE subpopulations that differ in their clustering properties (Figures 4.6 and 4.7), as well as in their shapes (Figures 4.3 and 4.4).

6. C

Since our morphological subdivision of the dEs into several subpopulations is now established, the next step would obviously be to compare their stellar population properties. Given that the SDSS imaged every galaxy in five bands, it should be able to provide some insight into their stellar content,

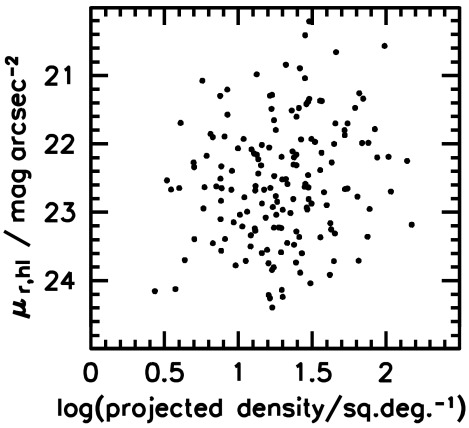

F 4.8. **Surface brightness vs. density.** The mean surface brightness in r within the half-light aperture is compared to local projected density for the combined sample of bright dE(N)s and dE(nN)s, in order to test for a possible classification bias as conjectured by Côté et al. (2006) (see text). No correlation is seen, ruling out such a bias.

even though it is basically impossible to disentangle ages and metallicities with optical broadband photometry alone. However, the issue is complicated by the fact that the u and z band images, which would be very important for an analysis of the stellar content, have a very low S/N (see Section 3). It is therefore important to perform a thorough study of the dE colours and colour gradients that properly takes into account measurement errors and the different S/N levels for objects of different magnitudes and surface brightnesses. Such an investigation is beyond the scope of the present study and will be addressed in Chapters 5 and 6.

Nevertheless, in order to tackle the question about whether the dE subsamples differ in their colour properties, we present in Figure 4.9 the inner $u-g$ ("age-sensitive") versus $i-z$ ("metallicity-sensitive") colours for the bright ($m_r \leq 15\overset{\text{m}}{.}67$) dEs, measured within an aperture of $a = 0.5\,a_{\rm hl,r}$. This approach guarantees relatively small errors (typical values are shown in the lower left corner of the figure) that need not be taken into account individually. For each dE subsample, we indicate its median colour values with the black symbols drawn with thick lines.

However, a direct comparison of these values would be biased by the existence of a colour-magnitude relation: if different subsamples had, on average, significantly different magnitudes, they would be offset in our colour-colour diagram even if they followed exactly the same colour-magnitude relation. We therefore compute an approximate correction for this effect: first, we perform a linear least squares fit to the colour-magnitude relations (r versus $u-g$ and r versus $i-z$) of our full dE sample, clipping one time at $3\,\sigma$ and excluding the dE(bc)s because of their blue inner colours. We then derive the median r magnitude of each subsample, and use the linear fit to compute its expected colour offset from the sample of dE(nN)s, which we choose as reference. The so obtained corrected median colours are shown in Figure 4.9 as black symbols drawn with thin lines, and are connected with lines to their uncorrected values.

The dE(bc)s exhibit, as expected, the bluest colours of all subsamples, basically by definition, since we focus here on the inner galaxy colours. While the corrected colours of the dE(di)s are similar to those of the dE(nN)s, the dE(N)s are, on average, redder in $i-z$ and significantly redder in $u-z$. Given the very small colour correction and large sample size of the dE(N)s, this can be considered a robust result. In the inset shown in Figure 4.9, we compare the median values of the dE(nN)s and dE(N)s to two model tracks from stellar population synthesis calculations (Bruzual & Charlot 2003). Both tracks represent stellar populations formed through a single burst of star formation that exponentially decays with time ($\tau = 0.5$ Gyr), using Padova 2000 isochrones and a Chabrier IMF. The tracks are curves of constant metallicity (grey solid line: $Z = 0.008$, grey dotted line $Z = 0.004$); ages increase from bottom to top and are marked at 3, 6, 10, and 14 Gyr (the latter mark is outside of the plot area for the $Z = 0.008$ track). Our measured values lie along of the $Z = 0.008$ track, illustrating

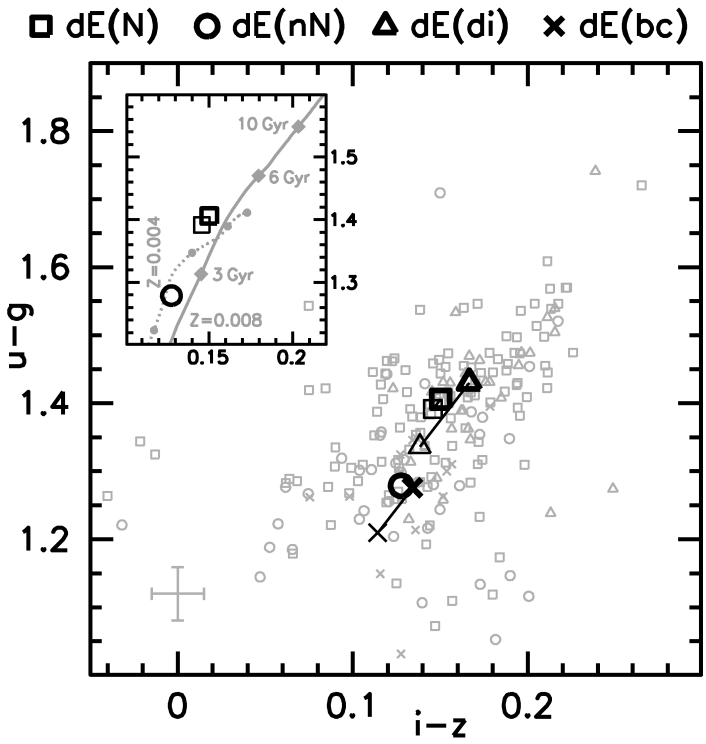

F 4.9. **Distribution in colour space.** Shown are the inner $u - g$ versus $i - z$ colours, measured within $a = 0.5\,a_{\rm hl,r}$, for all dEs brighter than the median r brightness of our full sample, $m_{\rm r} = 15\overset{\rm m}{.}67$, divided into the respective subsamples. Individual measurements are shown with small grey symbols (see the legend above the diagram). The median value of each subsample is shown as black symbol using thick lines. Black symbols drawn with thin lines represent the median values corrected for the effect of the colour-magnitude-relation (see text); lines connect them to the corresponding uncorrected values. The correction is chosen to be zero for the dE(nN)s. The inset shows again the median values (corrected and uncorrected) of the dE(N)s and dE(nN)s, along with two model tracks from stellar population synthesis calculations (Bruzual & Charlot 2003). Both tracks represent stellar populations formed through a single burst of star formation that exponentially decays with time ($\tau = 0.5$ Gyr), using Padova 2000 isochrones and a Chabrier IMF. The grey solid line is for a metallicity $Z = 0.008$; age steps are marked by the grey diamonds at 3 Gyr, 6 Gyr, and 10 Gyr. The grey dotted line is for $Z = 0.004$, with age steps marked by the grey circles at 3 Gyr, 6 Gyr, 10 Gyr, and 14 Gyr; the latter is also the end of the track.

that, within the framework of our simplified stellar population models, the colour difference between dE(nN)s and dE(N)s could be interpreted as a difference in age. According to this simple approach, the dE(N)s would be, on average, a few Gyr older than the dE(nN)s. However, the measurements also fall roughly along a virtual line connecting the 6 Gyr points of each model, showing that they might also be interpreted as a difference in metallicity. While this colour offset between the dE(N)s and dE(nN)s would be qualitatively consistent with the study by Rakos & Schombert (2004), who found the dE(N)s in the Coma and Fornax clusters to have older stellar populations than the dE(nN)s, reliable conclusions need to await a more comprehensive colour study of our dEs.

7. D

7.1. Interrelations between subclasses

The bright dE(nN)s and dE(di)s are both unrelaxed populations of relatively bright dEs shaped like thick disks. This also applies to the dE(bc)s, which could thus be candidates for being the direct progenitors of the former: the presently blue centers of the dE(bc)s will evolve to typical dE colours within 1 Gyr or less after the cessation of star formation (Chapter 3). Therefore, the bright dE(nN)s and dE(di)s could constitute those disk-shaped dEs where central star formation has already ceased. To test this hypothesis, we make the following considerations. There are 39 bright dE(nN)s, as well as 30 dE(di)s with $m_r \leq 15\overset{m}{.}67$, 7 of which are non-nucleated. This adds up to 69 "non-star-forming, disk-shaped dEs", 23 (33%) of which are nucleated. Among the dE(bc)s there are 15 galaxies with $m_r \leq 15\overset{m}{.}67$, 6 (40%) of which are nucleated. Thus, the fraction of nucleated galaxies would be compatible with our hypothesis within the errors, with the caveat that nuclei might still form in the centers of some dE(bc)s (see Oh & Lin 2000 and Chapter 3), which would raise the nucleated fraction of the dE(bc)s.

Now, 43% of the non-star-forming, disk-shaped dEs are dE(di)s, i.e., show disk *features* (not only an overall disk *shape*). If the dE(bc)s would contain the same fraction of galaxies that display disk features, we would expect 6.5 such objects among the 15 dE(bc)s, with a standard deviation of 1.9. The observed number of 4 lies within $1.3\,\sigma$ of the expected value and could thus still be reconciled with the above picture. However, since not only the dE(di)s, but also the bright dE(nN)s are disk-shaped, why do the latter not display disk *features* like the dE(di)s? This could either indicate a correlation between the presence of a significantly bright nucleus and the presence of disk substructure, or it could imply that there is more than one formation path towards disk-shaped dEs.

7.2. Formation mechanisms

If dEs originated from galaxies that fell into the cluster, how long ago could this infall have taken place? Conselice et al. (2001) derived a two-body relaxation time for the Virgo dEs of much more than a Hubble time. Even violent relaxation, which could apply for the case of infalling or merging groups, would take at least a few crossing times t_{cr}, with $t_{cr} \approx 1.7$ Gyr for the Virgo cluster (Boselli & Gavazzi 2006). Therefore, the majority of dE(N)s or their progenitors should have experienced infall in the earliest phases of the Virgo cluster (which is a rather young structure, see Binggeli et al. 1987 and Arnaboldi et al. 2004), or they could have formed in dark matter halos along with the cluster itself. All other dE subclasses are largely unrelaxed populations, implying that they have formed later than the dE(N)s, probably from (continuous) infall of progenitor galaxies. Our colour analysis in Section 6 would support this view, since it finds that the inner colours of the dE(N)s can be interpreted with an older stellar population than the dE(nN)s. This would be expected if one assumes that the progenitor galaxies had been forming stars until their infall into the cluster, resulting in a younger stellar population on average in the case of a later infall (neglecting possible metallicity differences). However, as stressed in Section 6, robust conclusions need to await a more detailed multicolour study of our dEs.

The galaxy harassment scenario (Moore et al. 1996) describes the structural transformation of a late-type spiral into a spheroidal system through strong tidal interactions with massive cluster galaxies. A thick stellar disk may survive and form a bar and spiral features that can be retained for some time, depending on the tidal heating of the galaxy (Mastropietro et al. 2005). Harassment could thus form disk-shaped dEs, and dE(di)s in particular. Moreover, it predicts gas to be funneled to the center and form a density excess there (Moore et al. 1998), which would be well suited to explain the central star formation in the dE(bc)s. Therefore, it appears possible that harassment could form disk-shaped dEs that first appear as dE(bc)s and then passively evolve into dE(di)s and bright dE(nN)s as their star formation ceases (see Section 7.1). It might also provide a way to form the fainter non-nucleated dEs, assuming that the tidal forces have a stronger effect on the shape of less massive galaxies, resulting in rounder objects on average. However, in order to explain all these subclasses by a single process,

one would need to invoke a correlation between the presence of a nucleus and of disk features, as discussed in Section 7.1.

Ram-pressure stripping (Gunn & Gott 1972) of dwarf irregulars (dIrrs) could be responsible for the fact that the disk-shaped bright dE(nN)s do not show disk *features* like the dE(di)s: dIrrs typically have no nucleus, and ram-pressure stripping exerts much less perturbing forces than a violent process like harassment, thus probably not triggering the formation of bars or spiral arms. Commonly discussed problems with this scenario are the metallicity offset between dEs and dIrrs (Thuan 1985; Richer et al. 1998; Grebel et al. 2003) and the too strong fading of dIrrs after cessation of star formation (Bothun et al. 1986). Also, the flattening distribution of Virgo cluster dIrrs – with intrinsic (primary) axial ratios ≥ 0.5 for most galaxies (Binggeli & Popescu 1995) – is not quite like that of our bright dE(nN)s. On the other hand, significant mass loss due to stripped gas might affect the stellar configuration of the galaxies and could thus possibly account for the difference. Moreover, the flattening distribution of the dIrrs is similar to that of the *faint* dE(nN)s (cf. Figure 9 of Binggeli & Popescu 1995), suggesting that these – and possibly not the *bright* dE(nN)s – might be stripped dIrrs.

Tidally induced star formation of dIrrs might be able to overcome the problems of the ram-pressure stripping scenario: the initially lower metallicity and surface brightness of a dIrr are increased by several bursts of star formation (Davies & Phillipps 1988), during which the galaxy appears as blue compact dwarf (BCD). After the last BCD phase it fades to become a dE, thereby providing an explanation how BCDs could be dE progenitors, which has frequently been discussed (e.g., Bothun et al. 1986; Papaderos et al. 1996; Grebel 1997; Chapter 3). The last star formation burst might occur in the central region, consistent with the appearance of the dE(bc)s.

In addition to the number of possible formation scenarios, the role of the nuclei provides another unknown element. If dE(N)s and dE(nN)s would actually form a continuum of dEs with respect to relative nucleus brightness as suggested by Grant et al. (2005), their significantly different population properties could be interpreted with a correlation between relative nucleus brightness and host galaxy evolution. Such a correlation could, for example, be provided by nucleus formation through coalescence of globular clusters (GCs): the infall and merging of *several* GCs – resulting in a rather bright nucleus like in a dE(N) – takes many Gyr (Oh & Lin 2000), consistent with the dE(N)s being in place since long. The dE(nN)s, on the other hand, were probably formed more recently, leaving time for only one or two GCs, or none at all, to sink to the center.

7.3. Remarks on previous work

Results similar to ours were derived by Ferguson & Sandage (1989), who also subdivided Virgo and Fornax cluster dEs with respect to magnitude and the presence or absence of a nucleus. In accordance with our results, they found that the dE(N)s are centrally clustered like E and S0 galaxies, while the bright dE(nN)s are distributed like spiral and irregular galaxies. They also found the axial ratios of the bright dE(nN)s to be flatter than those of the dE(N)s.

However, despite these similar results, their magnitude selection of "bright" and "faint" subsamples is actually quite different from ours. We initially selected only dEs with $m_B \leq 18\overset{m}{.}0$ mag (the completeness limit of the VCC), yielding a sample range of about $4\overset{m}{.}5$ in *B*, and then subdivided our full sample at its median *r* magnitude. In contrast to that, Ferguson & Sandage (1989) included VCC galaxies with $m_B < 17\overset{m}{.}5$ in their *bright* subsample, which therefore still spans a range of 4^m. Their *faint* subsample contains VCC galaxies with $m_B > 18\overset{m}{.}4$, which are not included in our study and already lie within the luminosity regime of Local Group dwarf spheroidals (e.g., Grebel et al. 2003). Therefore, their and our study can be considered complementary to some extent, in the sense that we probe different luminosity regimes with our respective subsample definitions.

8. C

We have presented a quantitative analysis of the intrinsic shapes and spatial distributions of various subsamples of Virgo cluster early-type dwarfs (dEs): bright and faint (non-)nucleated dEs (dE(N)s and dE(nN)s), dEs with disk features (dE(di)s), and dEs with blue centers dE(bc)s). The dE(bc)s, dE(di)s, and bright dE(nN)s are shaped like thick disks and show basically no central clustering, indicating that they are unrelaxed populations that probably formed from infalling progenitor galaxies. As opposed to that, the dE(N)s (both bright and faint) are a fairly relaxed population of spheroidal galaxies, though an oblate intrinsic shape is favored for them as well. The faint dE(nN)s appear to be somewhat intermediate: their shapes are similar to the dE(N)s, but they form a largely unrelaxed population as derived from their clustering properties. Taken together, these results define a morphology-density relation *within* the dE class.

Given that Ferguson & Sandage (1989) derived similar results for both Virgo and Fornax cluster galaxies, it is also clear that this zoo of different dE subclasses is not only specific to the Virgo cluster. Similarly, a significant number of Coma cluster dEs show a two-component profile and are flatter than the normal dEs (Aguerri et al. 2005). Moreover, Rakos & Schombert (2004) found the dE(N)s in Coma and Fornax to have older stellar populations than the dE(nN)s, consistent with our colour analysis of the Virgo cluster dEs. Thus, although the relative proportions of the dE subclasses might vary between the dynamically different Virgo, Coma, and Fornax clusters, the dE variety itself is probably similar in any galaxy cluster in the present epoch. We thus consider it important that future studies of dEs do not intermingle the different subclasses, but instead compare their properties with each other, e.g., their stellar content or kinematical structure. This will eventually lead to pinning down the actual significance of the various suggested formation paths, thereby unveiling an important part of galaxy cluster formation and evolution.

Acknowledgements

We thank the referees for useful suggestions that helped us improve the paper. We gratefully acknowledge support by the Swiss National Science Foundation through grants number 200020-105260 and 200020-105535. We thank J. Gallagher for stimulating discussions, and W. Löffler for his untiring computer support. This study is based on publicly available data from the SDSS.

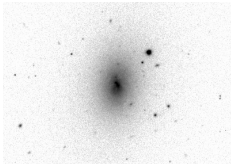

CHAPTER 5

T - : - , - , ?

"And when did the world become coloured?"
Young kid watching an old black-and-white movie

We present an analysis of the optical colours of 413 Virgo cluster early-type dwarf galaxies (dEs), based on Sloan Digital Sky Survey imaging data. Our study comprises (1) a comparison of the colour-magnitude relation (CMR) of the different dE subclasses that we identified in Chapter 4, (2) a comparison of the shape of the CMR in low and high-density regions, (3) an analysis of the scatter of the CMR, and (4) an interpretation of the observed colours with ages and metallicities from population synthesis models. We find that the CMRs of nucleated (dE(N)) and non-nucleated dEs (dE(nN)) are significantly different from each other, with similar colours at fainter magnitudes ($m_r \gtrsim 17^m$), but increasingly redder colours of the dE(N)s at brighter magnitudes. Furthermore, we find a small but significant dependence of the CMR on local projected galaxy number density, consistently seen in all of $u-r$, $g-r$, and $g-i$, and weakly $i-z$. At brighter magnitudes, the high-density CMR lies redward of the low-density CMR; both CMRs typically intersect at fainter magnitudes ($m_r \approx 17^m$). This is statistically significant for the dE(N)s and the full dE sample, but also seen for the dE(nN)s. It is not caused by possible differences in distance between the low and high-density subsamples.

We deduce that a significant intrinsic colour scatter of the CMR is present, even when allowing for a distance spread of our galaxies. Moreover, the colour residuals, i.e., the offsets of the data points from the linear fit to the CMR, are clearly correlated with each other in all bands for the dE(N)s and for the full dE sample. This implies that, at a given magnitude, a galaxy with an older stellar population than average typically also exhibits a larger metallicity than average. For the dE(nN)s, such a correlation is present at least between the $u-r$ and $g-i$ colours. From a comparison with theoretical colours from population synthesis models, we find the CMRs of the dE(N)s, the dE(di)s, and the full dE sample to be consistent with being mainly a relation of metallicity and luminosity, but reaching to slightly higher ages at lower metallicities. For the dE(nN)s, the CMR could as well be a relation of constant metallicity, but it is only weakly defined in the metallicity-sensitive colour $i-z$ due to a rather large scatter at fainter magnitudes. When comparing the colour values of the respective CMR fits at brighter magnitudes ($m_r \lesssim 15^m$), we find the dE(nN)s to be younger, and possibly also less metal rich, than the dE(N)s, while the dE(di)s are rather similar to the dE(N)s and seem to be only slightly younger on average.

This study was done together with Eva K. Grebel, Bruno Binggeli, and Mischa Vodička.

1. I

After having established a subdivision scheme of Virgo cluster early-type dwarf (dE) galaxies into subclasses with different shapes and distributions (Lisker et al. 2007, Chapter 4), we can now proceed to the next logical step, namely to exploiting the wealth of data provided by the Sloan Digital Sky Survey Data Release 5 (DR5, Adelman-McCarthy et al. 2007) in a multicolour analysis of our sample of 413 dEs. However, as we have already seen in Section 6 of the previous chapter, the colours of different dEs, or of dEs of different subclasses, can not straightforwardly be compared with each other: the existence of a relation between colour and magnitude requires such a comparison to be done either at fixed magnitude or with a correction for magnitude differences. For this reason, we shall explore the dE colours mainly through an analysis of their colour-magnitude relation (CMR).

It has been known since long that a close correlation exists between the colours and luminosities of early-type galaxies (e.g., Baum 1959; de Vaucouleurs 1961; Faber 1973; Sandage & Visvanathan 1978a; Caldwell 1983). While this has included the dEs, there has been disagreement about whether or not they follow the same CMR as the giant ellipticals: de Vaucouleurs (1961) found the dwarfs to be "systematically bluer" than the giants (but nevertheless following a CMR), whereas Caldwell (1983) reported a linear CMR over a range of $-15^{\mathrm{m}} \leq M_{\mathrm{V}} \leq -23^{\mathrm{m}}$. However, his Figure 3 actually suggests that the slope of the CMR might indeed be slightly different for the dEs, in the same way as the results of de Vaucouleurs (1961) suggested (i.e., with decreasing magnitude, dwarfs become bluer faster than giants do). NGC 205 is found to fall on the blue side of the relation of $U - V$ colour with magnitude (Faber 1973; Caldwell 1983), which is not surprising, since it displays blue central colours caused by young stars (Hodge 1973, also see Chapter 3). This shows again that it is advantageous to separate dEs with blue centers (dE(bc)s) from the other dE subclasses (Chapter 4), in order to avoid any bias that their blue colours might cause.

A striking observation is the universality of the CMR: it was found to be equal, within the measurement errors, for E and S0 galaxies within clusters, groups, or the field (Faber 1973; Sandage & Visvanathan 1978a,b; Bower et al. 1992), leading Faber (1973) to state that the colours of elliptical galaxies "are independent of all physical properties studied other than luminosity". Faber also showed that a similar relation exists between the strength of spectral absorption features and luminosity, which basically is the spectroscopic analogue to the CMR. He interpreted the CMR with an increase of metallicity with luminosity, which today is still considered to be the primary determinant of the CMR (e.g., Kodama & Arimoto 1997; Chang et al. 2006). This can be understood with a higher binding energy per unit mass of gas in more massive galaxies, leading to stronger enrichment of the stellar populations.

Recently, Bernardi et al. (2003) showed that colour seems to correlate even more strongly with velocity dispersion than it does with luminosity. This implies that the CMR itself is most likely just a combination of the relation of luminosity and velocity dispersion ("Faber-Jackson relation", Faber & Jackson 1976) and that of colour and velocity dispersion. As Matković & Guzmán (2005) point out, the latter might hint at a more fundamental relation, namely between galaxy metallicity and mass. However, Matković & Guzmán (2005) found a change in the slope of the Faber-Jackson relation for "faint early-type" galaxies — here, "faint" means $-17\overset{\mathrm{m}}{.}3 \leq M_{\mathrm{B}} \leq -20\overset{\mathrm{m}}{.}5$, thus reaching only slightly into the dwarf regime. Likewise, De Rijcke et al. (2005) found an even larger difference in slope for a sample of 15 dEs, but argued that this is consistent with theoretical models, due to the dynamical response to starburst-induced mass loss, which is stronger for objects of lower mass.

However, significant constraints to such models could only be provided with a better understanding of dE formation, and of how it compares to the formation of giant ellipticals. The latter have frequently been reported to be consistent with having formed the bulk of their stars at redshifts $z \gtrsim 2$ (e.g., Bower et al. 1992; Bender et al. 1996; however, also see Ferreras et al. 1999, who argued that giant ellipticals need not necessarily have formed their stars in a common epoch). In contrast, formation mechanisms proposed for dEs in clusters are typically not based on an early formation epoch, but rather, on infall and subsequent gas-stripping and transformation of late-type galaxies (e.g., Davies & Phillipps 1988; Moore et al. 1996; van Zee et al. 2004b). One would naively expect that, if two given

dE subclasses formed through different mechanisms, their resulting CMRs should display differences as well, since the relation of galaxy mass to the properties of its stellar population should depend to some extent on how and when the latter was formed. On the other hand, the apparent universality of the CMR – mainly defined for giant ellipticals – would seem to argue against such differences. Secker et al. (1997) found that the Coma cluster dEs follow "quite certainly" the CMR defined by the giant early-type galaxies of the cluster. However, while Conselice et al. (2003a) admitted that the *mean* relation of early-type dwarfs in the Perseus cluster still follows the CMR of the Es, they found considerable scatter at magnitudes $M_B \geq -15^m$, apparently caused by two different sequences of dwarfs in colour-magnitude space. They argue that the early-type dwarfs must have multiple origins — something that we should be able to test in more detail, given our "preparatory work", namely the separation of dE subclasses that have different shapes and distributions (Chapter 4). Moreover, the SDSS multicolour data enable us to construct CMRs in more than one colour, and also to analyze our galaxies in colour-colour space, thereby translating colours into ages and metallicities. Since Rakos & Schombert (2004) found the dE(nN)s in the Coma and Fornax clusters to be younger and to have a larger metallicity than the dE(N)s, we can perform a similar analysis for our Virgo cluster galaxies, allowing us to test the similarity of dE populations of different clusters.

2. D

The SDSS DR5 covers all galaxies listed in the Virgo cluster catalog (VCC, Binggeli et al. 1985), except for an approximately $2^\circ \times 2.^\circ5$ area at $\alpha \approx 186.^\circ2$, $\delta \approx +5.^\circ0$. It provides reduced images taken in the *u*, *g*, *r*, *i*, and *z* bands with an effective exposure time of 54s in each band (see also Stoughton et al. 2002), as well as the necessary parameters to flux calibrate them. The pixel scale of $0.''396$ corresponds to a physical size of 30 pc at our adopted Virgo cluster distance of $d = 15.85$ Mpc (distance modulus $m - M = 31.^m0$; see, e.g., Ferrarese et al. 2000), which we use throughout.

The SDSS imaging camera (Gunn et al. 1998) takes data in drift-scanning mode nearly simultaneously in the five photometric bands, and thus combines very homogeneous multicolour photometry with large area coverage and sufficient depth to enable a systematic analysis of dEs. The images have an absolute astrometric accuracy of RMS$\leq 0.''1$ per coordinate, and a relative accuracy between the *r* band and each of the other bands of less than 0.1 pixels (Pier et al. 2003). They can thus easily be aligned using their astrometric calibration and need not be registered manually. Furthermore, adjacent SDSS images can be accurately put together, allowing the extraction of cutout images that fully cover a given object, even if the latter lies at the edge of an SDSS image.

The RMS of the noise per pixel corresponds to a surface brightness of approximately 24.2 mag arcsec^{-2} in the u-band, 24.7 in *g*, 24.4 in *r*, 23.9 in *i*, and 22.4 in z. The typical total signal-to-noise ratio (S/N) of a bright dE ($m_B \approx 14^m$) amounts to about 1000 in the r-band within an aperture radius of approximately two half-light radii. For a faint dE ($m_B \approx 18^m$) this value is typically about 50. While the S/N in the *g* and i-band is similar, it is several times lower in the z-band and more than ten times lower in the u-band.

Since the sky level on the SDSS images can vary by some tenths of the noise level across an image, it is not sufficient to subtract only a single sky flux value from each image. We therefore determined the sky flux distribution across a given image using a thorough procedure, as described in detail in Chapter 4. The sky-subtracted images were then flux calibrated and corrected for Galactic extinction (Schlegel et al. 1998). We also correct for the reported[1] SDSS zeropoint offsets in the *u* and *z* bands from the AB system (Oke & Gunn 1983):

$$u_{AB} = u_{SDSS} - 0.^m04 \tag{7}$$

$$z_{AB} = z_{SDSS} + 0.^m02 \tag{8}$$

[1] see http://www.sdss.org/dr5/algorithms/fluxcal.html

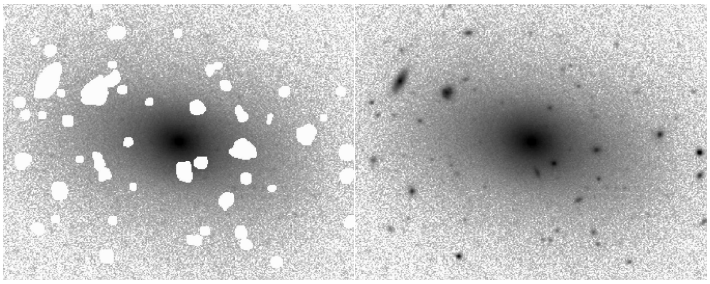

F 5.1. **Object masks.** Image of VCC 0437 with and without masking of disturbing foreground or background objects.

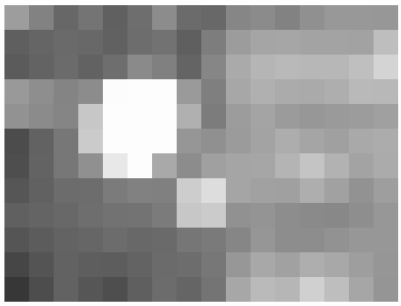

F 5.2. **Sky flux overestimation of the SDSS pipeline.** Image containing the sky background measurements of the SDSS photometric pipeline as pixel values. Brighter pixels indicate a higher measured background value. Shown is the field that contains VCC 0856, which leaves a clear imprint in this image (bright region towards the left), causing a significant overestimation of the local sky level.

3. S

Our working sample of Virgo cluster dEs contains 413 certain cluster members that were initially classified as early-type dwarfs in the VCC (''dE" or "dS0", including candidates), that are brighter than $m_B \leq 18\overset{m}{.}0$, that passed our visual examination for possible dwarf irregulars, and for which a Petrosian radius could be derived. The details of our sample selection are described in Chapter 4.

For each galaxy, we determined a "Petrosian semimajor axis" (hereafter Petrosian SMA, a_p), i.e., we use ellipses instead of circles in the calculation of the Petrosian radius (see, e.g., Lotz et al. 2004a). The total flux in the r band was measured within $a = 2\,a_p$, yielding a value for the half-light semimajor axis, $a_{hl,r}$. Axial ratio and position angle were then determined through an isophotal fit at $a = 2\,a_{hl,r}$. The details of this process are outlined in Chapter 4. Disturbing foreground or background objects were properly masked (see Figure 5.1), and these masks were corrected for in the determination of the total r magnitude. We also decided to mask the nuclei, if present, in order to guarantee that a nucleus with a different colour than its host galaxy would not affect our measurements of the inner galaxy colours.

For each galaxy and band, we measured the flux within three elliptical apertures: $a \leq 0.5\,a_{hl,r}$ ("small aperture"), $a \leq a_{hl,r}$ ("intermediate aperture" or half-light aperture), and $a \leq 2\,a_{hl,r}$ ("large aperture"). These measurements can be combined to yield the average colour within each of the three apertures, as well as the average colour within the elliptical annuli $0.5\,a_{hl,r} \leq a < a_{hl,r}$ and $a_{hl,r} \leq a < 2\,a_{hl,r}$.

4. E

The noise in every image was measured as the standard deviation around the mean of all unmasked pixels, clipped five times iteratively at 3σ. This noise level was used to determine an average S/N for each object, band, and aperture. The "S/N uncertainty" of a given flux measurement is then taken to be the inverse S/N value.

As stated in Section 2, an accurate determination of the sky flux level is important for our study. Consequently, we should take its uncertainty into account for our error estimation. We find that the mean pixel flux value of all unmasked pixels (see above) typically deviates from zero by 0.2% of the noise level, or less. We thus adopt this value as the uncertainty in the sky level (per pixel), and compute from it the total ''sky level uncertainty" for each galaxy, band, and aperture.

The uncertainty in the determination of the Petrosian SMA is difficult to estimate, and even more so the subsequent uncertainty in the total *r* band flux and the corresponding half-light SMA. Apart from proper masking of neighbouring or blended objects – which we assume to be done sufficiently accurate – the determination of the Petrosian SMA is strongly affected by a possible over- or underestimation of the sky level. Should the sky level be overestimated, as is the case in the measurements of the SDSS photometric pipeline (Figure 5.2), the Petrosian SMA will be underestimated, and vice versa. Thus, in the case of a sky level overestimation, the total galaxy flux will be underestimated due to both the sky flux oversubtraction and the lower-than-actual Petrosian SMA within which the flux is measured. We thus assume this "Petrosian uncertainty" to be of the same order as the sky level uncertainty (see above), which we therefore simply count twice in our calculation of total errors (see below).

The Petrosian uncertainty is not directly relevant for the calculation of a *colour* value of a given galaxy from the flux values of two bands, since the aperture used is the same for both bands, independent of whether its size was under- or overestimated. However, it is relevant for comparing the colour values of two different galaxies, since for one of them, the half-light SMA might have been underestimated, but overestimated for the other. In order to obtain a conservative error estimate for the colours, we therefore decided to take into account the Petrosian uncertainty in the same way as described above for the *r* band total flux, even if this might be somewhat too pessimistic in many cases.

The SDSS reports photometric calibration errors of $0\overset{\text{m}}{.}02$ in *g*, *r*, and *i*, and $0\overset{\text{m}}{.}03$ in *u* and *z*, which we adopt as the "calibration uncertainty". In addition, the natural red leak of the *u* filter is reported[2] to be not properly blocked, causing another uncertainty of $0\overset{\text{m}}{.}02$, the "*u*-leak uncertainty".

For each flux measurement f_x in a given band *x*, we combine all the different uncertainties to a single uncertainty Δf_x. This is done by adding the individual uncertainties quadratically, as exemplified below for the *u* band.

$$\Delta f_\text{u} = \sqrt{\left(\frac{\sigma_\text{u} \cdot \sqrt{N_\text{pix}}}{f_\text{u}}\right)^2 + 2 \cdot \left(\frac{0.002\,\sigma_\text{u} \cdot N_\text{pix}}{f_\text{u}}\right)^2 + (10^{0.4 \cdot 0.03} - 1)^2 + (10^{0.4 \cdot 0.02} - 1)^2} \tag{9}$$

Here, σ_u denotes the noise level per pixel, as described above. N_pix is the number of pixels included in the given aperture. The first term is the S/N uncertainty, the second term is the combination of sky level uncertainty and Petrosian uncertainty, and the last two terms are the calibration uncertainty and the *u*-leak uncertainty, respectively.

Errors on measured colour values are calculated by adding the relative flux errors from each band quadratically, and converting them to magnitudes. An example is given below for the $u - g$ colour error, $\Delta(u - g)$, calculated from the *u* band flux f_u, the *g* band flux f_g, and their respective errors.

$$\Delta\left(\frac{f_\text{u}}{f_\text{g}}\right) = \sqrt{\left(\frac{1}{f_\text{g}}\Delta f_\text{u}\right)^2 + \left(\frac{f_\text{u}}{f_\text{g}^2}\Delta f_\text{g}\right)^2} = \sqrt{\left(\frac{f_\text{u}}{f_\text{g}}\frac{\Delta f_\text{u}}{f_\text{u}}\right)^2 + \left(\frac{f_\text{u}}{f_\text{g}}\frac{\Delta f_\text{g}}{f_\text{g}}\right)^2} = \frac{f_\text{u}}{f_\text{g}}\sqrt{\left(\frac{\Delta f_\text{u}}{f_\text{u}}\right)^2 + \left(\frac{\Delta f_\text{g}}{f_\text{g}}\right)^2} \tag{10}$$

[2] see http://www.sdss.org/dr5/algorithms/fluxcal.html

$$\Rightarrow \quad \frac{\Delta(f_\mathrm{u}/f_\mathrm{g})}{(f_\mathrm{u}/f_\mathrm{g})} = \sqrt{\left(\frac{\Delta f_\mathrm{u}}{f_\mathrm{u}}\right)^2 + \left(\frac{\Delta f_\mathrm{g}}{f_\mathrm{g}}\right)^2} \tag{11}$$

$$\Rightarrow \quad \Delta(u-g) = -2.5\log\left(1 - \sqrt{\left(\frac{\Delta f_\mathrm{u}}{f_\mathrm{u}}\right)^2 + \left(\frac{\Delta f_\mathrm{g}}{f_\mathrm{g}}\right)^2}\right) \tag{12}$$

Equation 12 would actually yield only the errors on one side, whereas the errors on the other side would be calculated from $-2.5\log(1+\sqrt{...})$, and would consequently be smaller. However, we prefer the conservative approach to use the larger errors for both sides. Galaxies for which the relative flux error becomes ≥ 1 are excluded from the respective diagrams or calculations, since the argument to the logarithm in Equation 12 would become ≤ 0, denoting an uncertainty that is too large to be useful. This occurs only for five of the fainter objects for colours that include the *u* band.

5. L

Since colour-magnitude relations of early-type galaxies are found to be linear or nearly linear (e.g., Bower et al. 1992; Bernardi et al. 2003) we describe our relations by fitting a straight line to the data points. A common approach is the method of least-squares fitting, where the chi-square function, $\chi^2(a,b)$, is minimized:

$$\chi^2(a,b) = \sum_{i=0}^{N-1}\left(\frac{c_\mathrm{i} - a - b\cdot m_\mathrm{i}}{\sigma_\mathrm{i}}\right)^2 \tag{13}$$

where a and b are the zeropoint and the slope of the relation, respectively, m_i and c_i are magnitude and colour of the i-th galaxy, and σ_i is the corresponding colour uncertainty (or alternatively, any kind of inverse weight). However, least-squares fitting can sometimes lead to undesired results, e.g., a "best fit" with a slope that differs significantly from that defined by the bulk of data points (Press 2002, see their Figure 15.7.1). This is due to the fact that the chi-square function gives maximum likelihood estimations of a and b only if the measurement errors are normally distributed (Press 2002). However, true measurement errors are rarely normally distributed, and moreover, the scatter of the colour-magnitude relation (CMR) is usually larger than the errors alone would imply, since part of it is an intrinsic scatter (Conselice et al. 2002). We therefore prefer to use a so-called robust fitting technique, as described below.

A robust parameter estimation technique basically means a method whose results are not significantly affected by small deviations of the (real) data points from the (idealized) assumptions on which the method is based (Press 2002). For this purpose, we chose to use a so-called M-estimate, namely the mean *absolute* deviation (rather than the mean square deviation used for least-squares fitting), which was, e.g., used by Chang et al. (2006) to fit colour-magnitude relations, or by Ferreras et al. (2005) to estimate internal colour gradients. We thus minimize the function

$$\mu(a,b) = \sum_{i=0}^{N-1}\left|\frac{c_\mathrm{i} - a - b\cdot m_\mathrm{i}}{\sigma_\mathrm{i}}\right| \tag{14}$$

with notation as in Equation 13. We set σ_i equal to the respective colour error, neglecting magnitude errors, since they are small compared to the range of magnitudes that is considered (compare, e.g., Figure 5.3). Moreover, the magnitude errors mostly scale with the colour errors anyway, which would not alter the relative weights in Equation 14 significantly. We tested this for a few cases, where we set $\sigma_\mathrm{i} = \sqrt{(\Delta m_\mathrm{i})^2 + (\Delta c_\mathrm{i})^2}$, i.e., quadratically adding magnitude and colour error. We found no significant differences in the resulting best fit.

In order to perform the minimization numerically, we decided on an iterative procedure. For a given dataset, we derive a first guess for the slope and zeropoint of the CMR using the task *lsq2* of *SM* (Lupton & Monger 1997). We then derive the minimum of Equation 14 within values of ± 1 around

the first-guess slope and zeropoint, in steps of 0.01. Next, we determine the minimum in a range of ±0.04 around these new values, using steps of 0.0004. Finally, we derive the minimum in a range of ±0.002 around the new values, with steps of 0.00001, and calculate the RMS scatter of the data points around the fitted line. The fitting process is then repeated two times iteratively, excluding data points that are offset by more than 3σ from the fitted line. If the final parameter values fall at the edge of the respective search range, we perform another fitting iteration and use them as first-guess values. However, in no case did this lead to a visible difference between the fitted lines of the first and second run.

6. S

In the sections below, we would like to perform *quantitative*, statistical comparisons of two given colour-magnitude relations. Obviously, we would consider two CMRs to be different if either their slopes, their zeropoints, or both were significantly different from each other. Unfortunately, our method of linear fitting described in Section 5 does not yield errors on these parameters — but even with a method that would yield errors, like least-squares fitting, it would not always be clear whether one should trust these errors (Press 2002). The alternative to comparing the fitted lines would be to compare the two underlying datasets directly. However, here we face the problem that these might be sampled differently in magnitude, like, e.g., the dE(N)s and the dE(nN)s. For example, for two given datasets that follow exactly the same CMR but probe different magnitude regimes, a two-dimensional K-S test would yield a probability of zero that the datasets have the same underlying distribution, simply because they are significantly different in the magnitude-dimension. This is clearly not the sort of test we want to perform.

Given the above considerations, we decided on an approach that combines a comparison of the data points and of the fitted lines of two datasets A and B. First, we compute the colour residuals of the data points A and the data points B about the CMR A. This gives us two distributions of a single parameter, namely the residual about the CMR A, independent of magnitude. We can now compare these two distributions with each other through a (one-dimensional) K-S test, which compares the cumulative distributions, and through a Student's t-test for unequal variances, which compares the means of the distributions. We then compute analogously the residuals of the data points A and B about the CMR B. For the K-S test, we take the average of both values of the K-S statistic D (which is the maximum difference between two cumulative distributions, see Press 2002), and compute our final probability from it. For the t-test, we simply use the larger of the two probabilities as our final probability.

The K-S test has the advantage that it is sensitive to different distributions around the CMR, even if the mean of both was zero, e.g. if both CMRs had different slopes but crossed each other at the middle data point. The Student's t-test for unequal variances has the advantage of taking into account the scatter of each dataset around the mean, which implicitely includes the measurement errors. We thus decided to use the results of both tests for each comparison of a pair of CMRs; we will usually simply refer to the higher of the two probabilities. We typically consider two CMRs to be "significantly" different if the statistical comparison yields probabilities below a few percent.

Note that the goodness of the linear fit is only taken into account implicitely to a small extent: if one of the two linear relations was a rather bad fit or was based on a small sample with large scatter, this would partially be counterbalanced by the inverse comparison with the other CMR. If, however, both linear fits were rather weakly defined, the resulting probabilities might not be too useful.

7. C - -

In Chapter 4 we established a subdivision scheme for the dEs that comprises several subclasses with different properties: dEs with disk features like spiral arms or bars (dE(di)s), dEs with blue

centers (dE(bc)s) caused by recent or ongoing central star formation, bright and faint ordinary dEs (i.e., not displaying disk substructure or a blue center) that are nucleated (dE(N)s), and bright and faint ordinary dEs that have no nucleus, or only a weak nucleus that is below the detection limit of the VCC (dE(nN)s). The bright dE(nN)s, dE(di)s, and dE(bc)s are shaped like thick disks and show no central clustering, while the faint dE(nN)s and the dE(N)s have rounder shapes, and the dE(N)s are more strongly concentrated towards the cluster center. These results define a morphology-density relation *within* the dE class, and we now seek to investigate whether it is also correlated with colour.

In Figures 5.3 to 5.6 we present the relations of colour and r magnitude separately for dE(N)s, dE(nN)s, dE(di)s, and dE(bc)s, using the $u-r$, $g-r$, $g-i$, and $i-z$ colours, and measuring the colours within our three elliptical apertures. Our choice of presented colours relies partly on the considerations outlined in Section 11: $u-r$ colour is mainly age-sensitive, whereas $i-z$ is metallicity-sensitive. In addition, we also show the CMRs using $g-i$ colour, since it provides the largest wavelength baseline within the three high-S/N SDSS bands (g, r, i). Moreover, we present the CMRs using $g-r$ colour, with the idea of comparing them to the $u-r$ relations: the smaller wavelength range of $g-r$ is counterbalanced by the significantly smaller errors in g due to the much larger S/N as compared to u. The resulting parameters of the corresponding linear fits are given in Table 5.1.

Whether radial steps of colour or flux measurements should be presented in a differential or a cumulative way often depends on the gusto of the author. Obviously, if measurement errors were zero or extremely small, colour gradients could be identified more clearly with the differential than with the cumulative approach. However, for our galaxies with their low surface brightness outskirts, errors become considerably larger at larger radii when measuring colours differentially. In contrast, they remain moderate for cumulative measurements — with the tradeoff that any gradient stands out less clear. For example, Figure 5.10 presents the differential analogue to the cumulative measurements in Figure 5.6. Especially with the very steep slopes of the CMRs in $i-z$, the large errors in Figure 5.10 can lead to linear fits that might not seem trustworthy to the eye, or might at least seem equally likely than a number of other possible lines drawn through the data points. We thus decided on using cumulative measurements for our analysis of the CMRs. However, for the dE(bc)s, this approach bears the problem that the blue central colours of these objects contribute to *all* apertures, not only to the innermost one. Therefore, we present in Figures 5.7 to 5.10 the CMRs from differential measurements, which we will use below for the discussion of the properties of the dE(bc)s.

In each of Figures 5.3 to 5.10, the horizontal dotted line denotes the separation between our bright and faint subsamples. For the dE(N)s and dE(nN)s, we present in addition to the CMR of their full samples the CMRs of their bright and faint subsamples (thin solid and dotted lines, respectively). If one of these cannot be seen in the respective diagram, it falls onto the relation of the full sample and is thus covered by that line (see, e.g., the left upper panel of Figure 5.3). The CMRs of the full dE(N) sample, the full dE(nN) sample, the dE(di)s, and the dE(bc)s are compared to each other in the lowermost row of each of the figures. The CMRs of the bright and faint subsamples are not shown there, to avoid confusion.

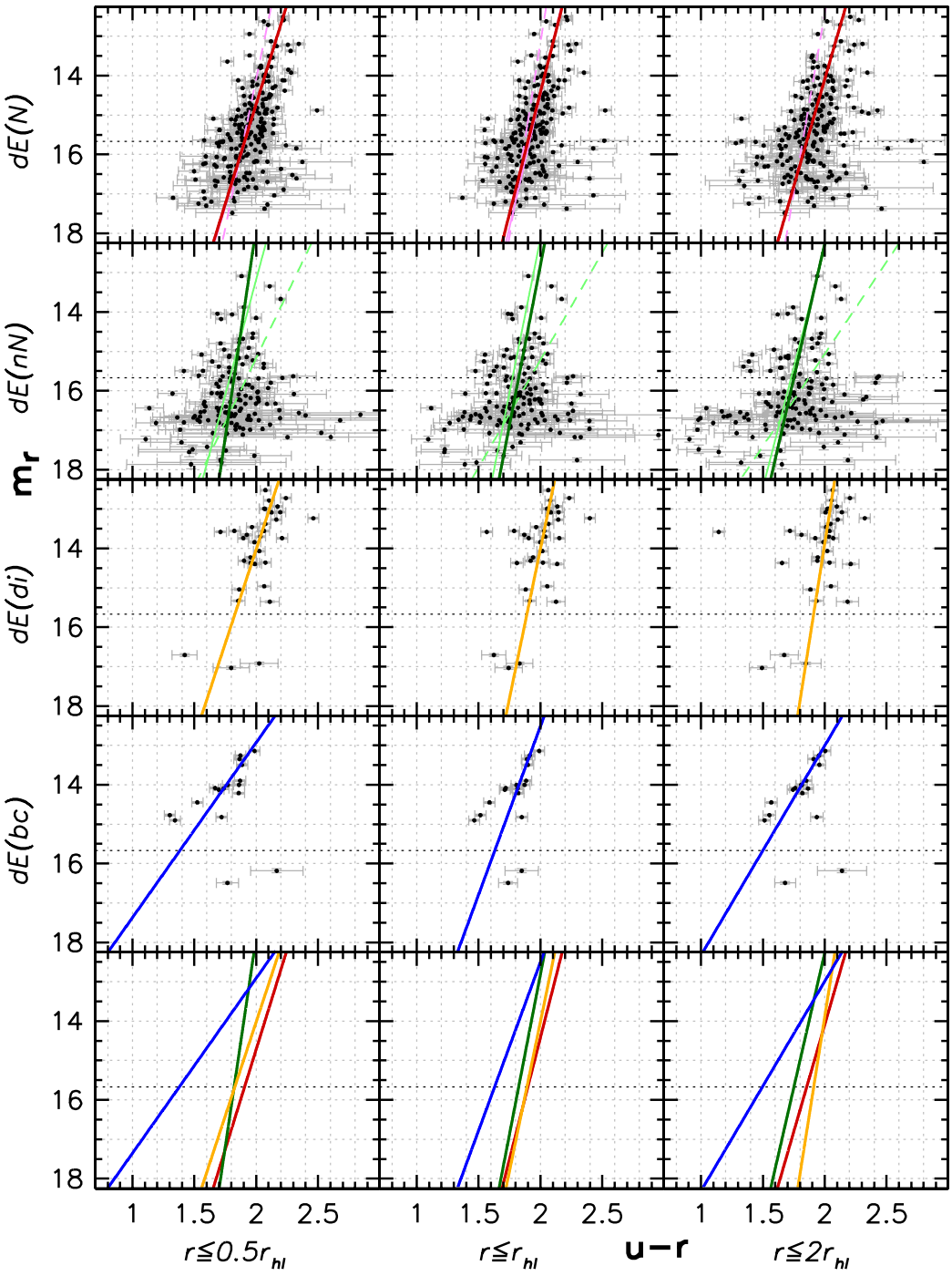

F 5.3. **Colour-magnitude relations of dE subclasses.** Shown are the relations of r magnitude with $u - r$ colour for the different dE subclasses (different rows, as labelled on the left-hand side) and for our three aperture sizes (different columns, as labelled below the diagrams). The linear fits to the CMR of each subclass are shown as lines of different colour (dE(N): red, dE(nN): green, dE(di): yellow, dE(bc): blue), and are plotted again in the bottom row for comparison. For the dE(N)s and dE(nN)s, we also show the linear fits to the respective bright (thin solid lines) and faint (thin dashed lines) subsamples (dE(N): pink, dE(nN): light green). If one of these cannot be seen, it falls onto the relation of the full sample and is thus covered by that line (as, e.g., in the upper left panel). These fits are not shown in the bottom row, to avoid confusion.

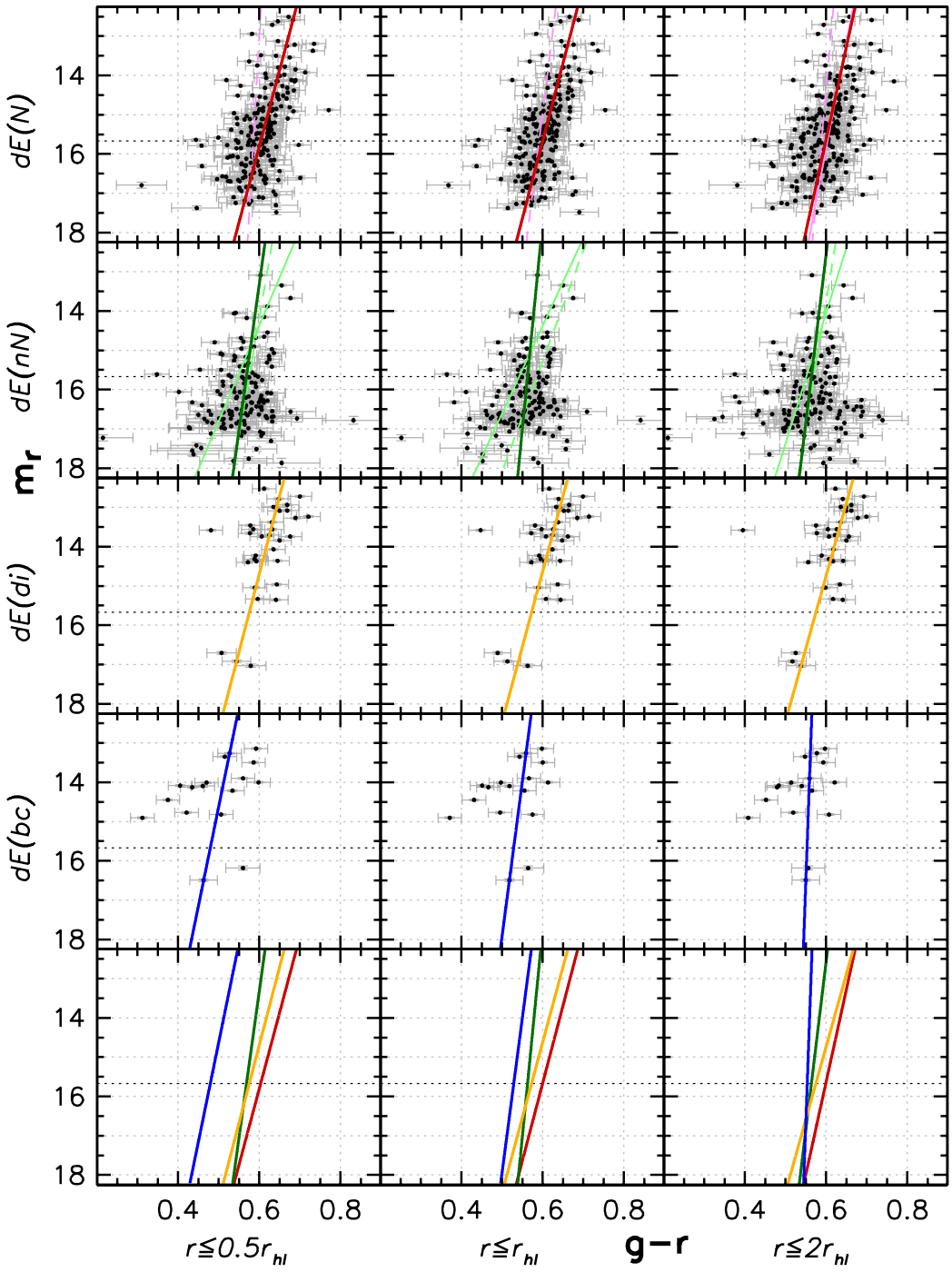

F 5.4. **Colour-magnitude relations of dE subclasses.** Same as Figure 5.3, but for $g - r$ colour.

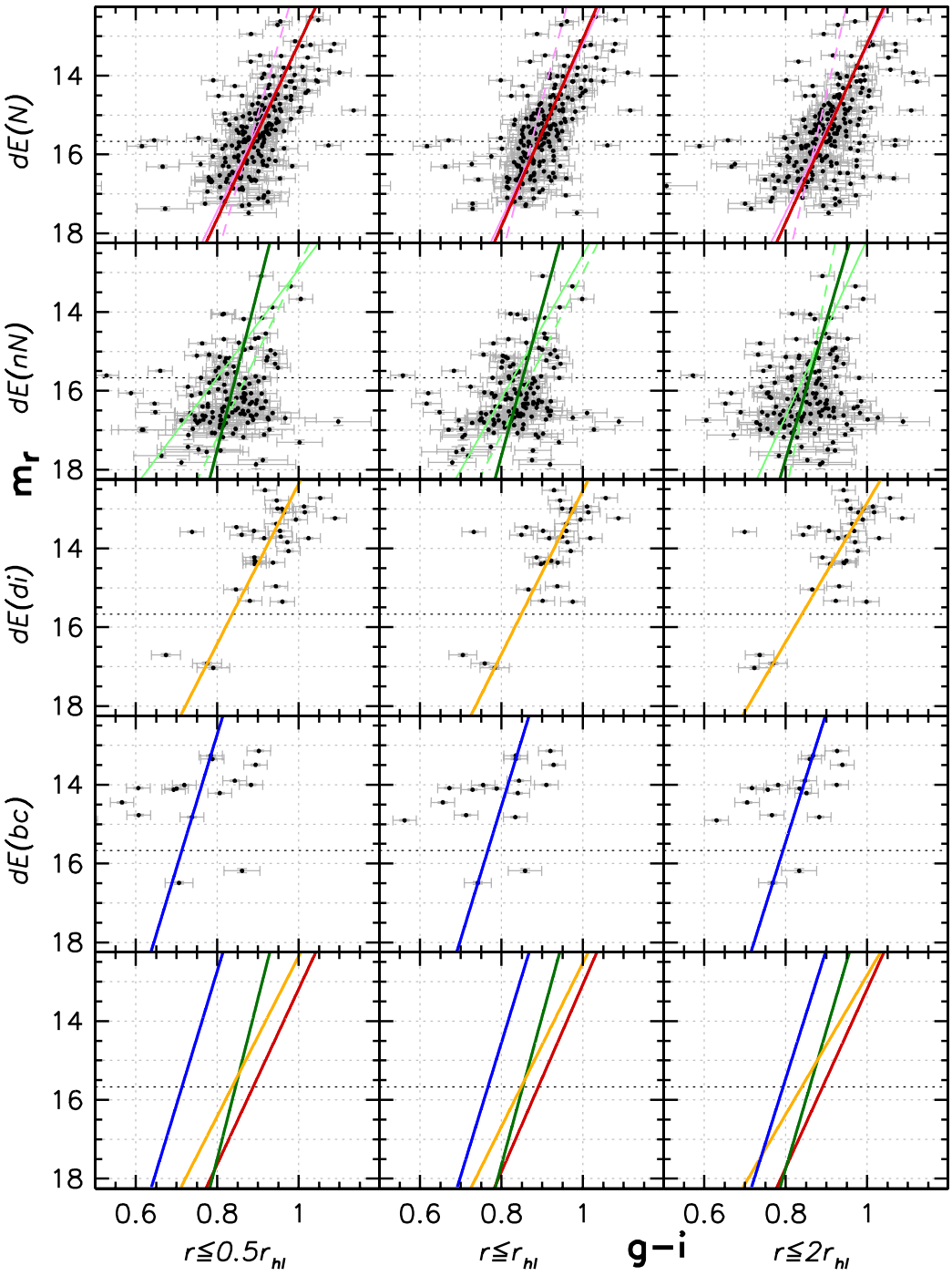

F 5.5. **Colour-magnitude relations of dE subclasses.** Same as Figure 5.3, but for $g - i$ colour.

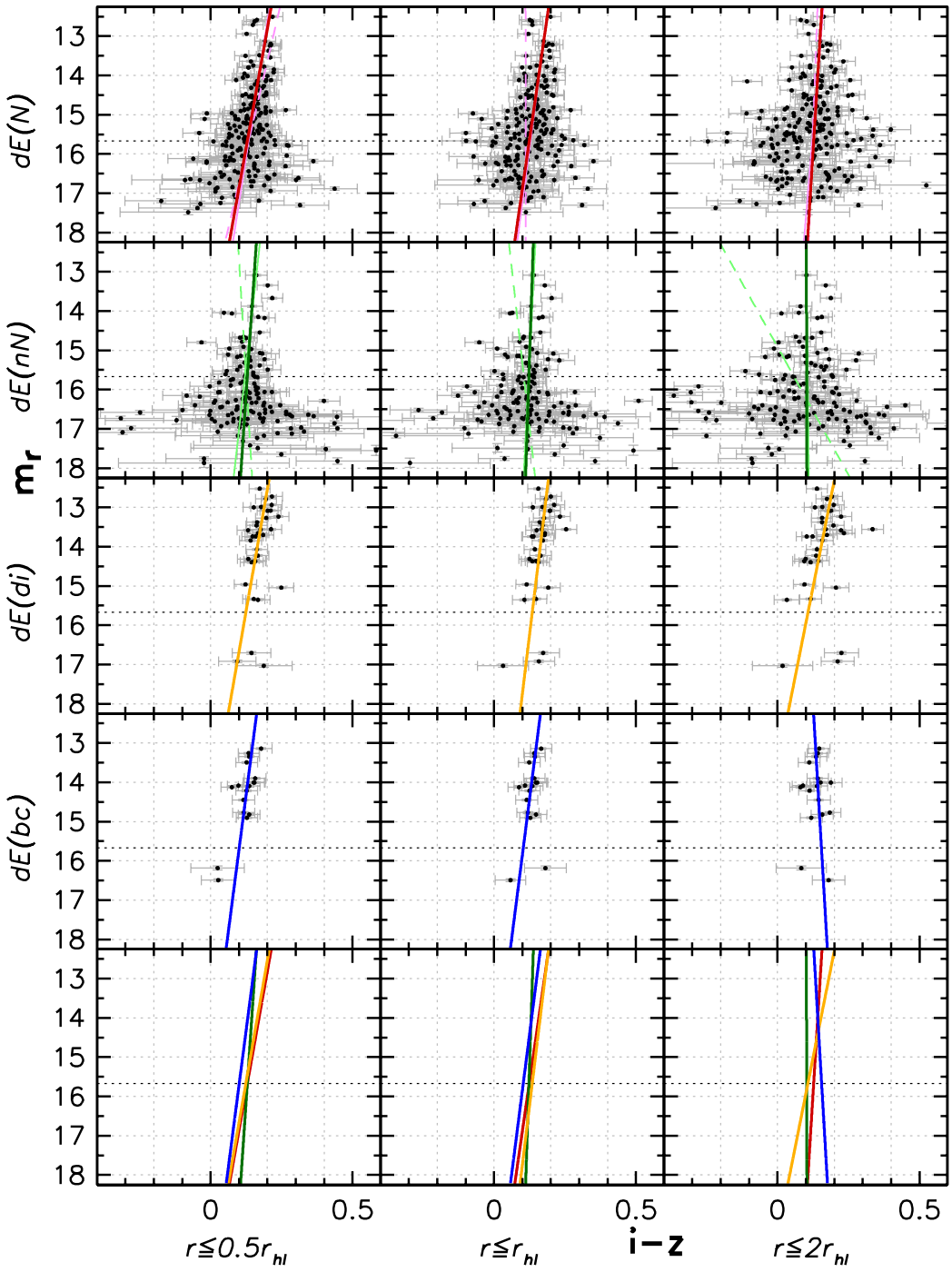

F 5.6. **Colour-magnitude relations of dE subclasses.** Same as Figure 5.3, but for $i - z$ colour.

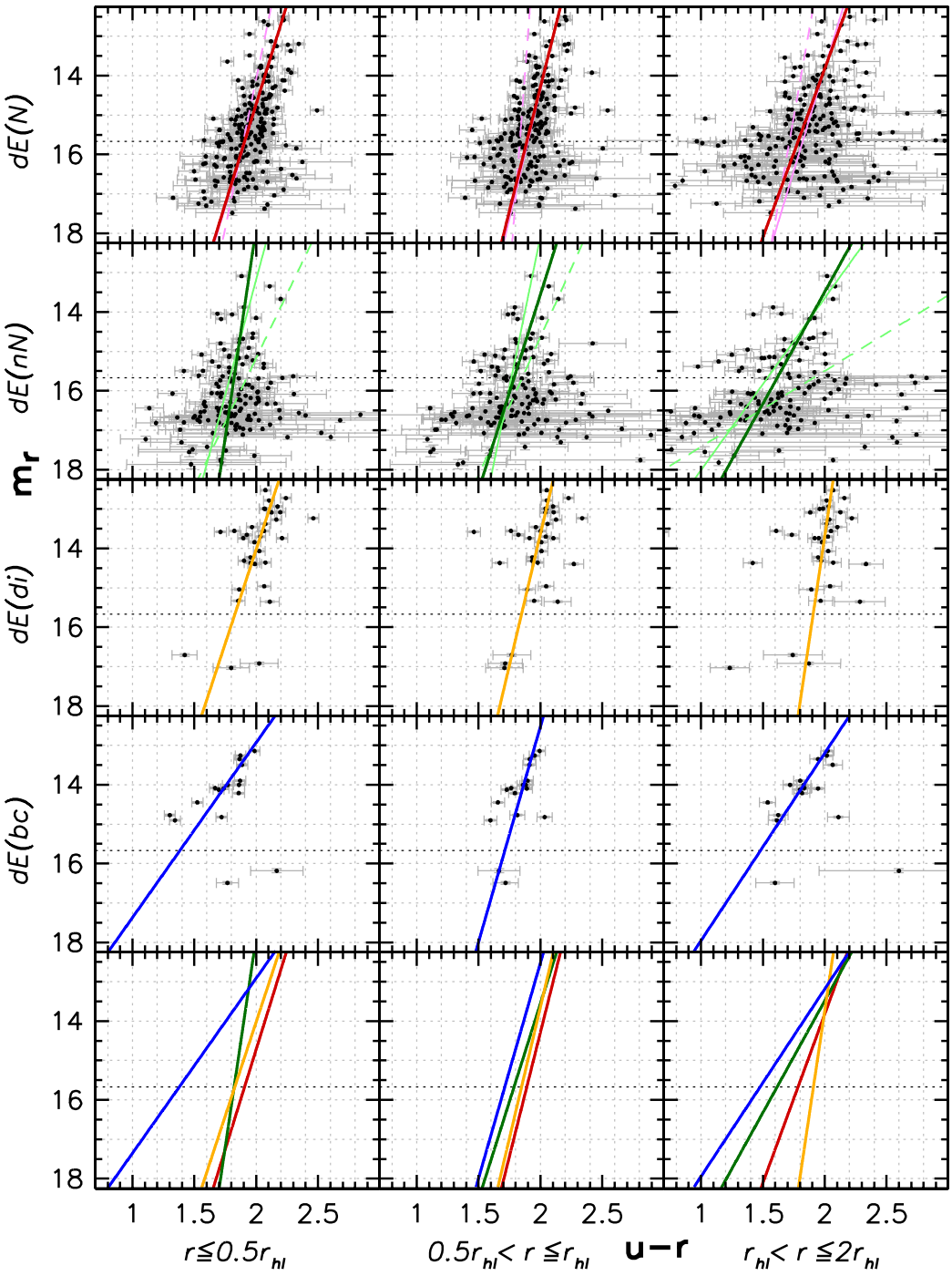

F 5.7. **Colour-magnitude relations of dE subclasses.** Same as Figure 5.3, but using differential radial steps instead of cumulative ones.

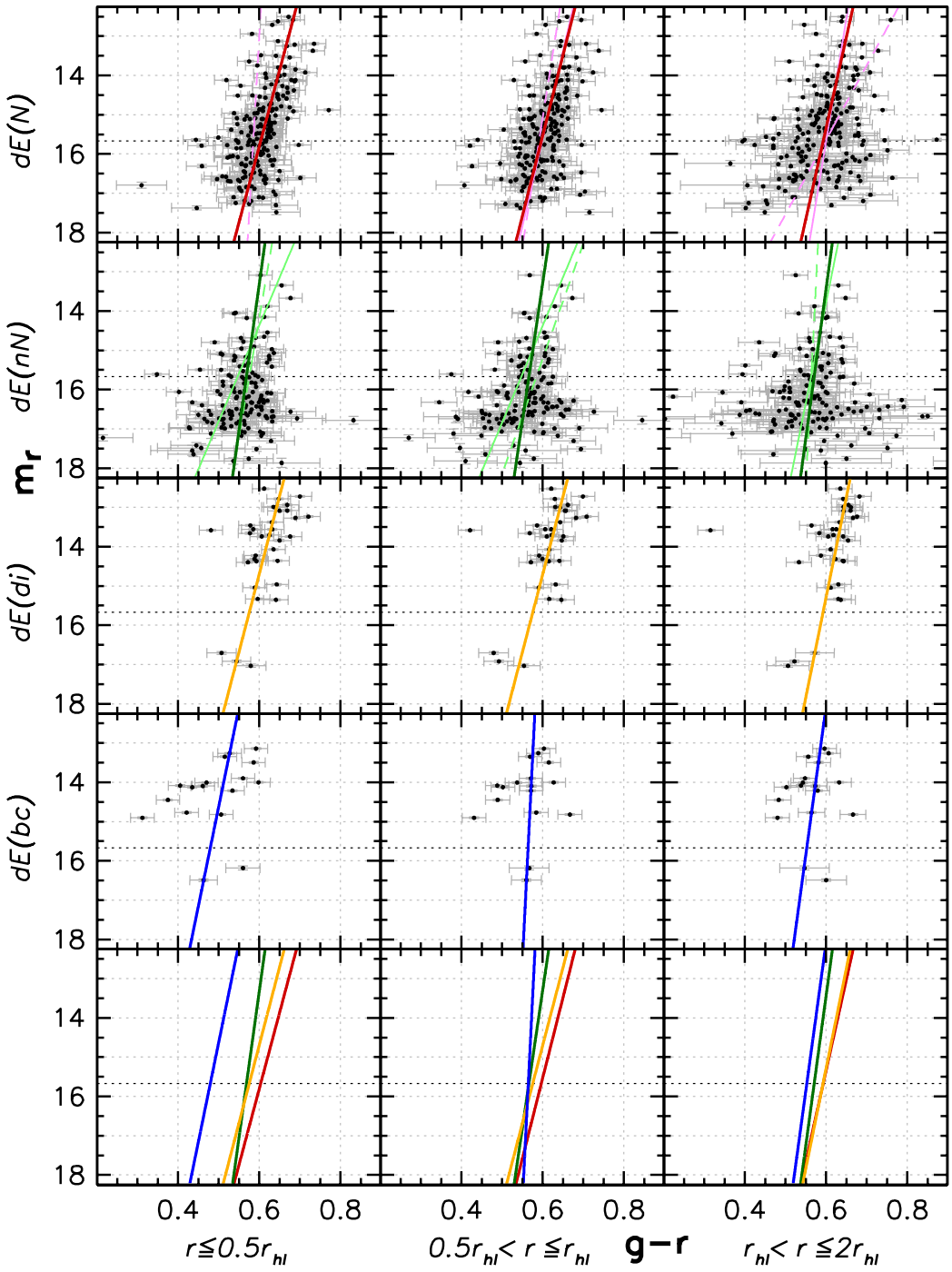

F 5.8. **Colour-magnitude relations of dE subclasses.** Same as Figure 5.7, but for $g - r$ colour.

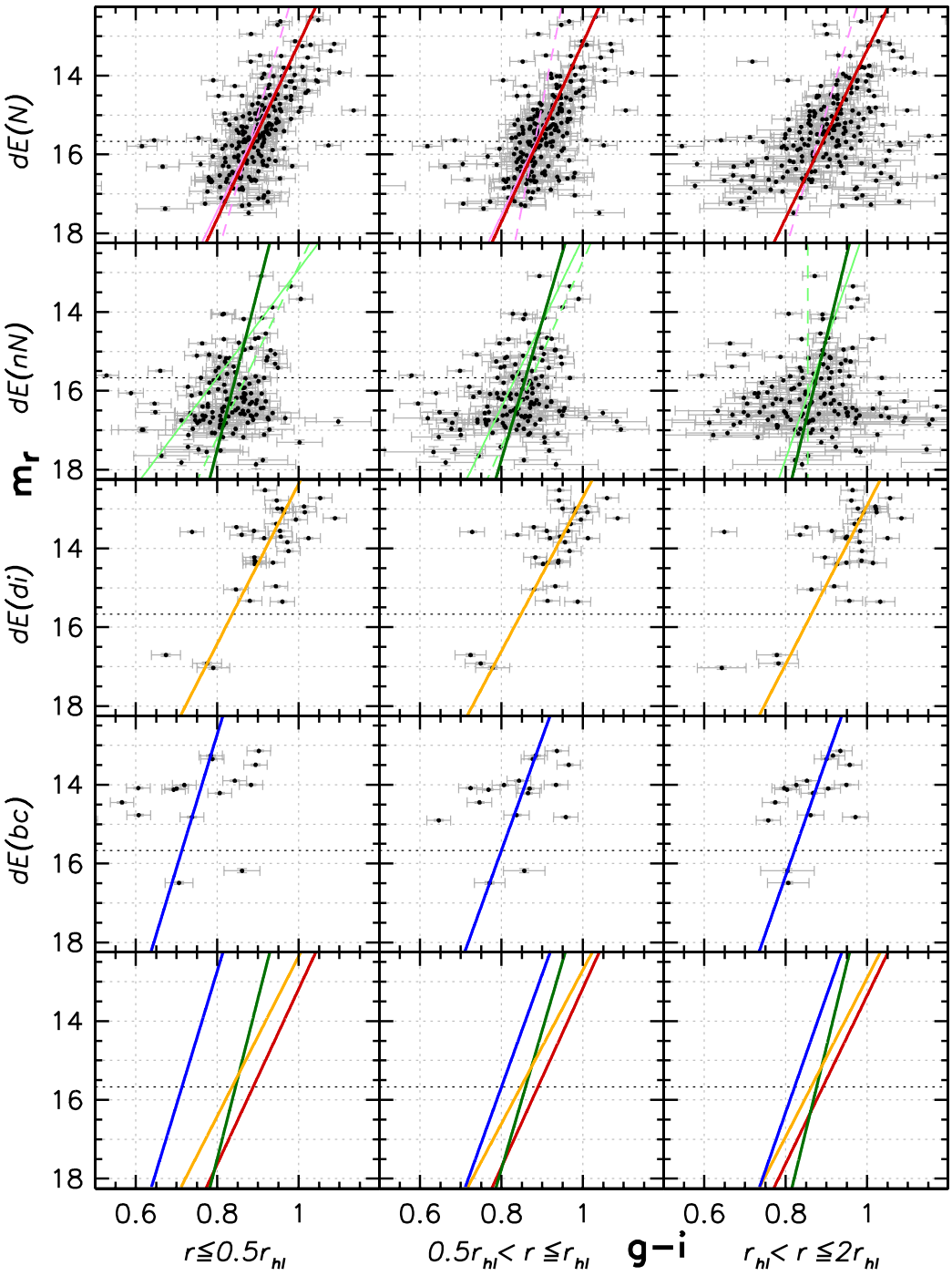

F 5.9. **Colour-magnitude relations of dE subclasses.** Same as Figure 5.7, but for $g - i$ colour.

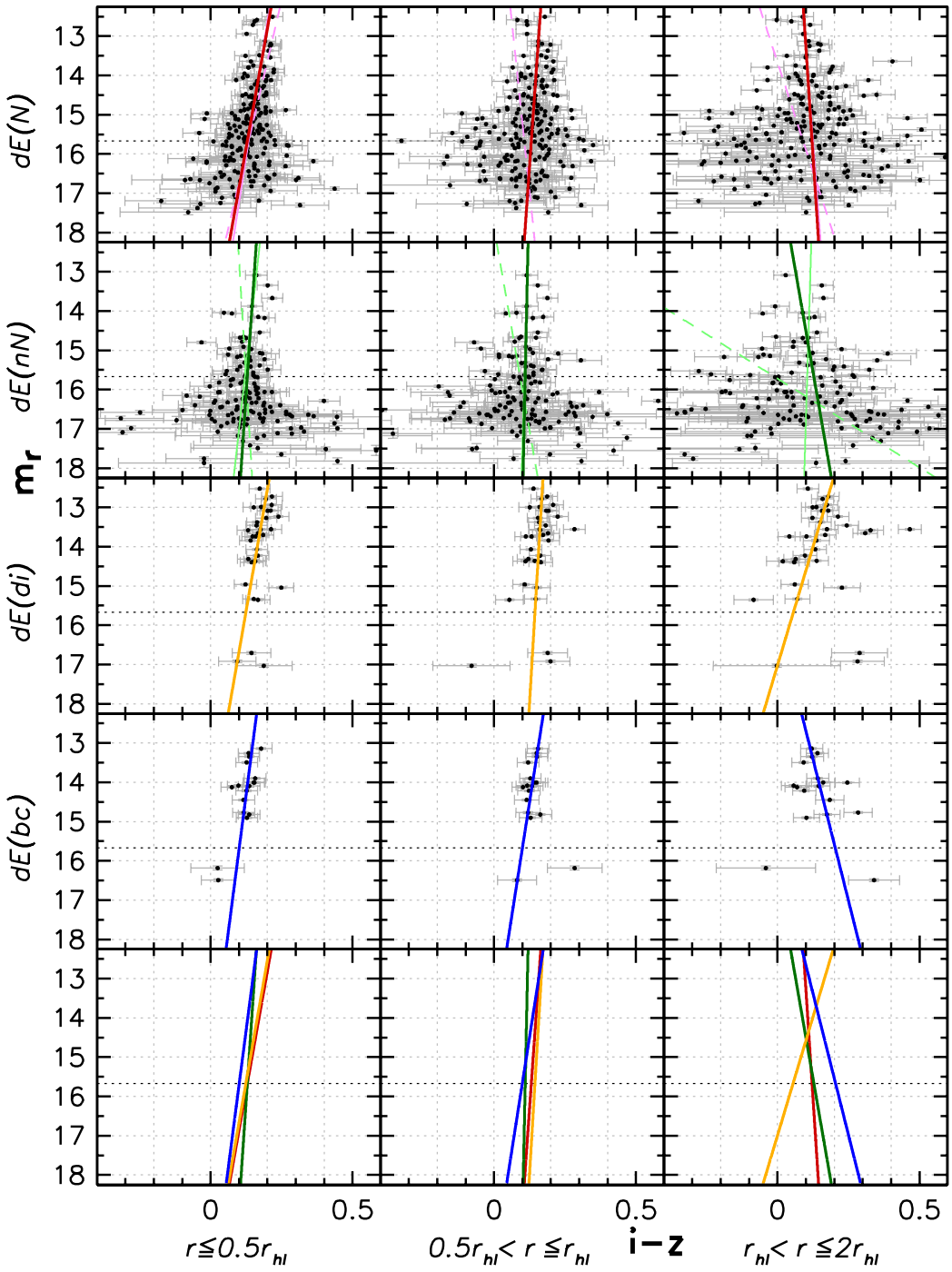

F 5.10. **Colour-magnitude relations of dE subclasses.** Same as Figure 5.7, but for $i - z$ colour.

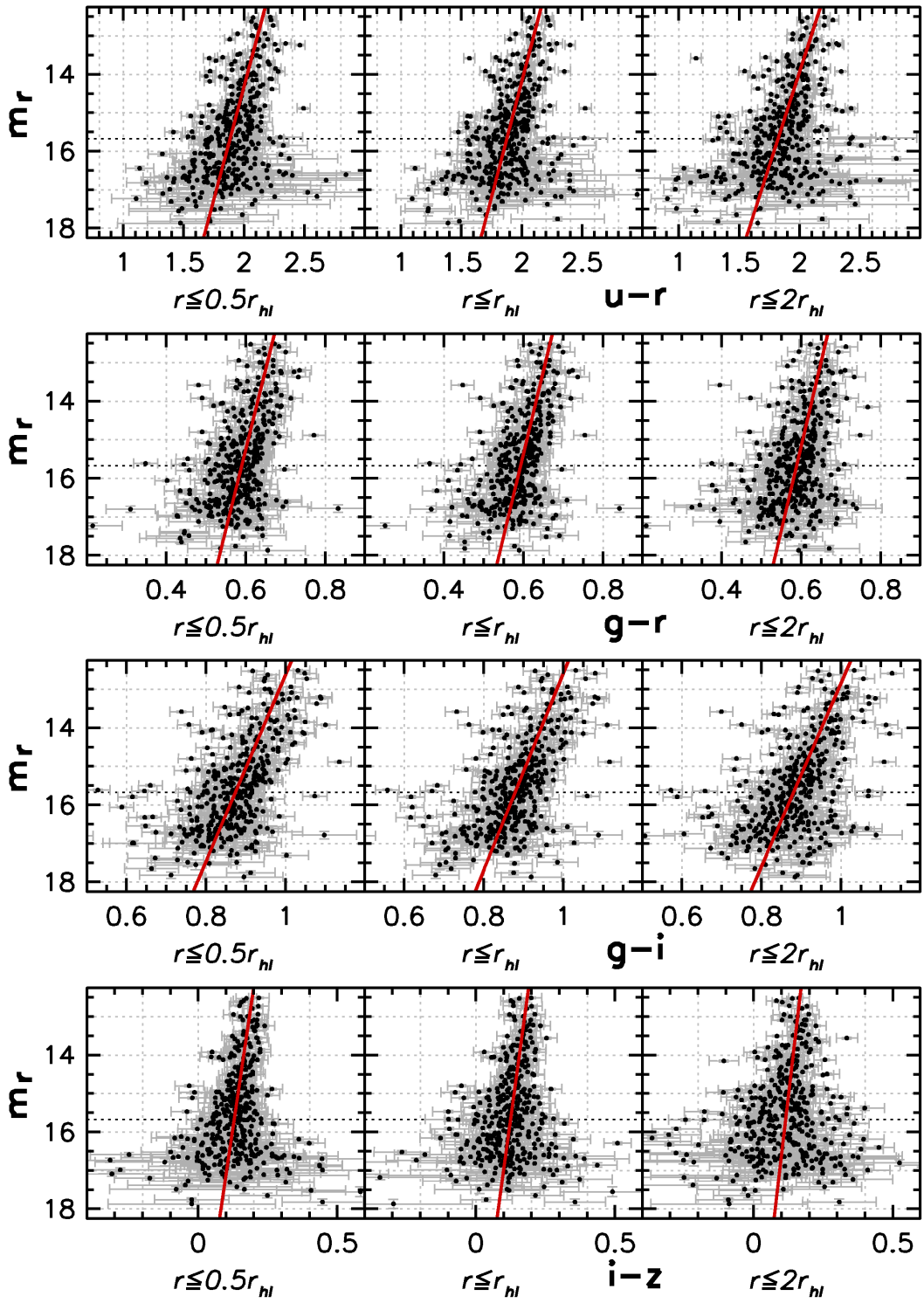

F 5.11. **Colour-magnitude relations of the full dE sample.** Shown are the relations of *r* magnitude with various colours (different rows) for the full dE sample, excluding dE(bc)s, for our three aperture sizes (different columns), along with their respective linear fits.

Let us first focus on the dE(bc)s. From Chapter 3, we would expect that the colours beyond $a > 0.5\,a_{\rm hl,r}$ are, on average, only slightly affected by the positive central colour gradient, and that the colours are not noticeably affected beyond $a > a_{\rm hl,r}$. However, in all of $u-r$, $g-r$, and $g-i$, the dE(bc)s are somewhat bluer than the other dE subclasses. Note that no precise statements can be made about the slope of their CMR, since it is constrained at the faint end by only two data points. Nevertheless, it can be seen that the scatter in $g-r$ and $g-i$ is somewhat larger than that of the other subclasses at the same magnitudes. This is confirmed by the respective values of the RMS scatter, which are larger by a factor of ∼1.5 for the dE(bc)s. In contrast, the dE(bc)s follow a surprisingly tight relation in $i-z$ within $a < a_{\rm hl,r}$. In the bin $0.5\,a_{\rm hl,r} < a \leq a_{\rm hl,r}$, the scatter is more than a factor of two lower than the RMS of the measurement errors[3] (see Table 5.1), and likewise, it is lower than the scatter of all other subclasses in this bin. At larger radii, the relation seems to turn around, i.e., such that brighter galaxies are bluer, but again, the small sample size does not allow robust conclusions. Nevertheless, a trend for the CMR to turn around is also seen for the dE(N)s and the dE(nN)s.

We now move on to the dE(di)s, considering here and in the following only the CMRs with cumulative radial bins (Figures 5.3 to 5.6), i.e., with apertures of increasing size, as explained above. Similar to the dE(bc)s, the CMR of the dE(di)s is constrained at the faint end by only three data points; we therefore concentrate on the brighter part of their and the comparison samples. In all of $u-r$, $g-r$, and $g-i$, their CMR is similar to that of the dE(N)s, but is always slightly bluer. According to our statistical tests, as described in Section 6 and presented in Table 5.2, this small difference is nevertheless significant in $g-i$: for all apertures, the probability of a common underlying distribution function[4] with the bright dE(N)s is ≤1.2%. For the small and intermediate apertures of $g-r$, it is ≤2.3%, and for the small aperture of $u-r$ it is still ≤4.4%. As stressed in Section 6, these values should be taken with a grain of salt, since the linear fit to the dE(di)s is partly constrained by just a few data points at the faint end, and since the sample is of only moderate size. Nevertheless, the slight blueward offset of the dE(di)s from the dE(N)s is consistently seen in all the above bands. In $i-z$, however, the dE(di)s basically follow the same relation as the dE(N)s within $a \leq a_{\rm hl,r}$. At larger radii they are slightly redder, but the difference is not significant (see Table 5.2).

The dE(nN)s follow a steeper CMR than the dE(N)s or the dE(di)s in all colours and apertures, including $i-z$ even though the difference is small there. They lie at about the same colour values at the faint end of the sample, but become red less strongly with increasing magnitude. The difference between the CMRs of the dE(nN)s and the dE(N)s is significant in all apertures of $g-r$ (probability of common distribution ≤0.5%) and $g-i$ (0.0%). It is, however, not significant in $i-z$ (≥15%), and hardly significant in $u-r$ (≤9%).

We need to point out, though, that we found significant differences in both the shapes and the distributions of faint and bright dE(nN)s (see Chapter 4). It might thus be not appropriate to fit a single CMR through their combined sample. Indeed, differences in the colour distributions of both samples can be seen. In $u-r$, most clearly in the large aperture, there appears to be a discontinuity between the faint and the bright dE(nN)s, with the latter being offset blueward. This break happens to occur at about our dividing magnitude between faint and bright objects. A similar effect can be seen for the small aperture of the $g-i$ colour, where again, several bright dE(nN)s seem to be offset towards bluer colours, but also, a number of objects lie redward of the colours of the faint dE(nN)s, again forming some sort of discontinuity. It seems thus more reasonable to consider faint and bright dE(nN)s separately. Note that Conselice et al. (2003a) observed a somewhat similar effect for their *full* sample of early-type dwarfs in the Perseus cluster, namely a considerable increase in the colour scatter when going to fainter magnitudes, possibly even forming a blue and a red sequence of galaxies. However, their effect is stronger than what we observe, and it is also not present for our dE(N)s.

[3] This, along with the tight relation of the dE(di)s, confirms that we did not underestimate our photometric errors

[4] While we always consider the probabilities from both the K-S test and the t-test, we recall that the t-test compares the *means* of the residuals about the CMR, not the distributions themselves. For simplicity, though, we shall continue speaking of the "probability of a common underlying distribution".

T 5.1. **Colour-magnitude relation parameters.** Results from the linear fits to the CMRs. "Zero" denotes the zeropoint, "RMS" is the root mean square of the colour residuals of our data points about the CMR fit, "E-RMS" is the root mean square of the colour errors, and "Ratio" is the ratio of RMS and E-RMS.

T	C	A	Z	S	RMS	E-RMS	R
dE(N)	$u-r$	small	3.451	−0.0986	0.146	0.139	1.046
dE(N)	$u-r$	interm.	3.168	−0.0810	0.127	0.102	1.236
dE(N)	$u-r$	large	3.299	−0.0922	0.177	0.113	1.567
dE(N)	$g-r$	small	1.008	−0.0258	0.040	0.035	1.150
dE(N)	$g-r$	interm.	0.996	−0.0253	0.033	0.032	1.017
dE(N)	$g-r$	large	0.931	−0.0212	0.045	0.034	1.341
dE(N)	$g-i$	small	1.593	−0.0450	0.050	0.035	1.429
dE(N)	$g-i$	interm.	1.549	−0.0421	0.045	0.033	1.395
dE(N)	$g-i$	large	1.581	−0.0441	0.062	0.034	1.797
dE(N)	$i-z$	small	0.516	−0.0246	0.066	0.067	0.990
dE(N)	$i-z$	interm.	0.437	−0.0200	0.066	0.056	1.168
dE(N)	$i-z$	large	0.262	−0.0086	0.103	0.060	1.706
dE(nN)	$u-r$	small	2.558	−0.0470	0.225	0.224	1.004
dE(nN)	$u-r$	interm.	2.789	−0.0616	0.255	0.165	1.548
dE(nN)	$u-r$	large	2.896	−0.0731	0.317	0.193	1.641
dE(nN)	$g-r$	small	0.778	−0.0134	0.055	0.044	1.253
dE(nN)	$g-r$	interm.	0.711	−0.0095	0.056	0.038	1.488
dE(nN)	$g-r$	large	0.747	−0.0117	0.068	0.042	1.642
dE(nN)	$g-i$	small	1.230	−0.0246	0.070	0.044	1.565
dE(nN)	$g-i$	interm.	1.268	−0.0265	0.067	0.038	1.741
dE(nN)	$g-i$	large	1.305	−0.0285	0.074	0.042	1.764
dE(nN)	$i-z$	small	0.276	−0.0093	0.104	0.096	1.080
dE(nN)	$i-z$	interm.	0.194	−0.0046	0.106	0.075	1.424
dE(nN)	$i-z$	large	0.098	0.0003	0.159	0.095	1.665
dE(di)	$u-r$	small	3.469	−0.1047	0.150	0.062	2.433
dE(di)	$u-r$	interm.	2.924	−0.0660	0.119	0.056	2.138
dE(di)	$u-r$	large	2.695	−0.0501	0.145	0.059	2.440
dE(di)	$g-r$	small	0.970	−0.0252	0.035	0.030	1.185
dE(di)	$g-r$	interm.	0.981	−0.0261	0.034	0.030	1.151
dE(di)	$g-r$	large	0.997	−0.0270	0.030	0.030	1.013
dE(di)	$g-i$	small	1.609	−0.0493	0.056	0.030	1.876
dE(di)	$g-i$	interm.	1.603	−0.0481	0.052	0.030	1.770
dE(di)	$g-i$	large	1.727	−0.0566	0.055	0.030	1.826
dE(di)	$i-z$	small	0.503	−0.0241	0.024	0.040	0.585
dE(di)	$i-z$	interm.	0.397	−0.0167	0.033	0.042	0.784
dE(di)	$i-z$	large	0.539	−0.0275	0.059	0.044	1.358

A comparison of the CMRs of bright and faint dE(nN)s (thin solid and dashed dark green lines in Figures 5.3 to 5.6) with each other indeed yields a probability of ≤0.2% for the small $g-i$ aperture for a common underlying distribution, and of also ≤0.2% for the small $u-r$ aperture. The difference is less pronounced for the intermediate $u-r$ aperture (≤6.2%), but still quite significant for the large $u-r$ aperture (≤2.4%). One caveat, though, that needs to be kept in mind here is the accuracy with which a straight line can be fitted to the data points at all: for both bright and faint dE(nN)s, the scatter is rather large — it is typically larger by ∼1.5 than that of the respective dE(N) subsample (Table 5.1).

T 5.1. ***Continued.***

T	C	A	Z	S	RMS	E-RMS	R
$dE(N)_{bri.}$	$u-r$	small	3.430	−0.0969	0.115	0.071	1.630
$dE(N)_{bri.}$	$u-r$	interm.	3.084	−0.0747	0.105	0.062	1.684
$dE(N)_{bri.}$	$u-r$	large	3.301	−0.0923	0.129	0.072	1.794
$dE(N)_{bri.}$	$g-r$	small	1.005	−0.0256	0.036	0.030	1.198
$dE(N)_{bri.}$	$g-r$	interm.	0.989	−0.0248	0.033	0.030	1.095
$dE(N)_{bri.}$	$g-r$	large	0.892	−0.0184	0.039	0.030	1.277
$dE(N)_{bri.}$	$g-i$	small	1.617	−0.0469	0.050	0.030	1.644
$dE(N)_{bri.}$	$g-i$	interm.	1.593	−0.0450	0.044	0.030	1.455
$dE(N)_{bri.}$	$g-i$	large	1.629	−0.0474	0.047	0.031	1.535
$dE(N)_{bri.}$	$i-z$	small	0.473	−0.0217	0.038	0.043	0.887
$dE(N)_{bri.}$	$i-z$	interm.	0.415	−0.0183	0.051	0.042	1.227
$dE(N)_{bri.}$	$i-z$	large	0.303	−0.0115	0.079	0.045	1.771
$dE(nN)_{bri.}$	$u-r$	small	3.124	−0.0853	0.151	0.065	2.306
$dE(nN)_{bri.}$	$u-r$	interm.	2.777	−0.0640	0.166	0.064	2.599
$dE(nN)_{bri.}$	$u-r$	large	3.010	−0.0818	0.176	0.066	2.655
$dE(nN)_{bri.}$	$g-r$	small	1.188	−0.0410	0.045	0.030	1.497
$dE(nN)_{bri.}$	$g-r$	interm.	1.244	−0.0448	0.041	0.030	1.365
$dE(nN)_{bri.}$	$g-r$	large	1.022	−0.0301	0.041	0.031	1.326
$dE(nN)_{bri.}$	$g-i$	small	1.940	−0.0728	0.065	0.030	2.146
$dE(nN)_{bri.}$	$g-i$	interm.	1.688	−0.0549	0.059	0.030	1.972
$dE(nN)_{bri.}$	$g-i$	large	1.541	−0.0445	0.060	0.031	1.957
$dE(nN)_{bri.}$	$i-z$	small	0.364	−0.0155	0.042	0.044	0.962
$dE(nN)_{bri.}$	$i-z$	interm.	0.231	−0.0069	0.053	0.042	1.261
$dE(nN)_{bri.}$	$i-z$	large	0.081	0.0016	0.087	0.045	1.925
$dE(N)_{fai.}$	$u-r$	small	2.932	−0.0661	0.197	0.204	0.968
$dE(N)_{fai.}$	$u-r$	interm.	2.670	−0.0509	0.160	0.150	1.070
$dE(N)_{fai.}$	$u-r$	large	2.683	−0.0549	0.244	0.183	1.339
$dE(N)_{fai.}$	$g-r$	small	0.671	−0.0055	0.045	0.040	1.141
$dE(N)_{fai.}$	$g-r$	interm.	0.781	−0.0121	0.038	0.036	1.065
$dE(N)_{fai.}$	$g-r$	large	0.724	−0.0087	0.051	0.038	1.347
$dE(N)_{fai.}$	$g-i$	small	1.321	−0.0281	0.050	0.041	1.216
$dE(N)_{fai.}$	$g-i$	interm.	1.269	−0.0252	0.049	0.036	1.343
$dE(N)_{fai.}$	$g-i$	large	1.221	−0.0222	0.075	0.039	1.925
$dE(N)_{fai.}$	$i-z$	small	0.641	−0.0323	0.096	0.090	1.066
$dE(N)_{fai.}$	$i-z$	interm.	0.111	0.0000	0.088	0.071	1.237
$dE(N)_{fai.}$	$i-z$	large	0.205	−0.0052	0.136	0.081	1.682
$dE(nN)_{fai.}$	$u-r$	small	4.323	−0.1532	0.238	0.260	0.915
$dE(nN)_{fai.}$	$u-r$	interm.	4.788	−0.1832	0.283	0.189	1.500
$dE(nN)_{fai.}$	$u-r$	large	5.217	−0.2135	0.358	0.228	1.568
$dE(nN)_{fai.}$	$g-r$	small	0.835	−0.0166	0.058	0.047	1.215
$dE(nN)_{fai.}$	$g-r$	interm.	1.142	−0.0355	0.060	0.040	1.506
$dE(nN)_{fai.}$	$g-r$	large	0.813	−0.0155	0.076	0.045	1.703
$dE(nN)_{fai.}$	$g-i$	small	1.587	−0.0458	0.072	0.049	1.474
$dE(nN)_{fai.}$	$g-i$	interm.	1.633	−0.0487	0.072	0.041	1.764
$dE(nN)_{fai.}$	$g-i$	large	1.155	−0.0191	0.077	0.045	1.709
$dE(nN)_{fai.}$	$i-z$	small	−0.006	0.0083	0.123	0.110	1.119
$dE(nN)_{fai.}$	$i-z$	interm.	−0.137	0.0155	0.138	0.089	1.554
$dE(nN)_{fai.}$	$i-z$	large	−1.142	0.0766	0.181	0.108	1.673

T 5.1. ***Continued.***

T	C	A	Z	S	RMS	E-RMS	R
dE(bc)	$u-r$	small	4.911	−0.2251	0.184	0.049	3.771
dE(bc)	$u-r$	sm.→in.	3.145	−0.0915	0.097	0.068	1.442
dE(bc)	$u-r$	interm.	3.463	−0.1169	0.135	0.057	2.388
dE(bc)	$u-r$	in.→la.	4.773	−0.2101	0.155	0.073	2.106
dE(bc)	$u-r$	large	4.445	−0.1879	0.127	0.050	2.533
dE(bc)	$g-r$	small	0.789	−0.0198	0.078	0.030	2.576
dE(bc)	$g-r$	sm.→in.	0.640	−0.0048	0.056	0.031	1.804
dE(bc)	$g-r$	interm.	0.727	−0.0127	0.066	0.030	2.198
dE(bc)	$g-r$	in.→la.	0.759	−0.0132	0.049	0.034	1.429
dE(bc)	$g-r$	large	0.607	−0.0035	0.058	0.030	1.930
dE(bc)	$g-i$	small	1.175	−0.0295	0.116	0.030	3.811
dE(bc)	$g-i$	sm.→in.	1.347	−0.0349	0.080	0.032	2.528
dE(bc)	$g-i$	interm.	1.230	−0.0296	0.094	0.030	3.121
dE(bc)	$g-i$	in.→la.	1.352	−0.0338	0.058	0.035	1.649
dE(bc)	$g-i$	large	1.270	−0.0304	0.078	0.030	2.556
dE(bc)	$i-z$	small	0.382	−0.0180	0.030	0.045	0.670
dE(bc)	$i-z$	sm.→in.	0.439	−0.0216	0.017	0.042	0.408
dE(bc)	$i-z$	interm.	0.380	−0.0177	0.019	0.039	0.482
dE(bc)	$i-z$	in.→la.	−0.340	0.0347	0.062	0.047	1.306
dE(bc)	$i-z$	large	0.028	0.0081	0.033	0.044	0.750
dE	$u-r$	small	3.213	−0.0848	0.179	0.172	1.042
dE	$u-r$	interm.	3.176	−0.0830	0.186	0.128	1.459
dE	$u-r$	large	3.425	−0.1023	0.238	0.145	1.646
dE	$g-r$	small	0.966	−0.0240	0.049	0.038	1.283
dE	$g-r$	interm.	0.957	−0.0233	0.047	0.034	1.362
dE	$g-r$	large	0.946	−0.0228	0.053	0.036	1.461
dE	$g-i$	small	1.521	−0.0413	0.062	0.039	1.611
dE	$g-i$	interm.	1.492	−0.0391	0.058	0.035	1.684
dE	$g-i$	large	1.539	−0.0420	0.069	0.037	1.858
dE	$i-z$	small	0.448	−0.0204	0.072	0.076	0.946
dE	$i-z$	interm.	0.420	−0.0189	0.078	0.061	1.275
dE	$i-z$	large	0.367	−0.0161	0.119	0.074	1.597

For example, in $g-i$, it seems to the eye that one could find a number of slightly different lines that would fit the data points equally well. The linear fits to the CMRs of faint and bright dE(nN)s thus need to be taken with a grain of salt — but obviously, there are some differences between the colours of these datasets.

Given the above considerations, we should consequently reiterate on our comparison of dE(N)s and dE(nN)s. A comparison of bright dE(N)s and bright dE(nN)s yields an even more pronounced difference than what was found for the full samples: their probability for a common underlying distribution is 0.0% in all of $u-r$, $g-r$, and $g-i$. In $i-z$, the difference is still not significant, with probabilities $\geq$6.7%. For the faint subsamples of dE(nN)s and dE(N)s, a comparison only yields significant differences for the small and intermediate apertures of $g-r$ and $g-i$, with probabilities of $\leq$1.6% and $\leq$3.6%, respectively. Note that, while the linear fits to the full sample of dE(nN)s yielded CMRs that are steeper than those of the dE(N)s, this is not anymore the case for the separate examination of bright and faint subsamples — instead, the difference is now mainly a difference of the zeropoint of the relations.

T 5.2. **Statistical comparisons of CMRs of different subclasses.** We compare the CMRs of a pair of dE subclasses (1st and 2nd column) for a given colour (3rd column) and aperture (4th column). Probabilities for a common underlying distribution are derived from a K-S test (5th column) and a Student's t-test for unequal variances (6th column); see text for details. The corresponding CMRs are shown in Figures 5.3 to Figures 5.6.

T 1	T 2	C	A	K-S	-
dE(N)	dE(nN)	$u-r$	small	0.00%	8.55%
dE(N)	dE(nN)	$u-r$	interm.	0.00	6.02
dE(N)	dE(nN)	$u-r$	large	0.02	9.10
dE(N)	dE(nN)	$g-r$	small	0.00	0.00
dE(N)	dE(nN)	$g-r$	interm.	0.00	0.00
dE(N)	dE(nN)	$g-r$	large	0.00	0.04
dE(N)	dE(nN)	$g-i$	small	0.00	0.01
dE(N)	dE(nN)	$g-i$	interm.	0.00	0.00
dE(N)	dE(nN)	$g-i$	large	0.00	0.53
dE(N)	dE(nN)	$i-z$	small	15.29	68.98
dE(N)	dE(nN)	$i-z$	interm.	16.48	68.92
dE(N)	dE(nN)	$i-z$	large	15.89	29.76
dE(N)	dE(di)	$u-r$	small	0.33	1.69
dE(N)	dE(di)	$u-r$	interm.	14.86	27.66
dE(N)	dE(di)	$u-r$	large	15.43	80.99
dE(N)	dE(di)	$g-r$	small	1.17	2.28
dE(N)	dE(di)	$g-r$	interm.	0.40	1.00
dE(N)	dE(di)	$g-r$	large	3.50	11.25
dE(N)	dE(di)	$g-i$	small	0.05	0.38
dE(N)	dE(di)	$g-i$	interm.	0.03	0.92
dE(N)	dE(di)	$g-i$	large	0.74	1.60
dE(N)	dE(di)	$i-z$	small	3.89	59.39
dE(N)	dE(di)	$i-z$	interm.	0.66	16.25
dE(N)	dE(di)	$i-z$	large	1.07	48.83
dE(nN)	dE(di)	$u-r$	small	1.99	25.19
dE(nN)	dE(di)	$u-r$	interm.	2.80	37.77
dE(nN)	dE(di)	$u-r$	large	0.07	50.74
dE(nN)	dE(di)	$g-r$	small	8.60	37.56
dE(nN)	dE(di)	$g-r$	interm.	2.90	67.77
dE(nN)	dE(di)	$g-r$	large	4.59	87.08
dE(nN)	dE(di)	$g-i$	small	11.43	39.27
dE(nN)	dE(di)	$g-i$	interm.	11.52	53.16
dE(nN)	dE(di)	$g-i$	large	3.04	10.28
dE(nN)	dE(di)	$i-z$	small	1.16	40.18
dE(nN)	dE(di)	$i-z$	interm.	0.02	8.62
dE(nN)	dE(di)	$i-z$	large	0.11	41.91

In order to further quantify the above considerations, one would want to compare average colour values of the subsamples. The problem with this approach is that the samples are not distributed equally in magnitude; the average colours could thus come out different just because of the existence of a colour-magnitude relation (also see Section 6 of Chapter 4). Therefore, we compare instead the colour values of the linear fits to the CMRs at a fixed magnitude. We choose two magnitude values for this comparison, namely the median r magnitude of our bright dEs, $m_{\mathrm{r,bri.}} = 14\overset{\mathrm{m}}{.}77$, and the median

T 5.2. ***Continued.***

T 1	T 2	C	A	K-S	-
$dE(N)_{bri.}$	$dE(nN)_{bri.}$	$u-r$	small	0.00%	0.00%
$dE(N)_{bri.}$	$dE(nN)_{bri.}$	$u-r$	interm.	0.01	0.02
$dE(N)_{bri.}$	$dE(nN)_{bri.}$	$u-r$	large	0.00	0.01
$dE(N)_{bri.}$	$dE(nN)_{bri.}$	$g-r$	small	0.00	0.00
$dE(N)_{bri.}$	$dE(nN)_{bri.}$	$g-r$	interm.	0.00	0.00
$dE(N)_{bri.}$	$dE(nN)_{bri.}$	$g-r$	large	0.00	0.00
$dE(N)_{bri.}$	$dE(nN)_{bri.}$	$g-i$	small	0.00	0.00
$dE(N)_{bri.}$	$dE(nN)_{bri.}$	$g-i$	interm.	0.00	0.00
$dE(N)_{bri.}$	$dE(nN)_{bri.}$	$g-i$	large	0.00	0.00
$dE(N)_{bri.}$	$dE(nN)_{bri.}$	$i-z$	small	15.32	6.68
$dE(N)_{bri.}$	$dE(nN)_{bri.}$	$i-z$	interm.	14.63	13.93
$dE(N)_{bri.}$	$dE(nN)_{bri.}$	$i-z$	large	42.50	22.87
$dE(N)_{fai.}$	$dE(nN)_{fai.}$	$u-r$	small	53.95	80.60
$dE(N)_{fai.}$	$dE(nN)_{fai.}$	$u-r$	interm.	11.50	66.40
$dE(N)_{fai.}$	$dE(nN)_{fai.}$	$u-r$	large	36.85	88.30
$dE(N)_{fai.}$	$dE(nN)_{fai.}$	$g-r$	small	1.64	1.44
$dE(N)_{fai.}$	$dE(nN)_{fai.}$	$g-r$	interm.	0.04	1.32
$dE(N)_{fai.}$	$dE(nN)_{fai.}$	$g-r$	large	2.41	9.56
$dE(N)_{fai.}$	$dE(nN)_{fai.}$	$g-i$	small	1.00	3.59
$dE(N)_{fai.}$	$dE(nN)_{fai.}$	$g-i$	interm.	0.01	2.44
$dE(N)_{fai.}$	$dE(nN)_{fai.}$	$g-i$	large	18.38	18.10
$dE(N)_{fai.}$	$dE(nN)_{fai.}$	$i-z$	small	11.89	29.63
$dE(N)_{fai.}$	$dE(nN)_{fai.}$	$i-z$	interm.	54.26	69.48
$dE(N)_{fai.}$	$dE(nN)_{fai.}$	$i-z$	large	38.78	56.16
$dE(N)_{bri.}$	dE(di)	$u-r$	small	1.25	4.41
$dE(N)_{bri.}$	dE(di)	$u-r$	interm.	17.54	26.28
$dE(N)_{bri.}$	dE(di)	$u-r$	large	38.14	39.48
$dE(N)_{bri.}$	dE(di)	$g-r$	small	1.57	2.29
$dE(N)_{bri.}$	dE(di)	$g-r$	interm.	0.99	1.68
$dE(N)_{bri.}$	dE(di)	$g-r$	large	3.40	9.96
$dE(N)_{bri.}$	dE(di)	$g-i$	small	0.16	0.43
$dE(N)_{bri.}$	dE(di)	$g-i$	interm.	0.16	0.63
$dE(N)_{bri.}$	dE(di)	$g-i$	large	0.30	1.19
$dE(N)_{bri.}$	dE(di)	$i-z$	small	20.50	33.54
$dE(N)_{bri.}$	dE(di)	$i-z$	interm.	2.54	7.85
$dE(N)_{bri.}$	dE(di)	$i-z$	large	6.90	22.01
$dE(nN)_{bri.}$	dE(di)	$u-r$	small	1.59	5.05
$dE(nN)_{bri.}$	dE(di)	$u-r$	interm.	0.80	1.66
$dE(nN)_{bri.}$	dE(di)	$u-r$	large	0.02	4.19
$dE(nN)_{bri.}$	dE(di)	$g-r$	small	14.73	23.50
$dE(nN)_{bri.}$	dE(di)	$g-r$	interm.	28.77	53.23
$dE(nN)_{bri.}$	dE(di)	$g-r$	large	5.80	9.56
$dE(nN)_{bri.}$	dE(di)	$g-i$	small	34.24	69.83
$dE(nN)_{bri.}$	dE(di)	$g-i$	interm.	24.96	20.48
$dE(nN)_{bri.}$	dE(di)	$g-i$	large	61.96	33.95
$dE(nN)_{bri.}$	dE(di)	$i-z$	small	2.77	2.19
$dE(nN)_{bri.}$	dE(di)	$i-z$	interm.	0.26	0.49
$dE(nN)_{bri.}$	dE(di)	$i-z$	large	1.98	6.64

T 5.2. ***Continued.***

T 1	T 2	C	A	K-S	-
$dE(N)_{bri.}$	$dE(N)_{fai.}$	$u-r$	small	6.68%	36.24%
$dE(N)_{bri.}$	$dE(N)_{fai.}$	$u-r$	interm.	4.96	63.61
$dE(N)_{bri.}$	$dE(N)_{fai.}$	$u-r$	large	4.75	69.74
$dE(N)_{bri.}$	$dE(N)_{fai.}$	$g-r$	small	0.66	95.73
$dE(N)_{bri.}$	$dE(N)_{fai.}$	$g-r$	interm.	2.15	80.19
$dE(N)_{bri.}$	$dE(N)_{fai.}$	$g-r$	large	0.69	9.88
$dE(N)_{bri.}$	$dE(N)_{fai.}$	$g-i$	small	8.64	55.09
$dE(N)_{bri.}$	$dE(N)_{fai.}$	$g-i$	interm.	4.73	62.36
$dE(N)_{bri.}$	$dE(N)_{fai.}$	$g-i$	large	0.36	53.62
$dE(N)_{bri.}$	$dE(N)_{fai.}$	$i-z$	small	0.20	95.15
$dE(N)_{bri.}$	$dE(N)_{fai.}$	$i-z$	interm.	0.54	80.55
$dE(N)_{bri.}$	$dE(N)_{fai.}$	$i-z$	large	1.82	55.91
$dE(nN)_{bri.}$	$dE(nN)_{fai.}$	$u-r$	small	0.00	0.18
$dE(nN)_{bri.}$	$dE(nN)_{fai.}$	$u-r$	interm.	0.03	6.17
$dE(nN)_{bri.}$	$dE(nN)_{fai.}$	$u-r$	large	0.00	2.40
$dE(nN)_{bri.}$	$dE(nN)_{fai.}$	$g-r$	small	1.13	26.22
$dE(nN)_{bri.}$	$dE(nN)_{fai.}$	$g-r$	interm.	0.00	0.01
$dE(nN)_{bri.}$	$dE(nN)_{fai.}$	$g-r$	large	1.32	20.46
$dE(nN)_{bri.}$	$dE(nN)_{fai.}$	$g-i$	small	0.00	0.25
$dE(nN)_{bri.}$	$dE(nN)_{fai.}$	$g-i$	interm.	0.06	0.11
$dE(nN)_{bri.}$	$dE(nN)_{fai.}$	$g-i$	large	13.20	68.00
$dE(nN)_{bri.}$	$dE(nN)_{fai.}$	$i-z$	small	3.01	62.11
$dE(nN)_{bri.}$	$dE(nN)_{fai.}$	$i-z$	interm.	7.22	84.35
$dE(nN)_{bri.}$	$dE(nN)_{fai.}$	$i-z$	large	0.40	34.04

r magnitude of our faint dEs, $m_{r,fai.} = 16\overset{m}{.}51$ (which we refer to hereafter as the bright and faint "reference magnitude", respectively). The corresponding colour values for the different subclasses and colours are given in Tables 5.3 and 5.4.

The values so derived confirm our above comparisons of the various CMRs: the dE(N)s are redder than the dE(nN)s in $u-r$, $g-r$, and $g-i$ at both the bright and the faint reference magnitudes, with the difference being smaller for the latter. In $i-z$, the dE(N)s are still redder at the bright reference magnitude, whereas no clear difference is present at the faint reference magnitude, also given the rather large scatter of the CMR. These statements hold true also for the separate comparison of the bright and faint subsamples, with the exception that the faint dE(nN)s tend to be somewhat redder than the faint dE(N)s in $i-z$. The dE(di)s, which we consider only at the bright reference magnitude, are intermediate between the (bright) dE(nN)s and the (bright) dE(N)s in $u-r$, $g-r$, and $g-i$. In $i-z$, their colours are very similar to those of the (bright) dE(N)s, again confirming our above analysis of the CMRs. In Section 12, we will attempt to interpret these colour values in terms of age and/or metallicity differences.

8. C -

Tables 5.3 and 5.4 can also be used to compare the behaviour of the CMR of a given dE subsample with aperture size. Both the bright dE(N)s and the bright dE(nN)s become, on average, slightly bluer in $u-r$ and in $i-z$ with increasing aperture size. The faint dE(N)s and dE(nN)s still follow this trend in $u-r$, while in $i-z$, it becomes less clear for the faint dE(nN)s, and even turns around for the faint dE(N)s (the considerable scatter of the CMR needs to be kept in mind though). In contrast, the

T 5.3. **Colour comparison of the dE subclasses.** Colour values of the CMRs at the bright reference magnitude, $m_{\mathrm{r,bri.}} = 14\overset{\mathrm{m}}{.}77$ (see text), for the three different apertures (2nd column).

Colour	Aperture	dE(N)	dE(nN)	dE(di)	dE(bc)	dE	$\mathrm{dE(N)_{bri.}}$	$\mathrm{dE(nN)_{bri.}}$
$u-r$	small	1.995	1.863	1.922	1.585	1.960	1.999	1.864
$u-r$	interm.	1.971	1.879	1.950	1.736	1.950	1.980	1.832
$u-r$	large	1.938	1.817	1.956	1.669	1.914	1.937	1.802
$g-r$	small	0.627	0.580	0.598	0.497	0.611	0.627	0.583
$g-r$	interm.	0.622	0.571	0.596	0.540	0.613	0.623	0.582
$g-r$	large	0.618	0.574	0.599	0.556	0.608	0.620	0.578
$g-i$	small	0.929	0.867	0.881	0.739	0.911	0.925	0.865
$g-i$	interm.	0.928	0.876	0.892	0.793	0.914	0.929	0.878
$g-i$	large	0.930	0.884	0.891	0.820	0.918	0.928	0.883
$i-z$	small	0.152	0.138	0.146	0.117	0.148	0.154	0.135
$i-z$	interm.	0.142	0.127	0.150	0.119	0.141	0.145	0.128
$i-z$	large	0.135	0.103	0.132	0.148	0.129	0.133	0.105

T 5.4. **Colour comparison of the dE subclasses.** Colour values of the CMRs at the faint reference magnitude, $m_{\mathrm{r,fai.}} = 16\overset{\mathrm{m}}{.}51$ (see text), for the three different apertures (2nd column).

Colour	Aperture	dE(N)	dE(nN)	dE(di)	dE(bc)	dE	$\mathrm{dE(N)_{fai.}}$	$\mathrm{dE(nN)_{fai.}}$
$u-r$	small	1.823	1.781	1.740	1.193	1.812	1.839	1.794
$u-r$	interm.	1.830	1.772	1.835	1.532	1.806	1.829	1.762
$u-r$	large	1.777	1.690	1.868	1.341	1.736	1.775	1.691
$g-r$	small	0.582	0.557	0.554	0.463	0.569	0.581	0.561
$g-r$	interm.	0.578	0.555	0.551	0.518	0.573	0.581	0.556
$g-r$	large	0.581	0.554	0.552	0.550	0.569	0.581	0.557
$g-i$	small	0.850	0.824	0.795	0.688	0.839	0.857	0.831
$g-i$	interm.	0.855	0.830	0.808	0.741	0.846	0.852	0.829
$g-i$	large	0.853	0.835	0.792	0.767	0.845	0.854	0.840
$i-z$	small	0.109	0.121	0.104	0.086	0.112	0.107	0.132
$i-z$	interm.	0.107	0.119	0.121	0.088	0.108	0.111	0.118
$i-z$	large	0.120	0.103	0.084	0.162	0.101	0.119	0.123

dE(di)s become, on average, slightly *redder* in $u-r$ with increasing aperture size. However, in $i-z$, they become slightly bluer, similar to the bright dE(N)s and dE(nN)s.

All these differences with aperture size are not overly large; they are typically less than half of the RMS scatter of the respective CMRs. According to our statistical comparisons of the inner and outer (cumulative!) CMRs of each subclass (Table 5.5), significant differences only occur for the (bright) dE(N)s in $u-r$ and $i-z$ (probabilities for a common underlying distribution $\leq$2.2% and $\leq$2.9%, respectively), as well as for the full sample of dE(nN)s in $i-z$ ($\leq$3.8%). Interestingly, the differences described above in $u-r$ and $i-z$ for the bright dE(nN)s are not or only marginally significant (probabilities $\geq$16.9% and $\geq$9.8%, respectively). This is presumably due to the only moderate sample size of the bright dE(nN)s, and the comparably large scatter of their CMRs (see Section 7).

In $g-r$ and $g-i$, practically no change of the CMRs with aperture size is seen (apart from the dE(bc)s of course). The colour values (Tables 5.3 and 5.4) remain surprisingly constant, given the gradients seen in both $u-r$ and $i-z$. The "strongest" effect is the change of the bright dE(nN)s in $g-i$ of 0.02 — far from being significant though (Table 5.5). The fact that gradients are seen in $u-r$, but not in $g-r$, shows that the $u-r$ colour does provide information beyond that contained in $g-r$.

T 5.5. **Statistical comparisons of CMRs for different apertures.** For a given dE subclass (1st column) and colour (2nd column), we compare the CMRs based on the small and the large aperture, to see whether systematic radial gradients are present. Probabilities for a common underlying distribution are derived from a K-S test (3rd column) and a Student's t-test for unequal variances (4th column).

T	C	K-S	-
dE(N)	$u-r$	0.06%	1.61%
dE(N)	$g-r$	28.27	47.19
dE(N)	$g-i$	64.19	42.34
dE(N)	$i-z$	0.08	2.85
dE(nN)	$u-r$	7.57	14.24
dE(nN)	$g-r$	74.63	84.51
dE(nN)	$g-i$	33.44	11.95
dE(nN)	$i-z$	0.20	3.85
dE(di)	$u-r$	70.87	26.55
dE(di)	$g-r$	89.68	68.52
dE(di)	$g-i$	70.87	59.80
dE(di)	$i-z$	7.73	31.82
dE(bc)	$u-r$	38.74	52.07
dE(bc)	$g-r$	19.00	4.69
dE(bc)	$g-i$	12.64	3.33
dE(bc)	$i-z$	52.24	24.16
$dE(N)_{bri.}$	$u-r$	0.12	2.28
$dE(N)_{bri.}$	$g-r$	10.71	50.84
$dE(N)_{bri.}$	$g-i$	87.91	47.33
$dE(N)_{bri.}$	$i-z$	0.04	1.01
$dE(nN)_{bri.}$	$u-r$	16.93	19.21
$dE(nN)_{bri.}$	$g-r$	80.25	94.32
$dE(nN)_{bri.}$	$g-i$	42.51	43.15
$dE(nN)_{bri.}$	$i-z$	9.80	13.67
$dE(N)_{fai.}$	$u-r$	31.34	19.59
$dE(N)_{fai.}$	$g-r$	73.05	71.58
$dE(N)_{fai.}$	$g-i$	53.91	65.90
$dE(N)_{fai.}$	$i-z$	8.27	35.67
$dE(nN)_{fai.}$	$u-r$	8.56	25.60
$dE(nN)_{fai.}$	$g-r$	39.75	80.97
$dE(nN)_{fai.}$	$g-i$	44.72	17.82
$dE(nN)_{fai.}$	$i-z$	2.46	6.79

It would thus be desirable to have a better S/N in the *u* band, in order to gain more from it than what is possible with our present data.

While at this stage of our study, it would certainly be interesting to calculate individual colour gradients for each galaxy, and to examine their relations with other quantities, such an analysis would go beyond the scope of the present work, and is therefore deferred to later investigations. Instead, we keep our focus on comparing the colour-magnitude relations of different samples, and proceed with analyzing samples selected by density. Note, however, that the distribution of colour gradients across the Virgo cluster is part of the study presented in Chapter 6.

9. C - -

A weak dependence of the stellar population ages of early-type galaxies on local environmental density has recently been reported by Bernardi et al. (2006), based on a study of Lick indices. These authors found early-type galaxies in high-density environments to be slightly older than at lower densities. Our large sample size allows us to test whether this is the case for dEs as well — we can of course only probe a cluster environment, but the range in local densities (see, e.g., Chapter 4) should be large enough to find such an effect, if present.

We thus subdivide the sample of dE(N)s, dE(nN)s, and our full dE sample (excluding dE(bc)s) at their respective median local projected densities. These are, in units of the logarithm of the number of galaxies per square degree, 1.374 for the dE(N)s, 1.198 for the dE(nN)s, and 1.293 for the full dE sample. As described in the previous chapters, local projected density is calculated by defining a circular area around each galaxy that includes its ten nearest neighbour cluster members, independent of galaxy type (Dressler 1980; Binggeli et al. 1987).

The resulting CMRs are shown in Figures 5.12 to 5.15 for the dE(N)s and dE(nN)s, and in Figures 5.16 to 5.19 for the full dE sample (excluding dE(bc)s). The respective subsamples are denoted by a subscript “low” for the low-density subsample, and “high” for the high-density subsample. As before, we also show the CMR separately for each bright and faint subsample. Note that the subdivision into bright and faint subsamples is done after the subdivision by density, not vice versa. The pairwise statistical comparisons of the CMRs of low and high-density subsamples are given in Table 5.6 for the full samples, and in Table 5.7 for the faint and bright subsamples.

In all of $u-r$, $g-r$, and $g-i$, the dE(N)s, dE(nN)s, and the full dE sample consistently follow a steeper CMR at lower densities than at higher densities. Typically, the CMRs intersect at the fainter magnitudes of our sample, and with increasing magnitude, galaxies are on average redder in the high-density regime. In $i-z$, the full dE sample also displays a steeper CMR at lower densities for the small and intermediate apertures, but the intersection occurs at brighter magnitudes. For the large aperture, the higher density CMR is somewhat steeper, but all these effects are rather small as compared to the scatter of the CMR. Similarly, no general trend can be seen in $i-z$ for the dE(N)s or the dE(nN)s.

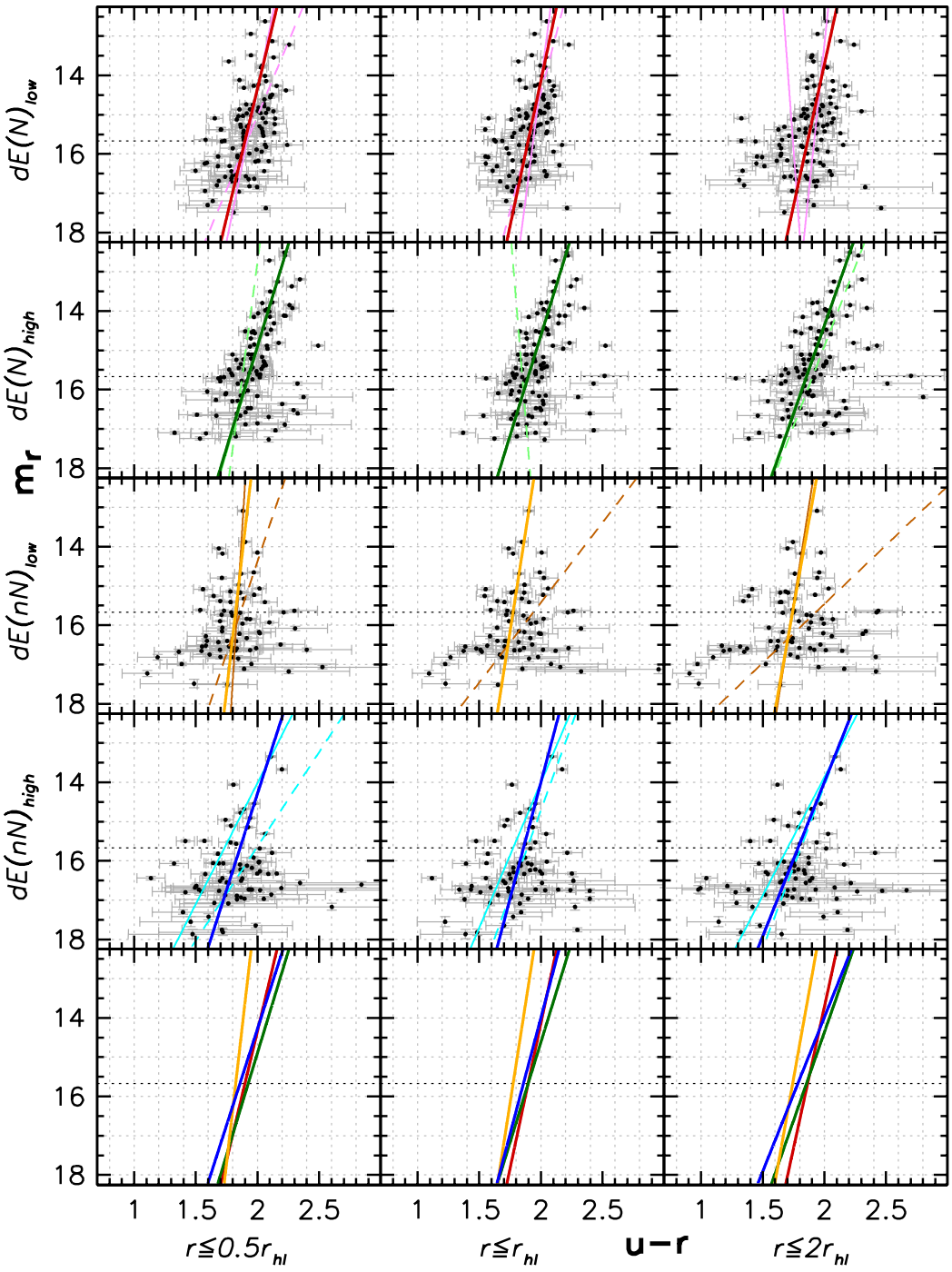

F 5.12. **Colour-magnitude relations for different densities.** Similar to Figure 5.3, but showing the CMR of the low-density and high-density subsamples of the dE(N)s and the dE(nN)s, as labelled on the left-hand side. Again, thin solid lines give the linear fits to the respective bright subsample, while thin dashed lines represent the fit to the respective faint subsample.

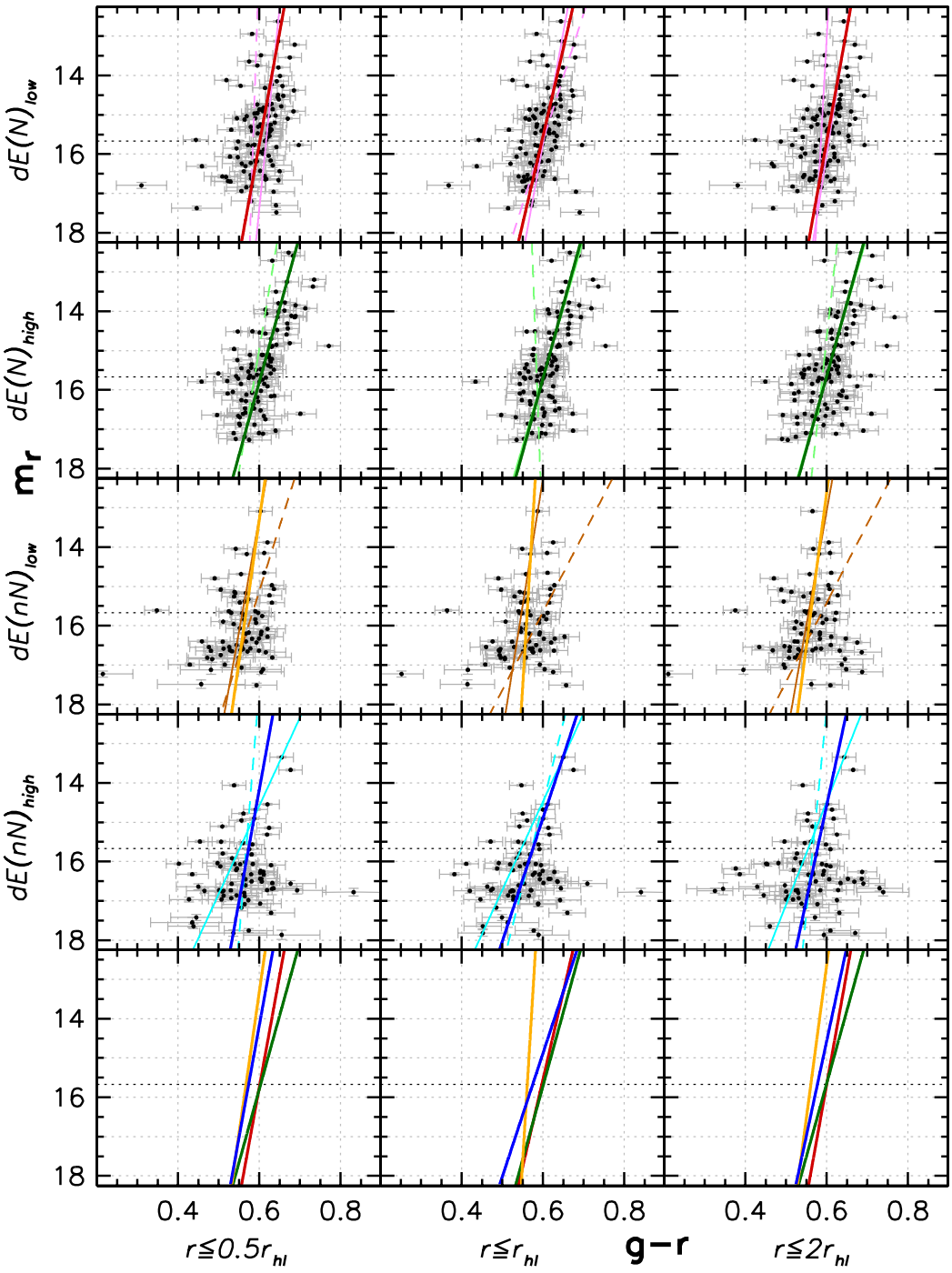

F 5.13. **Colour-magnitude relations for different densities.** Same as Figure 5.12, but for $g - r$ colour.

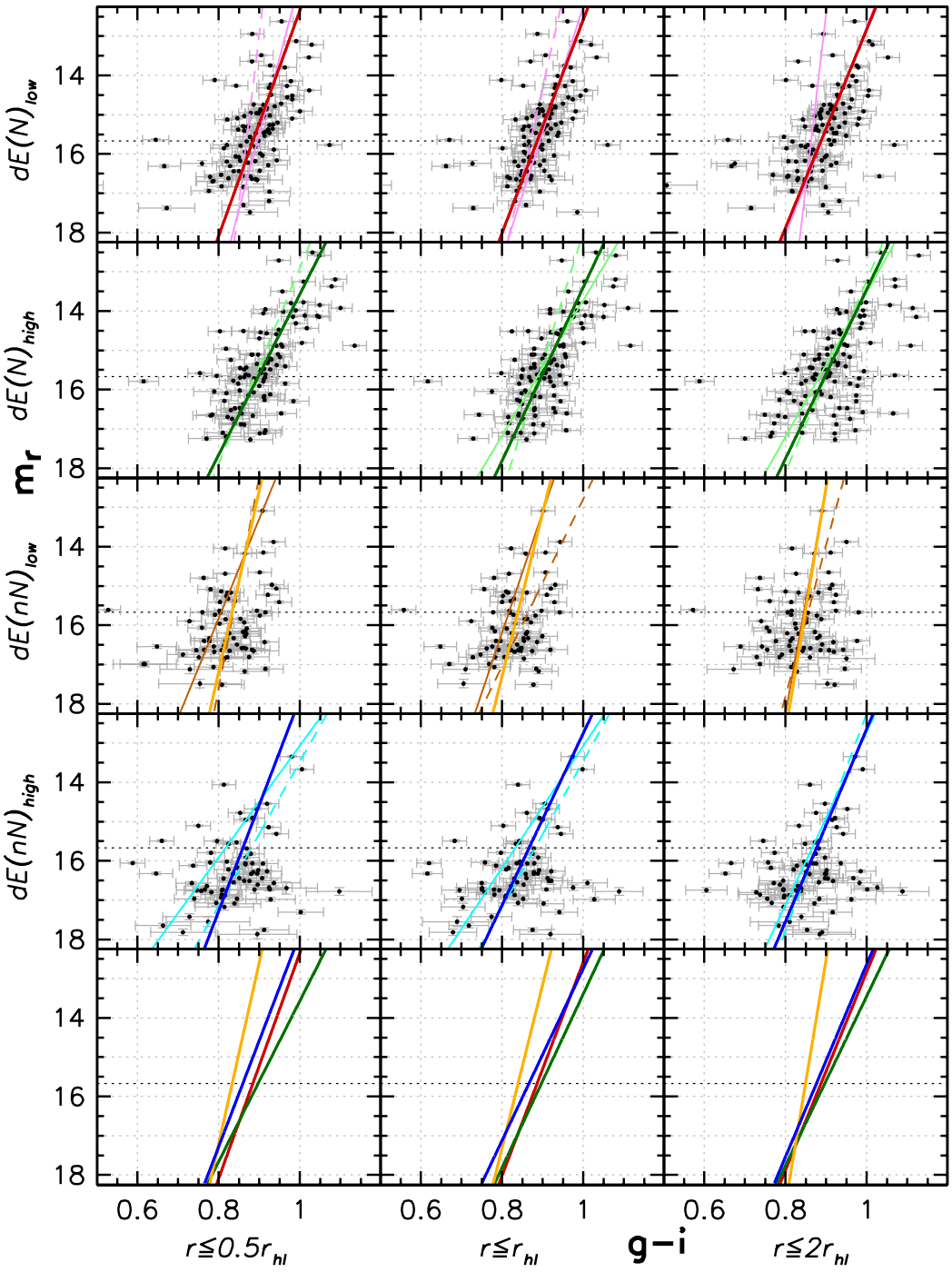

F 5.14. **Colour-magnitude relations for different densities.** Same as Figure 5.12, but for $g - i$ colour.

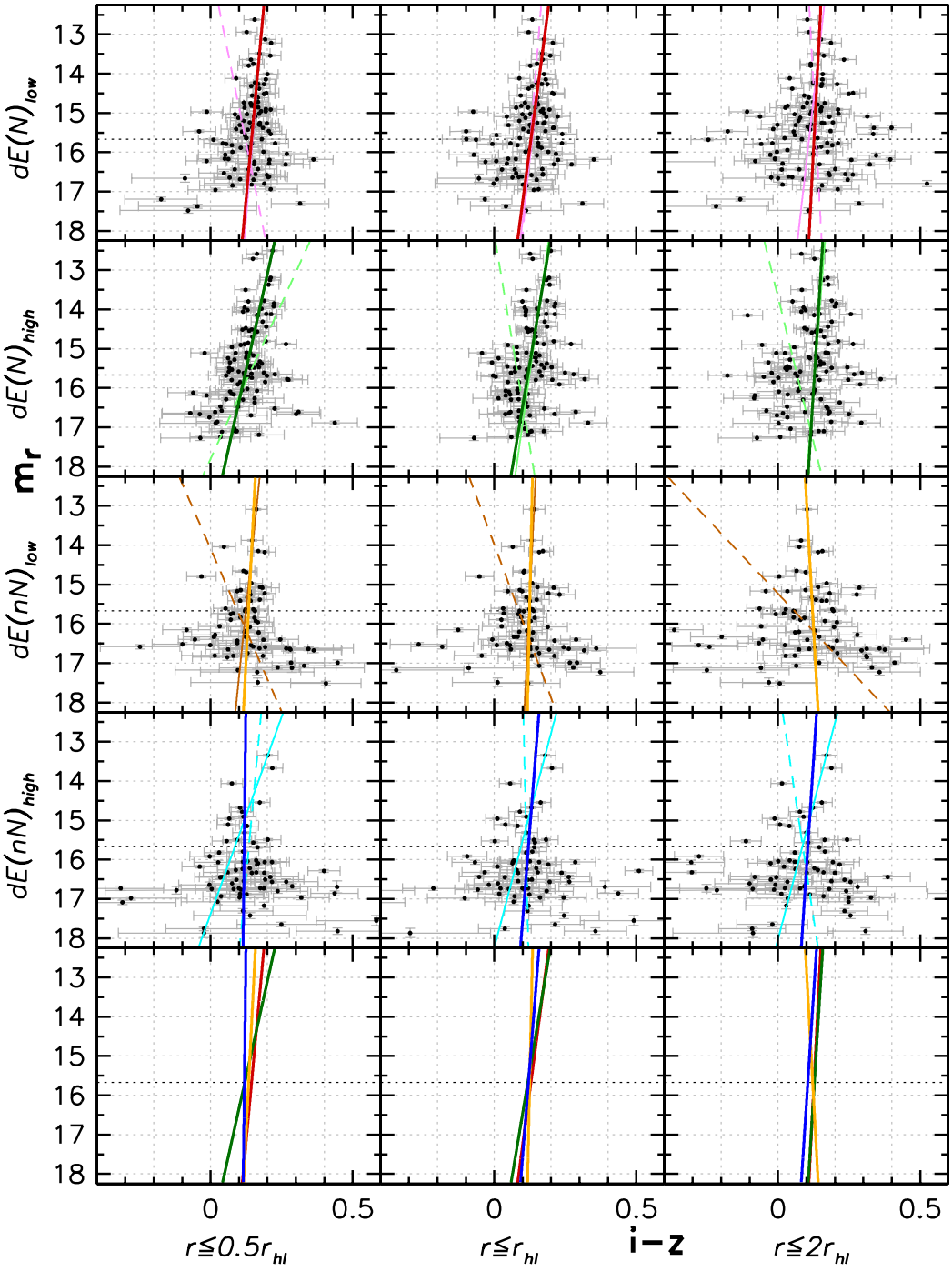

F 5.15. **Colour-magnitude relations for different densities.** Same as Figure 5.12, but for $i - z$ colour.

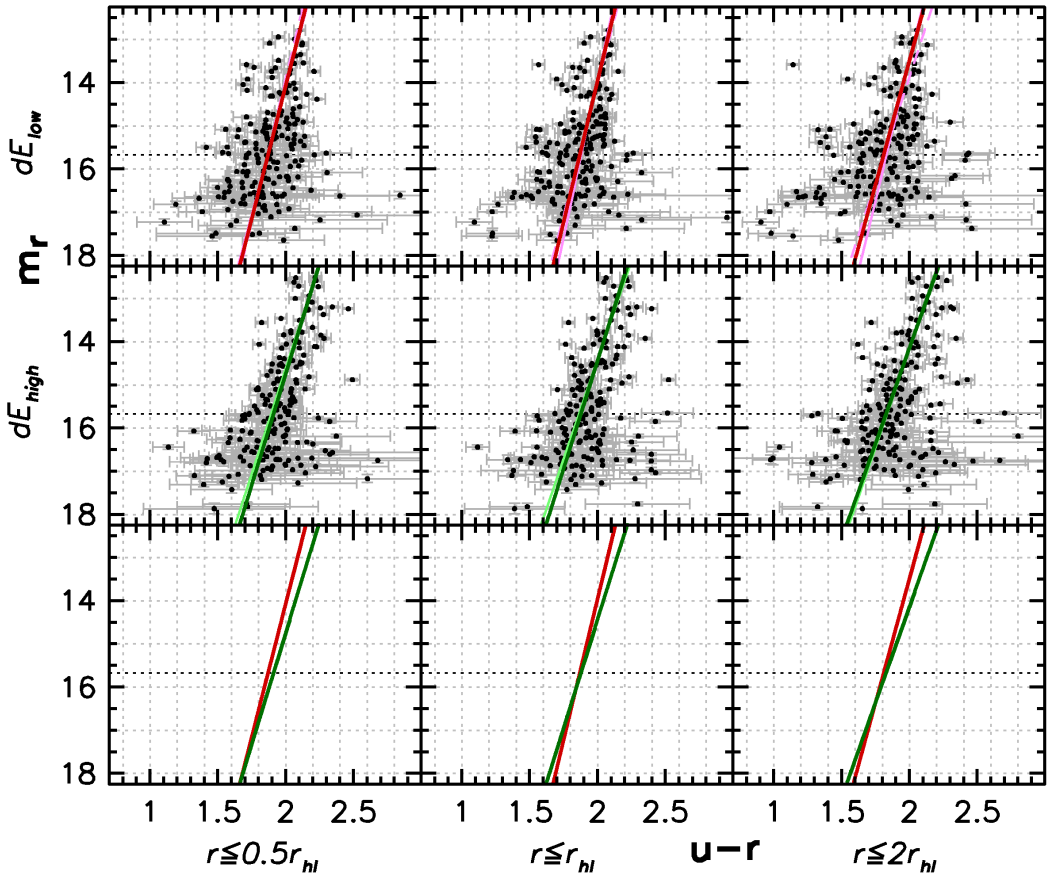

F 5.16. **Colour-magnitude relations for different densities.** Same as Figure 5.12, but for the full dE sample, excluding dE(bc)s.

The above observations are confirmed by the statistical comparisons of the CMRs (Tables 5.6 and 5.7): the difference between the low and high-density subsamples of our full dE sample is significant in $u-r$ (probabilities for a common underlying distribution ≤3.0%), and even more significant in $g-r$ (≤0.9%) and $g-i$ (0.0%). At first glance, one might conjecture that this difference between the density-selected subsamples of the *full* dE sample stems from the difference seen between the dE(N)s and the dE(nN)s, which are populating different density regimes and display significantly different CMRs (see Section 7 and Chapter 4). While this correlation certainly contributes to the present considerations, it is not the only cause of the observed differences: the dE(N)s alone also display significant differences between the two density regimes, namely for the intermediate apertures in each of $u-r$ (probability ≤1.9%) , $g-r$ (≤3.2%), and $g-i$ (≤2.2%). The fact that the percentages are not as low as for the full dE sample, and that significant differences are not found for all apertures, is at least partly due to the lower sample size as compared to the full sample. For the dE(nN)s, the lowest probabilities for a common distribution occur in $g-i$ for the small aperture (≤6.7%) and the intermediate aperture (≤ 10.2%). Here, probably the subsample sizes are too small and the scatter of the CMRs too large for the rather small differences to be significant. Likewise, a further subdivision into bright and faint subsamples, in addition to the subdivision by density, only yields significant differences for the full dE sample. Among the dE(N)s and dE(nN)s, however, the lowest probability is that for the bright dE(N)s in $g-i$ for the small aperture, with ≤6.6%.

The differences between the CMRs in low and high-density regions could either be caused by a *direct* correlation with local density, or it could mainly be a difference between the cluster center and the other cluster regions. In the latter case, the correlation with density would be a *consequence*, rather than a direct relation. Since the cluster center is a region of high density, these two possibilities

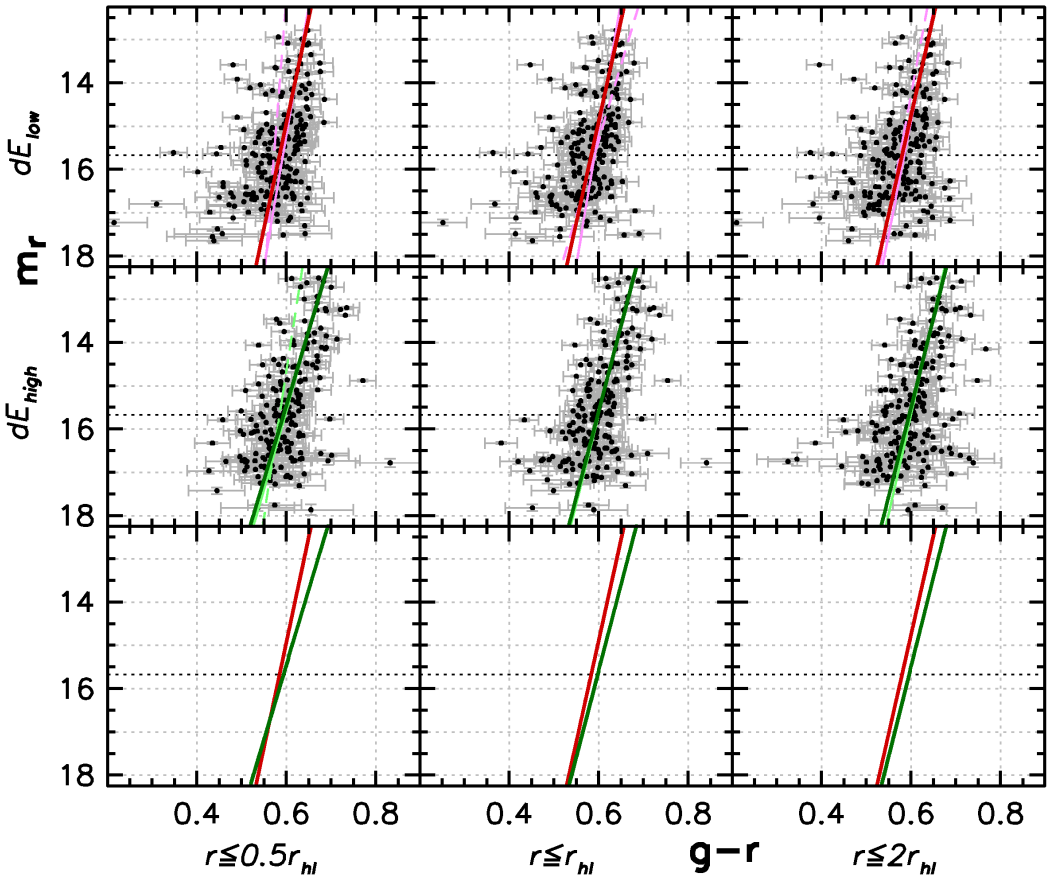

F 5.17. **Colour-magnitude relations for different densities.** Same as Figure 5.16, but for $g - r$ colour.

are obviously similar to each other, but they are not completely the same. In order to compare them, we put together a subsample of each of the dE(N)s, the dE(nN)s, and all dEs (excluding dE(bc)s), comprising all objects within two degrees of the coordinates $\alpha = 187.^{\circ}3$, $\delta = 12.^{\circ}4$. This is roughly the cluster center, as deduced from the number density distribution of cluster member galaxies (see Figure 6.1 of Chapter 6). Of course, most galaxies of this "central subsample" are also included in the high-density subsample: 86% for the dE(N)s, 100% for the dE(nN)s, and 95% for all dEs. Contrary to that, a significant fraction of the objects in the high-density subsample are *not* located within the central region as defined above: 28% of the high-density dE(N)s, 57% of the dE(nN)s, and 37% of all dEs are *not* included in the respective central subsample.

For the dE(nN)s, the central sample comprises only 32 galaxies, of which only 4 lie at brighter magnitudes, preventing a reliable fit to the CMR. The central subsamples of the dE(N)s and of all dEs, though, comprise 87 and 129 objects, respectively, and allow reliable comparisons to be done. It turns out that in all colours, the fits to the CMR of the central subsample and of the high-density subsample are basically equal, within the errors. This is exemplified in Figure 5.20, where we show the CMRs of the respective subsamples for $g - i$, measured within the half-light aperture. These results suggest that the shape of the CMR is most likely *directly* correlated with local density, rather than being predominantly determined by whether or not the sample galaxies lie within the cluster center — otherwise, the CMRs of the central subsamples should be flatter than those of the high-density samples, since the former provide a much cleaner selection of galaxies in the central region. Also, note that, typically, any correlation with *projected* density would be even stronger with true *volume* density, since projection always causes some objects to apparently lie close to the center that actually are situated in front of or behind the center.

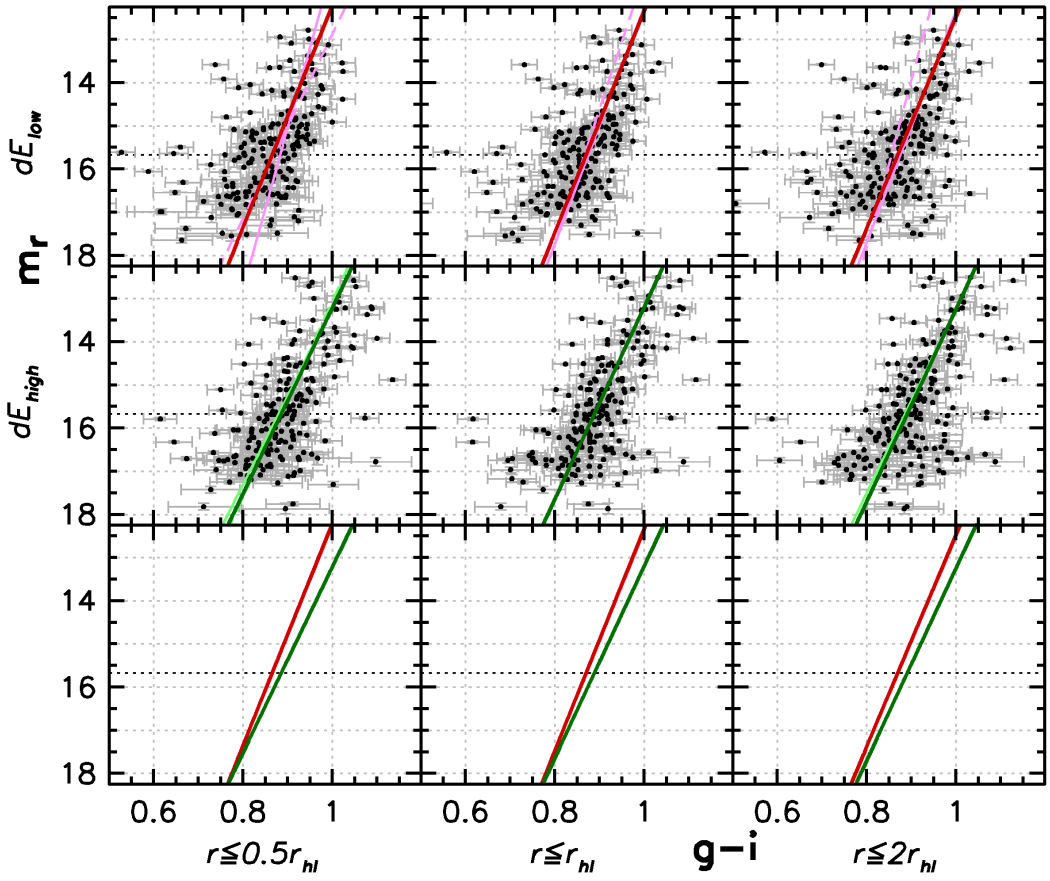

F 5.18. **Colour-magnitude relations for different densities.** Same as Figure 5.16, but for $g - i$ colour.

So far, we did not consider the possibility that the density dependence of the CMR could be caused by different average distances of the subsamples along the line of sight. Thus, let us compare the low and high-density subsample of all dEs (excluding dE(bc)s) in $g-i$, using the half-light aperture (cf. Figure 5.18). At the colour value that the CMR of the high-density subsample has at the bright reference magnitude, the CMR of the low-density subsample is $0\overset{\text{m}}{.}62$ brighter. Assuming an average distance modulus of $m - M = 31\overset{\text{m}}{.}0$, this would correspond to an average offset of the subsamples along the line of sight of 4.5 Mpc. Moreover, both CMRs intersect at the fainter magnitudes – thus, the brighter dEs that are in regions of higher projected density would have to be, *on average*, 4.5 Mpc closer to us than the fainter dEs in the same projected regions. What we would "need" to explain our CMR differences is a lower distance for part of the low-density subsample, as compared to the other part of it *and* to the other subsample. If this would be given, it would automatically account partly (but only partly) for the intersection of the CMRs at fainter magnitudes, since the closer objects would be offset to brighter apparent magnitudes. It would not work the other way around: if part of the higher-density subsample was offset to larger distances, this part would have a *fainter* apparent brightness on average, and therefore the difference of the CMRs would have to be larger at fainter magnitudes. In any case, the distributions of r magnitudes of the two subsamples are very similar, and their median magnitudes differ by $0\overset{\text{m}}{.}07$ only.

A difference in distance modulus of $1\overset{\text{m}}{.}0$ between the Virgo cluster parts termed "cluster A" (i.e., basically the part of the cluster that has a declination $\delta \gtrsim 10°$, see Binggeli et al. 1993) and the western part of "cluster B" (southward of cluster A and within a circular region around M 49) was reported by Gavazzi et al. (1999), such that the latter part would be further away by 8.6 Mpc. Their study is based on a combined sample of early-type and late-type galaxies. While the number of dEs

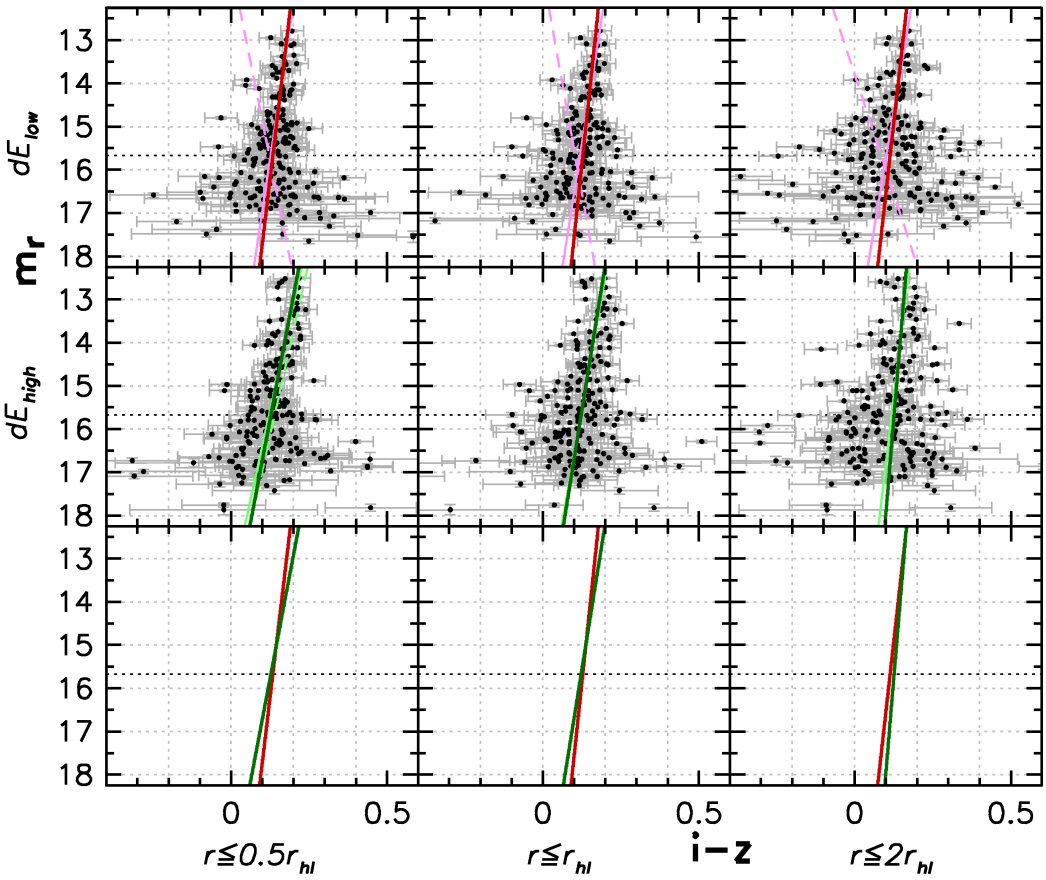

F 5.19. **Colour-magnitude relations for different densities.** Same as Figure 5.16, but for $i - z$ colour.

in this region would most likely be too small to be able to account for the differences that we see in the CMRs, we nevertheless test this possibility by excluding all galaxies below a declination $\delta < 10°$. However, the difference between the low and high-density CMR is still equally large. Within cluster A, Gavazzi et al. (1999) give a dispersion of $0\overset{m}{.}45$ in their determination of the distance modulus — but they note that this value is comparable to the nominal uncertainty in the methods used. Based on the surface brightness fluctuations of 16 Virgo dEs, Jerjen et al. (2004) found a distance dispersion of ±1.45 Mpc, too low to be able to explain the observed differences. From these considerations it is clear that the significant correlation of the CMR with local density is real and can not be explained with differences in distance.

10. T -

In order to obtain a rough estimate of the *true* scatter of the CMR (i.e., that is not caused by measurement errors), we can compare the observed scatter with our measurement errors. The respective values are given in Table 5.1: the column “RMS” gives the root mean square of the colour residuals about the linear fit to the CMR, while the column “E-RMS” gives the root mean square of the errors. If the observed scatter was solely due to measurement errors, these two values should be similar, at least for the larger (i.e., statistically robust) dE subsamples. The ratio of the two values, which is given in the last column of the table, is thus an indirect measure of the true scatter; we shall term it the “RMS-ratio” hereafter. Note that the true scatter can be a combination of an intrinsic colour scatter and a distance spread; we shall consider the latter at the end of this section.

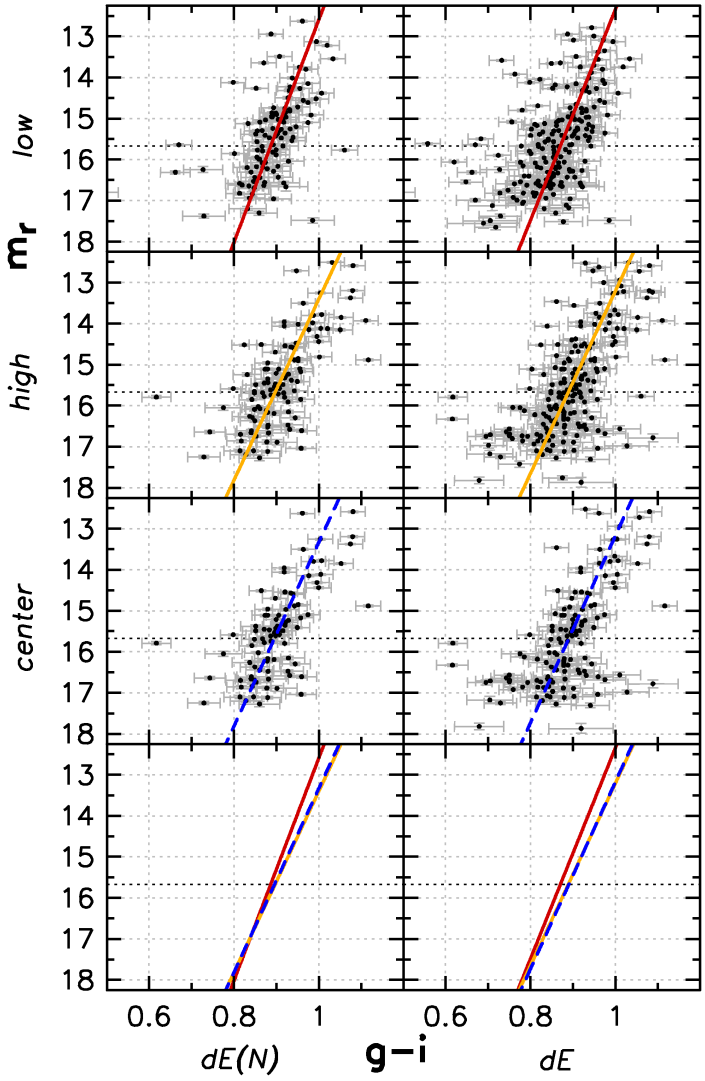

F 5.20. **Colour-magnitude relations for different densities and positions.** Here we show the CMRs of the dE(N)s (left column) and of all dEs (right column, excluding dE(bc)s) for the low-density subsample (top row), the high-density subsample (middle row), and the central subsample (bottom row), using $g-i$ colour and the intermediate aperture. The central subsample contains galaxies within two degrees of the Virgo cluster center; see text for details.

We first note that for most CMRs, the RMS-ratio increases with aperture size. As for a possible intrinsic colour scatter, it can hardly be deduced if, and how strongly, it increases from the inner to the outer parts of the dEs. As for our measurement errors, we know that they consist of one part that remains constant with aperture size, namely the error on the photometric calibration zeropoint ("calibration uncertainty", see Section 4), and another part that increases with aperture size, namely the S/N uncertainty and the sky level uncertainty. It thus appears likely that an overestimation of the calibration uncertainty causes, at least partly, the observed increase in the RMS-ratio with aperture size: due to this uncertainty, the measurement errors do not approach zero with increasing S/N, but instead reach a finite value. If this value – which is provided directly by the SDSS for each colour – would be overestimated, the RMS-ratio would fall below a value of 1 for high-S/N measurements, which is indeed the case for some of the small-aperture CMRs, like e.g., for the bright dE(N)s in $i-z$. Again, we are not able to tell how much of the increase in the RMS-ratio is an intrisic effect, but the

T 5.6. **Statistical comparisons of CMRs for different densities.** For a given dE subclass (1st column), colour (2nd column), and aperture (3rd column), we compare the CMRs of the low and high-density subsamples (see text). Probabilities for a common underlying distribution are derived from a K-S test (4th column) and a Student's t-test for unequal variances (5th column).

T	C	A	K-S	-
dE(N)	$u-r$	small	7.85%	4.02%
dE(N)	$u-r$	interm.	1.95	0.56
dE(N)	$u-r$	large	32.11	3.87
dE(N)	$g-r$	small	93.16	24.89
dE(N)	$g-r$	interm.	6.43	3.23
dE(N)	$g-r$	large	24.55	3.14
dE(N)	$g-i$	small	8.22	2.97
dE(N)	$g-i$	interm.	1.84	2.18
dE(N)	$g-i$	large	4.83	1.09
dE(N)	$i-z$	small	5.58	44.52
dE(N)	$i-z$	interm.	65.68	86.18
dE(N)	$i-z$	large	74.50	72.22
dE(nN)	$u-r$	small	23.48	35.72
dE(nN)	$u-r$	interm.	15.43	51.11
dE(nN)	$u-r$	large	31.48	29.56
dE(nN)	$g-r$	small	47.96	19.16
dE(nN)	$g-r$	interm.	68.69	41.28
dE(nN)	$g-r$	large	35.95	52.74
dE(nN)	$g-i$	small	6.70	2.13
dE(nN)	$g-i$	interm.	10.24	4.26
dE(nN)	$g-i$	large	18.33	6.35
dE(nN)	$i-z$	small	26.07	63.19
dE(nN)	$i-z$	interm.	61.61	70.99
dE(nN)	$i-z$	large	47.96	73.07
dE	$u-r$	small	0.46	0.66
dE	$u-r$	interm.	3.01	1.65
dE	$u-r$	large	0.67	0.93
dE	$g-r$	small	0.92	0.01
dE	$g-r$	interm.	0.10	0.00
dE	$g-r$	large	0.23	0.00
dE	$g-i$	small	0.01	0.00
dE	$g-i$	interm.	0.00	0.00
dE	$g-i$	large	0.02	0.00
dE	$i-z$	small	13.24	21.72
dE	$i-z$	interm.	64.87	55.68
dE	$i-z$	large	86.48	52.66

above considerations suggest that the photometric calibration might be at least somewhat better than estimated.

We now attempt to derive an estimate for how large the true scatter is with respect to our measurement uncertainties, i.e., which of the two dominates the observed scatter. Given the above findings, we focus only on the RMS-ratios for the large-aperture CMRs, in order to not underestimate the true scatter. When we consider only the larger dE subsamples, i.e., the bright and faint dE(N)s, the faint

T 5.7. **Statistical comparisons of CMRs for different densities.** Similar to Table 5.6, but giving the statistical probabilities separately for a comparison of the bright low and high-density subsamples (4th and 5th column) and the faint low and high-density subsamples (6th and 7th column).

T	C	A	K-S (.)	(.)	K-S (.)	(.)
dE(N)	$u-r$	small	12.55%	2.46%	59.53%	38.04%
dE(N)	$u-r$	interm.	9.32	0.48	22.77	19.06
dE(N)	$u-r$	large	29.55	4.22	65.79	29.42
dE(N)	$g-r$	small	32.00	9.59	72.83	95.29
dE(N)	$g-r$	interm.	13.58	1.84	20.11	46.66
dE(N)	$g-r$	large	18.00	3.16	48.34	35.52
dE(N)	$g-i$	small	6.63	2.72	64.81	34.89
dE(N)	$g-i$	interm.	6.79	1.30	37.82	43.01
dE(N)	$g-i$	large	21.51	1.79	9.83	19.03
dE(N)	$i-z$	small	37.71	51.80	40.36	63.30
dE(N)	$i-z$	interm.	74.75	82.48	38.49	94.32
dE(N)	$i-z$	large	91.31	77.68	26.07	81.32
dE(nN)	$u-r$	small	95.04	90.02	36.67	36.91
dE(nN)	$u-r$	interm.	46.25	74.88	60.38	59.70
dE(nN)	$u-r$	large	44.26	69.56	78.74	37.14
dE(nN)	$g-r$	small	63.50	61.09	56.54	32.05
dE(nN)	$g-r$	interm.	31.74	27.44	84.14	52.01
dE(nN)	$g-r$	large	33.37	10.44	90.07	97.45
dE(nN)	$g-i$	small	12.86	52.84	11.67	3.42
dE(nN)	$g-i$	interm.	6.21	18.04	16.18	9.14
dE(nN)	$g-i$	large	10.63	2.68	70.81	25.36
dE(nN)	$i-z$	small	36.78	76.71	59.09	60.17
dE(nN)	$i-z$	interm.	70.22	61.45	71.26	72.98
dE(nN)	$i-z$	large	84.76	51.59	59.70	79.67
dE	$u-r$	small	0.42	0.01	40.35	40.38
dE	$u-r$	interm.	2.21	0.05	67.99	49.69
dE	$u-r$	large	0.81	0.35	40.13	19.77
dE	$g-r$	small	2.47	0.07	22.40	1.53
dE	$g-r$	interm.	0.27	0.00	5.09	2.25
dE	$g-r$	large	0.19	0.00	18.83	4.59
dE	$g-i$	small	0.63	0.02	1.84	0.06
dE	$g-i$	interm.	0.18	0.00	0.52	0.30
dE	$g-i$	large	0.17	0.00	4.18	0.64
dE	$i-z$	small	48.17	98.56	16.10	17.38
dE	$i-z$	interm.	49.12	71.70	21.49	39.17
dE	$i-z$	large	50.57	67.07	43.01	40.22

dE(nN)s, and the full samples of dE(N)s, dE(nN)s, and all dEs, we find that the RMS-ratio always lies between 1.3 and 2. With the simplified assumption that the RMS of the true scatter and the RMS of the measurement uncertainties add quadratically to yield the observed RMS, these values would imply that the RMS of the true scatter lies between 0.8 and 1.7 of that of the measurement uncertainties. However, one obvious caveat needs to be discussed: it cannot be excluded from the values per se that we simply underestimated the measurement errors, and that the true uncertainties could

fully account for the observed scatter. To assess this possibility, we consider below the correlation of colour residuals about the CMRs in different colours.

If the observed scatter would be solely due to measurement uncertainties, no correlation should be observed between the residuals in two different colours — except, obviously, for colours that share a certain band, like, e.g., $u-r$ and $g-r$. If, on the other hand, a significant true scatter is present, one would expect at least some correlation between the residuals: a dE that is *intrinsically bluer* in $u-r$ than most of the other galaxies should typically not be *intrinsically redder* in $g-i$ than most other dEs, since the wavelength ranges covered by these colours overlap significantly. (It would, of course, be "allowed" to be redder in $i-z$.) Likewise, if the scatter was due to a spread in distance and therefore in magnitude, most galaxies would fall on the same side of the CMR in all colours.[5] We therefore present in Figure 5.21 a pairwise comparison of the colour residuals for $u-r$ vs. $g-i$, $u-r$ vs. $i-z$, and $g-r$ vs. $i-z$. Here, we use the colours measured within the half-light (i.e., intermediate) aperture, to avoid too large measurement uncertainties. Our above concerns about using smaller apertures need not be considered here, since our measurement error estimates do not enter here.

A correlation is clearly seen for the dE(N)s and for all dEs (excluding dE(bc)s) in $u-r$ vs. $g-i$, and also in $u-r$ vs. $i-z$ and weakly in $g-r$ vs. $i-z$. The dE(nN)s seem to show a correlation only in $u-r$ vs. $g-i$. To quantify these visual impressions, we calculate for every quadrant the fraction of objects that falls within it (red numbers, given as percentages). These values confirm the above findings: for the dE(N)s and for all dEs in $u-r$ vs. $g-i$, more than twice as many objects lie within the upper right and lower left quadrant than within the other two. In $u-r$ vs. $i-z$, the correlation is somewhat weaker, and again slightly weaker in $g-r$ vs. $i-z$. For the dE(nN)s, only $u-r$ vs. $g-i$ shows a clear correlation. These results indicate that there must be a significant true scatter of the CMR, similar to the results of Secker et al. (1997) for the Coma cluster.

As a further statistical test, we try to estimate how the fraction of galaxies within the different quadrants would be distributed given a perfect correlation plus measurement errors. With "perfect correlation", we mean that each galaxy falling on one side of the CMR in one colour falls on the same side of the CMR in the other colour. We only care about the *direction* of the colour offset, i.e., the sign of the residual, not about its absolute value. In the following, we describe for the correlation of $u-r$ vs. $g-i$ how we simulate a CMR scatter. This simulation is done in the same way for the other colour pairs.

In order to keep our approach simple, yet still instructive, we refrain from choosing a certain analytic model distribution for the true scatter of $u-r$ and $g-i$. Instead, we adopt the *observed* distribution of colour values as one possible example for a true distribution. To guarantee that a given galaxy falls on the same side of the CMR for both colours, simulating a perfect correlation, we assign to the $g-i$ residual of each galaxy the sign of its corresponding $u-r$ residual (but keep its absolute value). This represents our simulated distribution of true[6] residuals. For simulating the distribution of measurement uncertainties, we use again the observed distribution of colour residuals, but redistribute these values randomly among our galaxies, and assign them random signs. We then add these values to the simulated true residuals, thereby yielding simulated observed residuals. Note that in this case, the RMS of the true scatter and of the measurement uncertainties are obviously equal, since we used the same absolute values. This can be altered by multiplying the simulated true residuals with a certain factor.

The simulation described above was performed for the full dE sample (excluding dE(bc)s), and was repeated 1000 times for all three colour pairs used above. We considered the case of the RMS value of the true scatter being 0.8 and 1.7 times as large as the RMS of the measurement uncertainties, in order to test our values deduced above. For simplicity, we term these two cases the "0.8-case" and "1.7-case", respectively. For $u-r$ vs. $g-i$, the resulting median fraction of galaxies within the upper

[5] We say "most" instead of "all" galaxies, since it depends to some extent on the linear fit to the CMR, and not only on the galaxy in question.

[6] Our word choice here ("*simulated* distribution of *true* residuals") might not be ideal, but we want to avoid speaking of an "intrinsic distribution", since the true scatter can be a combination of an intrinsic colour scatter and a distance spread. With "true", we only mean that it is not caused by measurement uncertainties.

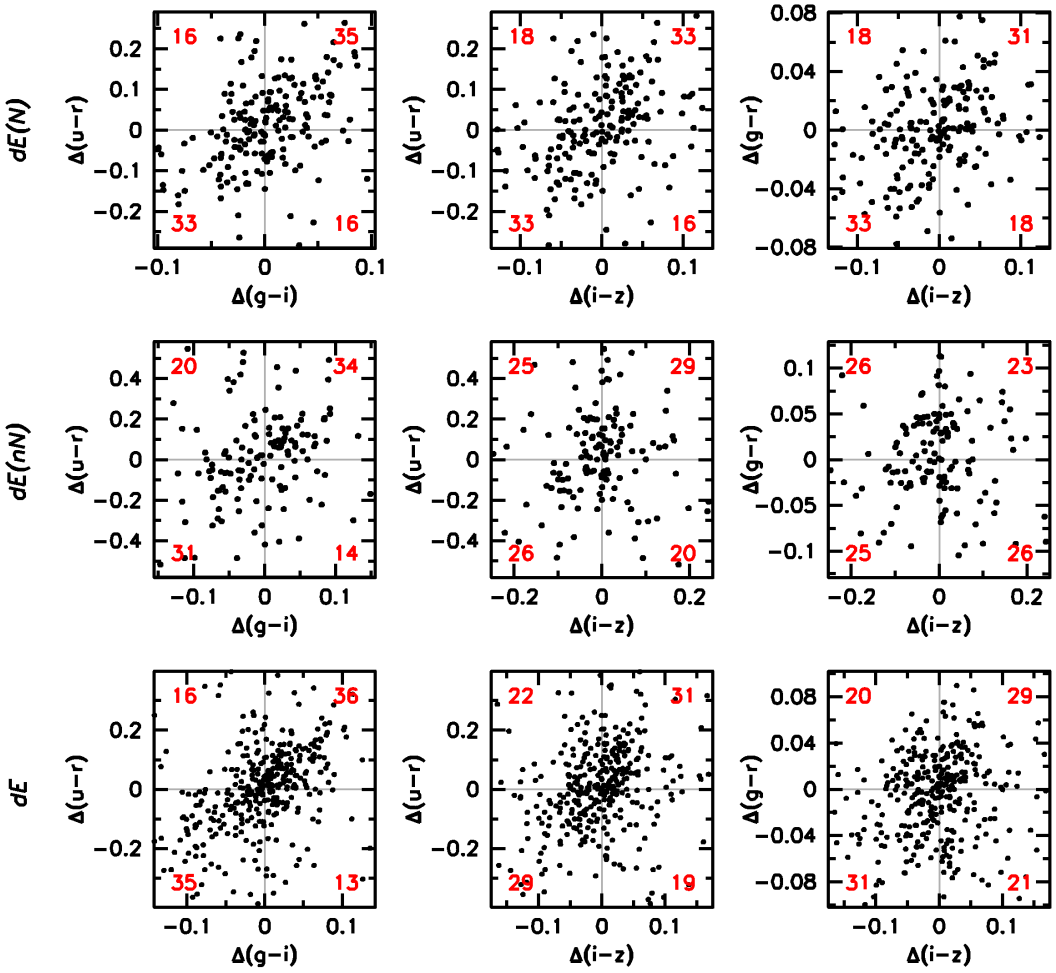

F 5.21. **Correlation of colours.** Pairwise comparison of the colour residuals about the respective CMRs, for colours measured within the half-light aperture. For a given galaxy, $\Delta(u-r) := (u-r) - (u-r)_{\rm CMR}$, where $(u-r)$ is the galaxy's colour, and $(u-r)_{\rm CMR}$ is the colour value of the linear fit to the CMR at the r magnitude of the galaxy; same for the other colours. The red numbers in the corners of the diagrams give the percentage of galaxies within the respective quadrant, bordered by the grey lines.

right and lower left quadrants is 63% for the 0.8-case, and 72% for the 1.7-case. For both $u-r$ vs. $i-z$ and $g-r$ vs. $i-z$, the corresponding values are 62% and 72%. Our observed value for $u-r$ vs. $g-i$ (70%) lies between the two simulated cases and closer to the 1.7-case. For $u-r$ vs. $i-z$, the observed value is 60%, and for $g-r$ vs. $i-z$, it is 59% — both values are only slightly below the simulated 0.8-case. These results confirm that our galaxy colours can well be explained by a true scatter within the range deduced above, and that the dEs, or at least the dE(N)s, are consistent with exhibiting a strong correlation of colour residuals between different colours.

We now need to investigate whether part of the scatter of the CMR could be caused by a spread in distance, which would lead to a certain scatter in magnitude, and would thus contribute to the scatter of the CMR. We concentrate on the CMR of the dE(N)s in $g-i$ for the large aperture. Here, the RMS of our measurement errors is $0\overset{\rm m}{.}034$ (Table 5.1). Assuming the 0.8-case, the true RMS scatter woud be $0\overset{\rm m}{.}027$. The slope of the CMR is -0.044 (Table 5.1). Consequently, a scatter of $\pm 0\overset{\rm m}{.}027$ around the CMR would mean a scatter of $\pm 0\overset{\rm m}{.}61$ in the distance modulus, or $^{+5.14}_{-3.88}$ Mpc at our adopted Virgo cluster distance of 15.85 Mpc ($m - M = 31\overset{\rm m}{.}0$). Such a huge (RMS!) scatter can certainly be excluded. For example, Jerjen et al. (2004) deduced a true dispersion in distance modulus of $\pm 0\overset{\rm m}{.}177$, corresponding to $^{+1.35}_{-1.24}$ Mpc (when using our distance modulus). While their

result is based on the surface brightness fluctuations of a rather small sample of 16 Virgo dEs, they noted that this dispersion, compared to the tangential extension of the cluster, implies a prolate spatial distribution of the galaxies that excellently agrees with other studies (Neilsen & Tsvetanov 2000; West & Blakeslee 2000). For comparison, we consider the projected offset of the dE(N)s from the cluster center (adopted to be at $\alpha = 187\overset{\circ}{.}3$, $\delta = 12\overset{\circ}{.}4$, as above for the "central subsample"), and find a RMS value of 0.86 Mpc. Together with the distance dispersion of Jerjen et al. (2004), this would again imply a significantly prolate distribution.

When we thus adopt the value of Jerjen et al. of $\pm 0\overset{\mathrm{m}}{.}177$ as RMS distance scatter, the resulting colour scatter for the CMR in question is $\pm 0\overset{\mathrm{m}}{.}008$ in $g - i$ colour for the above CMR. While this is rather small, it is nevertheless almost one third of the inferred true scatter in the 0.8-case (see above). However, the RMS scatter from different uncertainties does most likely not add linearly — if the "distance uncertainty" was added *quadratically* to the intrinsic colour scatter, it would have a very small effect only. In any case, while a small but finite distance scatter is naturally unavoidable, we conclude that a significant *intrinsic* colour scatter must be present for our galaxies, with a strong correlation between the different colours.

11. P :

We now attempt to use our colour measurements for drawing conclusions about the actual stellar population characteristics of our galaxies. For this purpose, we construct several stellar population models, using the population synthesis code from Bruzual & Charlot (2003). Following the recommendation of the authors, we use "Padova 1994" isochrones (Bertelli et al. 1994), as well as a Chabrier initial mass function (IMF; Chabrier 2003). We use the Bruzual & Charlot high resolution files, which rely on the STELIB spectral library in the wavelength range 3200 – 9500 Å and on the BaSeL 3.1 spectral library outside this range (see Bruzual & Charlot 2003, and references therein). All Bruzual & Charlot models were calculated with fixed metallicity, i.e., they do not take into account chemical enrichment. When adopting a concordance cosmology ($H_0 = 71$ km s^{-1} Mpc^{-1}, $\Omega_\mathrm{m} = 0.27$, $\Omega_\Lambda = 0.73$), it is now 13.67 Gyr since the Big Bang (Wright 2006). We thus assume that the first stars have formed ~13.5 Gyr ago (also see Kashlinsky et al. 2006), which is particularly relevant for our model with constant star formation rate (see below). All of our models are constructed for three of the seven available metallicities, namely $Z = 0.008$ ($[Fe/H] = -0.33$), $Z = 0.004$ ($[Fe/H] = -0.64$), and $Z = 0.0004$ ($[Fe/H] = -1.65$).

Firstly, we construct a commonly used model, namely a stellar population formed through a single burst of star formation that exponentially decays with time (illustrated in the top panel of Figure 5.22). We choose decay times of $\tau = 1$ Gyr (the *exp-1* model) and 2 Gyr (*exp-2* model). The resulting model tracks are shown in the left column of Figure 5.23 in various colour-colour diagrams. The tracks are curves of constant metallicity, and span a range of ages, from 1 to 13.5 Gyr. Here, "age" means the time since the beginning of the star formation burst.

Secondly, we construct a model based on the study of Davies & Phillipps (1988), who proposed a scenario for dE formation in which a dwarf irregular (dIrr) experiences several short intense bursts of star formation, during which it would appear as blue compact dwarf (BCD). These bursts would increase the initial metallicity and surface brightness of the dIrr, such that, after some time of passive evolution and fading, it would eventually appear as dE. Davies & Phillipps suggest ten bursts within a period of 1 Gyr, each one with a duration of 10 Myr. We thus construct a corresponding model (*burst* model) with 10 bursts of star formation, the tenth one occuring 0.9 Gyr after the beginning of the first one (middle panel of Figure 5.22). Each "burst" is a period of constant star formation rate (SFR) with a duration of 10 Myr. The corresponding model tracks are shown in the middle column of Figure 5.23. Here, "age" means the time since the beginning of the first star formation burst.

Thirdly, we construct a model that is intended to represent the common scenario of dE formation through infall of a late-type galaxy into the cluster and subsequent loss or consumption of gas. This model is defined by a constant SFR (*const* model) since 13.5 Gyr, i.e., since the formation of the

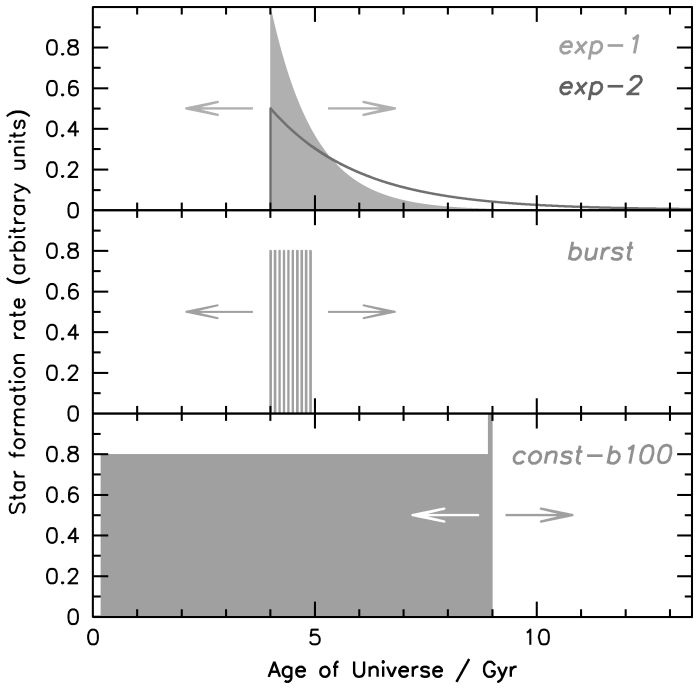

F 5.22. **Star formation histories.** Illustration of the star formation histories used for our population synthesis models. *Top panel:* The *exp* models. *Middle panel:* The *burst* model. *Lower panel:* The *const-b100* model, in which the final burst reaches a SFR of 80 in the units adopted here. See text for details.

first stars within our adopted cosmology (see above). Star formation is then truncated a a certain epoch (lower panel of Figure 5.22). The corresponding model tracks, shown in the right column of Figure 5.23, are thus not tracks along different formation ages, but along different truncation times. The analogue to a *young age* in the *exp* and the *burst* models therefore is a *recent truncation* of star formation in the *const* model, whereas a larger age would correspond to a less recent truncation of star formation. Note that the model tracks shown for the *exp* and the *burst* models actually consist of all age points provided by Bruzual & Charlot (2003) (60 points or more), whereas the truncation times of the *const* model have only been calculated by us for the points shown in the figure, which we then simply connected by lines.

The reason for plotting the model tracks in a number of different colour-colour diagrams is to find out which combination of colours would come closest to breaking the famous age-metallicity degeneracy (even if this cannot be achieved entirely with only optical photometry at hand). In addition, we also need to take into account that the three bands *g*, *r*, and *i* provide the best S/N, whereas the S/N in *z* is a few times lower, and about ten times lower in *u*. Each colour-colour diagram basically relates a "blue" colour (on the y-axis) to a "red" colour (on the x-axis).

It can be clearly seen in Figure 5.23 that the age-metallicity degeneracy is very strong in the cases in which the *r* band is used in the red colour — $i - z$ therefore is the obvious choice, since it provides the reddest possible colour. For the blue colour, we first note that $u - r$ does a better job in breaking the degeneracy than $u - g$, since the colour ranges covered by the models are larger for the former, but the errors are similar, if not smaller, in $u - r$. However, given the considerably smaller errors, $g - r$ is a useful alternative. We will therefore use both the $u - r$ vs. $i - z$ and the $g - r$ vs. $i - z$ diagram in our analysis in Section 12. As an aside, note that for the *burst* model, the tracks are somewhat less squeezed together in $g - r$ vs. $i - z$ than in $u - r$ vs. $i - z$.

Before we proceed towards the application of our models, we construct variations of the *exp* and the *const* models, in order to understand better the "behaviour" of the model colours. We modify the *const* model by adding a final burst of star formation with a duration of 10 Myr, just before star

formation is truncated. This is intended to represent the scenario in which a late-type galaxy falling into the cluster experiences enhanced star formation through forces like gas compression, before it gets stripped of its remaining gas. We construct one model version in which the SFR is boosted by a factor of 100 during the burst (*const-b100*; lower panel of Figure 5.22), and another one in which a factor of 300 is adopted (*const-b300*). These numbers are chosen such that, if the burst occurred after 10 Gyr, it would make up 10% and 30% of the final stellar mass, respectively.

The *const* model and its variants are compared to each other in Figure 5.24. The *const* model itself is shown in the left column, the *const-b100* model in the middle column, and the *const-b300* model in the right column. The main effect of the final burst is a shift towards less recent truncation times: in the case of no final burst and star formation being truncated 0.5 Gyr ago, the colours are similar to the *const-b100* model and truncation occuring 1 Gyr ago, or to the *const-b300* model and truncation occuring ∼1.5 Gyr ago. Apart from this effect, the location of the tracks within the various diagrams does not change noticeably between the model variants. We therefore decided to pick only the *const-b100* model for our analysis in the following section, and to keep in mind that different variations of the model would simply lead to less or more recent truncation times.

Finally, we consider an obvious variation of the *exp* models, namely a truncation of star formation at a given epoch, similar to the *const* model. Figure 5.25 shows our *exp* models like in Figure 5.23, but now with star formation being truncated 6 Gyr (left column), 4 Gyr (middle column), and 2 Gyr (right column) after its beginning. Apart from the (expected) shift towards younger ages for a given colour value in the case of earlier truncation, the tracks of different metallicity approach each other, causing the degeneracy of age and metallicity to become even stronger. Interestingly, this effect is very pronounced in the diagrams using $u - g$ and $u - r$, where the tracks are basically squeezed together, but it is weaker in $g - r$, somewhat similar to what is seen for our *burst* model in Figure 5.23. In our following analysis, we will continue using the *exp* models without truncation, but keep in mind the difference that such a truncation could make in the application of the model tracks.

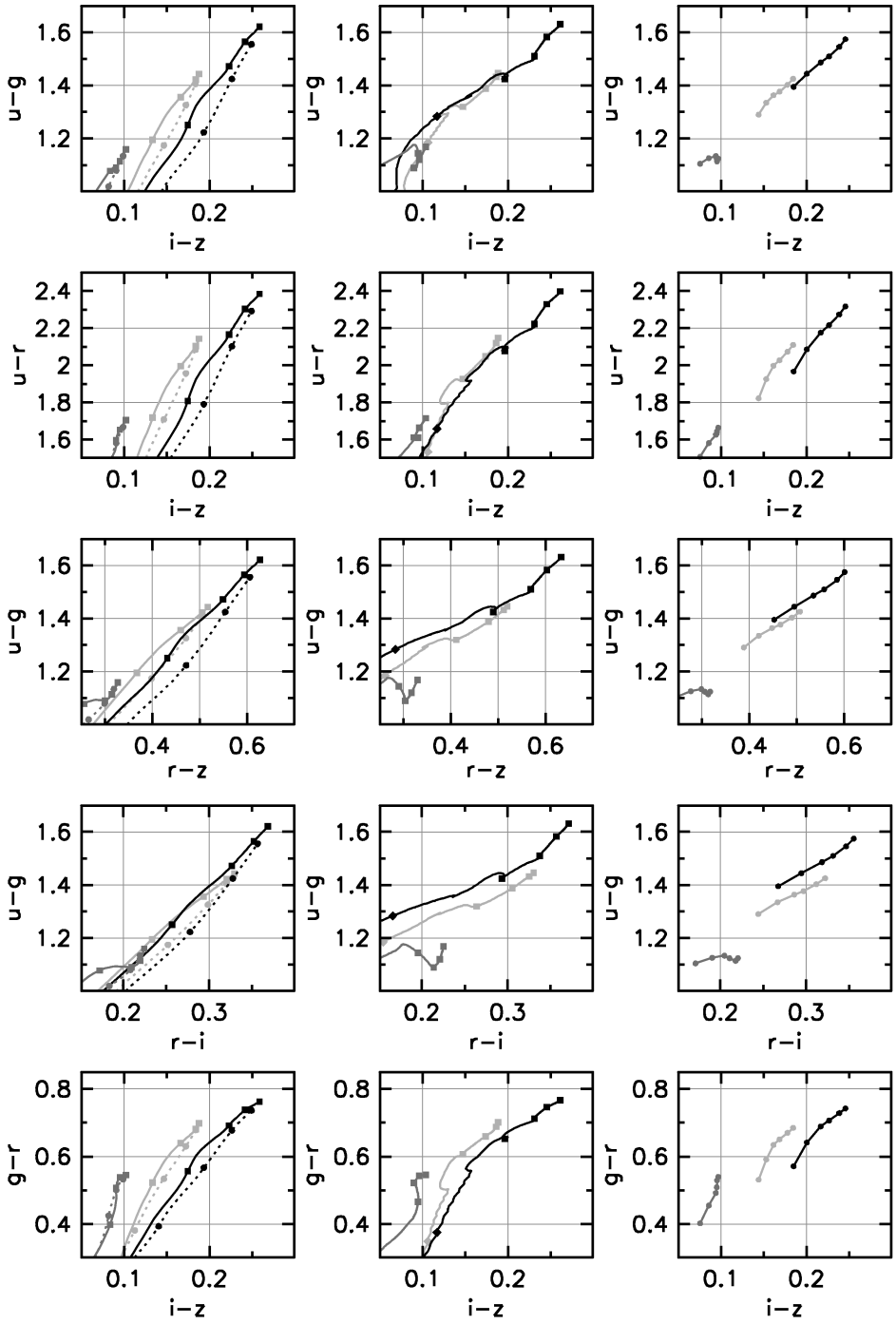

F 5.23. **Population synthesis models.** Shown are theoretical galaxy colours along Bruzual & Charlot model tracks of constant metallicity, namely $Z = 0.008$ ($[Fe/H] = -0.33$, black), $Z = 0.004$ ($[Fe/H] = -0.64$, light grey), and $Z = 0.0004$ ($[Fe/H] = -1.65$, dark grey). The left column shows our *exp* model, i.e., an exponentially decaying burst with a decay time of $\tau = 1$ Gyr (solid lines) and 2 Gyr (dotted lines). The middle column shows our *burst* model, i.e., 10 short bursts of star formation occuring within 1 Gyr. For both the *exp* and the *burst* models, each model track reaches from an age of 1 Gyr (lower end, typically outside the plotting range) to 13.5 Gyr (upper end). Ages are marked at 4.5, 7.5, 10.5, and 13.5 Gyr with filled squares or filled circles (*exp-2* model). For the *burst* model, we give another age mark at 1.5 Gyr (filled diamond). The right column shows our *const* model, i.e., constant star formation that is truncated at a certain epoch. For this model, the model tracks actually are simply lines that connect the data points for a truncation of star formation that, from bottom to top, occured 0.5, 1, 2, 3, 5, and 7 Gyr ago.

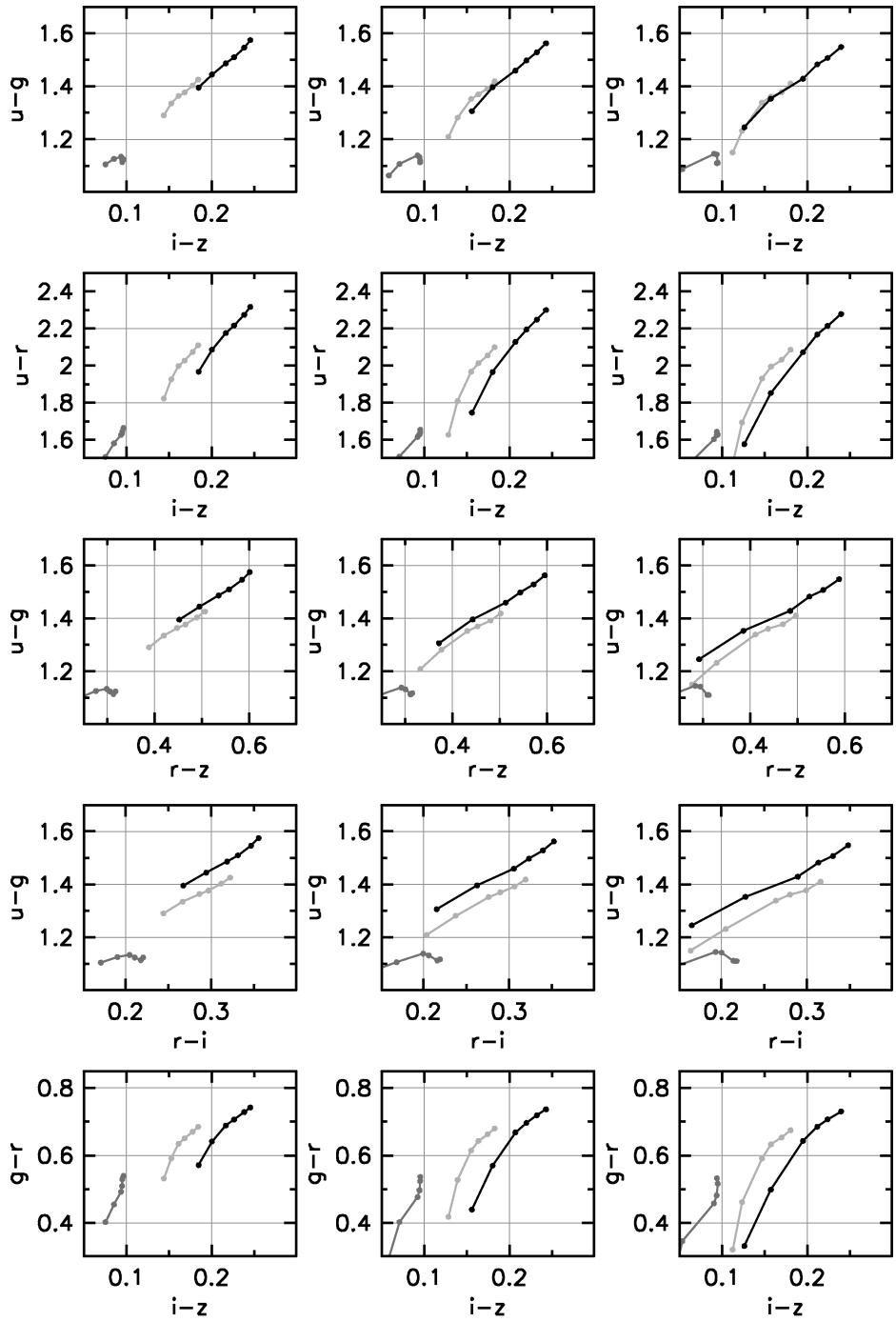

F 5.24. **Variants of the *const* model.** Similar to Figure 5.23, but showing the *const* model in the left column, the *const-b100* model in the middle column, and the *const-b300* model in the right column. The *const-b100* and *const-b300* models are variants of the *const* model in that they have an additional final burst of star formation during which the SFR is boosted by a factor of 100 and 300, respectively. See text for more details.

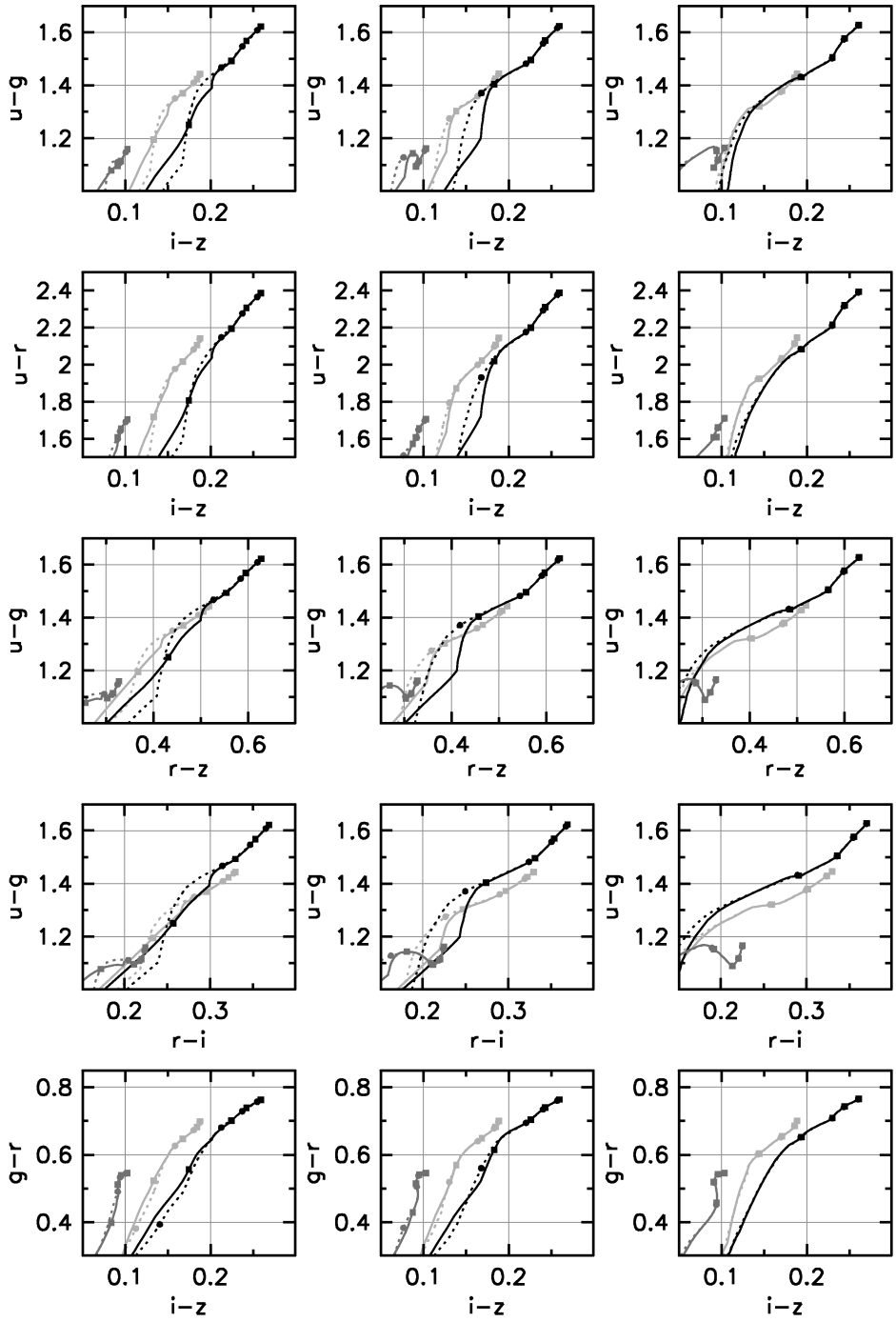

F 5.25. **Variants of the *exp* model.** Similar to Figure 5.23, but showing the *exp* model with additional truncation of star formation after 6 Gyr (left column), 4 Gyr (middle column), and 2 Gyr (right column).

12. P :

In Figures 5.26 to 5.28, we show the $u - r$ vs. $i - z$ and $g - r$ vs. $i - z$ diagrams for the *exp*, *burst*, and *const-b100* model, along with the fits to the respective CMRs for the dE(N)s, dE(nN)s, and dE(di)s, derived for the half-light aperture (see Figures 5.3 to 5.6). For the dE(N)s and dE(nN)s, we also show the CMRs for the bright and faint subsamples. For the full dE sample (lowermost row in each of Figures 5.26 to 5.28), we show instead the CMRs for the low and high-density subsamples (see Figures 5.16 to 5.19). The individual data points are included as small dots, in order to illustrate the scatter around the CMR.

We first focus on the question whether our fitted CMRs would be consistent with being mainly a luminosity-metallicity relation, which is the common interpretation of the CMR for early-type galaxies. As can be seen in the figures, the CMRs would be generally consistent with this interpretation, but would then also imply larger ages or less recent truncation times at lower metallicities. An possible exception is the CMR of the dE(nN)s, which could be explained in the $u - r$ vs. $i - z$ diagram with a variation of age only — however, in the $g - r$ vs. $i - z$ diagram, it would be consistent with a variation in metallicity and a roughly constant age.

A general problem is that in many cases, the fainter end of the CMR seems to lie at a too large age, i.e., it falls above the age of the Universe in the adopted concordance cosmology. In the $u - r$ vs. $i - z$ diagrams, this concerns an even larger part of the CMR, since in them, the overall ages would be somewhat larger than in the $g - r$ vs. $i - z$ diagrams. However, we must stress that many simplifications are included here that might account for these results, like the fact that the models are calculated at a fixed metallicity, or the rather simple star formation histories that we consider. Moreover, the choice of the isochrones or the spectral library also affect the model colours to some extent (see Chapter 7). It is thus important to point out that all our interpretations of the observed colours are always done within this simplified framework of stellar population models.

Let us now turn to a comparison of the dE(N)s, dE(nN)s, and dE(di)s. In all models, the CMR of the dE(di)s spans a metallicity range very similar to that of the dE(N)s, but lies at a few Gyr younger ages. For example, in the *exp-1* model, the brightest dE(N)s would have ages between 10 and 14 Gyr, while the brightest dE(di)s would be 6 to 10 Gyr old. For the dE(nN)s, the main characteristic is that their *range* of ages and metallicities is considerably smaller: the brightest dE(nN)s lie at lower metallicities and ages than the brightest dE(N)s or dE(di)s, and would be more similar to the intermediate-luminosity galaxies of the latter subclasses. However, the faintest dE(nN)s do not reach to metallicities as low as those of the faintest dE(N)s or dE(di)s. Note, though, that the separate CMR fits of the bright and faint dE(nN)s differ significantly from the fit to the full dE(nN) sample, which makes the ages and metallicities of the dE(nN)s difficult to interpret. The CMR of the bright dE(nN)s alone would actually be more or less consistent with being solely a relation of luminosity and age, in both the $u - r$ vs. $i - z$ and the $g - r$ vs. $i - z$ diagrams. While the CMR of the faint dE(nN)s would not fit in any of the above pictures, and would instead imply higher metallicities at lower luminosities, a strong caveat certainly is whether or not the linear fit in $i - z$ is at all useful, given the rather large scatter (see Section 7).

For the density-selected dE subsamples, we find that the CMR spans a slighty smaller range in metallicity at lower densities, and reaches to somewhat younger ages at its fainter part, than for higher densities. The brightest galaxies reach slightly higher metallicities in the high-density sample, but the faintest galaxies also reach slightly lower metallicities. At a given metallicity, the age is similar for the brighter galaxies in both subsamples, but is lower for the fainter galaxies of the low-density subsample. For clarity, note that in Figures 5.26 to 5.28, the cyan line whose tip reaches above the blue line for the full sample is the one for higher densities, i.e., the dashed one.

We now make use of our definition of two "reference magnitudes" in Section 7, in order to provide a somewhat more illustrative comparison of the different subclasses. As stressed above, it is generally difficult to directly compare average colour values of different dE subsamples, since they are usually not sampled equally in luminosity, and thus already have different colours due to the correlation of colour and magnitude. Therefore, we simply compare the colour values of the linear fits to the CMR of

each subsample, measured at the bright and faint reference magnitudes. This is shown in Figure 5.29, along with the model tracks. In the left part of the figure, we use the $u-r$ vs. $i-z$ diagrams for comparison with the models, while the $g-r$ vs. $i-z$ diagrams are used in the right part. On each side, the respective left column shows the colour values at the bright reference magnitude, while the right column shows the values at the faint reference magnitude. We also compare the colours measured within our three different apertures: the smallest symbol represents the small aperture, the largest symbol stands for the large aperture, so that gradients can be recognized. Remember that the CMRs of the dE(bc)s and dE(di)s are only constrained by a handful of data points at fainter magnitudes. The resulting colour values should thus be taken with a grain of salt, at least at the faint reference magnitude.

Let us first concentrate on the colour values at the bright reference magnitude. A clear gradient can be seen for the dE(N)s and the dE(nN)s, in the sense that the stars in the inner regions of the galaxies have, on average, higher metallicities. The dE(nN)s also appear to have somewhat younger ages in the inner regions. For the dE(N)s, it is hard to decide from the given model tracks whether this might also be the case. No clear gradient can be seen for the dE(di)s, but again, this might be partly due to the only moderate sample size. The dE(bc)s seem to have higher metallicities in the outskirts than in the center — here, near-infrared photometry would be desirable to guarantee that the "red colour" used in the diagrams is not affected by the light of the young stars that are present in the center.

The figure illustrates that, within our simplified framework of models, the dE(nN)s are younger than the dE(N)s. Within the small aperture, they have similar metallicities, but the metallicity gradient seems to be stronger for the dE(nN)s. The dE(di)s are slightly younger on average than the dE(N)s, a result that is more pronounced in the $u-r$ vs. $i-z$ than in the $g-r$ vs. $i-z$ diagrams. They are, however, older than the dE(nN)s. The (average) metallicities of all subclasses lie roughly at or below the track for $[Fe/H] = -0.64$ — however, care must be taken with absolute numbers, given the assumptions and simplifications on which the models are based (also see Chapter 7).

At the faint reference magnitude, the dE(nN)s are still somewhat younger than the dE(N)s, but the difference is smaller. There is still a tendency for the dE(nN)s to have lower metallicities in the outer regions, while for the dE(N)s, there is a slight reverse trend. However, we recall that the scatter in $i-z$ at fainter magnitudes is rather large. Also note that we are using here the fits to the CMRs of the full samples, not of the bright and faint subsamples, of each subclass.

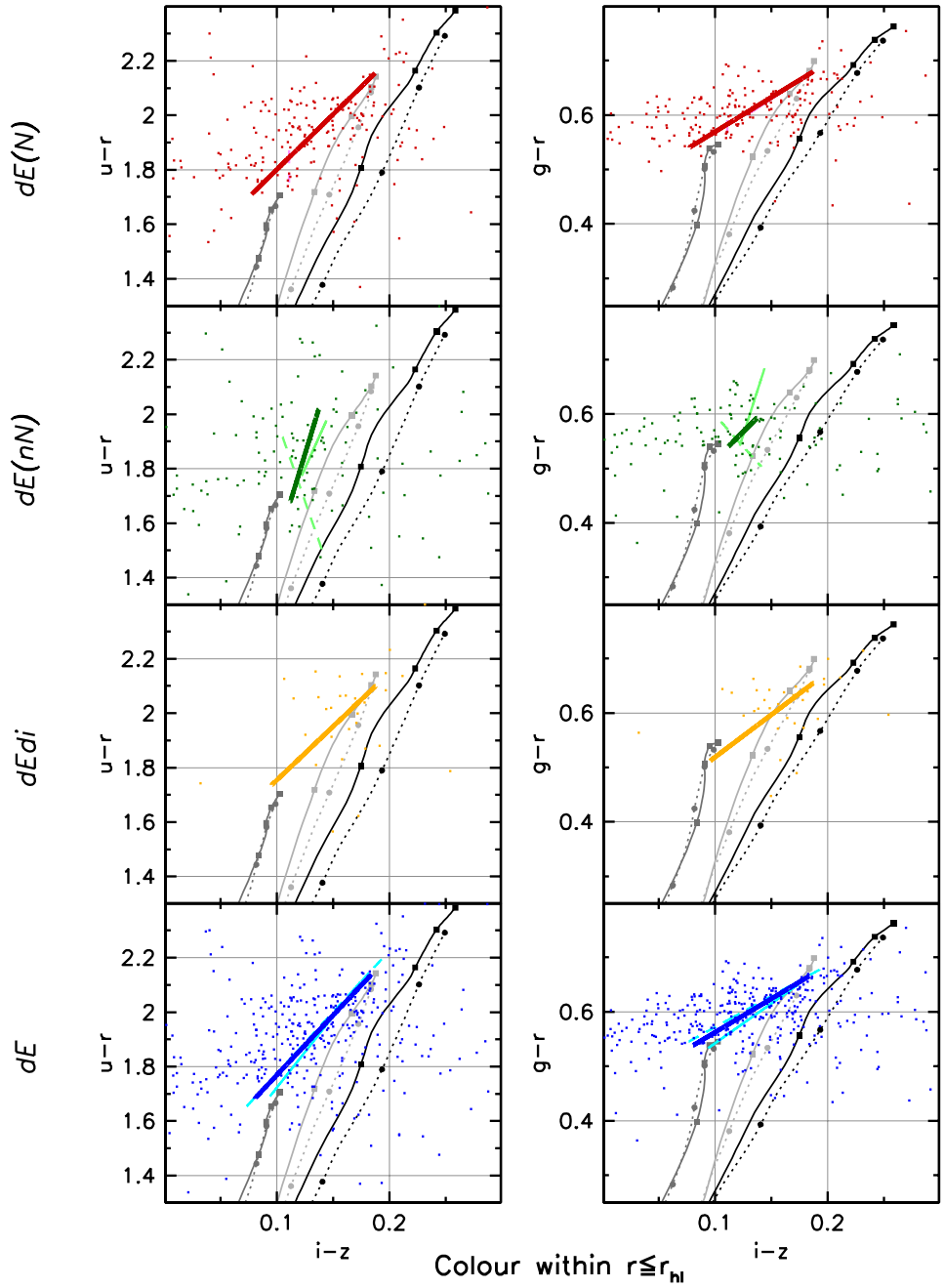

F 5.26. **Colour-magnitude vs. age-metallicity.** Location of the various CMRs in $u-r$ vs. $i-z$ and $g-r$ vs. $i-z$ diagrams, along with theoretical tracks for the *exp* models. The top three rows show the CMRs for (bright and faint) dE(N)s, dE(nN)s, and dE(di)s, using the same colours and line shapes as in Figures 5.3 to 5.6. The bottom row shows the CMR of the full dE sample (blue line, excluding dE(bc)s) from Figure 5.11, along with the separate fits to the low and high-density subsamples (thin solid cyan line and thin dashed cyan line, respectively) from Figures 5.16 to 5.19. The dots are the indiviual colours of the galaxies in the respective subsamples. Colours are shown for the half-light aperture.

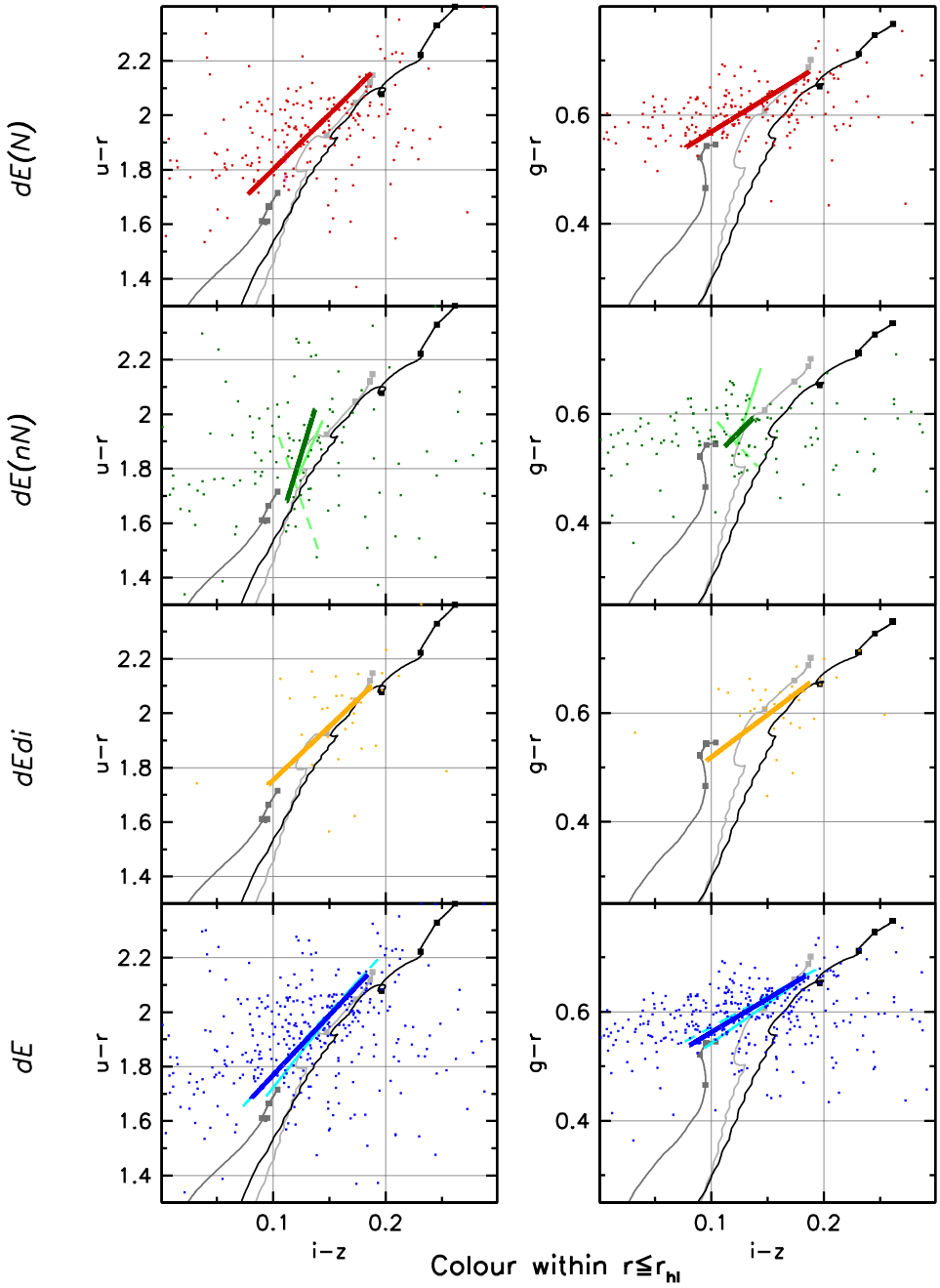

F 5.27. **Colour-magnitude vs. age-metallicity.** Same as Figure 5.26, but for the *burst* model.

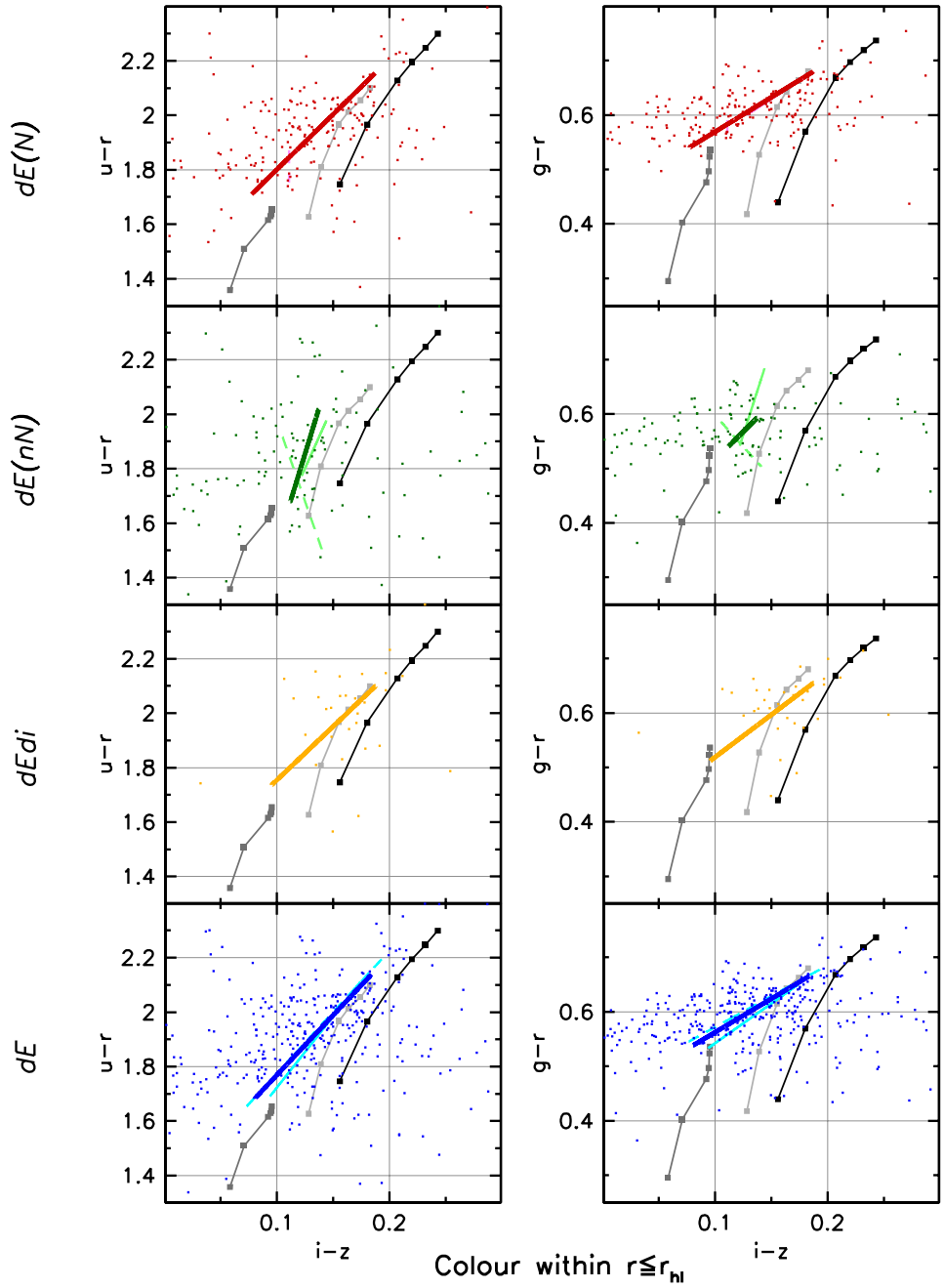

F 5.28. **Colour-magnitude vs. age-metallicity.** Same as Figure 5.26, but for the *const-b100* model.

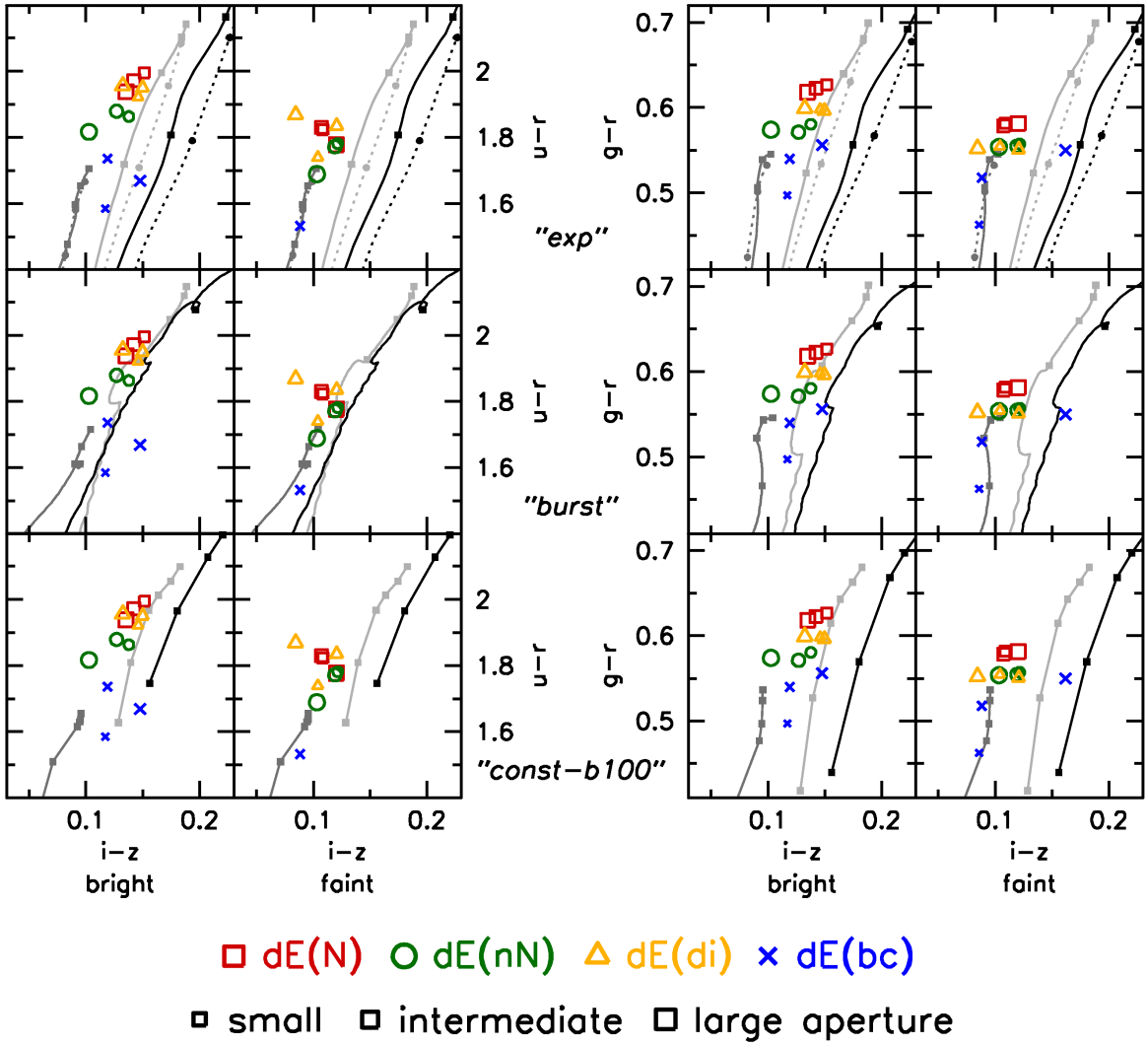

F 5.29. **Colour and stellar population properties of the dE subclasses.** Colour values of the CMRs of dE(N)s (red squares), dE(nN)s (green circles), dE(di)s (yellow triangles), and dE(bc)s (blue stars), measured at the bright and faint reference magnitudes, as labelled below the diagrams. Small symbols indicate colours measured within the small aperture, intermediate-size symbols represent the intermediate aperture, and large symbols mark the colours within the large aperture, to illustrate systematic gradients. In the left part of the figure we show $u - r$ vs. $i - z$ diagrams, while $g - r$ vs. $i - z$ diagrams are shown in the right part. Model tracks are shown for the *exp* models (top row), the *burst* model (middle row), and the *const-b100* model (bottom row).

13. S

We have analyzed the colours of 413 Virgo cluster dEs by constructing colour-magnitude relations (CMRs) for different dE subclasses and different local densities, as well as by comparing them to theoretical colours from population synthesis models of Bruzual & Charlot (2003). The CMRs of the dE(N)s, dE(di)s, and of the full dE sample (excluding dE(bc)s) are consistent with being mainly a relation of increasing metallicity with luminosity, with slightly smaller ages at higher metallicities. We found significant differences between the CMRs of dE(N)s and dE(nN)s, as well as between the CMRs at low and high local projected densities. The models imply that the dE(nN)s are younger than the dE(N)s, and possibly also have somewhat lower metallicities. The dE(di)s are more similar to the dE(N)s, yet are still found to be slightly younger on average. A significant intrinsic colour scatter of the CMR is present, and the colour residuals about the CMR are correlated between different colours for the dE(N)s, and partly also for the dE(nN)s, such that a galaxy falling on the blue side of the CMR in one colour also does so in the other colour.

While we found in Section 7 that dE(nN)s and dE(N)s follow different CMRs, we then discovered in Section 9 that the CMR depends on environmental density. Since we know that dE(nN)s and dE(N)s populate different density regimes, we should compare the CMR of the dE(nN)s to that of the *low-density* subsample of dE(N)s: the median density of the latter is 1.18 (in units of the logarithm of the number of galaxies per square degree), and it is 1.20 for the dE(nN)s. In contrast, the median density of the full sample of dE(N)s is 1.37. However, the CMR of the low-density dE(N)s is still significantly different from that of the dE(nN)s in $g-r$ and $g-i$; the probability for a common distribution is $\leq 0.1\%$ for the half-light aperture. Likewise, the colour difference at the bright reference magnitude between dE(N)s and dE(nN)s is $0\overset{\mathrm{m}}{.}09$ in $u-r$ and $0\overset{\mathrm{m}}{.}05$ in both $g-r$ and $g-i$ (half-light aperture), while between the low-density dE(N)s and the full dE(N) sample, it is only $0\overset{\mathrm{m}}{.}01$ in $u-r$ and $g-i$, and even lower in $g-r$. Thus, the colours of the (bright) dE(nN)s do differ from those of the dE(N)s even if we allow for the different sampling in density.

The same test can be done for the dE(di)s: their densities (median value 1.18) are also much more comparable to those of the low-density dE(N)s than to those of the full sample. However, their colours are already more similar to those of the dE(N)s: the differences to the full dE(N) sample at the bright reference magnitude are only $0\overset{\mathrm{m}}{.}02$ in $u-r$, $0\overset{\mathrm{m}}{.}03$ in $g-r$, and $0\overset{\mathrm{m}}{.}04$ in $g-i$. Nevertheless, the statistical comparison of the CMRs of the dE(di)s and the dE(N)s yielded significant differences for several colours and apertures. This changes when we compare the dE(di)s to only the low-density dE(N) sample: no statistically significant differences are found anymore. (Note, though, that the colours of the dE(di)s at the bright reference magnitude are still slightly bluer than those of the low-density dE(N)s.) Whether or not this could indicate a close relation between dE(di)s and dE(N)s despite their very different shapes will be discussed in Chapter 8.

We restricted our analysis of the dE colours to studying CMRs and mean colours instead of individual values — even though several CMRs are rather tight, their scatter is considerable in terms of the ages and metallicities that our model colours correspond to (see, e.g., Figure 5.26). Moreover, measurement uncertainties are of particular significance in $i-z$ because of the narrow range of model colours. This problem can be overcome by combining optical colours with near-infrared (NIR) photometry of similar S/N. Such NIR data is available for 22 of our dEs, and will be analyzed in Chapter 7. Nevertheless, in the optical we have the advantage of photometry being available for several hundred dEs — and we made use of this advantage by further exploring the colour scatter that we just mentioned. We found that the scatter is not of random nature, but that the colour residuals about the CMR are correlated between all colours for the dE(N)s, and between $u-r$ and $g-i$ for the dE(nN)s. Moreover, at least the dE(N)s are consistent with having a nearly "perfect" intrinsic correlation of colours, i.e., if the intrinsic $u-r$ colour of a dE(N) lies on the red side of the respective CMR, the same is true in almost all cases for the intrinsic $i-z$ colour. This is particularly interesting, since $u-r$ is more sensitive to the age of the stellar population, while $i-z$ is sensitive to metallicity. The straightforward interpretation would be that, when the stars in a dE are, on average, older than

the typical value at the dE's luminosity, then they are also more metal rich, and vice versa. Assuming a direct correlation between luminosity and galaxy mass, the intrinsic scatter of the CMR could thus be, for a given initial mass[7], reflecting a scatter in star formation rate (SFR), perhaps caused by environmental differences. A higher SFR at a given initial (gas) mass would, with neglect of other possible effects, lead to stronger enrichment, i.e. to a higher metallicity, than a lower SFR. The gas would be consumed more rapidly, thus reaching the end of star formation earlier than with a lower SFR, and consequently yielding older stars on average. Optical or even NIR photometry with higher S/N, especially in the important bands *u* and *z*, could provide further insight into this issue.

While a more extended discussion of dE formation will be presented in Chapter 8, we briefly want to compare our results to the ages and metallicities of dE(nN)s and dE(N)s derived by Rakos & Schombert (2004), based on narrow-band photometry for 91 dEs in the Coma and Fornax clusters. These authors derived ages above 8 Gyr for the dE(N)s, which they found to be about 5 Gyr older than the dE(nN)s. At least qualitatively, and in a relative sense, this would be consistent with our results, even though the age difference between the two subclasses seems to be smaller from our analysis. The latter might also be explained by the fact that the Virgo cluster is a dynamically less relaxed structure than the Coma and Fornax clusters. As for the metallicities, Rakos & Schombert found the dE(N)s to have *lower* metallicities than the dE(nN)s, conjecturing that "globular clusters and dEN galaxies are primordial and have metallicities set by external constraints such as the enrichment of their formation clouds." This is not in agreement with our results for the brighter magnitudes: there, we find the metallicities of the dE(N)s to be similar (in the inner part of the galaxies) or higher (for apertures larger than half-light) than those of the dE(nN)s (cf. Figure 5.29). However, for the fainter magnitudes and within the half-light radius, the dE(nN)s seem to be consistent with having slightly larger metallicities than the dE(N)s. This result is also illustrated in Figures 5.26 to 5.28, where it can be seen that the CMR of the dE(N)s spans a larger range in metallicity than that of the dE(nN)s, thus reaching below the latter at the faint end. However, for these magnitudes and apertures, the age difference that we find between the two subsamples is small compared to that found between the bright dE(N)s and dE(nN)s. We also note that the fainter dE(nN)s show a considerable colour scatter, and that the sample of Rakos & Schombert (2004) only comprises 10 dE(nN)s of the Coma cluster and 9 dE(nN)s of the Fornax cluster. Thus, while it would seem unlikely to us that the dE(nN)s and dE(N)s in Virgo behave inversely to those in the other clusters, there seem to be at least some possible explanations that could account for the different results of our studies. Whether or not dE(N)s could, from the perspective of our Virgo cluster study, be a primordial population of galaxies will be discussed in Chapter 8.

Acknowledgements

We are grateful to Niranjan Sambhus for useful suggestions on statistical tests, and to Ignacio Ferreras for information on studies of the colour-magnitude relation. This study is based on publicly available data from the SDSS.

[7] Of course, the initial *gas* mass can most likely not be mapped one to one with the final *stellar* mass, indicating that there might be many other possible interpretations.

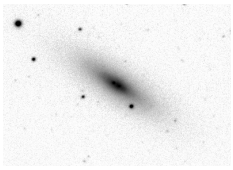

CHAPTER 6

S V

"Diversity is a good thing!"
Liese van Zee

Following up on our analysis of the optical colours and the stellar populations of 413 Virgo cluster early-type dwarf galaxies (dEs) from Chapter 5, we investigate whether colour and stellar population substructure is seen within the cluster, i.e., whether significant differences occur between different cluster regions. We find no significant variations across the cluster in the colour residuals about the fit to the CMR, neither for the dE(N)s, dE(nN)s, nor for the full dE sample. We then apply a simple mapping between observed and model colours, thereby translating colours into ages and metallicities. Most of the variations seen in the age and metallicity distribution across the cluster are not significant, based on Monte-Carlo simulated distributions. One structure, though, is strong enough to be real: within a region extending south-eastward from the Virgo cluster center, the stellar populations of the dE(N)s are, on average, somewhat older (~0.1 dex) than elsewhere in the cluster. We discuss this observation with regard to possible implications for dE formation.

This study was done together with Eva K. Grebel and Bruno Binggeli.

1. I

The Virgo cluster is a dynamically young structure — even its core is not yet relaxed (Binggeli et al. 1987, 1993; Arnaboldi et al. 2004). Its "central" galaxy, M 87, does actually not sit at the cluster center, neither in projected coordinates, nor in velocity space. However, it does coincide with the center of the X-ray emission from the intracluster medium (Böhringer et al. 1994). Furthermore, the cluster displays pronounced double structure (Figure 6.1, left panel): the main part, at declinations $\delta \gtrsim 10^{\circ}$ ("cluster A"; see Binggeli et al. 1993), and the concentration in the southern part ("cluster B") have significantly different velocity dispersions and galaxy compositions. Cluster B is, in contrast to cluster A, dominated by late-type galaxies, yet has a *smaller* velocity dispersion (Binggeli et al. 1987). Moreover, M 86, westward of M 87, appears to be part of a galaxy group that is in the process of merging with the main cluster (Binggeli et al. 1993; Böhringer et al. 1994). Obviously, the assembly of the Virgo cluster is still ongoing.

Based on the kinematic properties of Virgo cluster galaxies, Conselice et al. (2001) concluded that solely the population of giant elliptical galaxies (not including S0s) forms a relaxed or nearly relaxed system. No other (giant or dwarf) galaxy population shows characteristics of relaxation, consistent with the picture of a young, unrelaxed cluster, as described above. In Chapter 4, we analyzed the properties of several different subclasses of Virgo cluster early-type dwarf (dE) galaxies: dEs with disk features (dE(di)s), dEs with blue centers (dE(bc)s), nucleated ordinary dEs (dE(N)s), and ordinary dEs that have no or only a weak nucleus (dE(nN)s). We found that only the dE(N)s constitute a fairly relaxed population of galaxies. Moreover, our results are in agreement with those of Conselice et al. (2001): the distribution of the dE(N)s with local projected density is similar to those of the *combined* sample of Es and S0s, but the Es alone are, on average, located at even higher densities.

Potential colour and stellar population differences between the different dE subclasses have been analyzed in the previous chapter, with the result that the colour-magnitude relation (CMR) is different for dE(nN)s and dE(N)s, and also shows differences with local density. We now seek to use our sample of 413 Virgo cluster dEs, imaged with the Sloan Digital Sky Survey (Data Release 5, Adelman-McCarthy et al. 2007), to investigate whether the colours and stellar population characteristics of the dEs are homogeneously distributed throughout the cluster, or whether they show significant variation between different cluster regions. Given the amount of substructure that is present in the spatial and kinematical distribution of galaxies across the Virgo cluster (see above), it seems possible that the colours of the dEs reflect this substructure. If they indeed carried an imprint of their respective formation history, they could serve as tracers of the assembly history of the cluster.

Conselice et al. (2001) pointed out that the number of Virgo cluster dEs is more than a factor of 3 larger than what would be expected from just adding groups to the cluster. Similarly, van Zee et al. (2004b) argue that it is a reasonable assumption that most dEs do not enter the cluster as dEs, but that the cluster environment plays a crucial role in shaping them. It should thus be interesting to see whether we find any substructure in the distribution of the dE colours across the cluster that could be interpreted as originating from a group that has been recently accreted. If, instead, we would find substructure that traces the galaxy (or gas!) density within the cluster, this would support the picture that most dEs formed *within* the cluster potential. The proposed mechanisms for the transformation of late-type galaxies into dEs should typically be stronger or more efficient in the central regions of the cluster, or in regions of higher density: in the harassment scenario (Moore et al. 1996), the probability for close tidal encounters with massive cluster galaxies is higher in those regions. The same would be expected for the scenario of tidally induced star formation in dwarf irregulars (Davies & Phillipps 1988). Finally, the efficiency of ram-pressure stripping must obviously be larger in regions with a higher density of intracluster gas. We thus search for an imprint of these processes in the colours and stellar populations of our dEs, thereby trying to come one step closer to answering the question of "nature or nurture".

2. D

The SDSS DR5 covers all galaxies listed in the Virgo cluster catalog (VCC, Binggeli et al. 1985), except for an approximately $2^\circ \times 2.^\circ5$ area at $\alpha \approx 186.^\circ2$, $\delta \approx +5.^\circ0$. It provides reduced images taken in the *u*, *g*, *r*, *i*, and *z* bands with an effective exposure time of 54s in each band (see also Stoughton et al. 2002), as well as the necessary parameters to flux calibrate them. The pixel scale of $0.''396$ corresponds to a physical size of 30 pc at our adopted Virgo cluster distance of $d = 15.85$ Mpc (distance modulus $m - M = 31.^m0$; see, e.g., Ferrarese et al. 2000), which we use throughout. The RMS of the noise per pixel corresponds to a surface brightness of approximately 24.2 mag arcsec^{-2} in the u-band, 24.7 in *g*, 24.4 in *r*, 23.9 in *i*, and 22.4 in z.

The images have an absolute astrometric accuracy of RMS$\leq 0.''1$ per coordinate, and a relative accuracy between the *r* band and each of the other bands of less than 0.1 pixels (Pier et al. 2003). They can thus easily be aligned using their astrometric calibration and need not be registered manually. Furthermore, adjacent SDSS images can be accurately put together, allowing the extraction of cutout images that fully cover a given object, even if the latter lies at the edge of an SDSS image.

Since the sky level on the SDSS images can vary by some tenths of the noise level across an image, it is not sufficient to subtract only a single sky flux value from each image. We therefore determined the sky flux distribution across a given image using a thorough procedure, as described in detail in Chapter 4. The sky-subtracted images were then flux calibrated and corrected for Galactic extinction (Schlegel et al. 1998). We also correct for the reported SDSS zeropoint offsets in the *u* and *z* bands from the AB system (Oke & Gunn 1983, see http://www.sdss.org/dr5/algorithms/fluxcal.html), as described in more detail in Chapter 5.

Our working sample of Virgo cluster dEs contains 413 certain cluster members that were initially classified as early-type dwarfs in the VCC (''dE" or "dS0", including candidates), that are brighter than $m_B \leq 18.^m0$, that passed our visual examination for possible dwarf irregulars, and for which a Petrosian radius could be derived. The details of our sample selection are described in Chapter 4.

Total galaxy magnitude in the *r* band is measured within an elliptical aperture of two "Petrosian semimajor axes", i.e., ellipses instead of circles were used in the calculation of the Petrosian radius (Petrosian 1976; Lotz et al. 2004a); see Chapter 4 for further details. For each galaxy and band, we measured colours within three elliptical apertures: $a \leq 0.5\, a_{\rm hl,r}$ ("small aperture"), $a \leq a_{\rm hl,r}$ ("intermediate aperture" or half-light aperture), and $a \leq 2\, a_{\rm hl,r}$ ("large aperture"), where $a_{\rm hl,r}$ is the half-light semimajor axis in *r* (see Chapter 4).

3. T -

Our aim is to study the two-dimensional distribution of the stellar population properties of our dEs across the Virgo cluster. For this purpose, we define two-dimensional (2-D) circular bins within which we can calculate the average value of a given quantity, e.g., the average colour residual about the CMR. We choose the bin radius to be $1.^\circ46$, which corresponds to one tenth of the range in declination covered by the Virgo cluster member galaxies. A bin is placed every $0.^\circ37$ in right ascension and declination, which is one quarter of the bin radius. Instead of the "normal" right ascension, we use a "corrected" right ascension, defined as

$$\alpha_{\rm corr} = (\alpha - 182^\circ) \cdot \cos(\delta) + 182^\circ \quad , \tag{15}$$

to be able to perform all calculations in true degrees.

Figure 6.1 shows the distribution of all Virgo cluster member galaxies from the VCC (left panel). From this distribution, we obtain a map of galaxy density across the cluster (right panel): every pixel represents one of our bins, and the pixel value is, in this case, the number of galaxies within the circle defined above. For this density map, we compute isophotal contours that represent lines of constant galaxy number density (middle panel). Throughout this chapter, we will illustrate the results of our 2-D binning in the same way, i.e., by presenting an "image" of the Virgo cluster that contains the computed quantities as pixel values. The number density contours will be included in

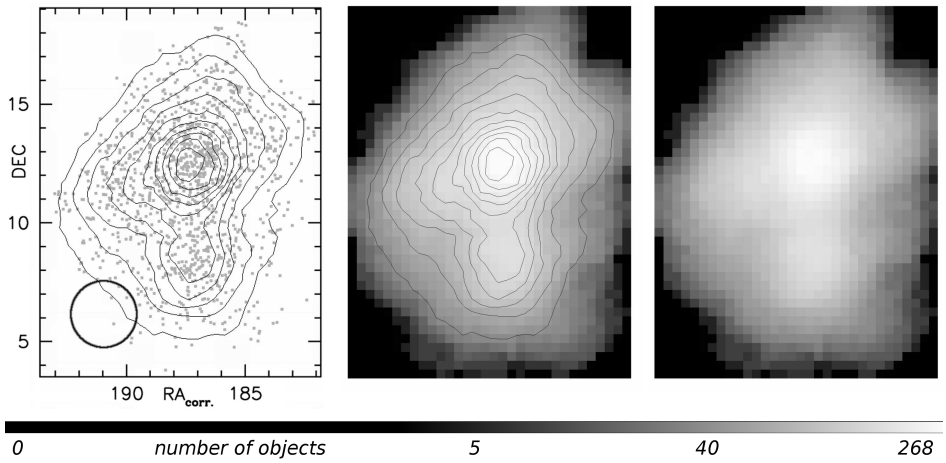

F 6.1. **Distribution of Virgo cluster galaxies.** *Left:* Projected spatial distribution of all Virgo cluster galaxies that are certain cluster members (grey dots), along with an illustration of the size of our two-dimensional circular bin, and the number density contours (see below). The x-axis gives a "corrected" right ascension, such that the cos(δ) factor is taken into account: $\alpha_{\rm corr} = (\alpha - 182^\circ) \cdot \cos(\delta) + 182^\circ$ (labelled "$\rm RA_{corr.}$" in the figure). *Middle:* Image representing the number of galaxies within our circular bin, calculated at every pixel. Brighter pixels mean a larger number of objects; see the scale bar below the figure. Isophotal contours – equivalent to number density contours – are constructed with *SAOImage DS9* (Joye & Mandel 2003, using a "smoothness" value of 1), with the outermost contour at a value of 26 galaxies per bin, and the innermost one at 251 galaxies per bin, in linear steps of 25. *Right:* Same as middle panel, but without showing the contours.

those illustrations, acting as a crude map of the Virgo cluster and enabling a direct comparison of any potential substructure with galaxy clustering properties.

As a first application of the 2-D binning, we present in Figure 6.2 the distribution of *r* magnitudes of our dEs within the cluster, for the dE(N)s (top row), dE(nN)s (second row), dE(di)s (third row), and the full sample of dEs (bottom row). Here, pixel values are the average of the *r* magnitudes of the galaxies within a given bin, applying two iterations of clipping at $3\,\sigma$. The brighter a given pixel is, the brighter are, on average, the galaxies within it (see the scale bar below the figure for the corresponding values). Bin values are only calculated if three or more galaxies contribute to it. The second column illustrates the error estimate for each pixel's value. It is derived by quadratically adding the individual magnitude errors of the contributing galaxies. Where fewer objects contribute to a pixel, or where more faint objects contribute, the error will be larger, reflecting the larger uncertainty in the pixel value. As a further reference, we show in the third column the number of galaxies contributing to each bin, similar to Figure 6.1. A brighter pixel indicates a larger number of objects within the bin radius.

While the dE(N)s show a rather homogeneous distribution of magnitudes, the dE(nN)s are obviously fainter on average towards the cluster center and south-west from it. This simply reflects the clustering distributions found in Chapter 4: while the faint and bright dE(N)s are distributed similarly, the bright dE(nN)s are, on average, located in less dense regions than the faint dE(nN)s. For the dE(di)s, not much can be seen from the present figure, except that they are among the brightest dEs. Due to the small number of dE(di)s within each bin (third column), as well as in total, we do not consider the dE(di) sample in our following analysis of galaxy colour distributions. (However, the dE(di)s are of course kept in the full dE sample.)

In addition to the magnitude distribution, we show in the right panel of Figure 6.2 the distribution of apparent axial ratios across the Virgo cluster. Here, we calculated the mean of the axial ratios of the galaxies in each bin, again clipping two times iteratively at $3\,\sigma$. The axial ratio measurements are described in Chapter 4. The brighter a given pixel is, the larger is the average axial ratio, i.e.,

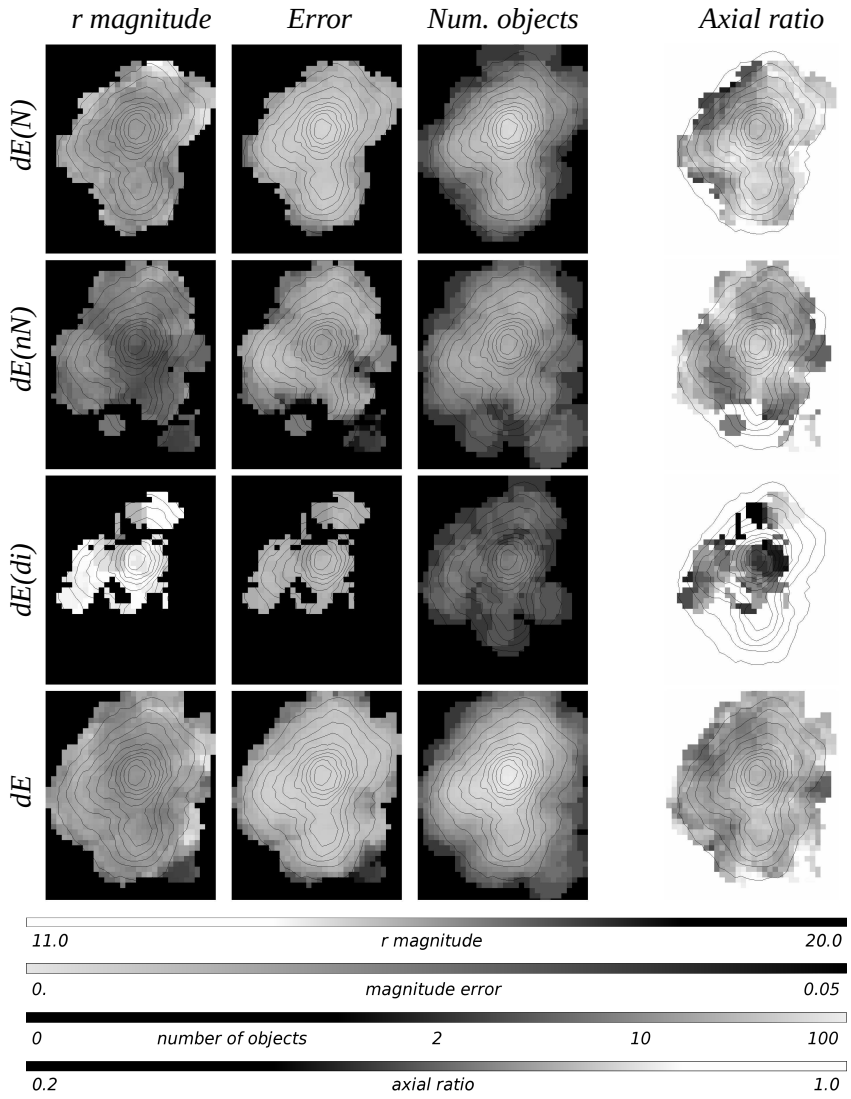

F 6.2. **Distribution of magnitudes and axial ratios.** *First column:* Distribution of *r* magnitudes for dE(N)s, dE(nN)s, dE(di)s, and all dEs, from top to bottom. Brighter pixels indicate a brighter mean magnitude; see the scale bar below the figure. *Second column:* Errors on each pixel, derived from the individual errors on the *r* magnitudes. Brighter pixels indicate lower errors. See text for details. *Third column:* Number of objects contributing to each pixel. Brighter pixels indicate a larger number of objects. *Fourth column:* Distribution of apparent axial ratios. Brighter pixels indicate larger axial ratios, i.e., rounder objects.

the rounder appear the galaxies within it. While we do not have an error estimate for the axial ratios themselves, the magnitude errors (second column) and the number of contributing galaxies (third column) again provide a useful reference for the reliability of the value of a given bin.

It can be clearly seen that the “axial ratio map” (rightmost column) and the “magnitude map” (leftmost column) of the dE(nN)s show very similar substructure. This is another way of illustrating the results found in Chapter 4: brighter dE(nN)s are located in regions of lower density *and* have flatter shapes than the fainter dE(nN)s. However, it is interesting that also for the dE(N)s, some substructure in the distribution of axial ratios is seen, different from the distribution of magnitudes. Apparently, the roundest objects on average are found in the north-western part of the cluster, as well as south-east from the center. The difference is not too large, though; the values at the cluster center are about 0.05 smaller than in the regions with the highest values. It might thus be that what we see is, at least partly, a statistical effect, caused by the fact that perfect “randomness” of the distribution

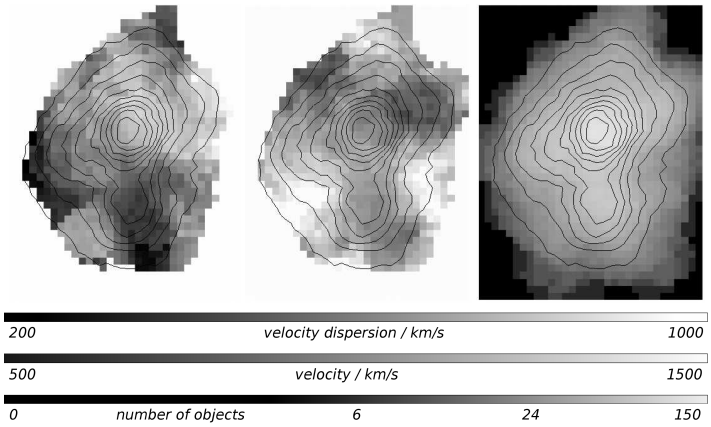

F 6.3. **Velocity distribution of Virgo cluster galaxies.** Velocities for 529 VCC galaxies are available from the NED. *Left:* Distribution of local velocity dispersion, i.e., the standard deviation around the mean value calculated for each bin. Brighter pixels indicate a larger velocity dispersion; see the scale bar below the figure. *Middle:* Distribution of velocities. Brighter pixels indicate a larger mean velocity. *Right:* Number of objects contributing to each pixel. Brighter pixels indicate a larger number of objects.

of inclination angles under which a galaxy is seen would require a larger number of galaxies per bin than present.

As another important issue, we point out that the size of any substructure will typically be *of the order of the bin size or larger*. To the eye of an astronomer who is used to faint galaxy images with a rather large noise level, a substructure like the one just described for the axial ratios of the dE(N)s looks significant; otherwise one would naively expect a noisier axial ratio map. This is, however, not the case: due to the fact that our bin size is several times larger than the steps between the bins, a tendency in one bin will always be present in the adjacent bins as well, creating the impression of well-defined substructure. We will come across this point again in our analysis of the colour distribution of our galaxies.

In Figure 6.3, we present, as another application of the 2-D binning technique, the distribution of local velocity dispersion, using all VCC member galaxies for which the NED provides velocity measurements (529 out of 1288 galaxies). At each pixel, we measure the standard deviation of heliocentric velocities (left panel) around the mean velocity (middle panel). The right panel illustrates the number of objects in each pixel that contributed to it. These maps provide an illustration of the distribution of velocities that is very similar to that of Binggeli et al. (1987, their Figures 24 and 26) and shows the same features. For example, the low velocity dispersion in the southern part of the cluster, extending south-westward from cluster B, had been interpreted by Binggeli et al. (1987) as an indication that cluster B is a separate cluster in its own right, not just a subconcentration. The region of lower than average mean velocity in the north-western part of the cluster might indicate galaxy infall from behind the cluster, while regions of higher than average mean velocity could imply infall into the cluster away from us (Binggeli et al. 1987). If we should find significant colour or stellar population substructure in our analysis below, we can make use of these velocity maps for comparing it to the kinematical substructure of the cluster.

4. C

We now want to analyze the distribution of the colour values of our dEs by applying the 2-D binning. However, a straightforward averaging of the colour values of the galaxies in each bin would not take into account that the primary determinant of a galaxy's colour is the colour-magitude relation (CMR; see Chapter 5). What we would actually like to know is whether galaxies in certain cluster

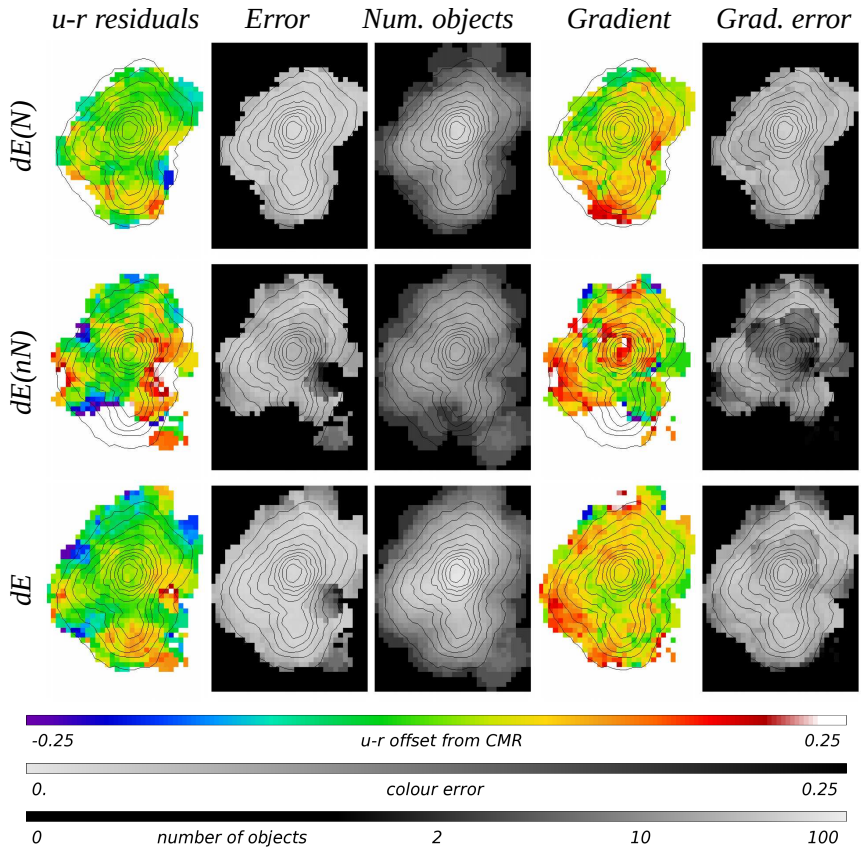

F 6.4. **Colour distribution within the Virgo cluster.** *1st column:* Map of the distribution of colour residuals about the respective CMR, for $u-r$ colour measured within the half-light aperture. Red pixels indicate positive residuals, i.e., colours that are redder than the CMR, blue pixels indicate negative residuals (bluer than the CMR); a scale bar is shown below the figure. From top to bottom, we show a map for the dE(N)s, the dE(nN)s, and for all dEs excluding dE(bc)s; each map is based on the CMR of the respective subsample. *2nd column:* Errors on the bin values in the left column, derived from quadratically adding the individual colour errors of each galaxy. Brighter pixels represent smaller errors; a scale bar is shown below the figure. *3rd column:* Number of galaxies contributing to each bin. Brighter pixels indicate a larger number of objects; see the scale bar below the figure. *4th column:* Map of the distribution of colour residual gradients, i.e., of the difference between the residuals measured for the small and the large aperture. Red pixels indicate that the residual is larger (i.e., redder) for the small aperture. The same scale bar applies as for the distribution of residuals shown in the first column. *5th column:* Errors on the bin values in the fourth column, derived from quadratically adding the individual colour gradient errors of each galaxy. These were obtained by quadratically adding the colour errors for the small and large aperture. Brighter pixels represent smaller errors; again, the same scale bar applies as for the colour errors shown in the second column.

regions are bluer or redder than others *with respect to the CMR*. Therefore, we compute for each 2-D bin the average colour *residual* about the CMR, instead of the average colour. As before, we apply two iterations of clipping values that deviate by more than $3\,\sigma$ from the mean.

In Figures 6.4 to 6.7, we present the distributions of $u-r$, $g-r$, $g-i$, and $i-z$ colour, respectively, for the dE(N)s, dE(nN)s, and for all dEs excluding dE(bc)s. The distributions of colour residuals, measured within the half-light aperture, is shown in the left column. The corresponding errors on each bin's value are given in the second column, derived from quadratically adding the individual colour errors of each galaxy. Brighter pixels represent smaller errors, i.e., more reliable measurements. The third column shows the number of galaxies contributing to each bin, as in the previous figures. The

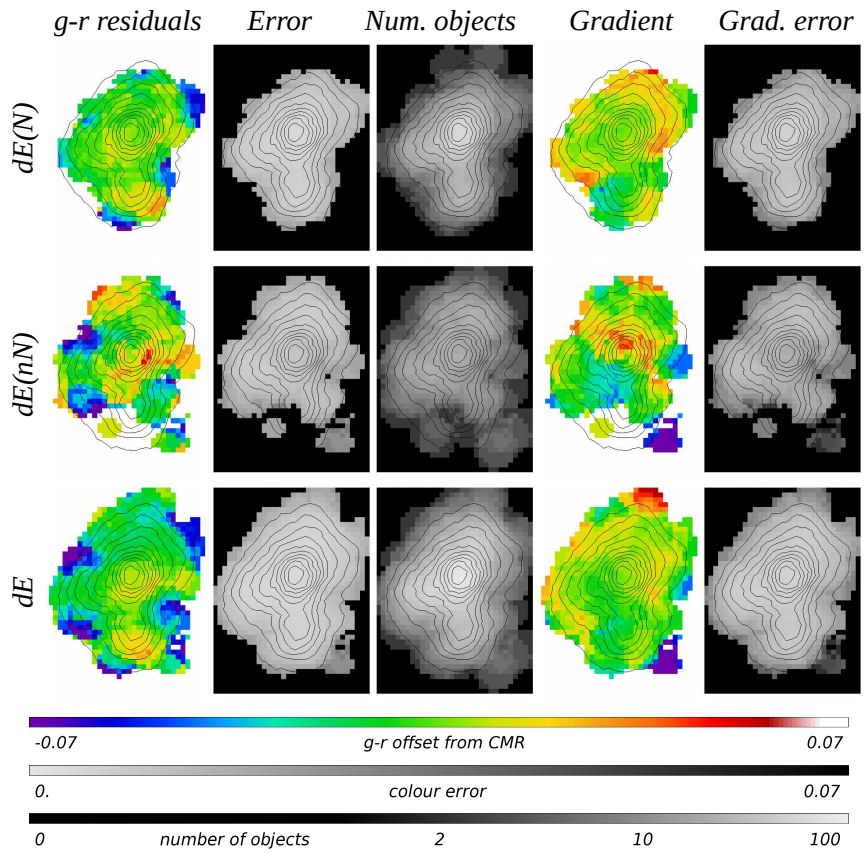

F 6.5. **Colour distribution within the Virgo cluster.** Same as Figure 6.4, but for $g - r$ colour.

fourth column contains the distribution of colour residual *gradients*, defined as the difference between the colour residual of the small and the large aperture. Red areas in the figure represent regions where the galaxy centers are, on average, redder than their outskirts — or more precisely, where the residuals about the CMR of the inner colours reach further towards the red than the residuals about the CMR of the outer colours. The corresponding errors on the bin values for the gradients are shown in the fifth column; they are calculated as above from the individual errors on the gradients. For a given galaxy, we compute the error on the colour gradient by quadratically adding the errors for the small and large aperture. Note that the scale bars below the figure apply equally to the colour values and colour gradients, as well as to the colour errors and gradient errors.

Colour substructure can be seen in basically all of Figures 6.4 to 6.7. A feature that is consistently present in all colours is the region at the southern end of the cluster where the dE(N)s are redder than average. For the dE(nN)s, the region westward of the cluster center displays redder than average colours in all of $u - r$, $g - r$, and $g - i$, while its $i - z$ values are bluer than in other regions. Note, however, that the number of galaxies in this region is also somewhat lower than in its surroundings. The full dE sample basically shows a combination of the above effects: the region of redder dE(N)s towards the southern cluster end is seen for the full sample as well, though somewhat weaker in $i - z$.

As for the colour gradients, no structure is really appearing consistently in all colours, or at least in all but $i - z$. It is suspicious that only weak systematic gradients seem to be present in $g - i$, where the errors are smallest, and rather strong gradients are seen in $u - r$ and $i - z$, where the errors are significantly larger. This makes clear that we need to test the reliability of any substructure seen in our colour maps. First, we need to know if and how strongly the residuals in a given colour are correlated with those in an other colour: the weaker these are correlated, the stronger is the confidence in any substructure that is seen in *all* colours. Second, since at least for the dE(N)s and for the full

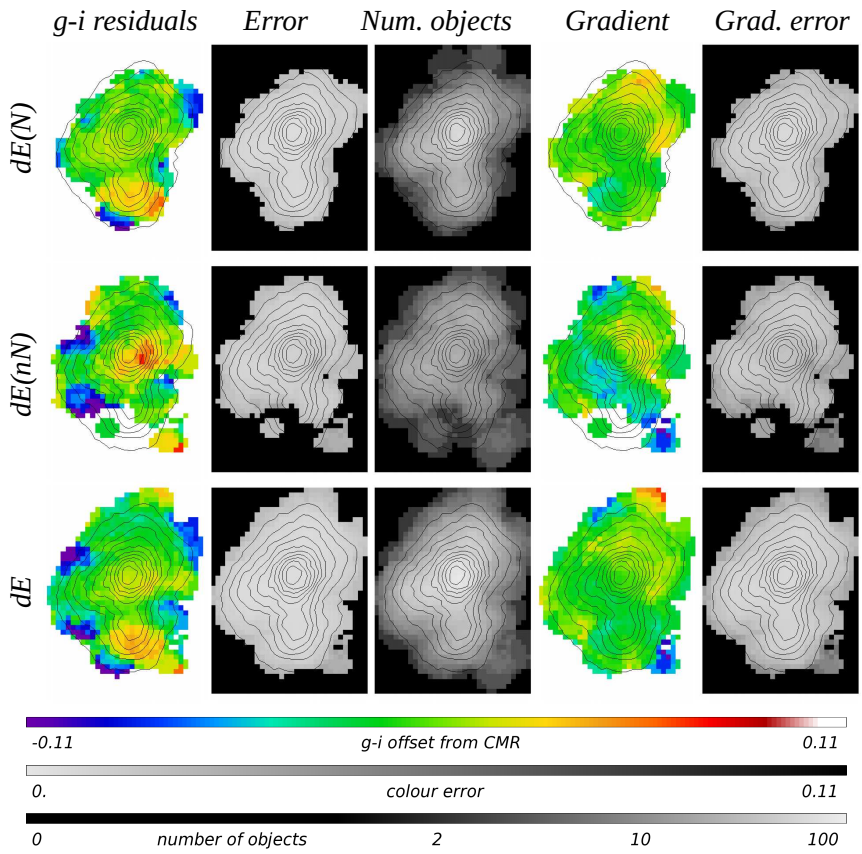

F 6.6. **Colour distribution within the Virgo cluster.** Same as Figure 6.4, but for $g - i$ colour.

sample, the CMR is fairly tight and well-defined (Chapter 5), we can create Monte-Carlo realizations of artificial colour maps by simply redistributing the residuals randomly among the galaxies.

The correlation of colour residuals between different colours has already been investigated in Chapter 5 (Section 10). We found there that the observed residuals are correlated between all colours for the dE(N)s and the full dE sample, and between $u - r$ and $g - i$ for the dE(nN)s. Moreover, the dE(N)s are consistent with having a nearly "perfect" intrinsic correlation of colours, i.e., if the intrinsic $u-r$ colour of a dE(N) lies on the red side of the respective CMR, the same is true in almost all cases for the intrinsic $i - z$ colour. This intrinsic correlation is, of course, diluted by the measurement uncertainties, which is why we can only state *consistency* with a "perfect" intrinsic colour correlation.

Due to these correlations, it is clear that the appearance of colour substructure in all bands for the dE(N)s (see above) and in all but $i - z$ for the dE(nN)s is *not* indicating a higher significance of the substructure — instead, it is simply a consequence of the colour correlations. We thus need to understand whether this substructure is significant at all, or whether it could be explained by statistical fluctuations alone. Therefore, we now proceed to the Monte-Carlo construction of artificial colour maps. What we would like to get an idea of is the strength and frequency of colour substructure that we would find due to sampling issues *only*, even if no true substructure was present and all galaxies followed exactly the same CMR. If we thus wanted to construct artificial colour maps from a given CMR and scatter, a crucial issue would be the modelling of this scatter: we find it to be larger than if it were caused only by measurement errors (Chapter 5), most likely due to the presence of at least some intrinsic scatter in the galaxy colours at a given magnitude. In principle, we could try to describe the scatter of the CMR by some analytic function (the common assumption of a Gaussian distribution is usually just wishful thinking), taking double care of the tails of the distribution in order to not underestimate possible substructure later. However, there is a more practical way that, at the same time, guarantees that the scatter is properly reproduced: we simply take the measured

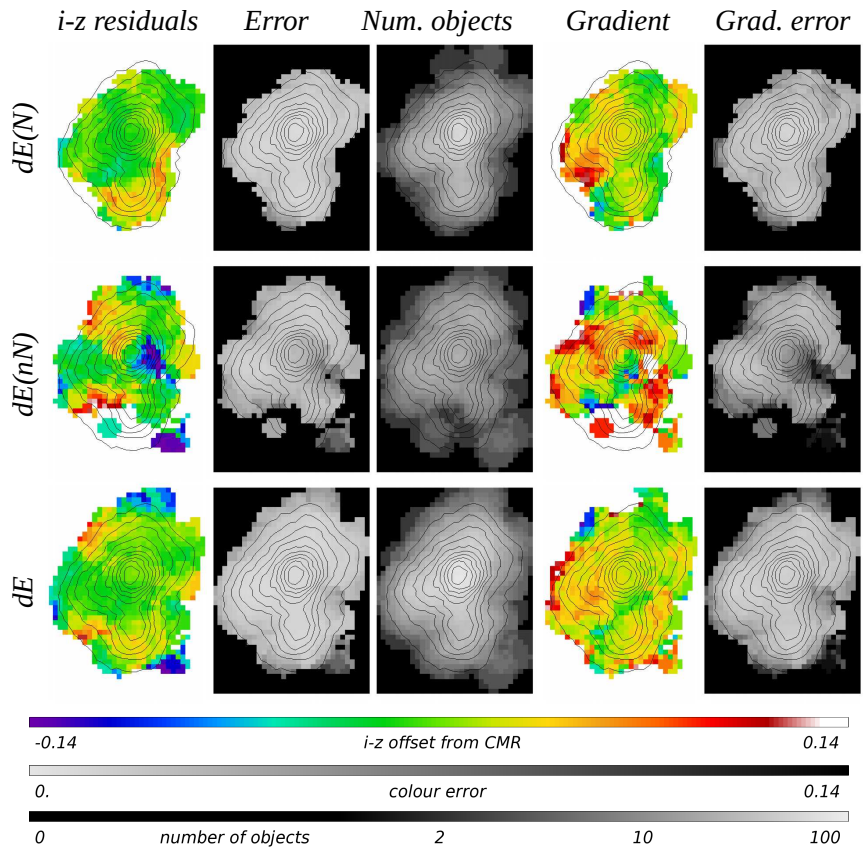

F 6.7. **Colour distribution within the Virgo cluster.** Same as Figure 6.4, but for $i - z$ colour.

colour residuals of our galaxies, and redistribute them randomly among them. The only critical issue here is whether or not the scatter of the CMR increases significantly with magnitude, such that, by random distribution, some "too large" residuals could be assigned to the brighter galaxies. However, if anything, this would make our method more conservative, since it would create too much artificial colour substructure.[1] Moreover, the CMRs of at least the dE(N)s and the full dE sample are fairly tight, supporting our approach.

Based on the above, we present in each of Figures 6.8 to 6.11 twelve artificial colour maps for the dE(N)s, resulting from random distributions of colour residuals. The same is shown for the dE(nN)s in Figures 6.12 to 6.15. Note that we redistributed the measurement errors along with the residuals: a residual could be large simply because of a large measurement error. Therefore, we do not split this "pair" of colour residual and error, but keep them together. These errors are used in the calculation of the errors of our bin values shown in the figures — if the value of a certain bin would be redder or bluer only because of large measurement errors that caused large residuals, this should be reflected in a rather large error for this bin.

Obviously, the amount and strength of substructure in our artificial colour maps is comparable to that in the observed ones. The observed substructure is thus not significant. Even for the southern feature of redder dE(N)s, which can be matched only by the strongest variations in the simulated colour maps at the given level of galaxy number density, we cannot reliably conclude that this feature is real. We also constructed colour maps and corresponding simulations using larger 2-D bins (bin radius $2\overset{\circ}{.}44$, not shown), in order to obtain more reliable values for each bin. However, while the artificial features in the simulated maps obviously become smaller, the real features do so as well, again leading to no significance of the structures seen — and again, the southern feature is rather

[1] Furthermore, this effect would only be present if the distribution of magnitudes across the cluster was not homogeneous, which is the case for the dE(nN)s, but only weakly for the dE(N)s.

strong as compared to the simulated variations, but not strong enough to be reliable. That the observed features become weaker with larger bin size could of course simply mean that no real substructure is present. It could, however, also mean that any real substructure occurs on smaller scales and is thus smoothed out — after all, the larger bins have a diameter equal to one third of the range in declination covered by the whole cluster. Note that the above considerations also apply to the colour residual gradients, since these are based on *two* sets of colours (those for the small and large aperture), and are thus even more prone to statistical variations.

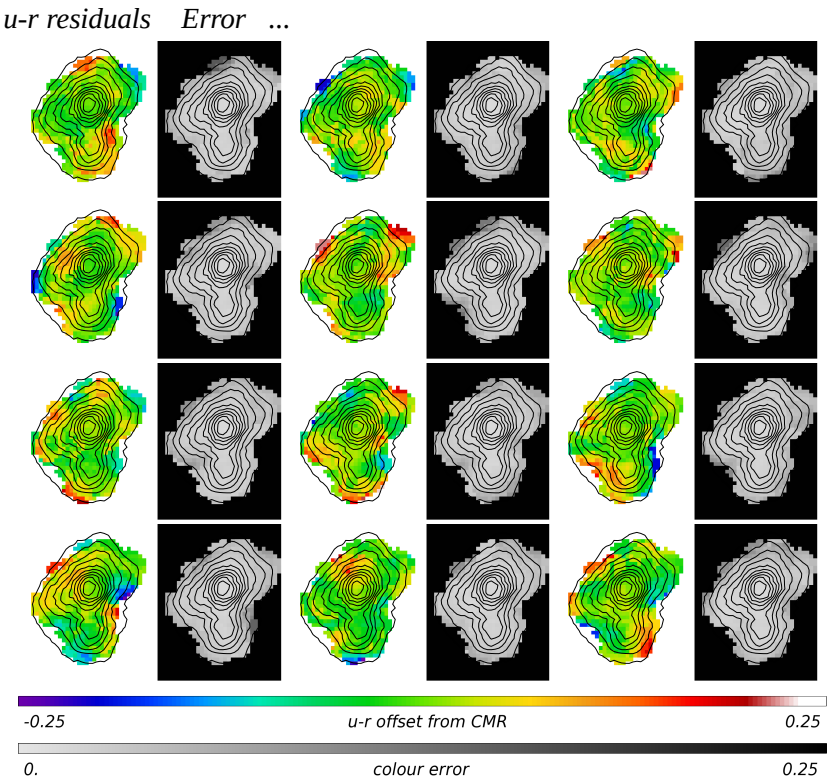

F 6.8. **Simulated colour distributions for dE(N)s.** Colour residual maps from twelve Monte-Carlo realizations of randomly distributed residuals of the dE(N)s in $u - r$ for the half-light aperture, along with corresponding error maps. See text for details.

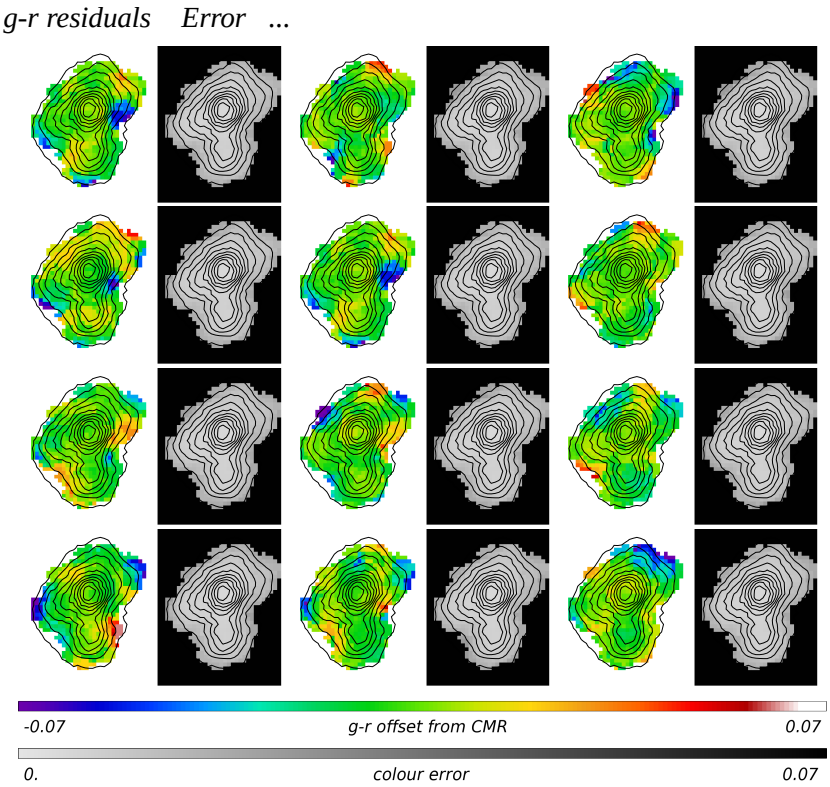

F 6.9. **Simulated colour distributions for dE(N)s.** Same as Figure 6.8, but for $g - r$ colour.

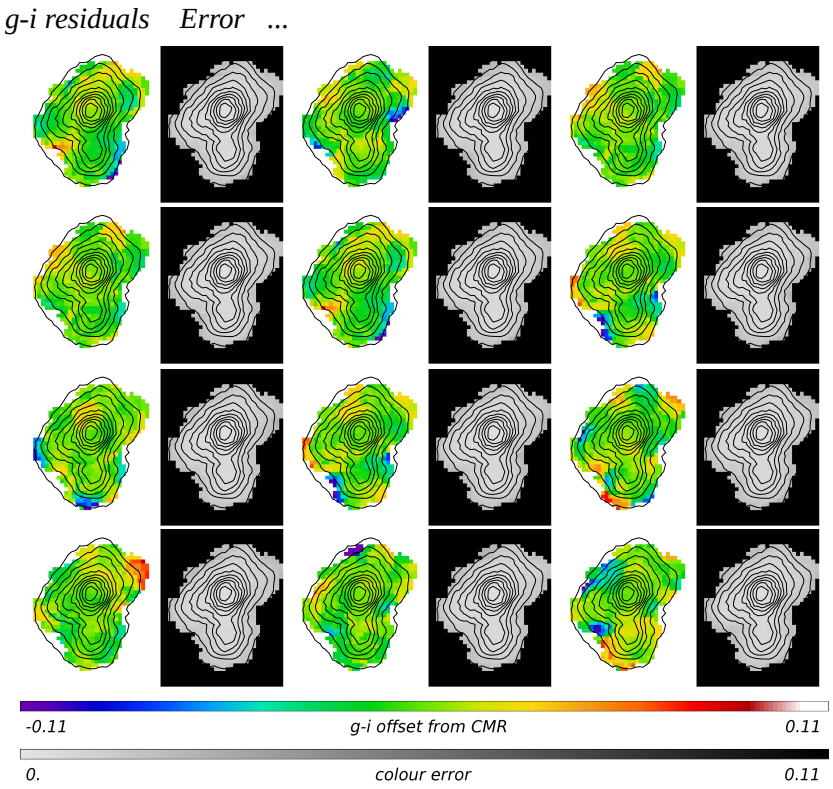

F 6.10. **Simulated colour distributions for dE(N)s.** Same as Figure 6.8, but for $g - i$ colour.

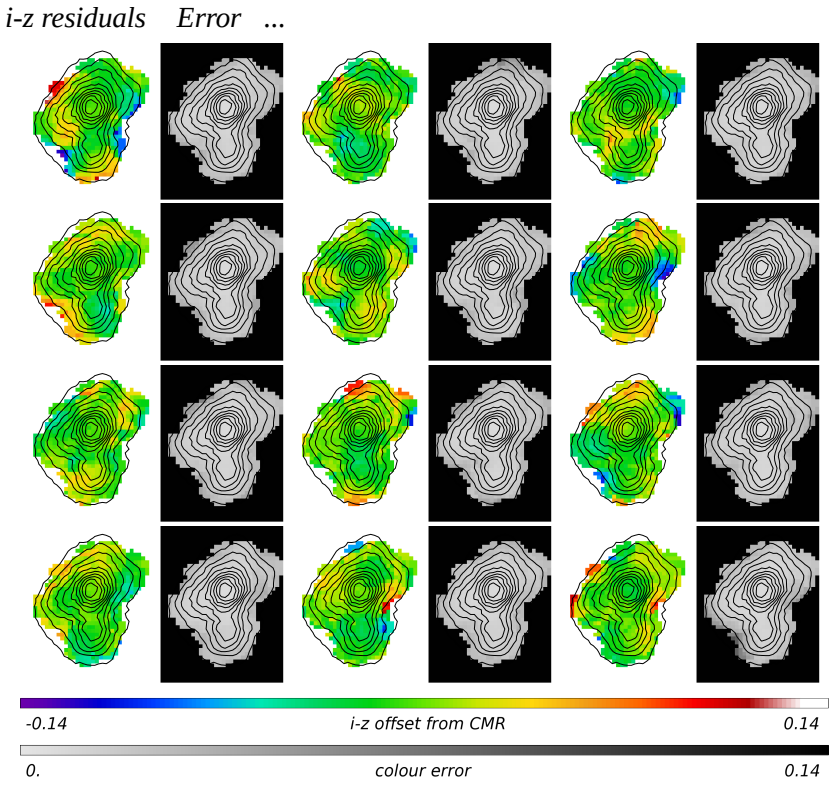

F 6.11. **Simulated colour distributions for dE(N)s.** Same as Figure 6.8, but for $i - z$ colour.

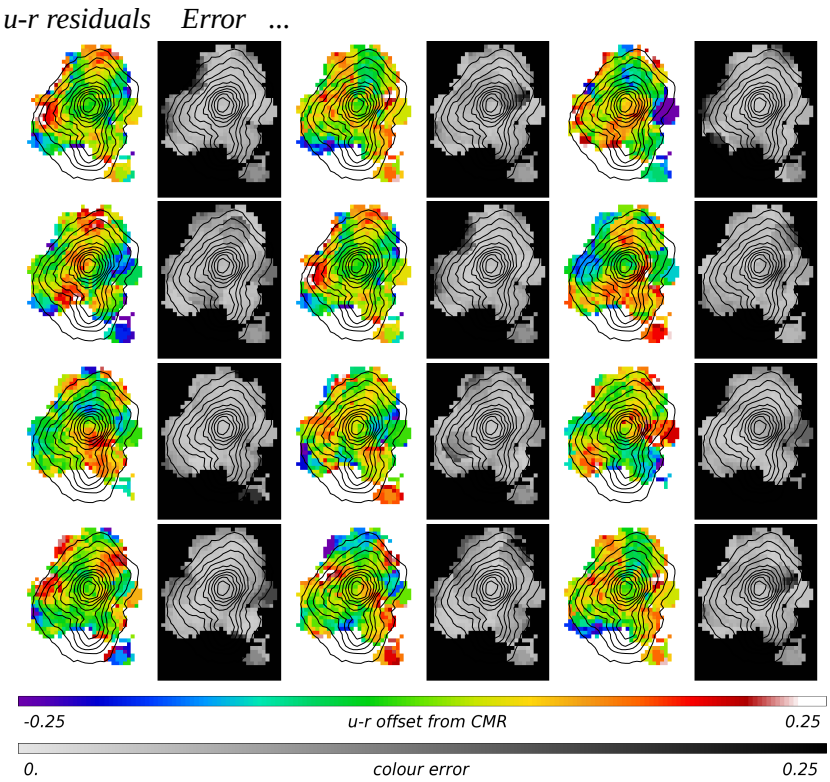

F 6.12. **Simulated colour distributions for dE(nN)s.** Same as Figure 6.8, but for the dE(nN)s.

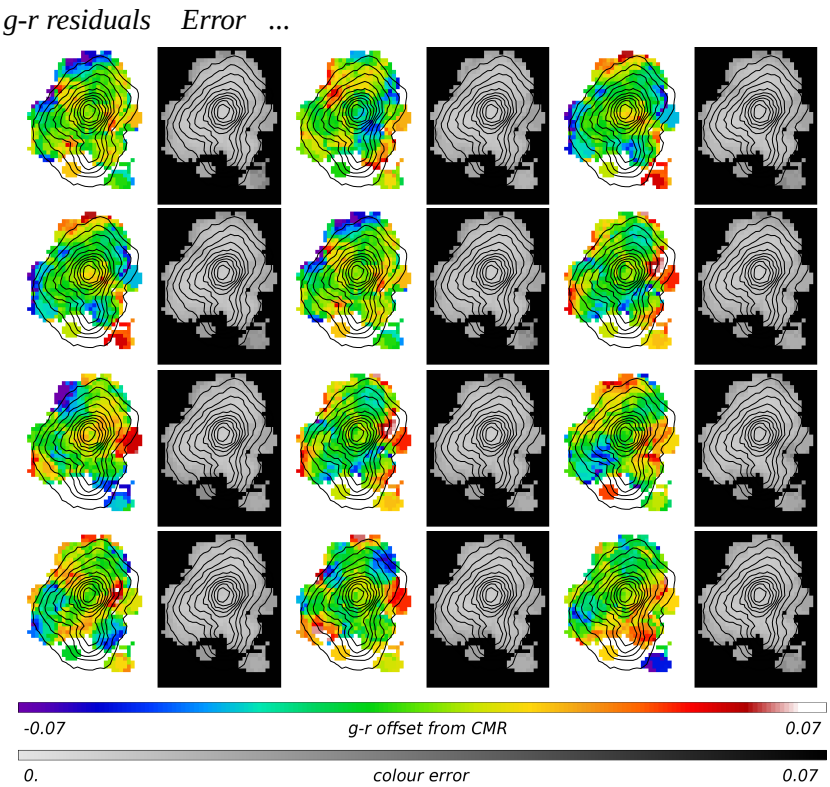

F 6.13. **Simulated colour distributions for dE(nN)s.** Same as Figure 6.12, but for $g - r$ colour.

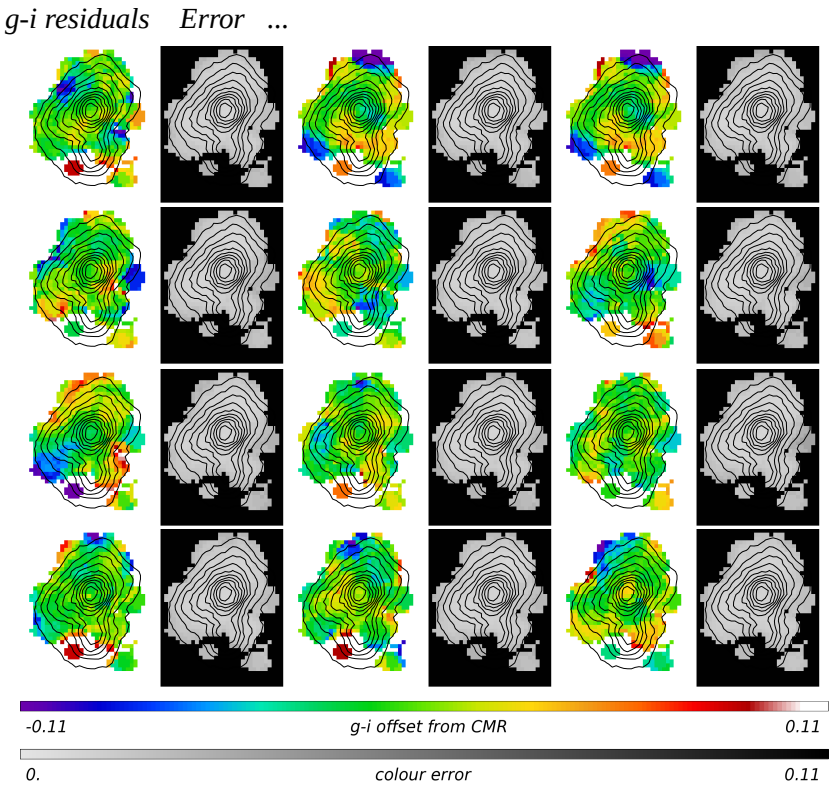

F 6.14. **Simulated colour distributions for dE(nN)s.** Same as Figure 6.12, but for $g - i$ colour.

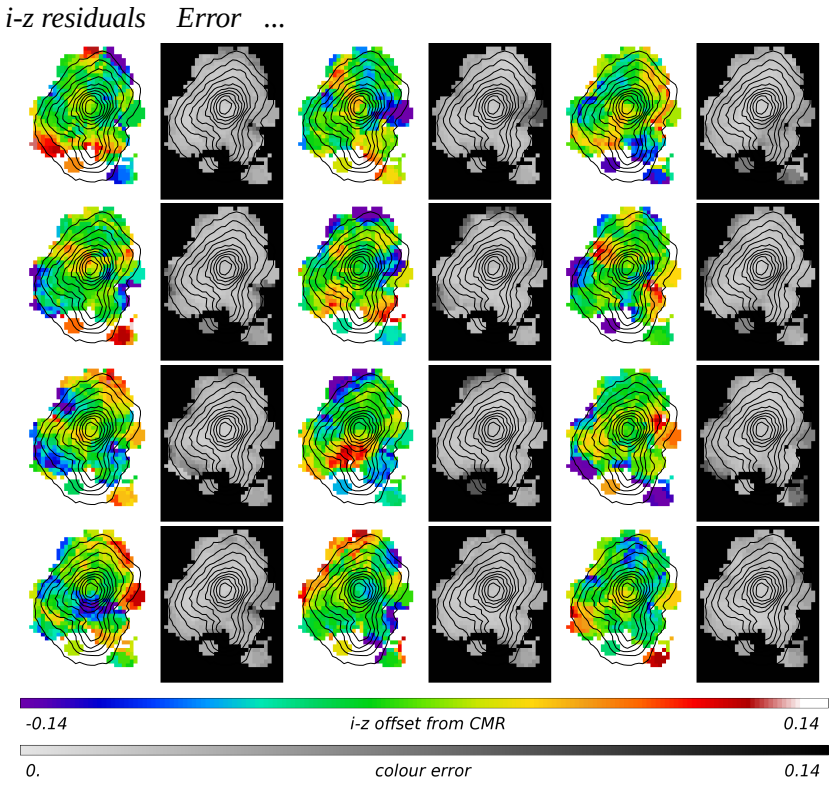

F 6.15. **Simulated colour distributions for dE(nN)s.** Same as Figure 6.12, but for $i - z$ colour.

5. T

Even though the colour residuals about the respective CMRs show no significant substructure, we aim at investigating whether the stellar population ages and/or metallicities do, since these rely on the actual colours, not on the colour residuals. For this purpose, we use some of our population synthesis models from Chapter 5, which are briefly described again below. We then proceed by assigning a value for age and metallicity to each galaxy by comparing observed and model colours.

5.1. Population synthesis models

Our population synthesis models are described in detail in Chapter 5. Briefly, they were constructed using the population synthesis code from Bruzual & Charlot (2003), with "Padova 1994" isochrones (Bertelli et al. 1994), a Chabrier initial mass function (IMF; Chabrier 2003), and the Bruzual & Charlot high resolution files, which rely on the STELIB spectral library in the wavelength range 3200 – 9500 Å and on the BaSeL 3.1 spectral library outside this range (see Bruzual & Charlot 2003, and references therein). We assume that the first stars have formed at about 13.5 Gyr, since we adopt a concordance cosmology with $H_0 = 71$ km s^{-1} Mpc^{-1}, $\Omega_\mathrm{m} = 0.27$, $\Omega_\Lambda = 0.73$, in which the Big Bang occured 13.67 Gyr ago (Wright 2006).

We constructed three main models: a single burst of star formation with exponential decay (*exp* model), a model consisting of ten short bursts of star formation occuring within 1 Gyr (*burst* model; cf. Davies & Phillipps 1988), and a model with constant star formation since the Big Bang that is truncated at a certain epoch (*const* model). From our comparison of several variants of these models in Chapter 5, we prefer to use in our analyses the following variation of the *const* model: at the point of time when star formation is truncated, the galaxy experiences one final short burst of star formation during which the star formation rate is boosted by a factor of 100 (*const-b100* model).

Given the definition of our models, the "age" of a given stellar population can have different meanings: for both the *exp* and *burst* models, "age" means the time since the beginning of star formation. For the *const-b100* model, the analogue to age is the time of truncation of star formation: younger ages correspond to more recent truncation times. Nevertheless, we prefer to speak only of "age" in our later analysis, thereby meaning either age or truncation time. Another difference is that due to the nature of the models, the model tracks (curves of constant metallicity) consist of 60 or more age points for the *exp* and the *burst* models, whereas the *const* model only consists of six different truncation times calculated by us.

5.2. Assigning ages and metallicities

Following the considerations in Chapter 5, we will use both the $u - r$ vs. $i - z$ and the $g - r$ vs. $i - z$ diagrams for interpreting colours with ages and metallicities. The $u - r$ colour has the advantage of a larger colour spread between different model ages, but our photometric errors are significantly lower in $g - r$, which is why the latter is similarly useful. Figure 6.16 shows the *exp* model tracks in both diagrams, along with the measured half-light aperture colour values of the dE(N)s (red dots, top panels). To illustrate that a large part of the scatter of the data points is caused by the measurement errors, these are shown in the bottom panels of the figure.

We now assign to each observed data point the "closest" model data point (see below). For an individual object, this might of course lead to stellar population parameters that are way off from the true ones — but *average* trends in ages and metallicities should be found by this method. In the $g - r$ vs. $i - z$ diagram, we define the distance between an observed and a model point by simply taking the square root of the sum of the squared $g - r$ and $i - z$ distances, as in a cartesian coordinate system. This means that we weight both colours equally, since the ranges of colour values covered by the bulk of data points have similar widths. For the $u - r$ vs. $i - z$ diagram, we chose to weight the $u - r$ colour by a factor of $1/4$, since the relevant range of colour values is $\sim$4 times larger than in $i - z$.

The assignment is illustrated in the top panels of Figure 6.16 for the galaxy VCC 0009 (pink dot and line). Note that the x and y-axis are not shown with equal spacing in the figure. Obviously, if

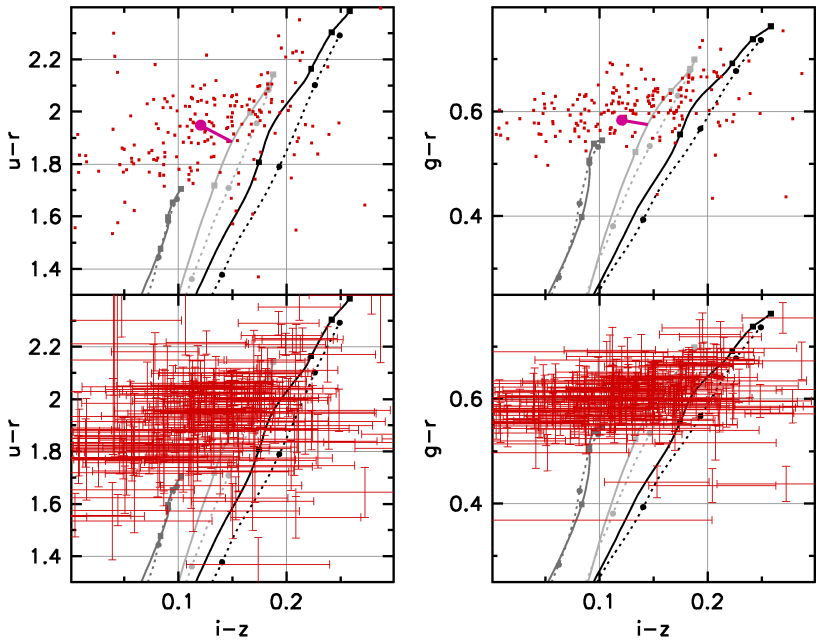

F 6.16. **Assigning ages and metallicities.** Shown are Bruzual & Charlot model tracks of constant metallicity for our *exp* models (see text) in the $u-r$ vs. $i-z$ and $g-r$ vs. $i-z$ diagrams. Metallicities are, from right to left, $Z = 0.008$ ($[Fe/H] = -0.33$, black), $Z = 0.004$ ($[Fe/H] = -0.64$, light grey), and $Z = 0.0004$ ($[Fe/H] = -1.65$, dark grey). The exponential decay time is $\tau = 1$ Gyr for the tracks shown as solid lines, and 2 Gyr for those shown as dotted lines. Ages are marked for each model track at 4.5, 7.5, 10.5, and 13.5 Gyr with filled squares (*exp-1* model) or filled circles (*exp-2* model). Moreover, we show the measured half-light aperture colour values of the dE(N)s (red dots, top panels), as well as the corresponding measurement uncertainties (red error bars, bottom panels). The top panels illustrate how an age and metallicity value is assigned to a given galaxy (pink dot and line); see text for details on how this is done.

this galaxy's $i-z$ colour would be just a bit bluer, it would not be assigned to the $Z = 0.004$ track, but instead to the $Z = 0.0004$ track and a much larger age. This shows the rather large uncertainty of this (and practically any other) procedure for an *individual* object; however, our aim is to derive *average* values, for which it should be useful. Error estimates for the assignment are obtained by propagating the colour errors through the distance calculation (and assuming zero error for the model points), which basically yields the error on the distance. In the 2-D diagrams below, the greyscale for these errors is chosen to range from 0 to $\sqrt{2} \cdot 0.05$; the latter is about one third of the relevant colour range for the assignment.

In order to see whether the colour-magnitude relation itself would lead to age and metallicity substructure within the cluster, e.g. due to regions with different average magnitude, we perform another assignment of ages and metallicities: instead of using the actual colour values of a given galaxy, we use the colour of the linear fit to the CMR at that galaxy's magnitude. We then perform the same assignment of ages and metallicities. This should also provide some insight into the effect that the discretization of metallicities can have on the assignment.

6. A -

After the assignment of ages and metallicities as described in the previous section, we apply our 2-D binning to these values. For each 2-D bin, we compute the average age and metallicity. Averaging is done on the logarithmic values, i.e., on log(*age*) and $[Fe/H]$, since ages are given in logarithmic

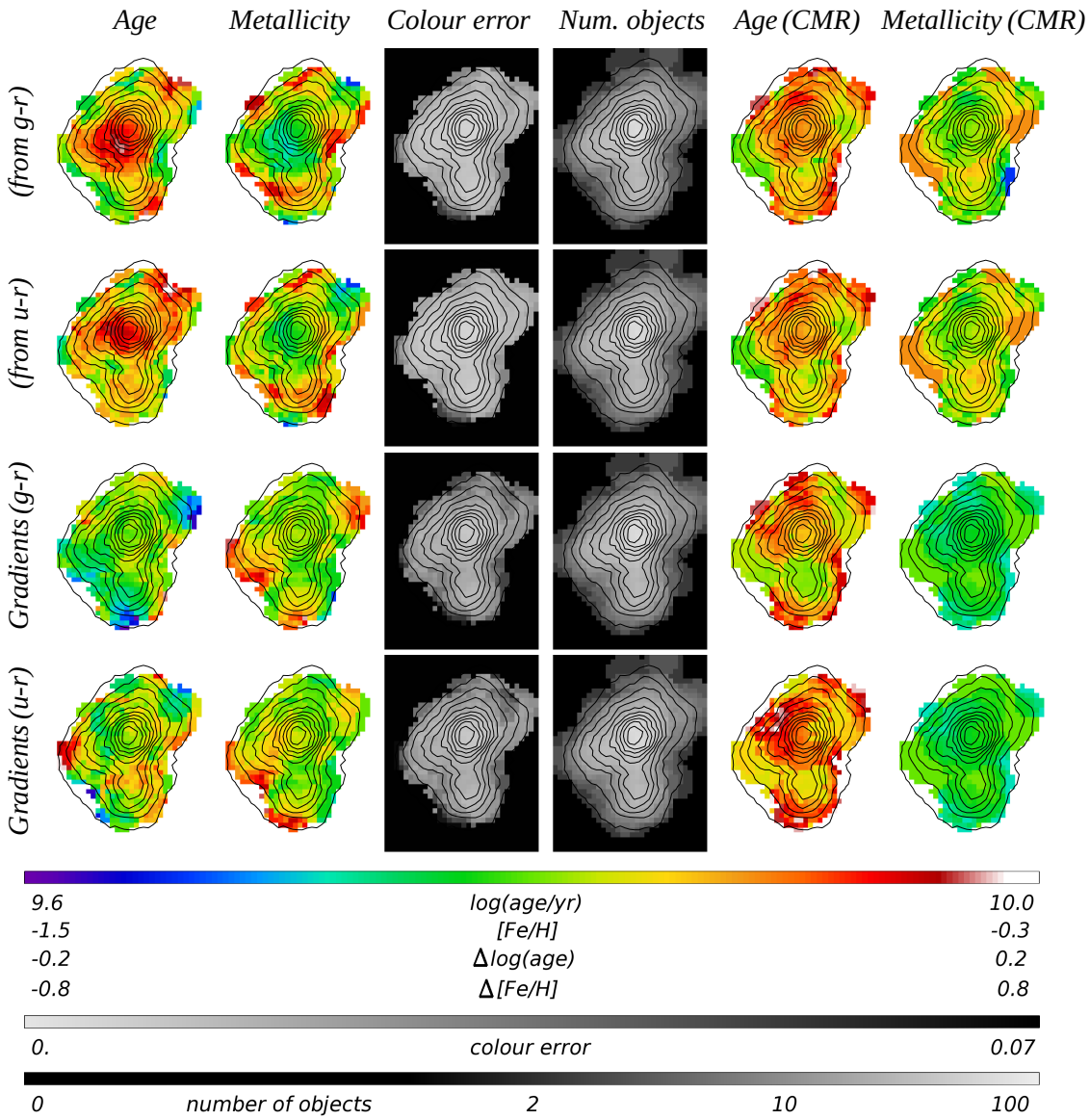

F 6.17. **Age and metallicity distribution of dE(N)s within the Virgo cluster.** *1st column:* In the top two rows, the age distribution is shown based on the *exp-1* model (see text), using the $g-r$ vs. $i-z$ colours (top row) and the $u-r$ vs. $i-z$ colours (second row), measured within the half-light aperture. The two bottom rows show the distribution of age gradients, i.e., the difference between the ages based on the small and the large aperture. Redder colour indicates a higher age in the inner regions of the galaxies; see the corresponding scale bar below the figure. *2nd column:* Same as the first column, but for metallicity. Redder colour indicates a higher metallicity (top two rows), or a higher metallicity in the inner regions of the galaxies as compared to the outskirts (bottom two rows). *3rd column:* Distribution of colour errors. For a given galaxy, an error for the age-metallicity assignment is derived by propagating its colour errors through the calculation of the distance to the model tracks in colour space. This basically corresponds to the error on that distance. For the gradients (bottom two rows), we add quadratically the errors for the small and the large aperture. The error on the value of a 2-D bin is then derived by quadratically adding the errors of the galaxies contributing to it. A corresponding scale bar is given below the figure. *4th column:* Number of galaxies contributing to each bin. Brighter pixels indicate a larger number of objects; see the scale bar below the figure. *5th column:* Age distribution as the first column, but based on the colour values of the CMR at each galaxy's magnitude, instead of the actual colour values of the galaxies. *6th column:* Same as the fifth column, but for metallicity.

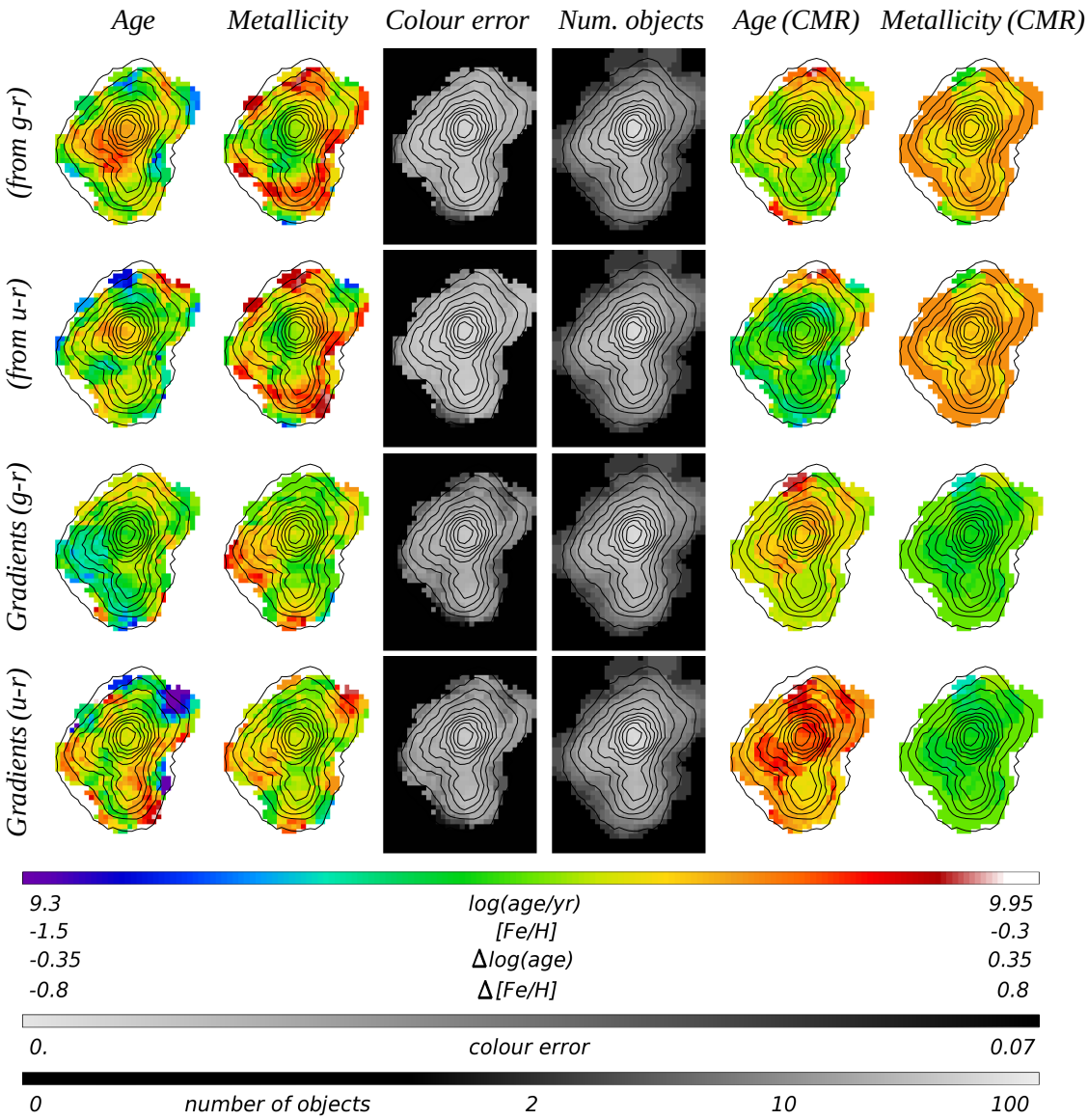

F 6.18. **Age and metallicity distribution of dE(N)s within the Virgo cluster.** Same as Figure 6.17, but based on the *burst* model.

units by the Bruzual & Charlot models, and since for metallicities, these are the common "working units" that provide an at least close-to-linear spacing between the models. In Figures 6.17 to 6.19, we show the age and metallicity distribution derived for the dE(N)s using the *exp-1*, the *burst*, and the *const-b100* model. The dE(nN)s are presented in Figures 6.20 to 6.22. Each figure shows in the top two rows the actual age and metallicity values, based on the half-light aperture, while in the bottom two rows, gradients are shown, i.e., the difference between the values based on the small and the large aperture. The maps on the left side were calculated from the individual colour values, while those on the right side are based on the colour values of the linear fit to the CMR, as described in Section 5.2. As labelled on the left side of each figure, we present the results based on the $g - r$ vs. $i - z$ diagrams (first and third row), as well as based on the $u - r$ vs. $i - z$ diagrams (second and fourth row), for comparison.

The dE(N)s seem to have higher ages and lower metallicities in, or close to, the central region of the cluster. Part of this is caused by the CMR itself, especially for the metallicities (rightmost column in the figures). Note that this anticorrelation of ages and metallicities reflects the position of the CMR

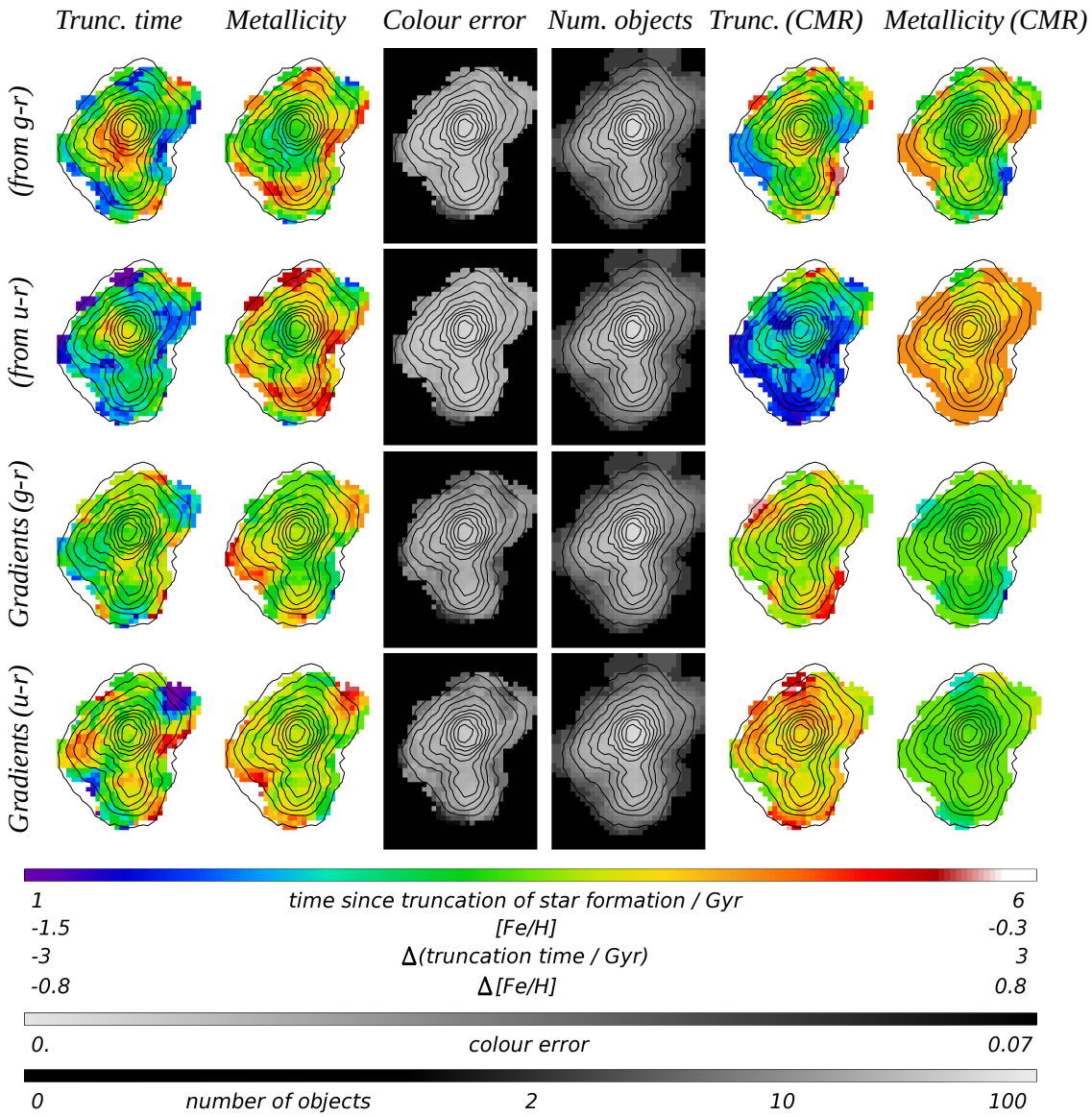

F 6.19. **Age and metallicity distribution of dE(N)s within the Virgo cluster.** Same as Figure 6.17, but based on the *const-b100* model.

in the colour-colour diagrams shown in Chapter 5, where typically, the faint, lower-metallicity end of the CMR reaches somewhat higher ages on the model tracks than the bright end.

The dE(nN)s show a patchier age and metallicity substructure than the dE(N)s. Due to the fact that their CMR spans a rather narrow range in the colour-colour diagrams (see Figures 5.26 to 5.28 of Chapter 5), the ages and metallicities derived from the CMR values show a strong discretization, and do not provide a very useful reference. This problem occurs – due to our simple approach of assigning ages and metallicities – when the colour range covered by the CMR is not much larger than the spacing between the model tracks.

Similar to the simulations of colour maps in Section 4, we can construct artificial Monte-Carlo realizations of age-metallicity distributions, in order to test the significance of the substructure seen. For this purpose, we first redistribute all colour residuals about the CMR randomly among our galaxies. Since a galaxy's colour is equal to the colour value of the CMR at the galaxy's magnitude plus

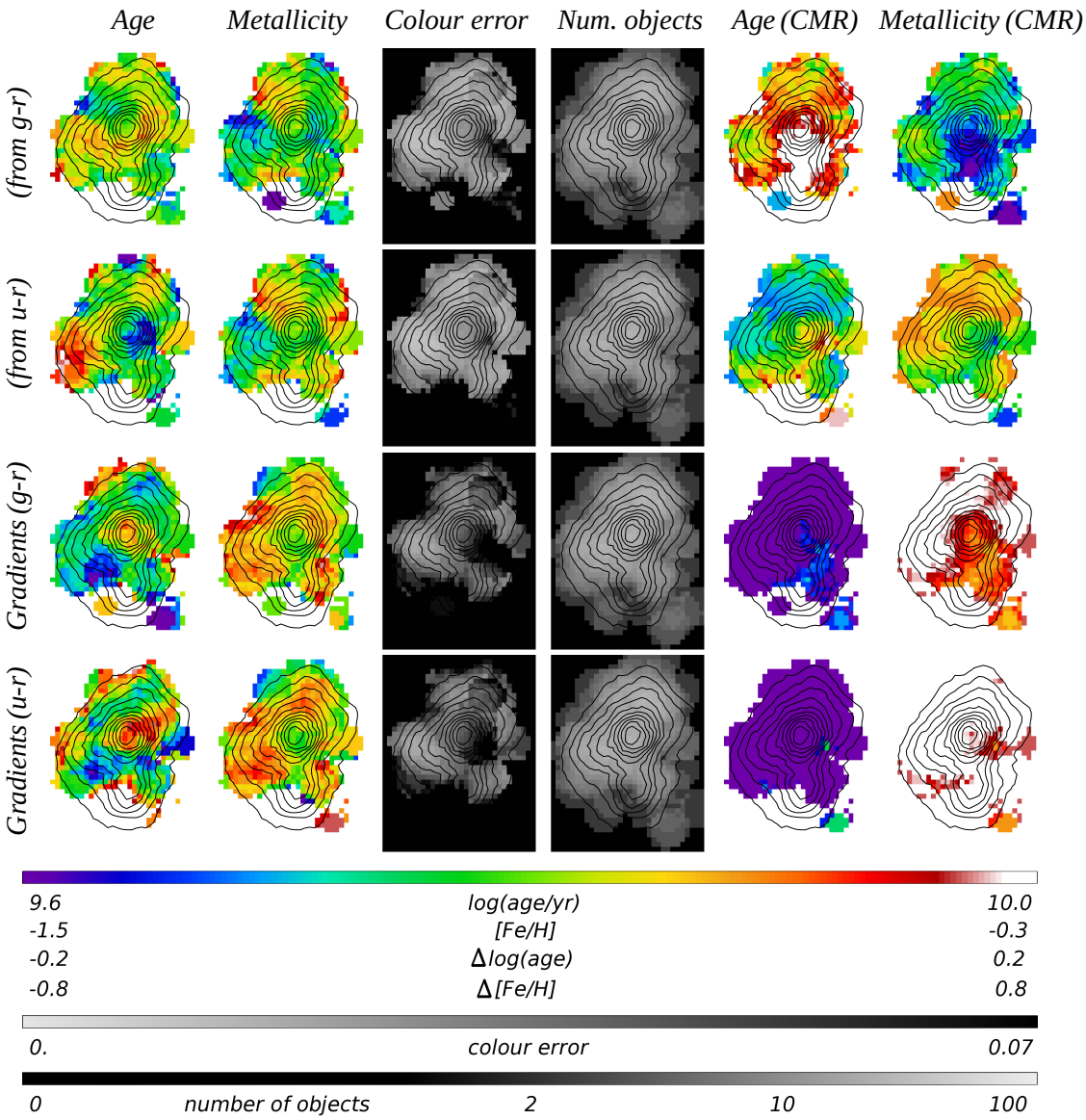

F 6.20. **Age and metallicity distribution of dE(nN)s within the Virgo cluster.** Same as Figure 6.17, but for the dE(nN)s.

the residual about the CMR, we obtain a new colour value for the galaxy through the random distribution of residuals. These new colours are assigned ages and metallicities, and corresponding maps are constructed like above with the same 2-D binning.

The resulting artificial age and metallicity maps are presented in Figures 6.23 and 6.24 for the dE(N)s and the dE(nN)s, each showing twelve realizations of age maps (top two rows) and twelve realizations of metallicity maps (bottom two rows), based on the *exp-1* model. From these figures it can be deduced that most age and metallicity substructure seen in Figures 6.17 to 6.22 (beyond that imposed by the CMR itself) can be explained with statistical fluctuations only, indicating that any real substructure is weaker, or, at best, equally strong than these. Since the use of larger 2-D bins did not yield to more significant results for the colours themselves (Section 4), we do not attempt to repeat this investigation here, because the derived ages and metallicities obviously rely on the very same colours.

One feature, though, appears to be stronger than what is seen in the simulations, namely the larger age of the dE(N)s at about the cluster center, but actually slightly offset towards the south-east (top

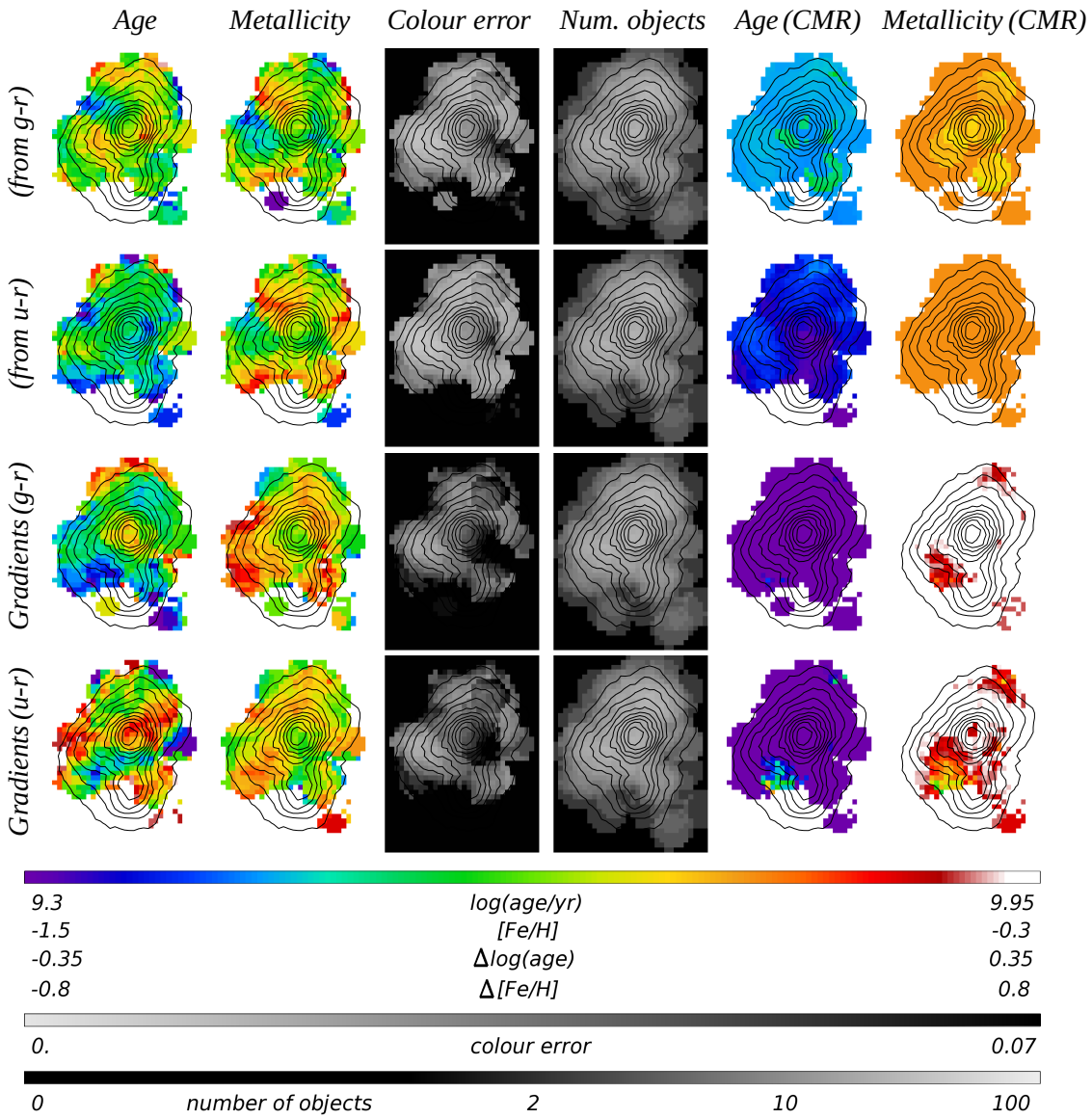

F 6.21. **Age and metallicity distribution of dE(nN)s within the Virgo cluster.** Same as Figure 6.20, but based on the *burst* model.

left panel in Figures 6.17 to 6.19). The difference to similar (but weaker) features in the artificial age maps is less than 0.1 dex, which, nevertheless, would mean a difference of about 20% for the actual value. Since we found a density dependence of the CMR in Chapter 5, we test whether this could be responsible for the feature we see. In Figure 6.25, we show the age maps separately for the low-density and high-density dE(N) subsample (divided at the median density of the dE(N)s; see Chapter 5). Interestingly, the region of redder colours appears in the maps of both subsamples. Now, while this structure seems to be real and not caused by random variations, we note that its size is comparable to the bin size that we use. Since there are typically 25 – 50 dE(N)s within the bins that are in focus here, we point out that a "real" feature could, in principle, be caused by only ~ten galaxies that have higher ages than the other ones (but in this case requiring their ages to be even more different from the rest than if a systematic effect would be present for all galaxies in the region).

The maps for the full dE sample (not shown) are basically a combination of those of the dE(N)s and the dE(nN)s. No additional significant substructure is seen in them. As for age and metallicity gradients, note that significance of substructure is even more difficult to achieve, since the statistically

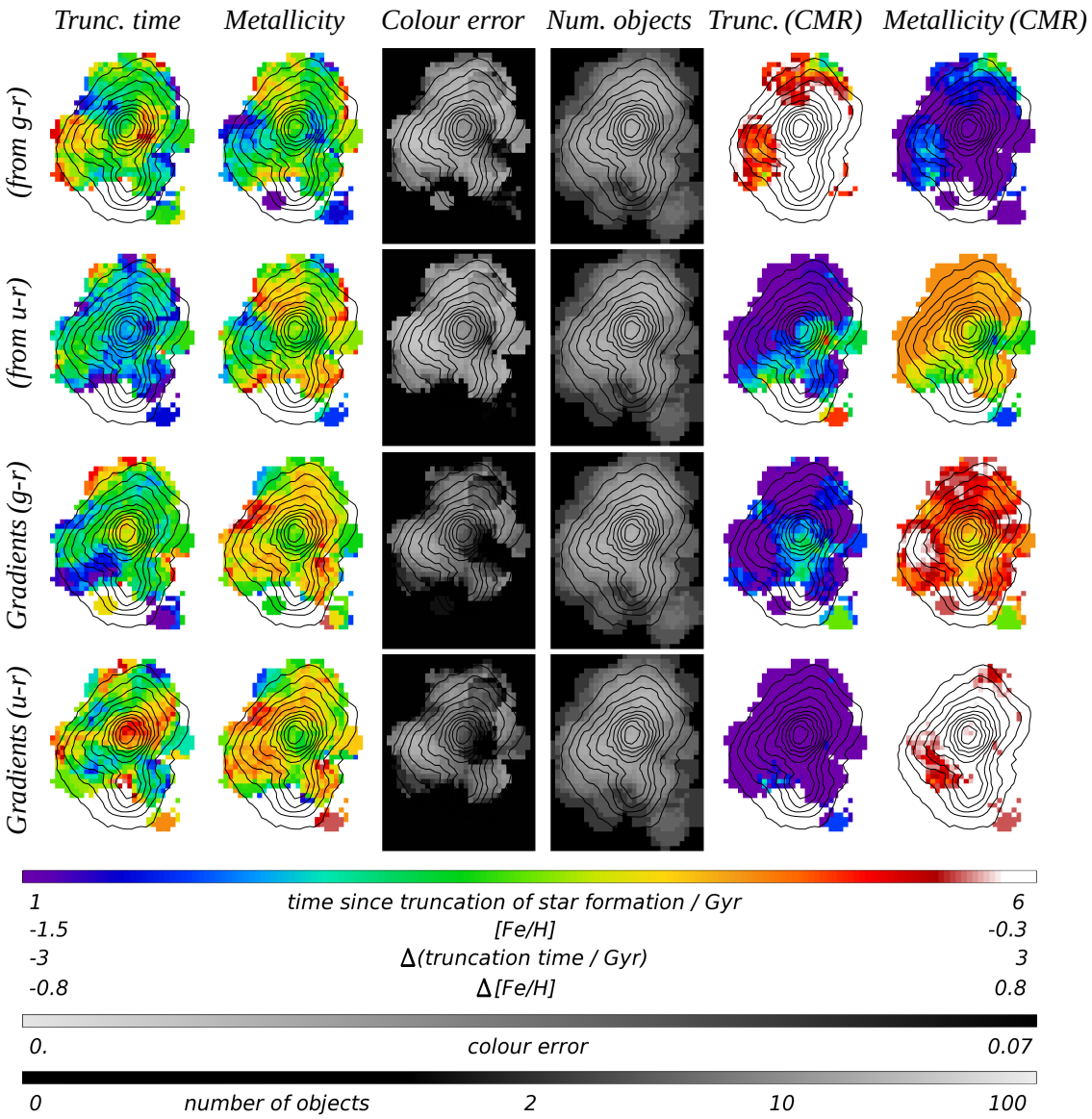

F 6.22. **Age and metallicity distribution of dE(nN)s within the Virgo cluster.** Same as Figure 6.20, but based on the *const-b100* model.

possible variations are, basically, stronger by $\sqrt{2}$ for them.[2] Since the substructure seen for the gradient maps is not stronger than that in the simulated age and metallicity maps, we consider it to be not significant.

[2] Possible variations would not be that large when a correlation between the inner and outer galaxy colours is assumed. Taking this into account quantitatively would mean to link the random distribution of colour residuals for the small aperture to that done for the large aperture, by invoking some prescription on the "allowed" range of colour gradients, thereby making it somewhat "less random". However, such an approach would hardly appear more reliable than straightforwardly assuming a factor of $\sqrt{2}$.

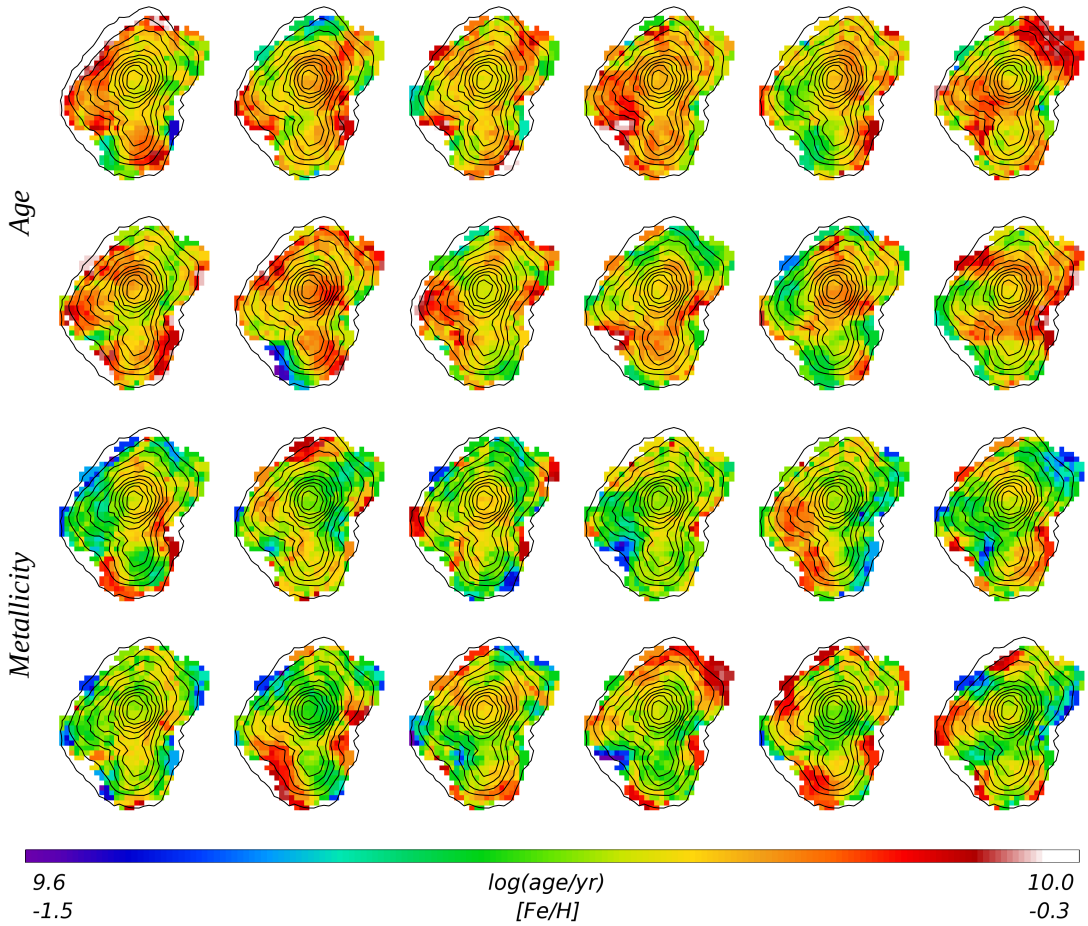

F 6.23. **Simulated age and metallicity distributions for dE(N)s.** Shown are age maps (top two rows) and metallicity maps (bottom two rows), each one resulting from a Monte-Carlo simulation of randomly distributed colour residuals about the CMR, based on the $g-r$ vs. $i-z$ colours measured within the half-light aperture, and on the *exp-1* model. See text for details on their construction. These simulated maps need to be compared to those shown in the two left panels of the top row of Figure 6.17, where the same colour mapping is used for ages and metallicities (see the scale bar below the figure).

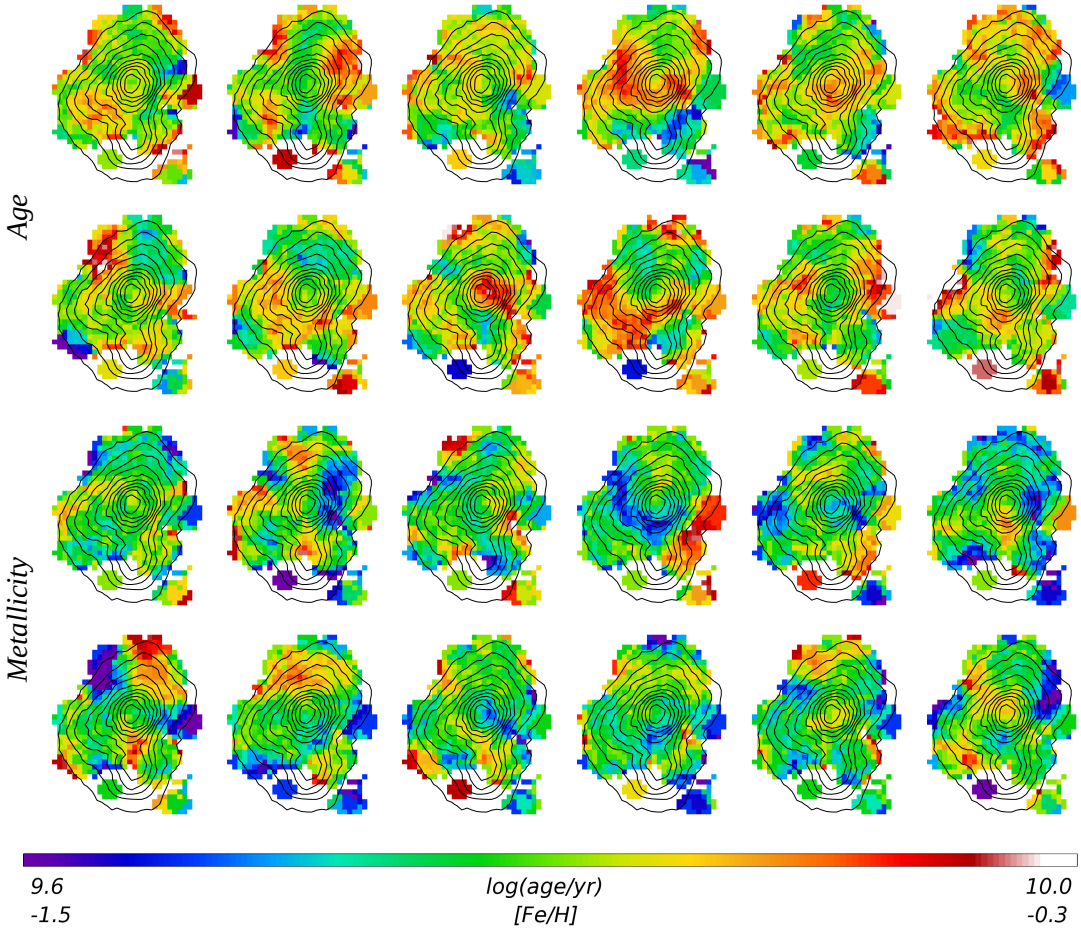

F 6.24. **Simulated age and metallicity distributions for dE(nN)s.** Same as Figure 6.23, but for the dE(nN)s.

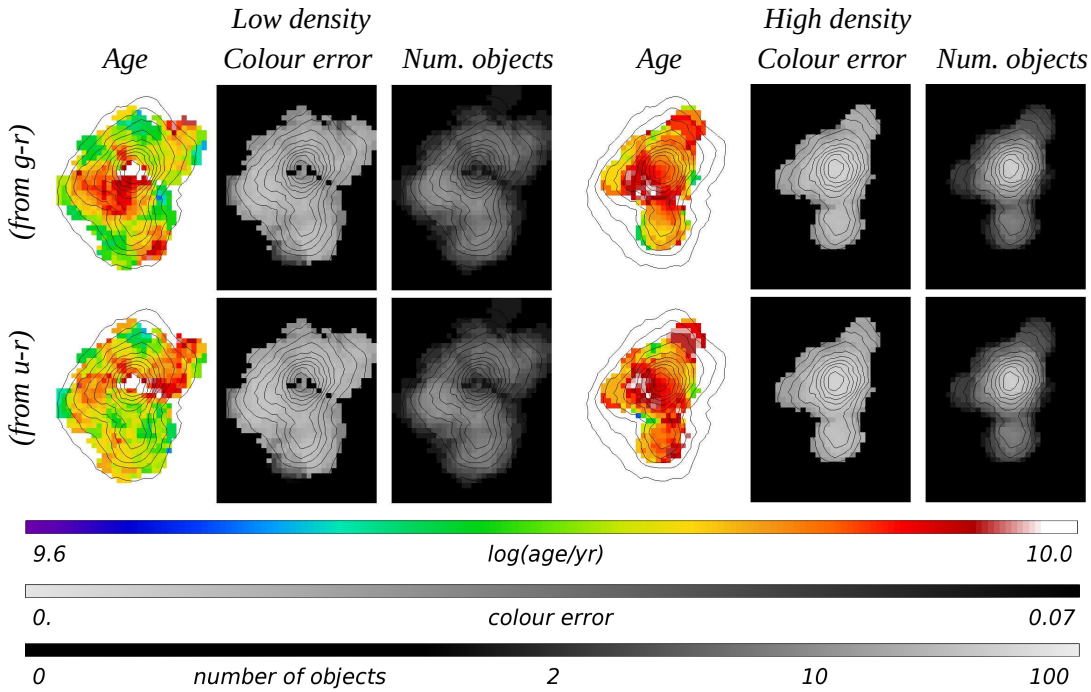

F 6.25. **Age distribution of dE(N)s at low and high densities.** Similar to the age distribution of the dE(N)s presented in Figure 6.17, using the *exp-1* model, but now considering the low and high-density subsamples separately (left three panels and right three panels, respectively).

7. S

We have analyzed the colours of our sample of 413 Virgo cluster dEs for the presence of substructure within the cluster, i.e., for whether there are regions where most dEs are offset from their CMR towards one side. While we do observe such features for both the dE(N)s and dE(nN)s, our complementary simulations based on the colour scatter of the CMR show that these features might not be more than just statistical fluctuations. We have then translated our observed colours into ages and metallicities, using the population synthesis code of Bruzual & Charlot (2003), and assigning each galaxy the model point closest to it in colour space. Like for the colours themselves, we find substructure in the age and metallicity distribution of the dE(N)s and dE(nN)s across the cluster. Our Monte-Carlo construction of artificial age-metallicity distributions, based on the observed CMR and scatter, shows that most substructure can be explained by random distribution of colours, except for a region slightly south-east from the cluster center, where the dE(N)s seem to have, on average, somewhat older stellar populations than elsewhere.

While nothing special about this region of higher ages is seen in the velocity maps (Figure 6.3), it coincides with the region of slightly larger axial ratios of the dE(N)s described in Section 3 (top right panel of Figure 6.2). A comparison of the distribution of X-ray emission in the Virgo cluster (Figure 6.26, adopted from Schindler et al. 1999) with the age structure of the dE(N)s (Figure 6.27) shows that the region of higher ages coincides with a region of stronger X-ray emission, indicating a higher density of intracluster gas. Note that the contours of galaxy number density in Figure 6.26 are different from ours; therefore we show a cross in both figures that marks the same position, which is supposed to be roughly the center of the region of higher age. The comparison with the X-ray distribution might imply that dE(N)s were formed through, or at least affected by, ram-pressure stripping, which is stronger in regions of higher gas density, and could thus leave an imprint in the stellar populations of the stripped galaxies. Whether or not this could also account for the slightly larger axial ratios can hardly be answered, since, as noted in Section 3, it is not clear anyway whether these are significant.

One caveat here is that, due to the motion of the galaxies within the cluster, a clear coincidence of gas and stellar population properties should only be seen immediately after the stripping process, especially given that the region in question is not the cluster center. However, the dE(N)s are the dE subclass with the oldest populations, and even in our *const-b100* model (see Section 5.1), their star formation would have been truncated 2 Gyr ago (for comparison, the cluster crossing time is $\sim$1.7 Gyr; Boselli & Gavazzi 2006). Another caveat has already been mentioned in the previous section: due to the size of our 2-D bins, it might be that only a small number of galaxies with high stellar population ages is responsible for this apparent region of high age, instead of a systematic effect that applies to most galaxies.

Let us briefly reiterate on the dependence of the CMR on density that we found in Chapter 5. There, we defined a "central subsample" of dE(N)s and of all dEs (excluding dE(bc)s), containing galaxies within two degrees of the cluster center, and compared its CMR to that of the high-density subsample. The fact that no difference was found was interpreted with a *direct* dependence of the CMR on density, rather than on location (the latter in the sense of "center vs. outskirts"). However, since we have now identified the region of higher ages, which is offset from the center, we can put together an analogous subsample, including all galaxies within two degrees of the position $\alpha = 188.^{\circ}3$, $\delta = 11.^{\circ}4$ (marked by the cross in Figure 6.27), which is simply one degree southward and one degree eastward of our adopted cluster center. The resulting CMR for $g - i$ is shown in the third row of Figure 6.28, which should be compared to Figure 5.20 in Chapter 5. This time, we see indeed a slightly flatter CMR of the dE(N)s for the region of higher ages, which was not the case for the central subsample. A similar effect, but also similarly small, is seen in $i - z$ (not shown). This seems to relativize our former conclusion about the direct density dependence of the CMR to a certain extent. However, we do not find a flatter CMR for the *full* dE sample, yet the density dependence was found equally strongly for it, and with even higher significance, than for the dE(N)s alone. Furthermore, the small difference between the CMR of the central subsample and that of the "high-age subsample" is

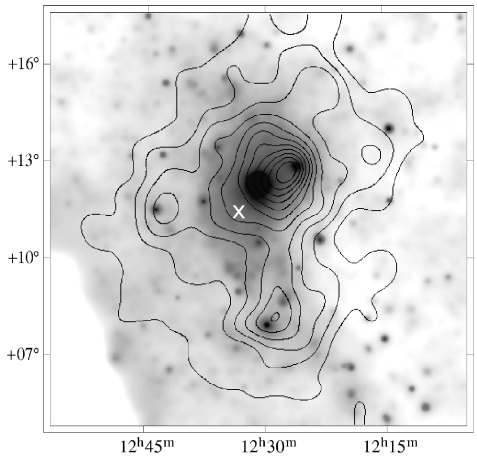

F 6.26. **Distribution of X-ray emission.** Adopted from Schindler et al. (1999, their Figure 1), but enhanced in contrast. The greyscale image shows the X-ray emission as observed by the ROSAT All-Sky Survey. The white cross has been visually chosen to roughly lie at the center of the region of higher ages shown in Figure 6.27. The contours follow constant galaxy number density — note that these contours are different from ours, which are used in all other figures. See Schindler et al. (1999) for more details and references. The figure was obtained from http://arxiv.org/e-print/astro-ph/9811464.

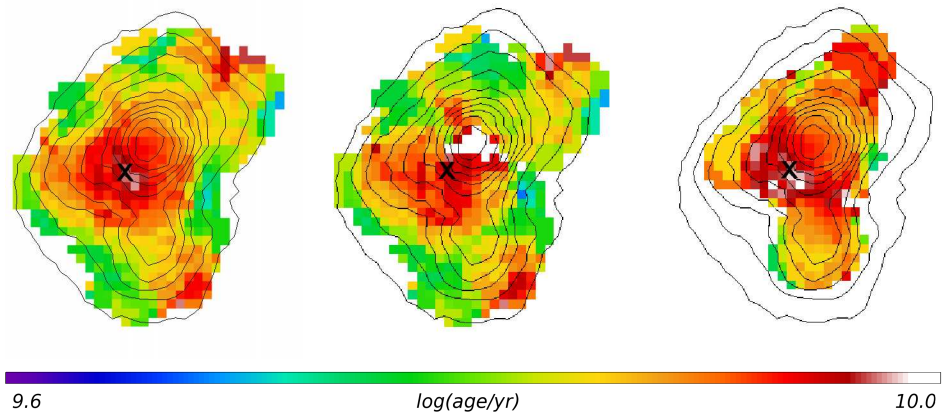

F 6.27. **Age distribution of dE(N)s.** For comparison with the X-ray map, this figure is showing again the age map of the dE(N)s derived with the *exp-1* model, for the full dE(N) sample (left), the low-density subsample (middle), and the high-density subsample (right). The black cross in each panel has been visually chosen to roughly lie at the center of the region of higher ages; it is also shown in white in Figure 6.26 to allow an easier comparison.

not at all significant, and, from looking at the figure, might possibly be blamed on just a few relevant galaxies at the bright and/or faint end of the magnitude range.

Given the amount of substructure that is present in the spatial and kinematical distribution of galaxies across the Virgo cluster (e.g., Binggeli et al. 1993; Gavazzi et al. 1999), is it surprising that we find no other significant age or metallicity substructure that is comparable to, or even stronger than, the one discussed above? To answer this question, let us have a look at how large the range of artificial substructure is in the simulated age and metallicity maps. For example, in the simulations for the dE(N)s in Figure 6.23, typical age differences between "bluer" and "redder" cluster regions of reasonable galaxy density are of the order of 0.1 dex, corresponding to differences of ~20 to 30%[3]. This would be equivalent to, e.g., an age range of 3.0 – 3.8 Gyr, 5.0 – 6.3 Gyr, or 10.0 – 12.6 Gyr.

[3] 0.1 dex translates into a factor of 1.26.

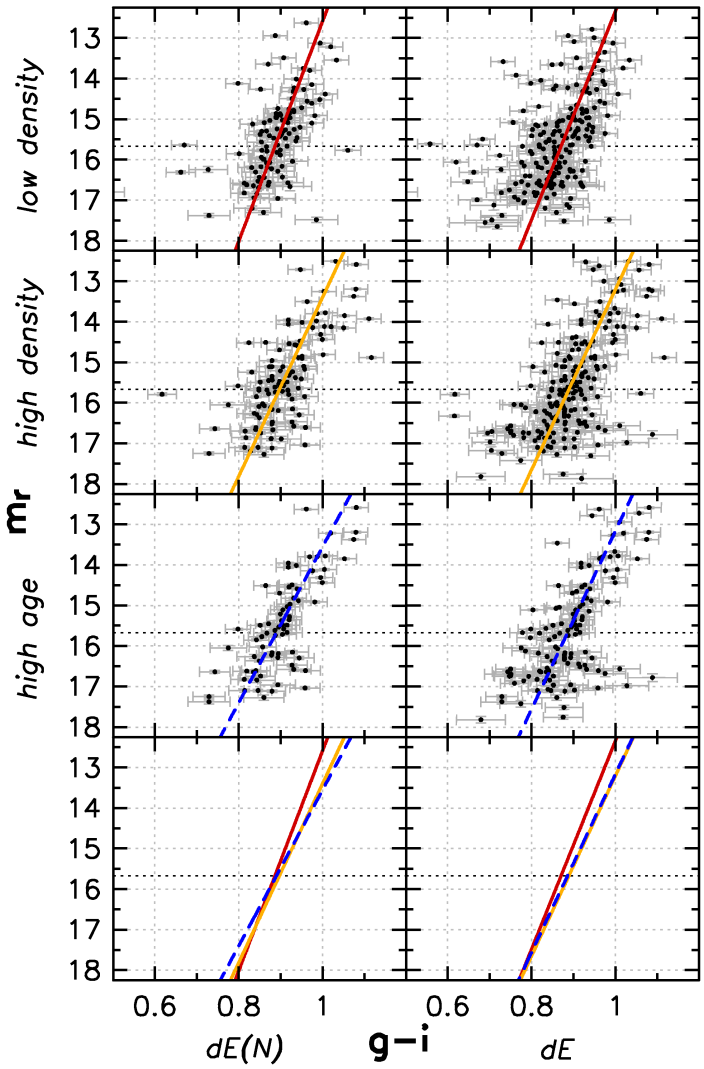

F 6.28. **Colour-magnitude relations for different densities and positions.** Similar to Figure 5.20 from Chapter 5, but now showing in the third row the subsample representing the region of higher age, instead of the central subsample (see text for details). CMRs are shown for dE(N)s (left column) and for all dEs (right column, excluding dE(bc)s), using $g-i$ colour and the half-light aperture.

Typical metallicity differences are of the order of 0.25 dex in $[Fe/H]$. Similar values are seen in the simulations for the dE(nN)s and for the full dE sample. Both the age and metallicity differences are not overly large, but at the same time, they are not so small that one would need to be extremely surprised about the homogeneity of the stellar populations across the cluster. Remember that, in order to yield 2-D age bins that are different by ∼20 to 30% from the others, the *average* age of the galaxies within each bin needs to be larger by that amount. Thus, if half of the galaxies showed "normal" ages, the other half would need to have higher/lower ages by $2 \cdot 0.1$ dex[4], or *by a factor of 1.6.* Likewise, in the same example, the metallicities of these galaxies would need to be higher/lower by 0.5 dex in [Fe/H]. Given these considerations, it appears not too surprising that no further significant substructure is seen.

The necessary "ingredients" for a search for substructure below our detection limits would obviously be a better photometric quality in *u* and *z*, especially given the small colour range covered by the models in $i-z$. Even better would be near-infrared (NIR) photometry of similar quality as our *g*,

[4] Remember that averaging is done in log(age).

r, and *i* bands: the "red colour" in our colour-colour diagrams could then rely on one optical and one NIR band, thereby spanning a range in colour values that is much larger than the measurement errors. A taste of the advantages of NIR photometry is given in the following chapter.

Acknowledgements

T.L. would like to thank Dolf Michielsen for valuable discussion. This study is based on publicly available data from the SDSS.

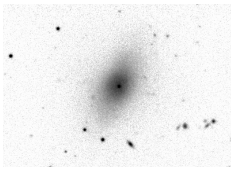

CHAPTER 7

T -

"I am too much in the sun."
Hamlet

We present an analysis of 22 Virgo cluster early-type dwarf (dE) galaxies with combined optical and near-infrared (H band) photometry, which allows us to deduce ages and metallicities with much smaller uncertainties than from optical colours alone. Our sample comprises dEs of each of the subclasses defined in Chapter 4: 9 dEs with disk features (dE(di)s), 5 dEs with blue centers (dE(bc)s), 6 ordinary dEs that are nucleated (dE(N)s), and 2 ordinary dEs that have no or only a weak nucleus (dE(nN)s). All of these are among the brighter dEs, with the faintest object having $m_r = 14^m.45$*. The majority of galaxies populate a rather narrow sequence in the respective colour-colour diagrams, which we find to be consistent with a curve of almost constant age that reaches from slightly supersolar metallicities to below* $[Fe/H] = -0.33$*. No systematic differences are found, within our rather small sample, between ages and metallicities of dE(N)s and dE(di)s. The metallicity range populated by the dE(bc)s is found to be similar to those of the other dEs. This study demonstrates the superiority of combined optical/near-infrared photometry to purely optical imaging data with regard to the determination of luminosity-weighted ages and metallicities.*

This study was done together with Eva K. Grebel and Bruno Binggeli.

1. I

In the previous chapters, it became clear that it is not only the famous age-metallicity degeneracy that prevents an unambiguous determination of luminosity-weighted ages and metallicities of our early-type dwarfs (dEs), but in addition, the $i - z$ colour range covered by the relevant models is very small, leading to large *relative* measurement uncertainties. For example, in our calculation of error estimates for the age and metallicity assignment in Chapter 6, the dominant colour uncertainty was that of $i - z$ and not that of $u - r$, even though the signal-to-noise ratio (S/N) of our galaxies is several times lower in u than in z. It would thus be ideal to extend the wavelength baseline of our "red colour" into the near-infrared (NIR).

A further advantage of the NIR is that it is largely insensitive to the presence of young stellar populations, and instead traces mainly the old ones. Thus, comparisons between early-type and late-type galaxies can be performed in a less biased way than with optical photometry. Along these lines, one of the first studies of dwarf galaxies with optical-NIR colours was that of Thuan (1985), who compared the properties of a sample of field dwarf irregulars (dIrrs) to those of a sample of Virgo cluster dEs. He found the dIrrs and dEs to have "mutually exclusive" metallicity ranges, with the metallicities of the dIrrs between 1/250th solar to one third solar, and those of the dEs between one third solar to solar. The time since the last burst of star formation in the dEs was found to lie between ∼1 and ∼8 Gyr, but for 10 out of 13 dEs it was found to be below 2 Gyr.

Given these results, it becomes clear that the study of optical-NIR colours can, for dEs, even be seen as a valuable alternative to spectral analyses, since the low surface brightnesses of the dwarfs make it very time-expensive to obtain spectra of sufficient S/N. Nevertheless, we are not going to enter deeper into the possiblities of NIR photometry in this chapter, since our working sample comprises only 22 Virgo dEs for which H band images of sufficient quality are available — and these 22 should, ideally, be split up into the respective dE subclasses (see Chapter 4). Therefore, our intention here simply is to reiterate on the stellar population properties of our galaxies, using the much wider colour space in which the theoretical model tracks can be placed, to test, e.g., our above conclusions about the similarity of the stellar populations of dE(N)s and dE(di)s.

2. D

In Chapter 4 we defined a sample of 413 Virgo cluster dEs that are certain cluster members and for which optical photometry from the Sloan Digital Sky Survey Data Release 5 (Adelman-McCarthy et al. 2007) is available. Our photometric measurements are described and presented in Chapter 5. For 22[1] of these dEs, near-infrared (NIR) images in the H band are available from the ESO/ST-ECF Science Archive facility[2], taken with ESO NTT/SOFI in the nights of March 26th and 27th, 2000 under programme ID 64.N-0288 (P.I.: A. Boselli). With a pixel scale of $0\farcs29$ and a detector size of 1024x1024 pixels, SOFI has a field-of-view of $\sim 5' \times 5'$. The seeing was reported to be mostly sub-arcsecond. See Gavazzi et al. (2001) for further details on the data.

While reduced images are available from the GOLDMine database[3] (Gavazzi et al. 2003), they apparently suffer from variations in the background level and from so-called ghost images (Figure 7.1, left panel). These are residuals of the process of combining the dithered individual exposures, suggesting that probably, galaxies (including the target) were not or not fully masked in the calculation of the background level. While photometric measurements of the galaxy shown in the figure might still not be too much affected by the surrounding ghost images, the problem is that we do not know whether a ghost image "sits" underneath the galaxy itself. We therefore decided to perform our own

[1] VCC 0021, VCC 0033, VCC 0170, VCC 0216, VCC 0227, VCC 0308, VCC 0437, VCC 0750, VCC 0856, VCC 0951, VCC 1036, VCC 1183, VCC 1392, VCC 1491, VCC 1514, VCC 1528, VCC 1549, VCC 1684, VCC 1695, VCC 1895, VCC 2042, VCC 2050.

[2] http://archive.eso.org

[3] http://goldmine.mib.infn.it/

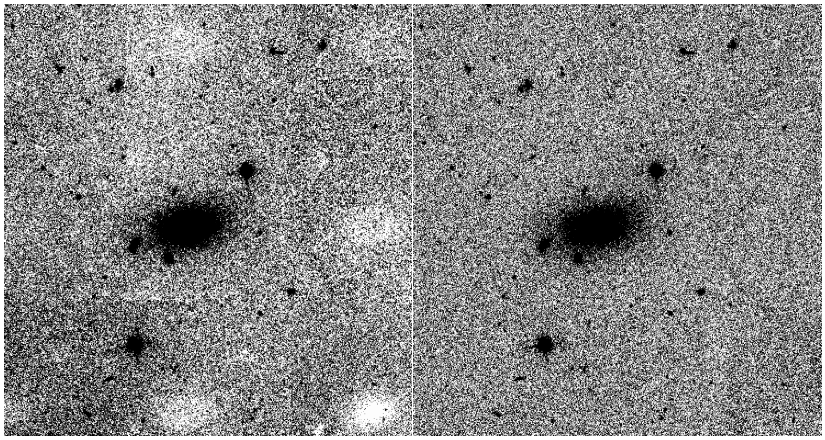

F 7.1. **Data reduction improvement.** Shown is the reduced *H* band image of VCC 0021 as obtained from the GOLDMine database (left), as well as from our own reduction (right). Scale and intensity mapping are the same for both images.

image reduction, taking special care with the background subtraction and the masking of objects, as described below.

2.1. Reduction

Without going into too much detail about NIR data reduction, we briefly describe the most important issues. The main concept of NIR observing and subsequent data reduction is that the images themselves can be used for determining and subtracting the sky background. This is achieved as follows: from one exposure to the next, the target galaxy is offset to a different position on the detector, thus ideally leaving blank sky where the galaxy had been a moment before, and vice versa. This process of performing repeated offsets within the detector area is known as "dithering". Let us assume for simplicity that the target galaxy, as well as all other objects in the field-of-view, occupy each position only once during the process. Then, by simply median-stacking[4] all images (without aligning them!), one would obtain a background image that is free of any source. This background image could then be subtracted from the individual images, and they could be aligned and stacked to form the final reduced image. However, this final image would look similar to, or worse than, the image in the left panel of Figure 7.1, i.e., it would be full of "ghost images". The reason for this is the following: even the median, which is known to be more stable than the mean, is affected to some extent by "outliers", i.e., by pixel values that are far above the actual background value — and such a situation obviously occurs when the target or some other source happens to fall on the pixel. If, in the process of stacking images, a given pixel would be occupied by a star or a galaxy in one or more images, these should be excluded from the calculation of the median, since the goal is to obtain a close-to-accurate estimate of the background flux. If those images would not be excluded, the median value would end up to be "one step higher" in the sequence of flux-sorted pixel values, thus leading to a larger pixel value in the final image of the sky background. When this background image is then subtracted from the individual images, a somewhat too large value is subtracted at the pixel that we just discussed, leading to a slightly negative value there, i.e., to a ghost image. Note, again, that the main problem are not the ghost images next to the target galaxies, but those that are beneath them!

The solution to this problem is to mask the target, as well as any other disturbing source, before the median-stacking is done. "Masking" here means that the respective pixels are excluded from the calculation of the median. This might sound simple, but it bears two main difficulties. The first one is that, depending on the number of individual exposures taken, on the number of disturbing foreground or background objects, and on the size and the pattern of the dithering offsets, there

[4] With this, we mean that the value of a given pixel in the final image is the median value of the corresponding pixels of the input images.

might be only a few images left at a given pixel that do not contain any source. This can lead to a rather noisy background image, on which one can possibly even distinguish by eye the regions with different numbers of unmasked pixels that contributed to them. This problem can be overcome to a large degree with thinking carefully about the best dithering strategy before doing the observations. If it is too late for that, interpolation across the smaller ones of the disturbing sources helps[5], done either on the individual images or on the final image. The second difficulty is that many objects are too weak to be seen in the individual images – thus being not masked – but they eventually appear in the final, co-added image. This is a crucial point for galaxies of low surface brightness, since it applies to their outskirts, too. Imagine the center of a dwarf galaxy would be properly masked in the calculation of the background, but its outskirts would not be masked, since they are not seen in the individual images. The resulting background image would thus have the "correct" pixel values at the position of the galaxy center, but would have too large values at the position of the galaxy's outskirts. Consequently, too much sky background would be subtracted for the outer parts of the galaxy, which can lead to artificial colour gradients when this image is used to measure colours. The solution to this problem is an iterative procedure: the first object masks are created from the individual images, and are used to calculate a first background image, which is then subtracted from the individual images. These are aligned and stacked, thus leading to the first "final image", which most likely still suffers from ghost images. This image is now used to construct improved object masks that, e.g., cover faint galaxy outskirts better, and the next iteration is performed, leading to an improved "final image" with no or weaker ghosts. This can be repeated a few times, until no ghost images are left in the final image. The result of this reduction procedure, which we performed mainly with various *IRAF*[6] tasks (Tody 1993), is shown in the right panel of Figure 7.1: no ghost images are left over, and moreover, the flux distribution in the direct vicinity of the target galaxy is much more homogeneous than before.

2.2. Calibration and alignment

Flux calibration of the final images was done based on the standard stars provided, with literature magnitudes taken from Persson et al. (1998). The images were corrected for Galactic extinction using the values of Schlegel et al. (1998). They were then demagnified to match the pixel scale of the SDSS images, using *IRAF*/*magnify* with spline interpolation and conservation of total flux. Each *H* band image was then registered to the corresponding combined image from three SDSS bands (*g*, *r*, and *i*; see, e.g., Chapter 2), using *IRAF*/*xregister*. The images were not aligned, but the resulting linear offset was simply added to the central coordinates of our apertures used for the photometry. Moreover, the objects masks that we had constructed for the optical images (see Figure 5.1 of Chapter 5) were shifted accordingly, to mask the same objects in the *H* band images. Note that a certain degree of rotational misalignment between the optical and NIR images is present for some of our galaxies. However, we find the amount of rotation to be $\sim 3^\circ$ at most. We have investigated this effect in a preparational study, based on the reduced images provided by the GOLDMine database, and found it to yield flux uncertainties below one percent, and typically below the flux uncertainty caused by noise. We thus decided to not correct for this effect, in order to avoid any further nonlinear interpolation of pixel fluxes.

Furthermore, we had initially intended to degrade the seeing of the demagnified *H* band images to that of the corresponding SDSS *i* band images. However, a test run with a simple Gaussian convolution led to strongly correlated noise in the images, which is why we preferred to use the unconvolved images. We expect seeing effects to be negligible for our study, for the following reasons. In addition to masking disturbing foreground stars or background objects, the nuclei, if present, are masked as well (see Chapter 4). The surface brightness distribution of our dEs is smooth and regular, and even for the object with the smallest half-light radius of our sample, the smallest aperture used by us still has a semimajor axis of 11 pixels (and is almost circular). For comparison, the largest seeing full

[5] Sometimes, a good deal of luck is needed, too.

[6] IRAF is distributed by the National Optical Astronomy Observatories, which are operated by the Association of Universities for Research in Astronomy, Inc., under cooperative agreement with the National Science Foundation.

width at half maximum (FWHM) of the *i* band image point spread function that we measured among our 22 dEs is 3.3 pixels. Seeing estimates were obtained by applying *IRAF*/*imexam* to stars in the images. The median ratio of the seeing FWHM of the *i* band and the demagnified *H* band images is 1.5. These considerations show that seeing differences should not affect our colour measurements.

As in the previous chapters, for each galaxy the flux was measured within three elliptical apertures: $a \leq 0.5\,a_{\rm hl,r}$ ("small aperture"), $a \leq a_{\rm hl,r}$ ("intermediate aperture" or half-light aperture), and $a \leq 2\,a_{\rm hl,r}$ ("large aperture"); $a_{{\rm hl},r}$ is the half-light semimajor axis in *r* (see Chapter 4). Errors were estimated, as described in Chapter 5, from quadratically adding the uncertainty caused by noise ("S/N uncertainty"), the uncertainy in the determination of the sky background ("sky level uncertainty", taken to be 0.3% of the noise level), and the flux calibration uncertainty. The latter is assumed to be $0\overset{\rm m}{.}02$, which corresponds to the RMS scatter about the linear fit of the relation between standard star flux and airmass.

3. A

With the optical photometry from Chapter 5 and the NIR photometry at hand, we can now construct an optical-NIR colour-colour diagram, in which we compare our measured colours to those predicted by population synthesis models. For the latter, we use the "*exp-1*" model from Chapter 5, which describes an exponentially decaying burst of star formation with a decay time of $\tau = 1$ Gyr. It was constructed for various metallicities, using the population synthesis code from Bruzual & Charlot (2003), with "Padova 1994" isochrones (Bertelli et al. 1994), a Chabrier initial mass function (IMF; Chabrier 2003), and the Bruzual & Charlot high resolution files, which rely on the STELIB spectral library in the wavelength range 3200 – 9500 Å and on the BaSeL 3.1 spectral library outside this range (see Bruzual & Charlot 2003, and references therein). The corresponding model tracks – curves of constant metallicity – are compared to our data in Figures 7.2 to 7.4, using $u - r$ or $g - r$ as "blue colour" and $i - H$ as "red colour". Figure 7.2 shows the colours measured within the small aperture, Figure 7.3 is for the intermediate (half-light) aperture, and Figure 7.4 for the large aperture. Even though our sample is rather small, we subdivide it into the different dE subclasses (Chapter 4), in order to avoid mixing galaxies with potentially different stellar populations. Our choice of $u - r$ vs. $i - H$ and $g - r$ vs. $i - H$ diagrams is based on the various diagrams shown in Figure 7.5: while the differences between $u - r$ vs. $i - H$ (second row), $u - r$ vs. $z - H$ (third row), and $u - i$ vs. $z - H$ (bottom row) are small, our data points seem to show the narrowest distribution in $u - r$ vs. $i - H$. As in Chapters 5 and 6, we present $g - r$ colour in addition to $u - r$ for comparison — measurement errors are considerably smaller in $g - r$, but at the same time, the relevant colour range is narrower. The comparison of the optical-NIR diagrams with the purely optical one (top row of Figure 7.5) illustrates the big advantage of using NIR photometry when trying to determine ages and metallicities.

The first thing to note is that the metallicities are rather large as compared to our results from Chapter 5, even when allowing for the fact that the 22 dEs considered here are among the brightest of our full sample. Indeed, one can see in Figure 7.5 that the same data points lie at lower metallicities in the optical-optical diagram than in the optical-NIR diagrams. A comparison of our data reduction with the one provided by Gavazzi et al. (2003) – even though we consider the latter to be not optimal (see Section 2) – yields a similar range of resulting optical/NIR colour values. We are thus confident that no systematic offset has been introduced in our reduction and calibration process. However, a systematic difference is present in the models: as stated above, they rely on the (high-resolution) STELIB spectral library in the wavelength range 3200 – 9500 Å, but for NIR colours, they are based on the (lower-resolution) BaSeL 3.1 library. We thus included an additional model track in the left panels of Figure 7.5 (red) that corresponds to the $Z = 0.008$ track, but was calculated only with the BaSeL 3.1 library over the full wavelength range. Indeed, there is a rather large offset between the two $Z = 0.008$ tracks in $i - z$ colour. Unfortunately, the offset goes into the "wrong" direction, i.e., the metallicity of our galaxies would now be even lower than before. In any case, this comparison shows

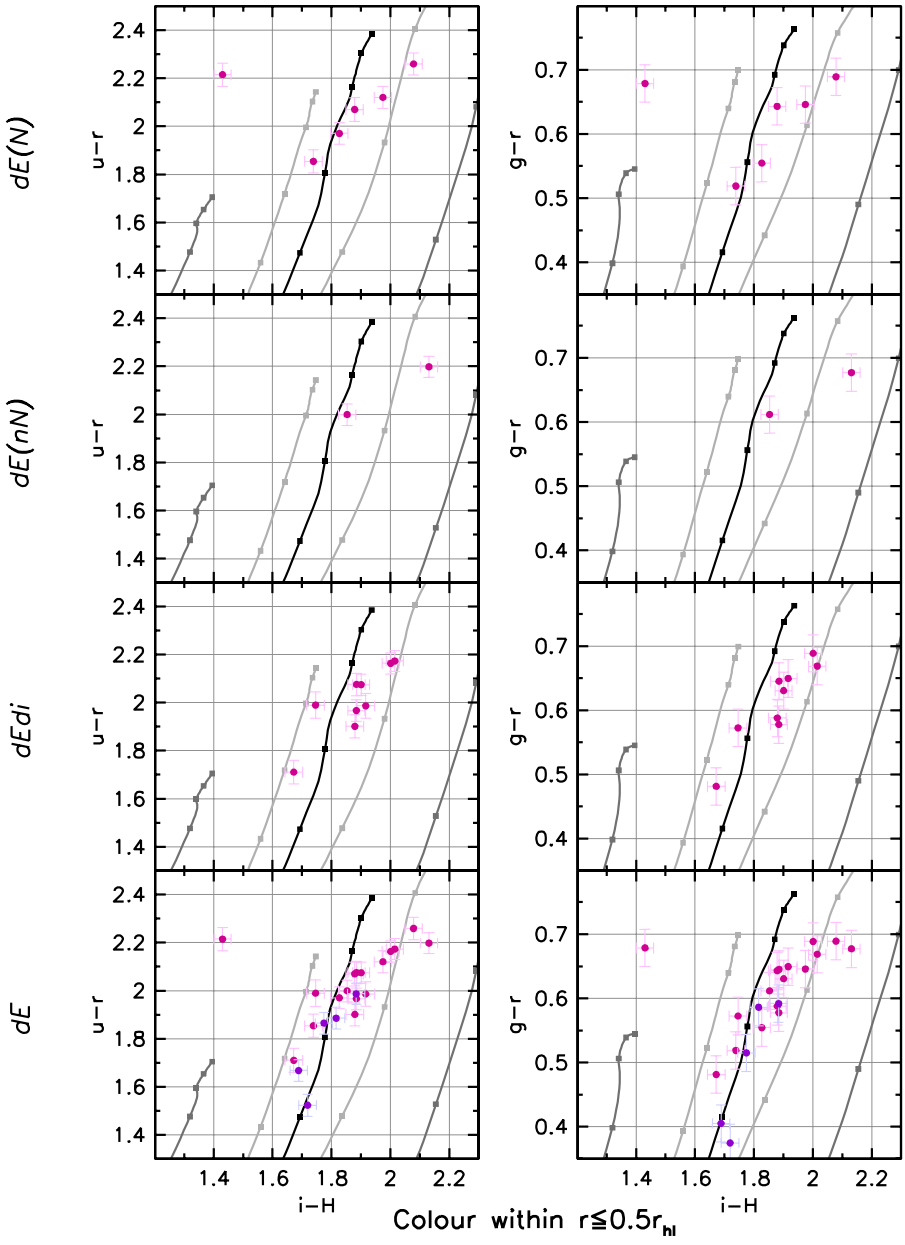

F 7.2. **Stellar population characteristics.** Shown are theoretical galaxy colours along Bruzual & Charlot model tracks of constant metallicity, namely, from left to right, $Z = 0.0004$ ($[Fe/H] = -1.65$), $Z = 0.004$ ($[Fe/H] = -0.64$), $Z = 0.008$ ($[Fe/H] = -0.33$), $Z = 0.02$ ($[Fe/H] = +0.09$), and $Z = 0.05$ ($[Fe/H] = +0.56$). The model describes an exponentially decaying burst of star formation with a decay time of $\tau = 1$ Gyr. Each model track is marked at ages of 3, 4.5, 7.5, 10.5, and 13.5 Gyr (upper end of track). The colours of our sample of 22 dEs, measured within the small aperture, are shown as pink dots for the dE(N)s, dE(nN)s, and dE(di)s, and as blue dots for the dE(bc)s.

the strong dependence of the model colours on the model ingredients — it thus appears wise to stick to *relative* statements about ages and metallicities, instead of quoting absolute values.

We now come back to Figures 7.2 to 7.4. No differences between dE(N)s and dE(di)s are seen, confirming that they have similar stellar populations. Furthermore, the dE(bc)s populate practically the same range in $i - H$ colour, implying that their metallicities are similar to those of the dE(N)s and dE(di)s. Thus, our conclusion from Chapter 3 that, after cessation of star formation and some time

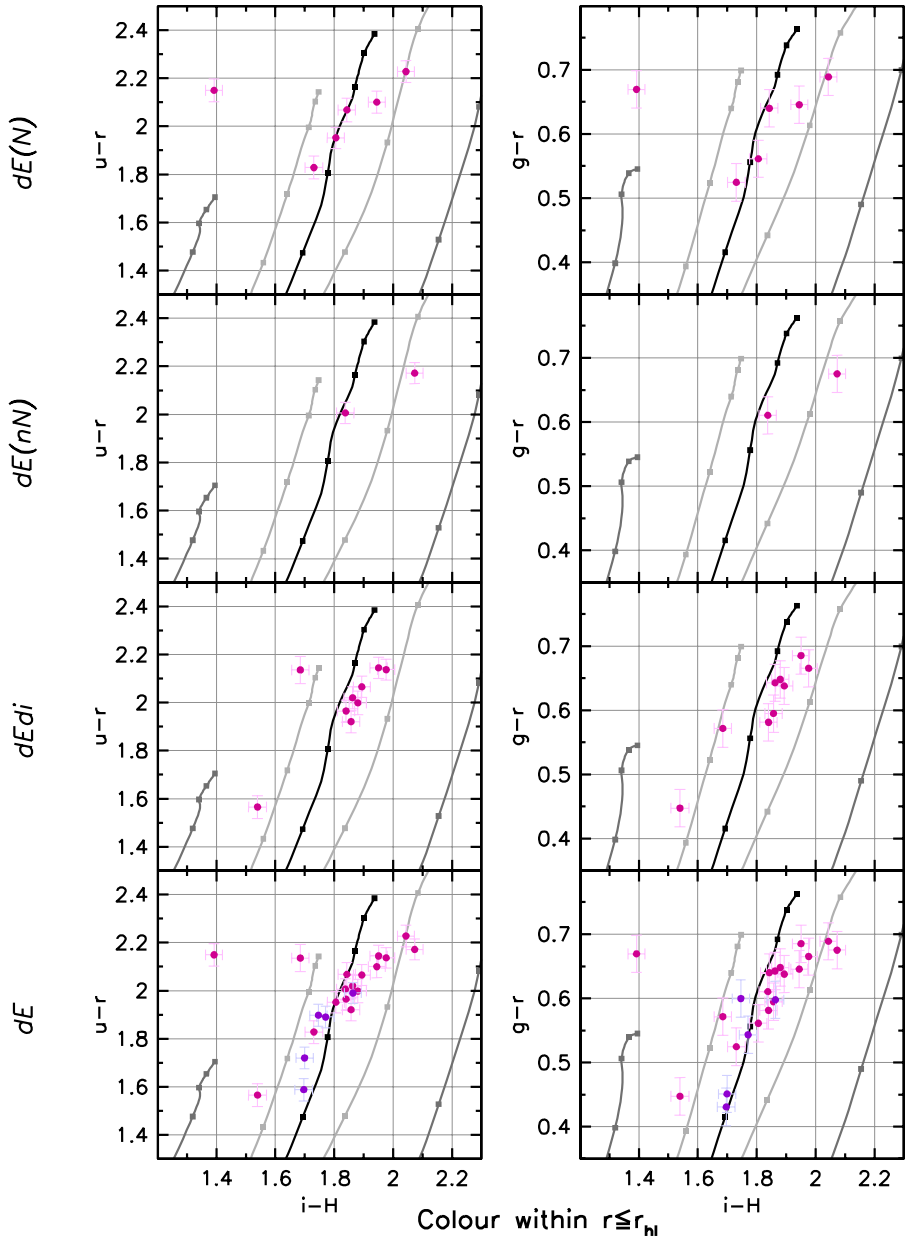

F 7.3. **Stellar population characteristics.** Same as Figure 7.2, but for colours measured within the intermediate aperture.

of passive evolution, the dE(bc)s will appear as ordinary dEs, can now be extended: not only their optical appearance will become indistinguishable from the other dEs, but also their stellar population characteristics (however, we still need to keep in mind our small sample sizes). This assumes, of course, that the stars that will still be formed in the dE(bc)s would not contribute a significant amount to the total final stellar mass, which seems reasonable given that their gas reservoirs are rather small, and that the current young population makes up only a few percent or less of the mass (Chapter 3).

For both the small and the intermediate aperture, the majority of data points forms a narrow sequence in $u - r$ vs. $i - H$, almost along points of constant age, but with a trend towards younger ages at lower metallicities. The latter is more pronounced in $g - r$ vs. $i - H$, where the scatter is also slightly larger. For the large aperture measurements, the galaxies are distributed differently than for the smaller apertures; this is clearly seen in $u - r$ vs. $i - H$, and also to some extent in $g - r$ vs.

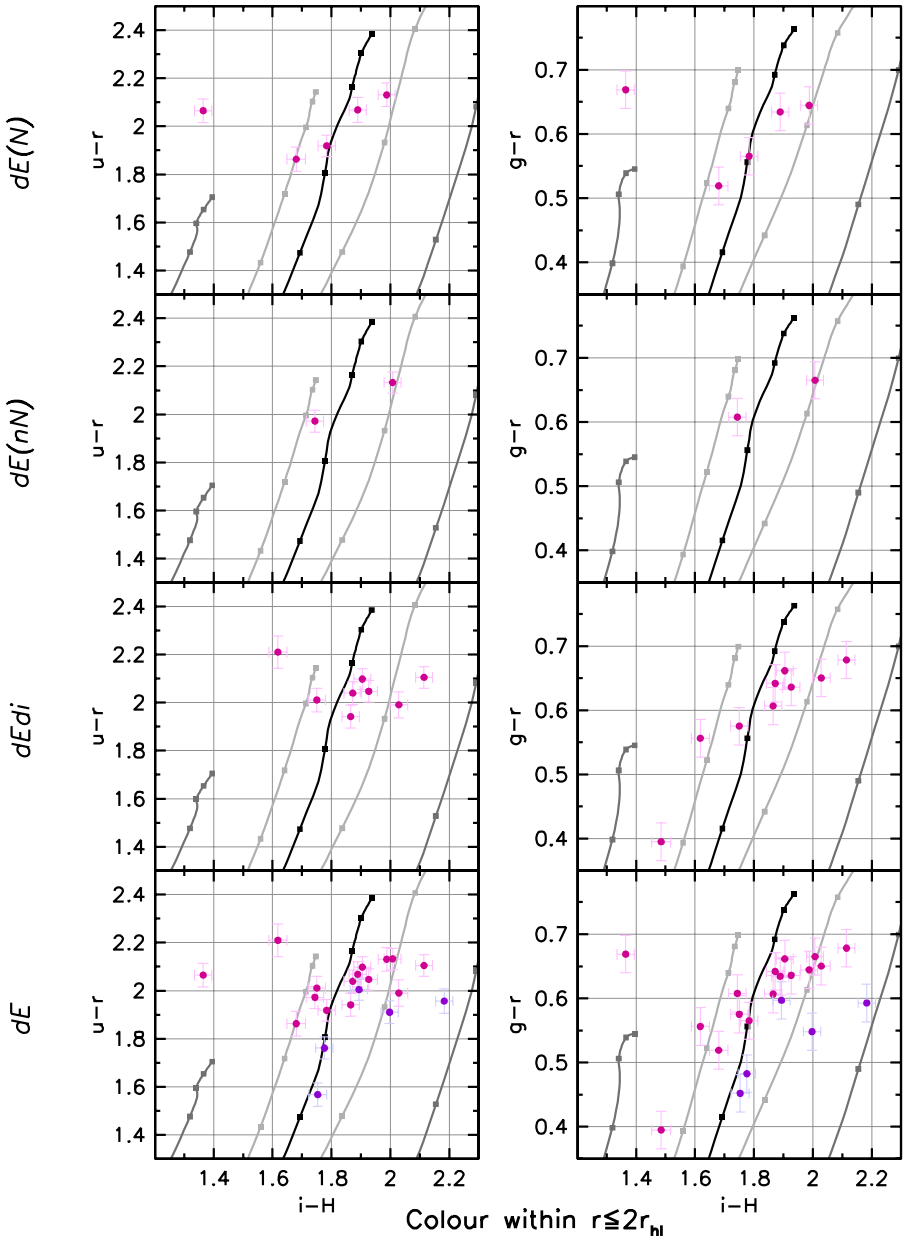

F 7.4. **Stellar population characteristics.** Same as Figure 7.2, but for colours measured within the large aperture.

$i - H$. However, no systematic colour gradient can be identified — the overall location of points is very similar for all apertures.

Can the sequence in colour-colour space be explained with the colour-magnitude relation? In Figure 7.6, we plot r magnitude against $i - H$ colour (upper panel), excluding the dE(bc)s. While this rather small number of points appears to be following a CMR, the scatter is larger than one might expect from the former diagrams. To see where the brighter and fainter galaxies lie with respect to the model tracks, we show those dEs with $m_r < 14\overset{m}{.}0$ as red symbols, while the other ones are shown as blue symbols. Their location in the colour-colour diagram is given in the lower panel of the figure. It seems as if only the brighter galaxies were responsible for the sequence seen, while the scatter of the fainter galaxies is comparable to the scatter of the (weakly defined) CMR. However, we point out that the two subsamples consist of only 8 and 9 data points, preventing any robust conclusions.

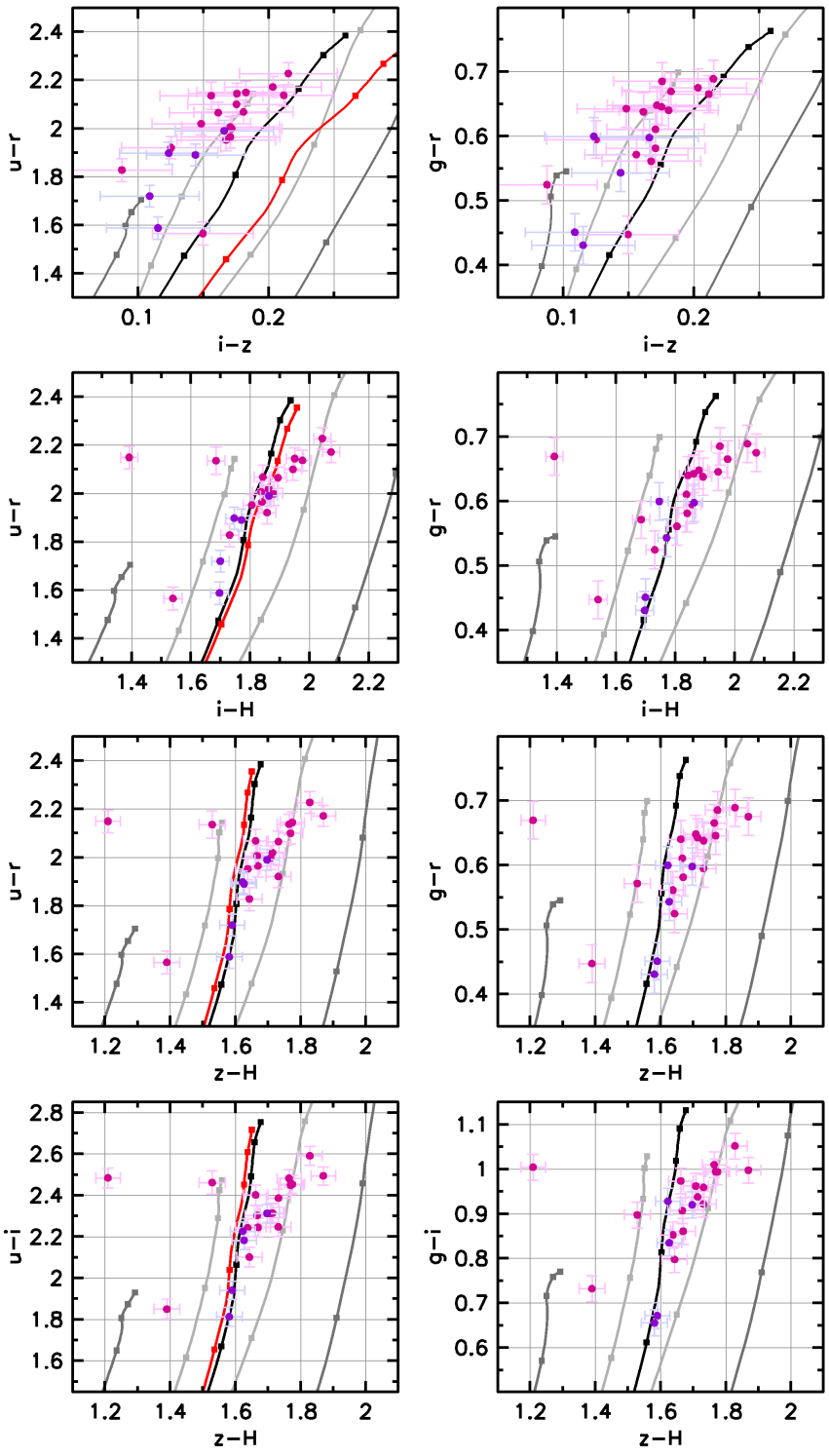

F 7.5. **Disentangling age and metallicity.** Purely optical colour-colour diagrams (top row) are compared to various optical-NIR diagrams. Symbols are the same as in Figure 7.2; colours are measured within the half-light aperture. Plot ranges are chosen to roughly cover the same age and metallicity ranges in each diagram. The left-hand diagrams include an additional model track for $Z = 0.008$ (red) that uses only the Bruzual & Charlot low resolution files, which are based on the BaSeL 3.1 library over the full wavelength range. All other tracks rely on the STELIB spectral library in the wavelength range 3200 – 9500 Å and on the BaSeL 3.1 spectral library outside this range. If both libraries would yield the same model colours, this track should be indistinguishable from the black $Z = 0.008$ track.

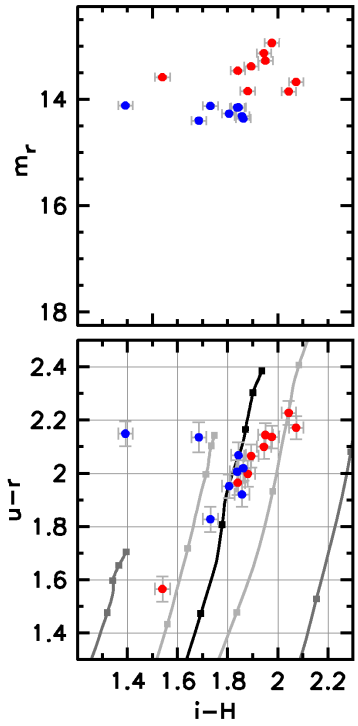

F 7.6. **Colour-magnitude relation I.** *Top panel:* r magnitude vs. $i-H$ colour for the dEs of our sample, excluding dE(bc)s. Red symbols mark objects brighter than $m_r = 14^m$, blue symbols stand for fainter objects. *Bottom panel:* $u-r$ vs. $i-H$ diagram as in Figures 7.2 to 7.4, with symbol colours as defined in the upper panel.

The narrow sequence defined by the majority of data points could perhaps be explained with a correlation between age and metallicity, like what was found in Chapter 5 for optical colours: if a dE is bluer in $u-r$ (i.e., younger) than the CMR at its magnitude, then it is, in most cases, also bluer in $i-z$ (i.e., less metal rich). We test the presence or absence of such a correlation in Figure 7.7, where we show the CMRs of the full dE sample for various colours. Objects from our working sample that fall on the blue side of the CMR in $u-r$ are shown with blue symbols, while objects falling on the red side are shown with red symbols. These symbol colours are kept in all panels of the figure. A correlation is seen for all optical colours, and also to some extent in $i-H$. It thus seems that this correlation could be responsible for the rather tight distribution of the majority of data points. However, reliable conclusions need to await the analysis of larger dE samples with NIR photometry.

4. S

We have presented an analysis of the optical and near-infrared colours of 22 Virgo cluster dEs, based on SDSS data as well as on ESO archival images. The majority of galaxies populate a rather narrow sequence in the $u-r$ vs. $i-H$ and $g-r$ vs. $i-H$ diagrams. Based on our population synthesis model (Bruzual & Charlot 2003) for an exponentially decaying burst of star formation, this sequence is similar to a curve of almost constant age. The metallicities of the majority of the (rather bright) dEs in our working sample range from slightly above solar to below the track for $Z = 0.008$ ($[Fe/H] = -0.33$); their ages lie between ∼4 and ∼6 Gyr. These values agree with the Lick index study of Geha et al. (2003), who analyzed 17 (also rather bright) dEs, and found a mean age of 5 Gyr and a mean metallicity of $[Fe/H] = -0.3$. While we have seen in the previous section that these absolute values depend to some extent on the ingredients of the population synthesis models, like the stellar libraries they are based on, the models used by Geha et al. are different from ours, thus

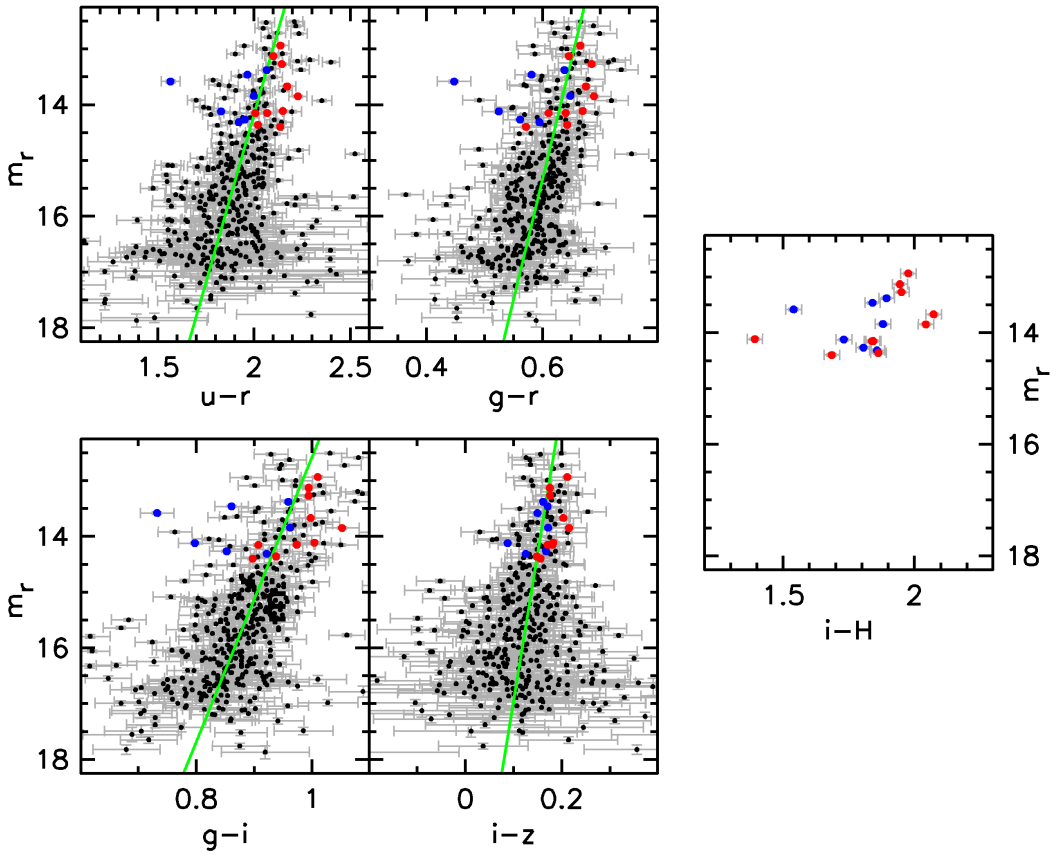

F 7.7. **Colour-magnitude relation II.** The four left panels show the optical colour-magnitude relations of our full sample of Virgo cluster dEs (excluding dE(bc)s) from Chapter 5 (Figure 5.11), based on the half-light aperture. The rightmost panel shows the colour-magnitude relation using $i - H$, as in Figure 7.6. Blue symbols mark those galaxies of our NIR sample that fall on the blue side of the CMR in $u - r$, red symbols mark objects that fall on the red side.

giving us somewhat more confidence in the above values. Note, though, that this statement applies only within the framework of single-burst models, which are most commonly used in the literature. Obviously, if we instead used a model with constant star formation rate, the derived ages would be different.

We found that the dE(N)s and the dE(di)s of our sample fall on the same sequence of data points, consistent with the similarity of their optical colours (Chapter 5). The dE(bc)s cover similar metallicities as the former, also consistent with their optical colours. However, note that the subsamples of dE(N)s, dE(di)s, and dE(bc)s only comprise 6, 9, and 5 galaxies, respectively. This is the disadvantage of our recommended (and necessary) separate treatment of different dE subclasses (Chapter 4): when performing this subdivision, the resulting subsamples are so small that they can hardly be used for drawing reliable stand-alone conclusions. Clearly, a much larger NIR dataset of Virgo cluster dEs would be desirable to perform a more comprehensive study of their stellar populations.

Acknowledgements

This study is based on publicly available data from the SDSS and the GOLDMine database.

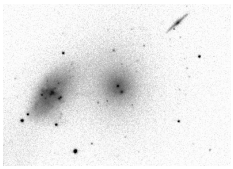

CHAPTER 8

D : ?

"And so you see I have come to doubt
all that I once held as true."
Simon & Garfunkel

In Chapters 2 to 4, we have established a subdivision of the dE class into those with and without disk features, those with and without a nucleus, and into brighter and fainter ones. We showed that significant differences between the shapes and distributions of these subclasses exist, which define a morphology-density relation, in the sense that the rounder dEs are preferentially located in regions of significantly higher density than the flatter ones. In Chapter 5, we then found that the bright dE(nN)s and dE(N)s have significantly different colours, and that the dE(di)s also slightly differ from the dE(N)s. Consequently, we could term these results a "morphology-density-colour relation". However, it is not the case that the flattest galaxies (the dE(di)s) have the bluest colours: they are only slightly bluer in $u - r$ than the roundest dEs (the dE(N)s), while the thick-disk-like bright dE(nN)s are bluer than both of the former, indicating younger mean ages. Given this diversity of subclass properties, it seems rather unlikely that a single formation process could account for all dEs. Still, we believe it is instructive to seek for a minimization of the number of formation scenarios required to interpret the dEs' properties, thereby trying to answer the question of how many different dE formation mechanisms there are *at least*.

Instead of proceeding with an attempt to assign a formation scenario to each dE subclass, let us tackle the above question in a different way, namely by first minimizing the number of actual subclasses. For example, how confident are we that the dE(di)s do not belong to the dE(N)s in some way or the other? The distribution of intrinsic shapes of the brighter dE(N)s, as deduced in Chapter 4, is rather broad and includes a significant number of flat objects, even down to axial ratios of below 0.3. Most of the range of intrinsic axial ratios of the dE(di)s is thus covered by the range of values of the dE(N)s, and after all, 73% of the dE(di)s are nucleated. While their colours are somewhat different from the full sample of dE(N)s, the difference is not anymore significant when compared only to the low-density dE(N)s, which have the same median density as the dE(di)s (Chapter 5). If disk substructure, like spiral arms or bars, could only occur in the flattest dEs, due to, e.g., the kinematical configuration of these objects, we would have automatically selected only intrinsically flat galaxies in our search for disk features (Chapter 2), and would obviously have found their flattening distribution to be consistent with disk galaxies. The fact that these show no central clustering could then be explained, for example, by the much stronger tidal heating that a galaxy experiences in denser regions of the cluster, leading to an earlier destruction of disk features (cf. Mastropietro et al. 2005). Similarly, if dE(N)s and dE(di)s originated from a morphological transformation of infalling late-type spirals through galaxy harassment (Moore et al. 1996), one could imagine that the amount of transformation depended on how close the encounters with massive galaxies were that led to it — and the probability for close(r) encounters is obviously higher in the cluster center, leading to rounder objects without disk features. Note, though, that we do not see a significant correlation between apparent shape and density *within* the dE(N)s — which, on the other hand, would be very difficult to discover, given that both shape and position within the cluster are seen in projection.

Why are there almost no fainter dE(di)s? While we found in Chapter 2 that we most likely missed a significant amount of dE(di)s at fainter magnitudes due to our detection limits, we also argued that the true number fraction *is* decreasing when going to fainter objects. As a simple possible explanation, we suggest that disk substructure might be less likely to occur in less massive galaxies, possibly connected to the presence of a certain amount of rotational velocity.

The nuclei in the dE(di)s and dE(N)s could either be the surviving nuclei of the progenitor galaxies, or they could have formed through central star formation from gas that was funneled to the center in the transformation process (cf. Chapter 3). If neither happened, a non-nucleated dE(di) could emerge. While these considerations unavoidably include a certain amount of speculation, they demonstrate that dE(di)s and dE(N)s could, in principle, have formed through the same formation process, keeping our counter of necessary dE formation mechanisms at 1 for the moment.

Let us now turn to the dE(nN)s. At least for the bright subsample, their colours differ significantly from those of the dE(N)s: they are clearly bluer in $u - r$ and $i - z$, probably indicating younger ages than those of the dE(N)s. This still holds true even when the different density distributions of dE(nN)s and dE(N)s are accounted for (Chapter 5). The colours of the faint dE(nN)s are still somewhat bluer in $u - r$ as compared to the faint dE(N)s, but their CMRs approach each other at these magnitudes. What could be the origin of the dE(nN)s? In Chapter 4, we noted that the faint dE(nN)s show a flattening distribution similar to that of the dwarf irregulars (dIrrs) given by Binggeli & Popescu (1995), and might thus have formed out of them through ram-pressure stripping or a similar process. Let us explore this possibility in somewhat more detail now. For 61 of the 70 dIrrs that are listed in the VCC and are certain cluster members, axial ratio estimates are provided by the VCC (column "log($R_{\rm est.}$)"). Thereby, we excluded galaxies with a "?" in the classification, or with uncertain type (e.g., "Im / dE"). While for the dE(nN)s, we could use our own axial ratio measurements, we aim at performing a valid comparison with the dIrrs, which would not be guaranteed when using axial ratios from two different datasets and methods. Instead, we use the values provided by the VCC for 148 of our 149 dE(nN)s. For our bright dE(nN)s, the median axial ratio is 0.51, while it is 0.71 for the faint dE(nN)s. A Student's t-test yields a probability of 0.0% for the two subsamples having the same mean value, similiar to what we found in Chapter 4. For the dIrrs, we did not perform any photometric measurements, and thus do not have r magnitudes available for a subdivision into bright and faint ones. Instead, we subdivide the dIrrs at their median B magnitude (provided by the VCC), $m_{\rm B} = 16\overset{\rm m}{.}40$. The brighter dIrrs have a median axial ratio of 0.54, while the value for the fainter ones is 0.63. A t-test yields a probability of 4.9% for the same mean value. If we separate the brighter and fainter dIrr subsamples more clearly, with requiring $m_{\rm B} \leq 16\overset{\rm m}{.}40 - 0\overset{\rm m}{.}50$ for the bright and $m_{\rm B} > 16\overset{\rm m}{.}40 + 0\overset{\rm m}{.}50$ for the faint subsample, the median axial ratios are 0.54 and 0.68, respectively, with a t-test probability of only 0.5%. These values, and the difference itself between the bright and faint dIrrs, are very similar to our results for the dE(nN)s, and imply that both the bright and faint dE(nN)s could indeed be stripped dIrrs.

In Figure 8.1, we compare the B magnitudes of dIrrs and dE(nN)s, in order to see whether the above scenario would be reasonable. It seems that with a certain amount of fading after the end of star formation (which is reasonable and necessary to assume), the dIrrs could at least qualitatively account for the dE(nN)s. However, the transformation of dIrrs into dEs or dSphs faces some commonly discussed problems: the offset in metallicity is too large, even when comparing only old stellar populations (Thuan 1985; Richer et al. 1998; Grebel et al. 2003), and the dIrrs were estimated to fade too strongly after cessation of star formation (Bothun et al. 1986). The latter argument is illustrated by a comparison of the images of three of the brightest dE(nN)s and three of the brightest dIrrs of the Virgo cluster in Figure 8.2: while one of these dE(nN)s seems to be similar in surface brightness to the dIrrs (but was actually classified as being peculiar), the surface brightness of the other two dE(nN)s is significantly higher. Allowing for some fading after the end of star formation in the dIrrs, it is clear that the surface brightnesses of the dIrrs would still have to be considerably increased if they were to evolve not only into faint, but also into bright dE(nN)s.

The above problems might be overcome by the scenario of tidally induced star formation in dIrrs (Davies & Phillipps 1988), in which the initially lower metallicity and surface brightness of a dIrr

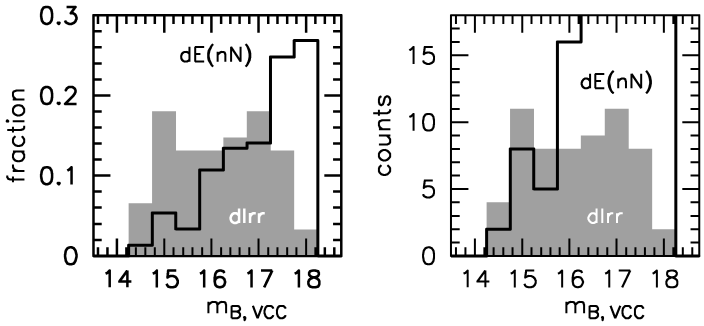

F 8.1. **Irregulars vs. dE(nN)s I.** The shaded grey histogram shows the distribution of *B* magnitudes (as given by the VCC) for the 61 dIrrs of the VCC (classified as "Im", including objects with a small uncertainty) that are certain cluster members and have $m_B \leq 18\overset{m}{.}0$ (the same magnitude selection is used throughout our studies). The black histogram shows the distribution of our sample of dE(nN)s. The left panel compares number fractions, while the right panel uses absolute numbers.

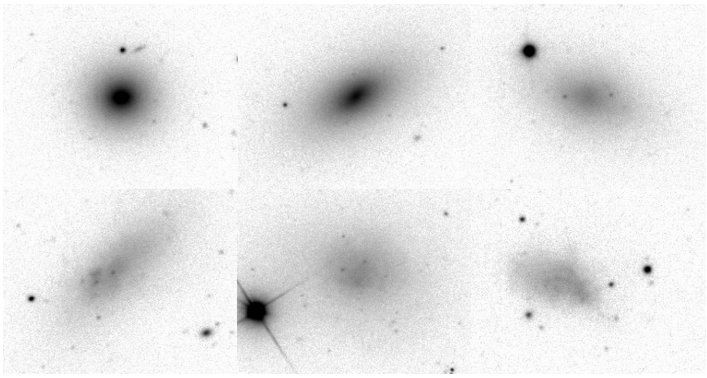

F 8.2. **Irregulars vs. dE(nN)s II.** SDSS images, constructed by co-adding the *g*, *r*, and *i* bands, for three of the brightest dE(nN)s (top row: VCC 1528, VCC 0543, VCC 1890) and three of the brightest dIrrs (bottom row: VCC 1114, VCC 1435, VCC 1200), based on VCC *B* magnitudes. All images are shown with the same scale, contrast, and intensity mapping.

are increased by several bursts of star formation, during which the galaxy appears as blue compact dwarf (BCD). After the last BCD phase it fades to become a dE. Whether or not this scenario is viable would require a comparison of the metallicities of dE(nN)s, dIrrs, and BCDs, e.g. with optical and near-infrared photometry (also see Chapter 7). An important step in this direction were the recent studies of Vaduvescu & McCall (2005) and Vaduvescu et al. (2006), who found BCDs to fall on the "fundamental plane of dIrrs", i.e., on a relatively tight relation between near-infrared (*K* band) absolute magnitude, central surface brightness, and H I line width. Vaduvescu & McCall (2005) showed that dEs follow the same relation when H I line width is substituted by stellar velocity dispersion, supporting the idea of an evolutionary relation between these types of galaxies.

From our optical colours, it seems that the dE(nN)s might have somewhat lower metallicities than the dE(N)s (though not necessarily in the inner regions, see Section 12), which could, in our above picture, be reflecting the fact that the dE(N)s originate from late-type spirals, while the dE(nN)s are formed from dIrrs. Both the dE(N)s and dE(nN)s show, on average, an internal colour gradient, which is likely to be a gradient of decreasing metallicity with radius. At least for the dE(nN)s, it seems that the stellar populations typically also are somewhat younger in the center than in the outer regions. This could be explained with the last star formation occuring in the galaxy centers, which probably happens for both tidally induced star formation (Davies & Phillipps 1988) and galaxy harassment (Moore et al. 1998). Therefore, the dE(bc)s – of which 7 out of 17 are nucleated and 4 display disk features – might not evolve into just one dE subclass, but might be a stage through which

every (proto-)dE goes. After all, it would seem hardly surprising if the last stages of star formation in a dE always occured in the center, independent of a particular formation scenario. A somewhat similar argument has been made by van Zee et al. 2004b, who stressed the inevitably gas-rich and star-forming nature of a dE progenitor. Note also that we found the metallicity of the dE(bc)s to be similar to that of the other dE subclasses. One caveat remains, though: the flattening distribution of the dE(bc)s suggests thick-disk-like shapes, similar to those of the bright dE(nN)s. On the other hand, if we considered the nucleated and non-nucleated dE(bc)s separately, their sample sizes would be too small to draw reliable conclusions on their intrinsic shapes.

We thus set our counter of necessary dE formation mechanisms to 2: the faint and bright dE(nN)s could have formed through one and the same mechanism, but for the dE(N)s and dE(di)s, the significantly different colours imply an other mechanism. The dE(bc)s might represent a common stage of dE formation.

Which other "combinations" of dE subclasses would seem possible? In our above discussion, we started by considering the differences in shape between the subclasses. Alternatively, we could start by considering the presence or absence of a nucleus. If nucleus formation would preferentially occur in the central cluster regions, like Oh & Lin (2000) predicted for nucleus formation through coalescence of globular clusters, this could explain the different clustering properties of dE(N)s and dE(nN)s without requiring them to be different dE types per se. However, why should the bright dE(nN)s then be flatter than the dE(N)s, and have significantly different colours? Moreover, why should bright and faint dE(nN)s have significantly different shapes, while bright and faint dE(N)s do not? Obviously, it would be important to gain a better understanding of nucleus formation, which currently is an active field of research (see, e.g., Grant et al. 2005; Côté et al. 2006; Wehner & Harris 2006) and will likely be better understood in the near future. For the time being, the perspective discussed here does not lead to an explanation of dE formation with less than two different mechanisms.

We finally perform another attempt of "formation scenario minimization", this time starting with colours and stellar population properties. Since the dE(nN)s seem to have younger ages than the dE(N)s, and are a much less relaxed population of galaxies, one might conjecture that they simply formed more recently, while the dE(N)s themselves are older (and thus, their stellar populations are older, too). The flatter shapes of the bright dE(nN)s could possibly be explained by the fact that they still need to experience several (further) encounters with massive galaxies, which will lead to further morphological transformation until they reach the shapes of the dE(N)s. Also, note that dE(N)s are far from being spherical, but are mainly consistent with oblate E4-shapes (Chapter 4). This scenario would require rather short relaxation timescales: today's dE(nN)s would need to be centrally clustered like the dE(N)s in a few gigayears from now, since this is the order of magnitude of their age difference. However, Conselice et al. (2001) derived a two-body relaxation time for the Virgo dEs of much more than a Hubble time. Even violent relaxation, which probably only applies for the case of infalling or merging groups, would take at least a few cluster crossing times $t_{\rm cr}$, with $t_{\rm cr} \approx 1.7$ Gyr for Virgo (Boselli & Gavazzi 2006). Despite these timescales, let us assume for the moment that dE(nN)s and dE(N)s indeed form an evolutionary sequence as outlined above, and that some mechanism for nucleus formation in the dE(nN)s' near future could be found as well. But how do we explain the dE(di)s in this picture? If they also belonged to the same galaxy population, how come that they are still flatter than the dE(nN)s, but already have colours similar to the dE(N)s, and how come that most of them already have nuclei? Obviously, also from this perspective, we need at least two different formation scenarios for the dE subclasses. We thus conclude by repeating the statement of van Zee et al. (2004b), "we caution against single-channel evolutionary scenarios." Early-type dwarfs are not a homogeneous class of objects, and we strongly recommend to separately analyze the properties of dEs belonging to different subclasses in any future study of dEs.

As for the question of "nature or nurture", we should perhaps give a definition of "nature" first. In the framework of hierarchical structure formation, galaxy clusters form by merging of smaller units, namely galaxy groups. "Nature" can thus not mean that dEs formed primordially in an ever-present cluster. Even the oldest and most relaxed population of galaxies, the bright ellipticals, might have been formed through mergers (e.g., Kauffmann & Charlot 1998), which would qualify as "nurture".

Likewise, preprocessing of dEs in groups would also be "nurture". The only "nature" dE formation would be if they formed out of their own gas clouds and their own dark matter halos, i.e., if they were a truly primordial population of galaxies, similar to what Rakos & Schombert (2004) suggested for the dE(N)s (see the discussion in Chapter 5). Since our results agree with theirs in that the dE(N)s appear to have the oldest stellar populations among the dE subclasses, let us try to test whether they could indeed be a primordial population that formed in groups, which later merged to form the Virgo cluster.

While the dE(N)s are not quite as strongly clustered as the Es are (see Chapter 4 and Conselice et al. 2001), maybe this could be explained with the much larger mass of the Es, whose kinematics are more "stable" to tidal encounters. It is perhaps more illuminating here to compare the colours of dE(N)s and Es. Based on SDSS data, Bernardi et al. (2003) derive a slope of the CMR in $g - r$ of -0.025 ± 0.003, equal to our value for the dE(N)s when using the half-light aperture. Our zeropoint is 0.996, and when we adopt $m - M = 31.^{\mathrm{m}}0$, the zeropoint of Bernardi et al. is 0.993, i.e., basically equal. While the same slope is found also by Chang et al. (2006) in an analysis of Es with SDSS data, their zeropoint is redder by 0.069. We refer to the discussion in Bernardi et al. (2003) about how slope and zeropoint depend on the aperture and the way in which colours are measured — unfortunately, the colour values were obtained in a different way in these studies and in our study. Nevertheless, it seems that dE(N)s and Es might follow the same CMR. However, the CMR of the dE(N)s shows a dependence on local density. In other words, the stellar populations of the dE(N)s are (slightly, but significantly) different in cluster regions of different density. How could this be explained if the stellar populations had already fully formed before they even entered the cluster? One possibility could be that, in the framework of hierarchical structure formation, denser groups form in denser regions of the Universe, merge earlier, and consequently end up in the central, dense regions of the cluster that we see today. However, we argued in Chapter 5 that the CMR is not simply different in the central cluster regions, but it probably depends directly on local density. A quarter of the galaxies in the high-density dE(N) subsample are *not* located in the cluster center, yet share the same CMR. How did their different progenitor groups "know of each other", also given that the CMRs of the high and low-density subsamples are both fairly narrow and have a similar RMS scatter? Note that these counter-arguments do not only apply to actual primordial formation, but also generally to preprocessing of dEs in groups that later end up in the cluster. While we cannot fully exclude the scenario that most or all dE(N)s formed in groups, the above considerations suggest that dE(N)s, as well as the dE(nN)s, probably formed within the cluster potential, thus favouring mechanisms that invoke the infall and transformation of late-type galaxies . We recall here the statement of Conselice et al. (2001), who pointed out that the number of Virgo cluster dEs is more than a factor of 3 larger than what would be expected from just adding groups to the cluster, supporting our "nurture" view.

Nevertheless, nature obviously sets some rules for the nurture of the dEs: their colours seem to be mainly determined by the CMR and its relation with density — even though we found a region with somewhat higher ages of dE(N)s as the only significant age substructure in the dynamically young Virgo cluster. Furthermore, the colour residuals about the CMR are clearly not just random scatter: a dE(N) that is bluer in $u - r$, i.e., younger, than average, is in most cases also bluer in $i - z$, i.e., less metal rich. At least for $u - r$ and $g - i$, this applies to the dE(nN)s as well. Thus, the final colour of a dE is more nature-determined than one might think in the light of the variety of possible nurture-processes. We therefore decided to answer the title question with a confident

"Nurture *within* nature!"

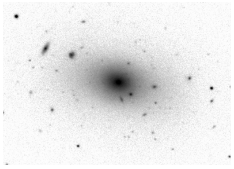

CHAPTER 9

S

"I'm just trying to matter."
June Carter

In order to provide a concise overview of our main conclusions without just repeating the individual summary of each chapter, we decided to highlight again those figures that we believe to contain the most important results of our research.

Figure 2.8: What creates and determines the shape of the spiral arms that are seen in some dEs? Our derived pitch angles, as well as the grand-design structure of the arms, clearly show that they cannot just be the remainder of the spiral arms of potential late-type progenitor galaxies.

Figure 3.9: While a young stellar population dominates the light at the centers of the dE(bc)s, 90% or more of the *mass* is made up by an old stellar population. Not long after cessation of star formation, these galaxies will just be ordinary dEs.

Figure 4.2: Several dE subclasses exist that have different shapes and different distributions within the cluster, defining a morphology-density relation within the dE class.

Figure 5.18: The colour-magnitude relation of the Virgo cluster dEs depends slightly, yet significantly, on local environmental density.

Figure 5.29: While the shape and distribution of the dE(di)s are much more like those of the bright dE(nN)s than like those of the dE(N)s, their stellar populations are similar to those of the dE(N)s, which in turn are significantly different from those of the dE(nN)s.

Figure 6.27: A region of higher stellar population ages of the dE(N)s is located south-east from the cluster center. It is consistently seen both for the low and the high-density subsample, and coincides with a region of stronger X-ray emission.

Figure 7.5: Complementing optical with near-infrared photometry enables a much more reliable analysis of ages and metallicities, and reveals a rather narrow sequence of dEs in colour space.

Even though we speculated in the previous chapter about possible evolutionary links between certain subclasses, the bottom line of our study is that the dEs are *not* a homogeneous class of galaxies, and can *not* be explained with just a single formation mechanism.

Bibliography

Abraham, R. G., Valdes, F., Yee, H. K. C., & van den Bergh, S. 1994, ApJ, 432, 75
Adelman-McCarthy, J. K., Agüeros, M. A., Allam, S. S., et al. 2006, ApJS, 162, 38
Adelman-McCarthy, J. K., Agüeros, M. A., Allam, S. S., et al. 2007, ApJS, submitted
Aguerri, J. A. L., Iglesias-Páramo, J., Vílchez, J. M., Muñoz-Tuñón, C., & Sánchez-Janssen, R. 2005, AJ, 130, 475
Arnaboldi, M., Gerhard, O., Aguerri, J. A. L., et al. 2004, ApJ, 614, L33
Barazza, F. D., Binggeli, B., & Jerjen, H. 2002, A&A, 391, 823
Barazza, F. D., Binggeli, B., & Jerjen, H. 2003, A&A, 407, 121
Baum, W. A. 1959, PASP, 71, 106
Bender, R., Ziegler, B., & Bruzual, G. 1996, ApJ, 463, L51
Bernardi, M., Nichol, R. C., Sheth, R. K., Miller, C. J., & Brinkmann, J. 2006, AJ, 131, 1288
Bernardi, M., Sheth, R. K., Annis, J., et al. 2003, AJ, 125, 1882
Bertelli, G., Bressan, A., Chiosi, C., Fagotto, F., & Nasi, E. 1994, A&AS, 106, 275
Bertin, E. & Arnouts, S. 1996, A&AS, 117, 393
Binggeli, B. 1985, in Star-Forming Dwarf Galaxies and Related Objects, ed. D. Kunth, T. X. Thuan, & J. Tran Thanh Van, 53
Binggeli, B. & Cameron, L. M. 1991, A&A, 252, 27
Binggeli, B. & Cameron, L. M. 1993, A&AS, 98, 297
Binggeli, B. & Popescu, C. C. 1995, A&A, 298, 63
Binggeli, B., Popescu, C. C., & Tammann, G. A. 1993, A&AS, 98, 275
Binggeli, B., Sandage, A., & Tammann, G. A. 1985, AJ, 90, 1681
Binggeli, B., Tammann, G. A., & Sandage, A. 1987, AJ, 94, 251
Böhringer, H., Briel, U. G., Schwarz, R. A., et al. 1994, Nature, 368, 828
Böker, T., Walcher, C. J., Rix, H. W., et al. 2004, in ASP Conf. Ser. 322: The Formation and Evolution of Massive Young Star Clusters, ed. H. J. G. L. M. Lamers, L. J. Smith, & A. Nota, 39
Boselli, A., Cortese, L., Deharveng, J. M., et al. 2005, ApJ, 629, L29
Boselli, A. & Gavazzi, G. 2006, PASP, 118, 517
Boselli, A., Iglesias-Páramo, J., Vílchez, J. M., & Gavazzi, G. 2002, A&A, 386, 134
Bothun, G. D., Mould, J. R., Caldwell, N., & MacGillivray, H. T. 1986, AJ, 92, 1007
Bower, R. G., Lucey, J. R., & Ellis, R. S. 1992, MNRAS, 254, 601
Brosch, N., Almoznino, E., & Heller, A. B. 2004, MNRAS, 349, 357
Bruzual A., G., & Charlot, S. 1993, ApJ, 405, 538
Bruzual A., G., & Charlot, S. 2000, Galaxy isochrone spectral synthesis evolution library (private communication)
Bruzual, G. & Charlot, S. 2003, MNRAS, 344, 1000
Buyle, P., De Rijcke, S., Michielsen, D., Baes, M., & Dejonghe, H. 2005, MNRAS, 360, 853
Caldwell, N. 1983, AJ, 88, 804
Caldwell, N., Rose, J. A., & Concannon, K. D. 2003, AJ, 125, 2891
Calzetti, D., Armus, L., Bohlin, R. C., et al. 2000, ApJ, 533, 682
Chabrier, G. 2003, PASP, 115, 763
Chang, R., Shen, S., Hou, J., Shu, C., & Shao, Z. 2006, MNRAS, 372, 199
Charbonnel, C., Maeder, A., Schaller, G., et al. 1993, A&AS, 101, 415
Charlot, S., & Bruzual A., G. 1991, ApJ, 367, 126

Cid Fernandes, R., Leão, J. R. S., & Lacerda, R. R. 2003, MNRAS, 340, 29
Conselice, C. J., Bershady, M. A., & Jangren, A. 2000, ApJ, 529, 886
Conselice, C. J., Gallagher, III, J. S., & Wyse, R. F. G. 2001, ApJ, 559, 791
Conselice, C. J., Gallagher, III, J. S., & Wyse, R. F. G. 2002, AJ, 123, 2246
Conselice, C. J., Gallagher, III, J. S., & Wyse, R. F. G. 2003a, AJ, 125, 66
Conselice, C. J., O'Neil, K., Gallagher, J. S., & Wyse, R. F. G. 2003, ApJ, 591, 167
Côté, P. 2005, in IAU Colloq. 198: Near-field cosmology with dwarf elliptical galaxies, ed. H. Jerjen & B. Binggeli, 269
Côté, P., Blakeslee, J. P., Ferrarese, L., et al. 2004, ApJS, 153, 223
Côté, P., Piatek, S., Ferrarese, L., et al. 2006, ApJS, 165, 57
Cuisinier, F., Westera, P., Telles, E., & Buser, R., 2006, A&A, 423, 133
Davies, J. I. & Phillipps, S. 1988, MNRAS, 233, 553
De Rijcke, S., Dejonghe, H., Zeilinger, W. W., & Hau, G. K. T. 2003, A&A, 400, 119
De Rijcke, S., Michielsen, D., Dejonghe, H., Zeilinger, W. W., & Hau, G. K. T. 2005, A&A, 438, 491
de Vaucouleurs, G. 1961, ApJS, 5, 233
de Vaucouleurs, G., de Vaucouleurs, A., Corwin, Jr., H. G., et al. 1991, Third Reference Catalogue of Bright Galaxies (Volume 1-3, XII, 2069 pp. 7 figs.. Springer-Verlag Berlin Heidelberg New York)
Dressler, A. 1980, ApJ, 236, 351
Drinkwater, M. J., Currie, M. J., Young, C. K., Hardy, E., & Yearsley, J. M. 1996, MNRAS, 279, 595
Drinkwater, M. J., Gregg, M. D., Holman, B. A., & Brown, M. J. I. 2001, MNRAS, 326, 1076
Erwin, P. 2004, A&A, 415, 941
Faber, S. M. 1973, ApJ, 179, 731
Faber, S. M. & Jackson, R. E. 1976, ApJ, 204, 668
Fagotto, F., Bressan, A., Bertelli, G., & Chiosi, C. 1994, A&AS, 105, 29
Falco, E. E., Kurtz, M. J., Geller, M. J., et al. 1999, PASP, 111, 438
Fall, S. M. & Frenk, C. S. 1983, AJ, 88, 1626
Ferguson, H. C. & Binggeli, B. 1994, A&A Rev., 6, 67
Ferguson, H. C. & Sandage, A. 1989, ApJ, 346, L53
Ferrarese, L., Côté, P., Jordán, A., et al. 2006, ApJS, 164, 334
Ferrarese, L., Mould, J. R., Kennicutt, Jr., R. C., et al. 2000, ApJ, 529, 745
Ferreras, I., Charlot, S., & Silk, J. 1999, ApJ, 521, 81
Ferreras, I., Lisker, T., Carollo, C. M., Lilly, S. J., & Mobasher, B. 2005, ApJ, 635, 243
Fluks, M. A., Plez, B., The, P. S., et al. 1994, A&AS, 105, 311
Fouqué, P., Bottinelli, L., Gouguenheim, L., & Paturel, G. 1990, ApJ, 349, 1
Gavazzi, G., Bonfanti, C., Pedotti, P., Boselli, A., & Carrasco, L. 2000, A&AS, 146, 259
Gavazzi, G., Boselli, A., Donati, A., Franzetti, P., & Scodeggio, M. 2003, A&A, 400, 451
Gavazzi, G., Boselli, A., Scodeggio, M., Pierini, D., & Belsole, E. 1999, MNRAS, 304, 595
Gavazzi, G., Boselli, A., van Driel, W., & O'Neil, K. 2005, A&A, 429, 439
Gavazzi, G., Zaccardo, A., Sanvito, G., Boselli, A., & Bonfanti, C. 2004, A&A, 417, 499
Gavazzi, G., Zibetti, S., Boselli, A., et al. 2001, A&A, 372, 29
Geha, M., Guhathakurta, P., & van der Marel, R. P. 2003, AJ, 126, 1794
Girardi, L., Bressan, A., Chiosi, C., Bertelli, G., & Nasi, E. 1996, A&AS, 117, 113
Girardi, L., Bressan, A., Bertelli, G., & Chiosi, C. 2000, A&AS, 141, 371 ("Padova 2000" isochrones)
Graham, A. W., Jerjen, H., & Guzmán, R. 2003, AJ, 126, 1787
Grant, N. I., Kuipers, J. A., & Phillipps, S. 2005, MNRAS, 363, 1019
Grebel, E. K. 1997, in Reviews in Modern Astronomy 10, ed. R. E. Schielicke, 29
Grebel, E. K. 2001, Astrophysics and Space Science Supplement, 277, 231
Grebel, E. K., Gallagher, J. S., & Harbeck, D. 2003, AJ, 125, 1926
Grogin, N. A., Geller, M. J., & Huchra, J. P. 1998, ApJS, 119, 277
Gu, Q., Zhao, Y., Shi, L., Peng, Z., & Luo, X. 2006, AJ, 131, 806
Gunn, J. E., Carr, M., Rockosi, C., et al. 1998, AJ, 116, 3040
Gunn, J. E. & Gott, J. R. I. 1972, ApJ, 176, 1

Guzman, R., Koo, D. C., Faber, S. M., et al. 1996, ApJ, 460, L5
Harbeck, D., Grebel, E. K., Holtzman, J., et al. 2001, AJ, 122, 3092
Hilker, M., Infante, L., Vieira, G., Kissler-Patig, M., & Richtler, T. 1999, A&AS, 134, 75
Hodge, P. W. 1963, AJ, 68, 691
Hodge, P. W. 1973, ApJ, 182, 671
Huchtmeier, W. K. & Richter, O.-G. 1986, A&AS, 64, 111
Huchtmeier, W. K. & Richter, O.-G. 1989, A&A, 210, 1
Jerjen, H. & Binggeli, B., eds. 2005, Near-field cosmology with dwarf elliptical galaxies
Jerjen, H., Binggeli, B., & Barazza, F. D. 2004, AJ, 127, 771
Jerjen, H., Kalnajs, A., & Binggeli, B. 2000, A&A, 358, 845
Jerjen, H., Kalnajs, A., & Binggeli, B. 2001, in ASP Conf. Ser. 230: Galaxy Disks and Disk Galaxies, 239
Johnson, R. A., Lawrence, A., Terlevich, R., & Carter, D. 1997, MNRAS, 287, 333
Joye, W. A. & Mandel, E. 2003, in ASP Conf. Ser. 295: Astronomical Data Analysis Software and Systems XII, 489
Kashlinsky, A., Arendt, R. G., Mather, J., & Moseley, S. H. 2006, ArXiv Astrophysics e-prints, astro-ph/0612447
Kauffmann, G. & Charlot, S. 1998, MNRAS, 294, 705
Knezek, P. M., Sembach, K. R., & Gallagher, J. S. 1999, ApJ, 514, 119
Kniazev, A. Y., Grebel, E. K., Pustilnik, S. A., et al. 2004, AJ, 127, 704
Kodama, T. & Arimoto, N. 1997, A&A, 320, 41
Kong, X., Charlot, S., Weiss, A., & Cheng, F. 2003, A&A, 403, 877
Le Borgne, J.-F., Bruzual A., G., Pell'o, R., et al. 2003, A&A, 402, 433
Leitherer, C., Schaerer, D., Goldader, J. D., et al. 1999, ApJS, 123, 3
Lejeune, T., Cuisinier, F., & Buser, R. 1997, A&AS, 125, 229
Lejeune, T., Cuisinier, F., & Buser, R. 1998, A&AS, 130, 65
Lilly, T. & Fritze-v. Alvensleben, U. 2003, in IAU Sympos. 221, 80
Lisker, T., Debattista, V. P., Ferreras, I., & Erwin, P. 2006a, MNRAS, 370, 477
Lisker, T., Glatt, K., Westera, P., & Grebel, E. K. 2006c, AJ, 132, 2432
Lisker, T., Grebel, E. K., & Binggeli, B. 2005, in IAU Colloq. 198: Near-field cosmology with dwarf elliptical galaxies, ed. H. Jerjen & B. Binggeli, 311
Lisker, T., Grebel, E. K., & Binggeli, B. 2006b, AJ, 132, 497
Lisker, T., Grebel, E. K., Binggeli, B., & Glatt, K. 2007, ApJ, in press, ArXiv Astrophysics e-prints, astro-ph/0701429
Lotz, J. M., Miller, B. W., & Ferguson, H. C. 2004b, ApJ, 613, 262
Lotz, J. M., Primack, J., & Madau, P. 2004a, AJ, 128, 163
Lupton, R. H. & Monger, P. 1997, The SM Reference Manual, http://www.astro.princeton.edu/~rhl/sm/sm.html
Ma, J. 2001, Chinese Journal of Astronony and Astrophysics, 1, 395
Ma, J., Zhao, J. L., Shu, C. G., & Peng, Q. H. 1999, A&A, 350, 31
Maraston, C. 2005, MNRAS, 362, 799
Marchant, A. B. & Olson, D. W. 1979, ApJ, 230, L157
Mastropietro, C., Moore, B., Mayer, L., et al. 2005, MNRAS, 364, 607
Mateo, M. L. 1998, ARA&A, 36, 435
Matković, A. & Guzmán, R. 2005, MNRAS, 362, 289
Mayer, L., Governato, F., Colpi, M., et al. 2001a, ApJ, 559, 754
Mayer, L., Governato, F., Colpi, M., et al. 2001b, ApJ, 547, L123
Meynet, G., Maeder, A., Schaller, G., Schaerer, D., & Charbonnel, C. 1994, A&AS, 103, 97
Mihalas, D. & Binney, J. 1981, Galactic astronomy: Structure and kinematics (San Francisco, CA, W. H. Freeman and Co.)
Moore, B., Katz, N., Lake, G., Dressler, A., & Oemler, A. 1996, Nature, 379, 613
Moore, B., Lake, G., & Katz, N. 1998, ApJ, 495, 139

Morelli, L., Halliday, C., Corsini, E. M., et al. 2004, MNRAS, 354, 753
Mori, M. & Burkert, A. 2000, ApJ, 538, 559
Neilsen, Jr., E. H. & Tsvetanov, Z. I. 2000, ApJ, 536, 255
Ochsenbein, F., Bauer, P., & Marcout, J. 2000, A&AS, 143, 23
Oh, K. S. & Lin, D. N. C. 2000, ApJ, 543, 620
Oke, J. B. & Gunn, J. E. 1983, ApJ, 266, 713
Osterbrock, D. E. 1989, Astrophysics of Gaseous Nebulae and Active Galactic Nuclei (Mill Valley: University Science Books)
Papaderos, P., Loose, H.-H., Fricke, K. J., & Thuan, T. X. 1996, A&A, 314, 59
Persson, S. E., Murphy, D. C., Krzeminski, W., Roth, M., & Rieke, M. J. 1998, AJ, 116, 2475
Petrosian, V. 1976, ApJ, 209, L1
Pier, J. R., Munn, J. A., Hindsley, R. B., et al. 2003, AJ, 125, 1559
Press, W. H. 2002, Numerical recipes in C++ : the art of scientific computing (ISBN : 0521750334)
Rakos, K. & Schombert, J. 2004, AJ, 127, 1502
Ramella, M., Geller, M. J., Pisani, A., & da Costa, L. N. 2002, AJ, 123, 2976
Richer, M., McCall, M. L., & Stasinska, G. 1998, A&A, 340, 67
Richstone, D. O. 1979, ApJ, 234, 825
Ryden, B. S. & Terndrup, D. M. 1994, ApJ, 425, 43
Ryden, B. S., Terndrup, D. M., Pogge, R. W., & Lauer, T. R. 1999, ApJ, 517, 650
Sandage, A. & Binggeli, B. 1984, AJ, 89, 919
Sandage, A. & Visvanathan, N. 1978a, ApJ, 223, 707
Sandage, A. & Visvanathan, N. 1978b, ApJ, 225, 742
Schaerer, D., Charbonnel, C., Meynet, G., Maeder, A., & Schaller, G. 1993a, A&AS, 102, 339
Schaerer, D., Meynet, G., Maeder, A., & Schaller, G. 1993b, A&AS, 98, 523
Schaller, G., Schaerer, D., Meynet, G., & Maeder, A. 1992, A&AS, 96, 269
Schindler, S., Binggeli, B., & Böhringer, H. 1999, A&A, 343, 420
Schlegel, D. J., Finkbeiner, D. P., & Davis, M. 1998, ApJ, 500, 525
Schmutz, W., Leitherer, C., & Gruenwald, R. 1992, PASP, 104, 1164
Schombert, J. M., Pildis, R. A., Eder, J. A., & Oemler, A. J. 1995, AJ, 110, 2067
Schröder, A. 1995, Ph.D. Thesis
Secker, J., Harris, W. E., & Plummer, J. D. 1997, PASP, 109, 1377
Simien, F. & Prugniel, P. 2002a, A&A, 384, 371
Simien, F. & Prugniel, P. 2002b, A&A, 384, 371
Smith, J. A., Tucker, D. L., Kent, S., et al. 2002, AJ, 123, 2121
Stoughton, C., Lupton, R. H., Bernardi, M., et al. 2002, AJ, 123, 485
Strader, J., Brodie, J. P., Spitler, L., & Beasley, M. A. 2006, AJ, 132, 2333, referring to submitted version, 2005 Jul 29, ArXiv Astrophysics e-prints, astro-ph/0508001
Strauss, M. A., Huchra, J. P., Davis, M., et al. 1992, ApJS, 83, 29
Thuan, T. X. 1985, ApJ, 299, 881
Tody, D. 1993, in ASP Conf. Ser. 52: Astronomical Data Analysis Software and Systems II, 173
Torres-Peimbert, S., Peimbert, M., & Fiero, J. 1989, ApJ, 345, 186
Tully, R. B. & Shaya, E. J. 1984, ApJ, 281, 31
Vaduvescu, O. & McCall, M. L. 2005, in IAU Colloq. 198: Near-field cosmology with dwarf elliptical galaxies, ed. H. Jerjen & B. Binggeli, 265
Vaduvescu, O., Richer, M. G., & McCall, M. L. 2006, AJ, 131, 1318
van den Bergh, S. 1986, AJ, 91, 271
van Driel, W., Ragaigne, D., Boselli, A., Donas, J., & Gavazzi, G. 2000, A&AS, 144, 463
van Zee, L., Barton, E. J., & Skillman, E. D. 2004a, AJ, 128, 2797
van Zee, L., Skillman, E. D., & Haynes, M. P. 2004b, AJ, 128, 121
Vigroux, L., Souviron, J., & Vader, J. P. 1984, A&A, 139, L9
Wehner, E. H. & Harris, W. E. 2006, ApJ, 644, L17
West, M. J. & Blakeslee, J. P. 2000, ApJ, 543, L27

Westera, P. 2001, PhD thesis, Univ. of Basel
Westera, P., Lejeune, T., Buser, R., Cuisinier, F., & Bruzual A., G. 2002, A&A, 381, 524
Westera, P., Cuisinier, F., Telles, E., & Kehrig, C. 2004, A&A, 423, 133
Wright, E. L. 2006, ArXiv Astrophysics e-prints, astro-ph/0609593
York, D. G., Adelman, J., Anderson, J. E., et al. 2000, AJ, 120, 1579
Young, C. K. & Currie, M. J. 1995, MNRAS, 273, 1141

Acknowledgements

First and foremost, I would like to thank Eva Grebel for the opportunity to do my PhD in Basel, which I have enjoyed immensely, as well as for her always excellent advice on matters of science, diplomacy, and chocolate. I would also like to express my gratitude to Bruno Binggeli for countless helpful, encouraging, and pleasant discussions, without which the thesis would not be what it has become. Moreover, thanks to all the current and former members of the Astronomical Institute Basel for a wonderful and unique atmosphere.

My warmest thanks go to my wife and my family, for their continuous support and encouragement. Furthermore, I am indebted to Victor Debattista, Ignacio Ferreras, Anna Pasquali, and Frank van den Bosch, for their friendly advice in times of difficult decisions, and for many enjoyable moments. I would also like to thank the people who "got me on track": Thomas Friedel, Herold Mönch, Stefan Bärthlein, and Uli Heber. Finally, I am grateful to Wolfgang Löffler for excellent computer support, Martin Altmann for some great SM *macros (check out his webpage at http://www.astro.uni-bonn.de/~maltmann/), Simon Lilly for a detailed introduction into near-infrared observing and data reduction, and everyone who helped me with all those technical things that one needs to know.*

The research presented in this thesis would not have been possible without the wealth of publicly available data from the SDSS, or without the fantastic work of those who created and maintain the SDSS webpages. Funding for the SDSS has been provided by the Alfred P. Sloan Foundation, the Participating Institutions, the National Science Foundation, the U.S. Department of Energy, the National Aeronautics and Space Administration, the Japanese Monbukagakusho, the Max Planck Society, and the Higher Education Funding Council for England. The SDSS Web Site is http://www.sdss.org/. The SDSS is managed by the Astrophysical Research Consortium for the Participating Institutions. The Participating Institutions are the American Museum of Natural History, Astrophysical Institute Potsdam, University of Basel, Cambridge University, Case Western Reserve University, University of Chicago, Drexel University, Fermilab, the Institute for Advanced Study, the Japan Participation Group, Johns Hopkins University, the Joint Institute for Nuclear Astrophysics, the Kavli Institute for Particle Astrophysics and Cosmology, the Korean Scientist Group, the Chinese Academy of Sciences (LAMOST), Los Alamos National Laboratory, the Max-Planck-Institute for Astronomy (MPIA), the Max-Planck-Institute for Astrophysics (MPA), New Mexico State University, Ohio State University, University of Pittsburgh, University of Portsmouth, Princeton University, the United States Naval Observatory, and the University of Washington.

This research has made extensive use of NASA's Astrophysics Data System Bibliographic Services, and of the NASA/IPAC Extragalactic Database (NED) which is operated by the Jet Propulsion Laboratory, California Institute of Technology, under contract with the National Aeronautics and Space Administration.

F , .
A ’ .

Jean-Luc Picard